

2 THE SCIENCE DRIVING THE 12 GeV UPGRADE OF CEBAF

2.A Gluonic Excitations and the Origin of Quark Confinement

2.A.1 Introduction

The primary goal of the GLUEX project is the definitive and detailed mapping of the spectrum of a new family of particles called *hybrid mesons*. Linearly polarized photons produced by electrons from an energy-upgraded CEBAF will be the probe used to uncover this spectrum. This experimental information is absolutely critical in finding the answer to an outstanding and fundamental questions in physics – a quantitative understanding of the confinement mechanism in quantum chromodynamics.

The spectrum of mesons and baryons uncovered during the 1960's led to the quark model within which mesons are bound states of a quark and antiquark, $q\bar{q}$, and baryons are bound states of three quarks, qqq . Further experimental work indicated that quarks are dynamical objects as well and this led to the development of quantum chromodynamics (QCD), the theory of quarks and gluons and their interactions modeled after the very successful theory of quantum electrodynamics (QED). Just as charged particles interact by the exchange of photons, quarks, with their color charge, interact by exchanging gluons. There are however important and fundamental differences between the two theories. There are three types of color charge as opposed to one kind of electrical charge. And the gluons of QCD also carry color charge and can interact with quarks and each other. In contrast, the photons of QED do not carry charge. Bound states involving quarks and gluons or quarks alone are thus possible and indeed should exist. QCD also incorporates the experimental fact that the quarks and gluons do not exist as free particles by requiring that only color singlet combinations exist as free particles in nature. In addition to the color singlet combinations $q\bar{q}$ and qqq others are possible, such as $q\bar{q}g$ (*hybrid mesons*) and gg or ggg (*glueballs*). These new states, collectively known as *gluonic excitations*, are fascinating since this is the only case of a theory in which the gauge particle is also a constituent. The analogous states in QED, like atoms of light, cannot exist. Although there is tantalizing evidence for these gluonic excitations, their spectra have not been mapped out.

The confinement of quarks and gluons within the particles of which they are the constituents is a unique feature of QCD. But a quantitative understanding of the confinement mechanism still eludes us. Theoretical progress is being made and lattice QCD, based on first-principle calculations, will ultimately be able to predict a detailed spectrum, including masses and decays, of hybrid mesons and glueballs. The experimental information about the spectrum of this new form of matter as predicted by QCD is an essential ingredient for the ultimate understanding of the confinement mechanism.

The low-lying glueball states will be searched for in the glue-rich J/ψ radiative decays as part

of the planned CLEO-c project at Cornell's CESR. However the low-lying glueballs possess J^{PC} quantum numbers that are the same as $q\bar{q}$ states and therefore mixing with conventional $q\bar{q}$ mesons is possible and that can complicate glueball identification. In contrast, hybrid mesons can possess J^{PC} quantum numbers not possible for $q\bar{q}$. These *exotic hybrid mesons* thus have a *smoking gun signature*. Just as nonets of $q\bar{q}$ mesons made of the three light quarks (u , d and s) exist, nature should also reveal nonets of hybrids with the same flavor quantum numbers but with now with the possibility of exotic J^{PC} . Hybrid mesons should also have widths comparable to conventional mesons. This is supported by theoretical considerations and by the possible sighting of an exotic hybrid in π^- -induced interactions.

Hybrid mesons can be thought of as $q\bar{q}g$ bound states in which the gluon is a constituent. An attractive alternative picture is one in which a gluonic flux tube forms between the q and \bar{q} in a meson. This flux tube forms because of the self-interaction of the gluons and qualitatively accounts for confinement. It leads to a linear potential, or a force that is constant as the distance between the quark and anti-quark varies. Infinite energy is required to separate the quarks to infinity, thus qualitatively accounting for confinement. This notion of a relativistic string or flux tube between the quarks was introduced in the 1970's to account for the observed linear dependence of particle mass-squared (m^2) on spin (J). The flux tube concept is supported by lattice QCD studies. Within this picture conventional mesons result when the flux tube is in its ground state. Hybrid mesons arise when the flux tube is excited. The lack of information on this spectroscopy is due in part to the complicated decay modes favored by these states and also due to the apparent suppression of exotic hybrid mesons in production mechanisms with π or K probes. On the other hand production of exotic hybrid mesons is expected to be favored using beams of photons and essentially no data exist on the photoproduction of light mesons. The GLUEX project will remedy this situation.

In addition to providing for a linearly polarized photon beam of sufficient energy, the GLUEX project includes construction of a hermetic detector to allow for particle identification and momentum and energy determination sufficient to allow for complete kinematic reconstruction of events with a wide variety of final states. This is essential for the spin analysis – partial wave analysis (PWA) – needed to determine the J^{PC} quantum numbers, to map out the flavor quantum numbers of the hybrid nonets and to test assumptions about the details of confinement that would lead to predicting specific decay modes.

In this chapter we expand on the following:

1. *Spectroscopy of Light Mesons*. This will include a brief review of the conventional quark model and the status of the light quark meson spectrum.
2. *Gluonic excitations and the role in QCD*. This will include a discussion of how the gluons form flux tubes, and how their excitations lead to QCD mesons, in particular exotic hybrids. This general picture is not restricted to a particular model but follows from the first-principles QCD calculations.

3. *The current evidence for gluonic excitations.* The evidence comes from overpopulation of conventional nonets and from possible glueball and exotic hybrid sightings in $\bar{p}p$ annihilations and π -induced interactions.
4. *Photons are expected to be particularly effective in producing exotic hybrids.* Its spin structure makes the photon a qualitatively different probe from π and K beams. The first excited transverse modes of the flux tube can lead to exotic hybrids only when the quark spins are aligned. This argument is consistent with expectations from models based on phenomenological analyses of existing data that predict cross sections for photoproduction of exotic hybrids comparable to those of normal mesons. And there are essentially no data on photoproduction of light mesons so this is *terra incognita*. The existing photoproduction data will be discussed.
5. *The complementarity of this study with other planned projects that will study gluonic excitations.* We will compare this to searches in the charm quark or beauty quark sectors or e^+e^- annihilations, in particular the GSI Project and the CLEO-c Project at Cornell.
6. *The importance of the PWA technique in uncovering exotic mesons.* The PWA is a powerful analysis tool that has been successfully employed in experiments to uncover states which are not evident from a simple examination of mass spectra (bump-hunting). PWA is absolutely essential for this project as is the development of the formalism for incident photon beams and an understanding of the phenomenology. The importance of a hermetic detector with excellent resolution and rate capability and sensitivity to a wide variety of decay modes will be discussed.
7. *Linear polarization of the photon beam is essential for this study.* Linear polarization is important in the determination of the J^{PC} quantum numbers and it is essential in determining the production mechanism. Linear polarization can be used as a filter for exotics once the production mechanism is isolated.
8. *The ideal photon energy range.* In order to reach the desired mass range we need to be far enough above threshold so that the decay products of produced mesons can be detected and measured with sufficient precision. High enough energies are also important to avoid line-shape distortions of higher-mass mesons. We also want to be high enough in energy to kinematically separate production of baryon resonances from production of meson resonances. This need for higher energies, however is balanced by the need to limit the maximum energy to allow for a solenoid-only-based detector to accurately determine the momenta of the highest energy charged particles. These considerations lead to an ideal photon energy in the range from 8 to 9 GeV.
9. *The desired electron energy.* Having established the desired photon beam energy of 9 GeV the electron energy must be sufficiently high compared to the desired photon beam energy to achieve a sufficient degree of linear polarization. With 12 GeV electrons, the degree of linear polarization is 40%. If the electron energy drops to 10 GeV the degree of polarization drops

to 5%. The ratio of tagged hadronic rate to total hadronic rate in the detector drops as the electron energy approaches the desired photon energy. The conclusion is that an electron energy of 12 GeV suffices but lower energies will severely compromise the physics goals.

2.A.2 Conventional light mesons

The early version of the quark model described the observed mesons as bound states of a quark and antiquark, where the quarks were assumed to be the u , d and s quarks. Thus mesons were grouped in families with nine members – a nonet – characterized by a given J^{PC} determined by the relative spin of the two quarks and their relative orbital angular momentum. Within the nonet three are members of an isotriplet with zero strangeness. Two are members of an isodoublet with positive strangeness and another two with negative strangeness. And the remaining two members have zero strangeness and isospin. This flavor pattern holds for all the nonets. Radial excitations are also allowed.

The rules for allowed values of J^{PC} follow from the requirements of a fermion–antifermion system: the quark spins can be parallel ($S = 1$) or antiparallel ($S = 0$) with relative orbital angular momentum (L), $\vec{J} = \vec{L} + \vec{S}$, $P = (-1)^{L+1}$ and $C = (-1)^{L+S}$. Thus the low-lying nonet with $\vec{L} = 0$ and $\vec{S} = 0$ leads to $J^{PC} = 0^{-+}$, the pseudoscalar nonet, including the π , K , η and η' mesons. The nonet with $\vec{L} = 0$ and $\vec{S} = 1$ leads to $J^{PC} = 1^{--}$, the vector mesons, including the ρ , K^* , ω and ϕ mesons. The combination $\vec{L} = 1$ and $\vec{S} = 1$ leads to three nonets: scalar ($J^{PC} = 0^{++}$), axial vector ($J^{PC} = 1^{++}$) and tensor ($J^{PC} = 2^{++}$).

Using the rules for determining J^{PC} for a fermion-antifermion system, certain J^{PC} combinations are not allowed for $q\bar{q}$ systems and these include $J^{PC} = 0^{--}, 0^{+-}, 1^{-+}, 2^{+-}, \dots$. Such combinations are referred to as *exotic* quantum numbers. Indeed, that such combinations were not initially observed gave credence to the quark model.

Figure 27 shows our current knowledge of conventional $q\bar{q}$ states. The exact association of an observed meson with a particular $q\bar{q}$ state within a nonet depends on a good understanding of the various decay modes of the meson as well as its mass, width and production characteristics. Figure 27 also shows the expected range of masses for glueballs, hybrid mesons and meson-meson molecular states. These will be described in more detail below.

The range of masses of the known conventional meson nonets and their radial excitations extend from the π mass up to about $2.5 \text{ GeV}/c^2$. Figure 28 shows the spectrum of $q\bar{q}$ states in more detail including radial excitations. There is also now clear evidence that the observed meson spectrum includes states which cannot be accommodated within the naive quark model. For example, there are at least five scalar states reported with masses below $2 \text{ GeV}/c^2$. These, along with indications of exotic J^{PC} sightings will be discussed below.

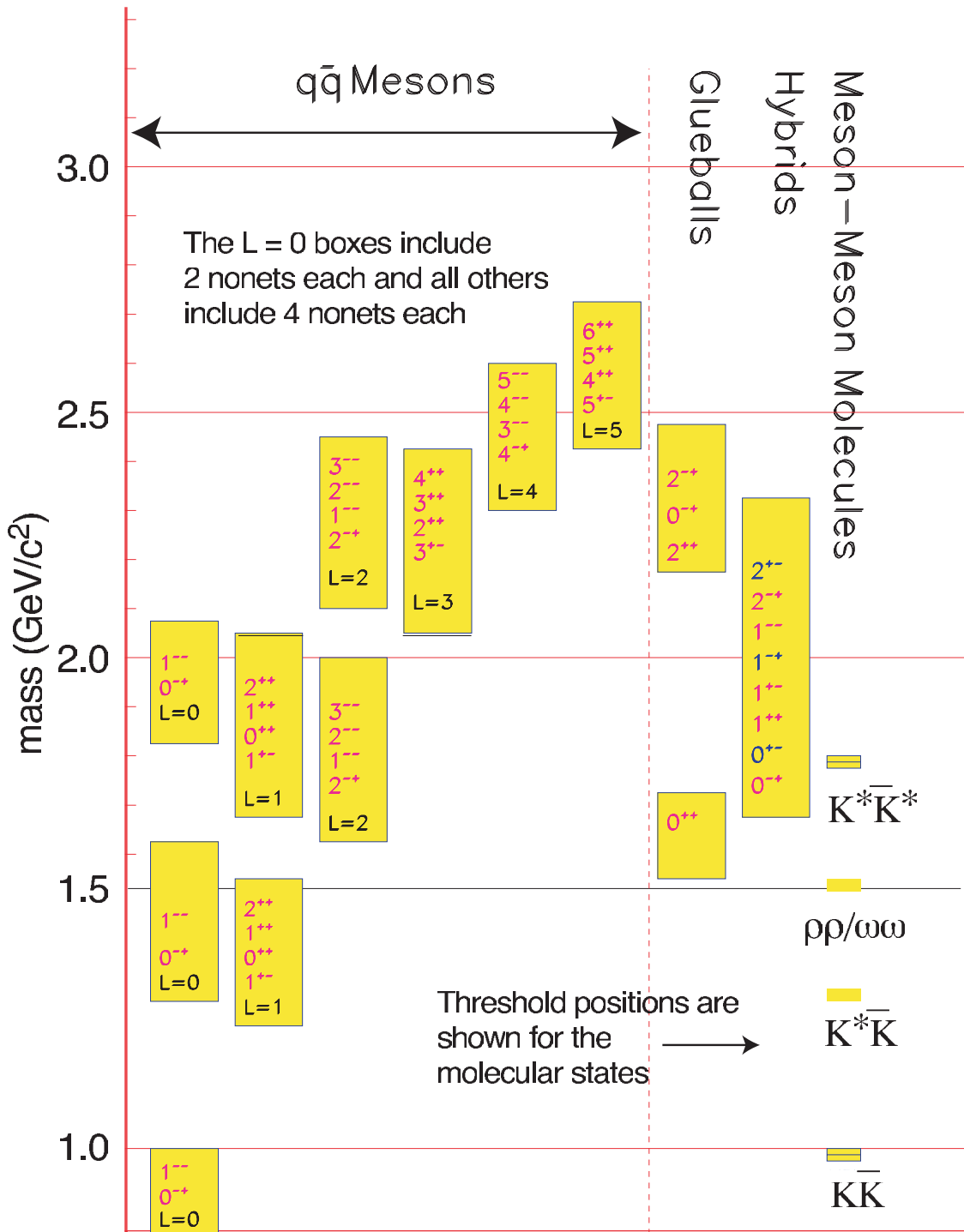


Figure 27: A level diagram showing conventional nonets and expected masses of glueballs, hybrids and molecular thresholds. The vertical axis is in units of GeV/c^2 . For the $q\bar{q}$ boxes the L refers to the angular momentum between the quarks and each J^{PC} refers to a nonet of mesons. Note also that exotic J^{PC} , -0^{+-} , 1^{-+} , 2^{+-} – occur only among the hybrids for the range of masses shown.

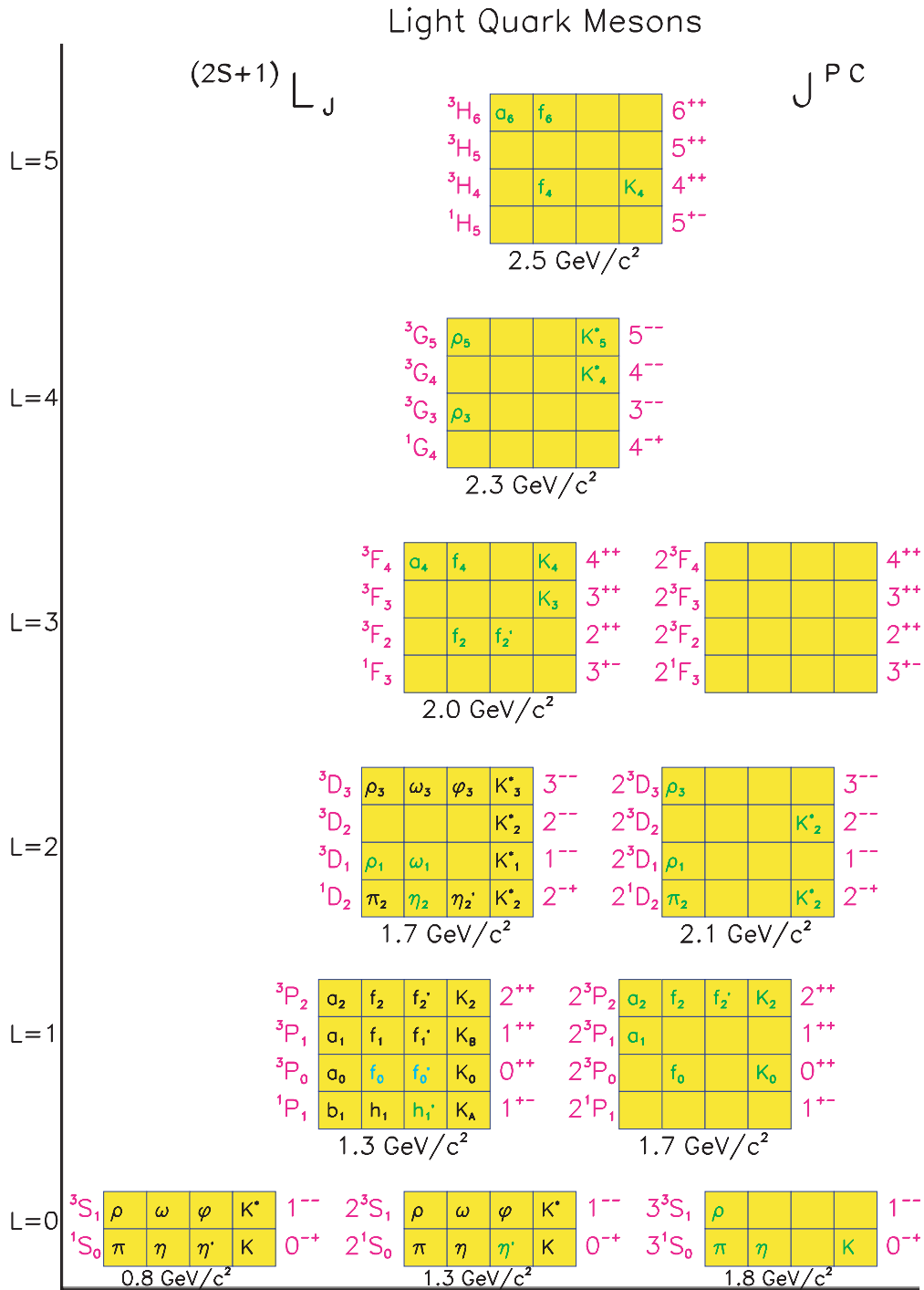


Figure 28: The $q\bar{q}$ spectrum of states. The assignments of the light colored states are speculative, while the empty boxes are missing states. The orbital angular momentum of the nonet is plotted on the vertical axis, while the towers of radial excitations are shown along the horizontal axis.

2.A.3 Gluonic excitations and confinement

The Standard Model of elementary particles includes the electroweak theory and QCD, the latter describing the strong interactions among the quarks and gluons. At short distances – the regime of asymptotic freedom – perturbative techniques are applicable and QCD describes high energy experimental phenomena both qualitatively and quantitatively. At large distance scales – the confinement regime – the situation is far different. Here the successful calculational techniques of the perturbative regime cannot be used. We must rely on first-principles lattice QCD calculations or QCD-inspired models. There has been significant theoretical effort in this area recently and more progress can be expected in the near future, especially as multi-teraflop lattice QCD centers come into operation.

Understanding confinement in QCD requires a detailed understanding of the role of gluons. QCD is distinct from QED in that the force carriers of the former (gluons) carry color charge whereas for the latter the photons are electrically neutral. As illustrated in Fig. 29, the force between two electrically charged particles falls off like the inverse square of the distance between the charges. The number of field lines intersecting a unit area midway between the charges and perpendicular to the line connecting them would decrease as the inverse square of the distance between the charges. In contrast, the color field lines between a quark and an anti-quark do not fill all of space as in the case with electrical charges. Rather the field lines form flux tubes. A unit area placed midway between the quarks and perpendicular to the line connecting them intercepts a constant number of field lines, independent of the distance between the quarks. This leads to a constant force between the quarks – and a large force at that, equal to about 16 metric tons. The potential associated with this constant force is linear and grows with increasing distance. It takes infinite energy to separate the quarks to infinity and thus, qualitatively at least, this accounts for confinement.

Lattice QCD calculations support this notion of the formation of a flux tube between the quark and anti-quark. Figure 30 shows the energy density in the color field between a quark and an anti-quark in a meson with a separation of 1.2 fm. The density peaks at the positions of the quarks and is confined to a tube between the quarks. This calculation is for heavy quarks in the quenched approximation. Figure 30 also shows the corresponding potential between the quarks. The ground state potential has a $1/r$ dependence at small distances and is linear for large distances.

This notion of the formation of flux tubes was first introduced in the 1970's by Yoichiro Nambu [Na70] to explain the observed linear Regge trajectories – the linear dependence of mass squared, m^2 , of hadrons on their spin, J . This linear dependence results if one assumes that massless quarks are tied to the ends of a relativistic string with constant mass (energy) per length with the system rotating about its center. The linear m^2 versus J dependence only arises when the mass density per length is constant, which is equivalent to a linear potential.

Within this picture, conventional mesons arise when the flux tube is in its ground state.

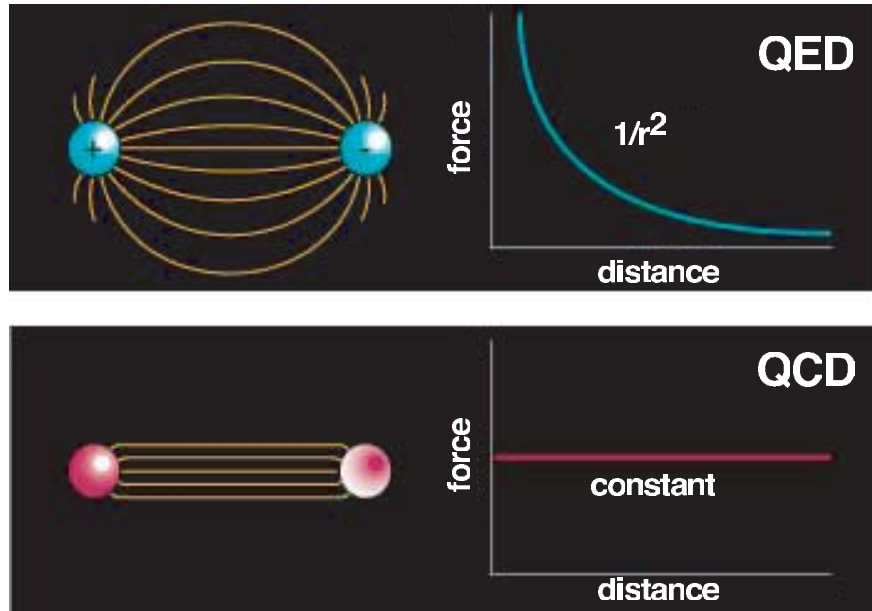


Figure 29: Field lines associated with the electrical force between two electrically charged particles (top) and the corresponding dependence of force on the distance between the charges and the field lines associated with the color force (bottom) between two quarks and the corresponding dependence of force on distance.

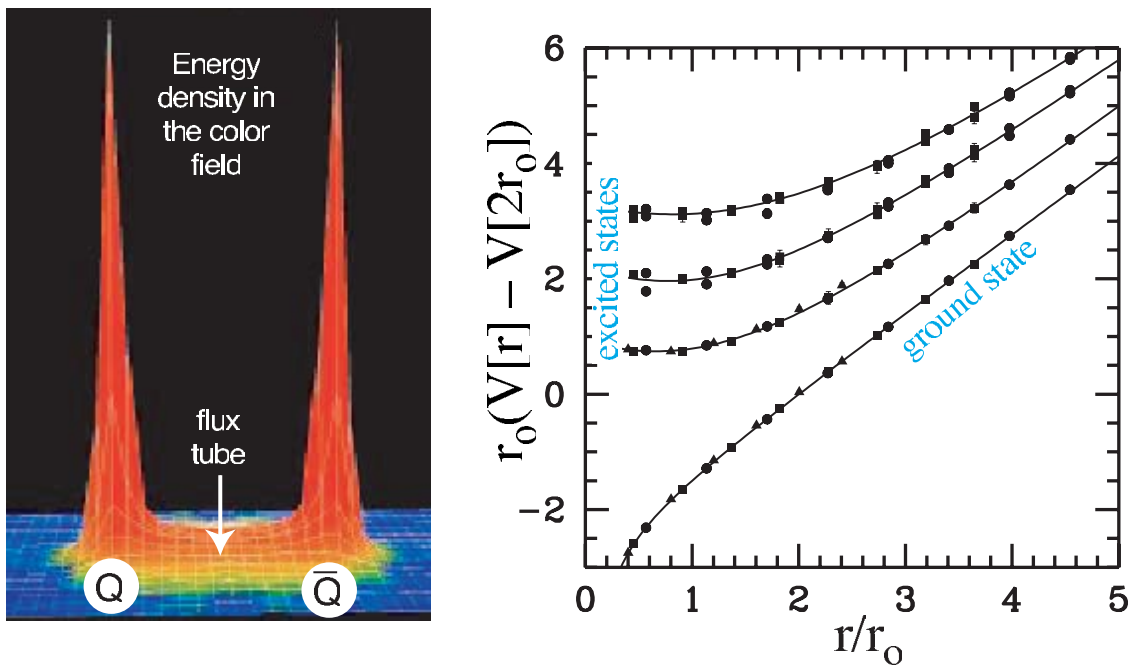


Figure 30: A lattice QCD calculation (left) of the energy density in the color field between a quark and an anti-quark. The density peaks at the positions of the quarks and is confined to a tube between the quarks. This calculation is for heavy quarks in the quenched approximation. The corresponding potential between the quarks (right). The ground state potential has a $1/r$ dependence at small distances and is linear for large distances.

Excitations of the flux tube lead to hybrid mesons that exhibit both the quark and gluonic degrees of freedom. The first excited state of the flux tube is a transverse excitation. The flux tube, or string, spins clockwise or counter-clockwise around the $q\bar{q}$ line leading to two degenerate states – degenerate since the energy should not depend on which way the flux tube is spinning. Lattice QCD and flux tube models both indicate that the lowest excited flux tube has $J = 1$ [Be97, Is85a, La97]. The linear combinations of the clockwise or counter-clockwise rotations are eigenstates of parity and charge conjugation leading to two possibilities for the excited flux tube: $J^{PC} = 1^{-+}$ or $J^{PC} = 1^{+-}$. Suppose we start with the $q\bar{q}$ in the $S = 0$ and $L = 0$ (or $J^{PC} = 0^{-+}$ – the π or K) configuration. Combining this with $J^{PC} = 1^{-+}$ or $J^{PC} = 1^{+-}$ of the excited flux tube results in hybrid mesons with $J^{PC} = 1^{++}$ or $J^{PC} = 1^{--}$. These are non-exotic quantum numbers. If, however, we start with $q\bar{q}$ in the $S = 1$ and $L = 0$ (or $J^{PC} = 1^{--}$ – the vector photon) configuration, the resulting hybrid meson can have $J^{PC} = [0, 1, 2]^{+-}$ for the flux tube with $J^{PC} = 1^{-+}$ and $J^{PC} = [0, 1, 2]^{-+}$ for the flux tube with $J^{PC} = 1^{+-}$. We note that of these six possible J^{PC} combinations, three are exotic: $J^{PC} = 0^{+-}$, $J^{PC} = 1^{-+}$ and $J^{PC} = 2^{+-}$. These states will not mix with $q\bar{q}$ and thus have unique signatures.

Meson production proceeds with an incoming probe interacting with the target particle and one result of the scattering can be the excitation of the flux tube. If the probe is a $q\bar{q}$ in $L = 0$ and $S = 0$ (π or K), production of exotic hybrids will not be favored. But if the $q\bar{q}$ probe has $L = 0$ and $S = 1$, for example a photon, one expects exotic hybrids to be produced readily.

Finally we consider the expected masses for hybrid mesons. We would expect the mass difference between the ground state (conventional) mesons and hybrid mesons to be given by the level spacing between the ground state of the flux tube and the first excited transverse mode and that is simply given by π/r where r is the quark separation. When translated to appropriate units this corresponds to about $1 \text{ GeV}/c^2$.

In this discussion the motion of the quarks was ignored, but we know from general principles [Is85] that an approximation that ignores the impact of the flux tube excitation and quark motion on each other seems to work quite well.

2.A.4 Observation of gluonic excitations

Glueballs Lattice QCD calculations indicate that lightest glueball is a scalar with a mass in the range from 1.5 to $1.7 \text{ GeV}/c^2$ [Mo97, Ba93, Se95, Ba98]. Indeed there is evidence from the Crystal Barrel experiment, which studied $p\bar{p}$ annihilations at CERN, that the $f_0(1500)$ is a leading candidate for a glueball [Am95, Am96]. There are, however, indications that this state is not a pure glueball but has some mixing with conventional $q\bar{q}$ [CI01]. There are also strong indications that the scalar meson sector contains one or more glueballs since there are several more observed states than can be accommodated in the simple $q\bar{q}$ model. However, the unique identification of a glueball is exacerbated by the possibility of mixing with $q\bar{q}$. Lattice QCD indicates a rich spectrum

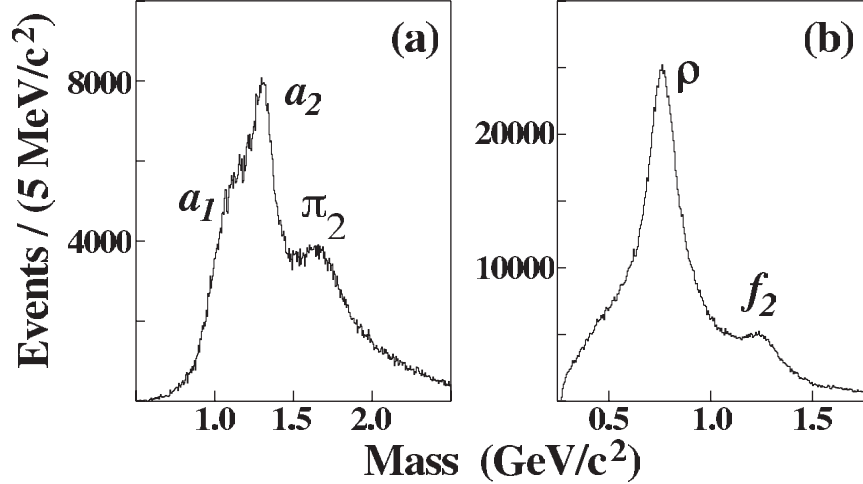


Figure 31: Acceptance corrected effective mass distributions for the (a) $\pi^+\pi^-\pi^-$ combination and (b) $\pi^+\pi^-$ combination (two entries per event) from E852 [Ad98].

of glueballs, all with non-exotic quantum numbers, from 1.5 to 2.5 GeV/c^2 . The lightest glueball with exotic quantum numbers is predicted to have $J^{PC} = 2^{+-}$ and to have a mass of 4 GeV/c^2 [Mo97].

Exotic hybrid mesons After about two decades of experimental searches there have been reports of experimental observations of states with exotic $J^{PC} = 1^{-+}$ by the Brookhaven E852 collaboration in π^-p interactions at 18 GeV/c . One of these has a mass of $(1593 \pm 8_{-47}^{+29}) \text{ MeV}/c^2$ and width of $(168 \pm 20_{-12}^{+150}) \text{ MeV}/c^2$ and decays into $\rho^0\pi^-$ [Ad98]. This state was observed in the reaction $\pi^-p \rightarrow \pi^+\pi^-\pi^-p$ at a beam momentum of 18 GeV/c . In Fig. 31, the acceptance-corrected (average acceptance was 25%) distributions of the $\pi^+\pi^-\pi^-$ and $\pi^+\pi^-$ effective masses are shown. The positions of well-established meson states are shown, including the $a_1(1260)$, which does not show up as a prominent peak in the overall mass distribution. The partial wave analysis (PWA) performed on these data assumes an *isobar model* – a parent decaying into a $\pi\pi$ state and an unpaired π followed by the decay of the $\pi\pi$ state. The resulting decomposition into various waves is shown in Fig. 32. The decomposition clearly shows the $\pi(1800)$ in the 0^{-+} wave, the $a_1(1260)$ in the 1^{++} wave, the $\pi_2(1670)$ in the 2^{-+} wave, and the $a_2(1320)$ in the 2^{++} wave. Evidence for the exotic 1^{-+} $\rho\pi$ is shown in Fig. 33. If an isovector $\rho\pi$ resonates in an $L = 1$ wave, it has $J^{PC} = 1^{-+}$. Also shown in this figure is the effect of leakage of non-exotic waves. Finally in Fig. 34 a coupled fit to the wave intensities and phase difference between the 1^{-+} and 2^{-+} waves is shown.

Another state reported by E852 has a similar mass, $(1597 \pm 10_{-10}^{+45}) \text{ MeV}/c^2$, but with a significantly larger width, $(340 \pm 40_{-50}^{+50}) \text{ MeV}/c^2$, and decays into $\eta'\pi^-$ [Iv01]. It has not been determined whether these represent two decay modes of the same state or whether they are due to two different mechanisms.

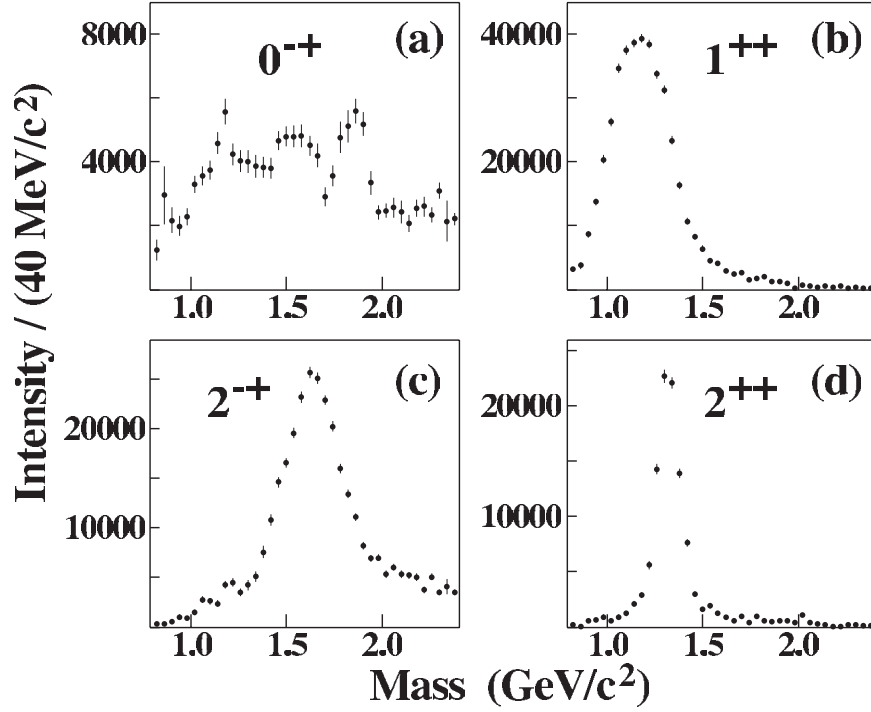


Figure 32: Combined intensities for all (a) 0^{-+} waves; (b) 1^{++} waves; (c) 2^{-+} waves; and (d) 2^{++} waves (from E852 [Ad98]).

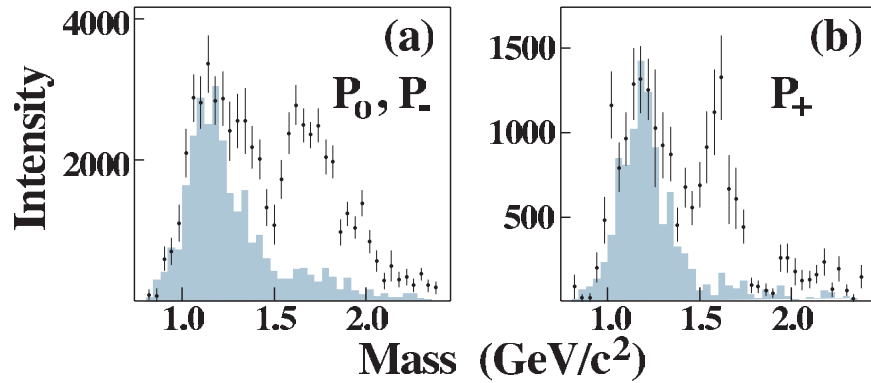


Figure 33: The intensities for the waves corresponding to 1^{-+} into $\rho\pi$. The shaded distributions are an estimate of leakage due to non-exotic waves (from E852 [Ad98]).

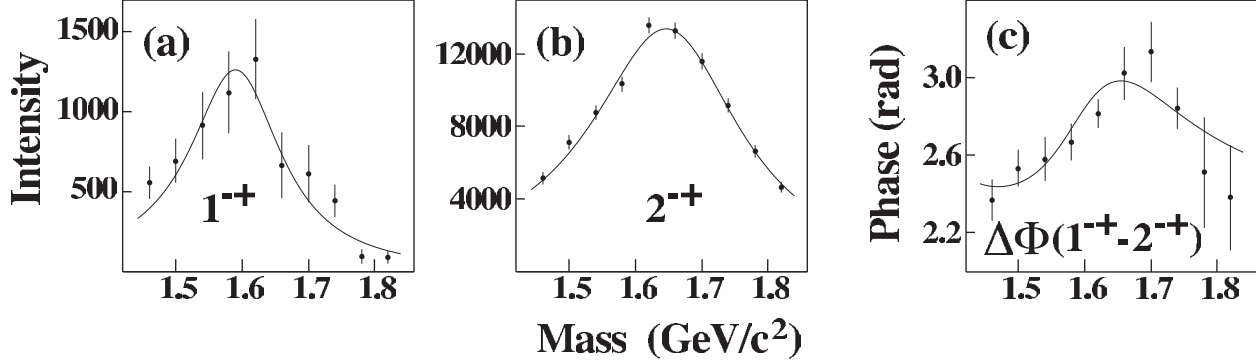


Figure 34: Results of a coupled mass-dependent Breit-Wigner fit of the 1^{-+} and 2^{-+} waves showing the phase difference as well (from E852 [Ad98]).

The E852 collaboration also reported observation of another $J^{PC} = 1^{-+}$ state with mass $(1370 \pm 16_{-30}^{+50})$ MeV/ c^2 and a width of $(385 \pm 40_{-105}^{+65})$ MeV/ c^2 decaying into $\eta\pi^{-}$ [Th97]. If an $\eta\pi$ system is in a P wave, the resulting J^{PC} quantum number combination is exotic (1^{-+}). In these studies the dominant state observed in the $\eta\pi$ channel is the $J^{PC} = 2^{++}$ $a_2(1320)$ seen in the D -wave. Critical to the identification of this state is not only showing the presence of a P -wave, but also that the resulting line shape is consistent with a Breit-Wigner and that the phase motion of the P , as determined by its interference with the dominant D -wave, cannot be due solely to the $a_2^{-}(1320)$ resonance. Soon after the E852 report, the Crystal Barrel Collaboration reported an exotic $J^{PC} = 1^{-+}$ state produced in $\bar{p}n \rightarrow \pi^{-}\pi^0\eta$ obtained by stopping antiprotons in liquid deuterium [Ab98]. They reported a mass of $(1400 \pm 20_{-20}^{+20})$ MeV/ c^2 and a width of $(310 \pm 50_{-30}^{+50})$ MeV/ c^2 .

The first claim of an exotic meson decaying into $\eta\pi^0$ with a mass of 1400 MeV/ c^2 was made by the GAMS collaboration in the reaction $\pi^{-}p \rightarrow \eta\pi^0n$ [Al88] but a later analysis by the group [Yu95] led to ambiguous results. The VES collaboration also presented evidence for a P -wave contribution in $\eta\pi$ [Be93] and at KEK a claim was made for an exotic $\eta\pi$ state [Ao93] as well, but with a mass and width close to that of the $a_2(1320)$; leakage from the dominant D wave could not be excluded.

In all the observations in π -induced reactions, the $\eta\pi$ P -wave enhancements have cross sections that are substantially smaller than the dominant $a_2(1320)$ so leakage, usually due to an imperfect understanding of experimental acceptance, is a source of concern. In contrast, the observed yield of the $\pi_1(1400)$ yield in $\bar{p}p$ annihilations is of the same magnitude as the $a_2(1320)$. Apart from these experimental issues, the interpretation of the nature of low-mass $\eta\pi$ P -wave amplitude and phase motion should be guided by the principle of parsimony – less exotic interpretations must also be considered. In a recent analysis of the $\eta\pi^0$ system in the reaction $\pi^{-}p \rightarrow \eta\pi^0n$ from data using the E852 apparatus, a P -wave is observed but it is not consistent with a Breit-Wigner resonance. The observed P -wave phase motion is consistent with $\eta\pi^0$ final state interactions. This could explain the relatively wide width of the observed $\eta\pi^{-}$ state and could also explain the broad $\eta'\pi^{-}$ enhancement. The $\pi^{-}p \rightarrow \eta\pi^0n$ and $\pi^{-}p \rightarrow \eta\pi^{-}p$ have some notable differences. For the former charge conjugation (C) is a good quantum number but not for the latter and for the former both

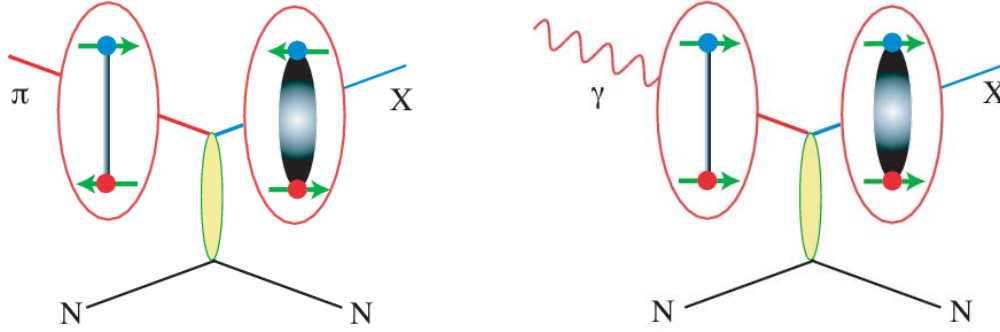


Figure 35: With a π probe (left) the incoming quarks have $L = 0$ and $S = 0$. The excited flux tube from the scattering results in hybrid mesons with non-exotic quantum numbers. With a photon probe (right) the incoming quarks have $L = 0$ and $S = 1$. When the flux tube is excited, hybrid mesons with exotic quantum numbers are possible.

the $a_0(980)$ and $a_2(1320)$ are prominently present but for the latter only the $a_2(1320)$ is strongly produced. This is an important factor in selecting the physical solutions among mathematically ambiguous solutions.

The conclusion from these studies is that there indeed are tantalizing hints of gluonic excitations in both the glueball and hybrid sectors but the results are not conclusive. The large statistics samples of high quality data to be collected with the GLUEX detector will provide the definite resolution of the murky situation. Furthermore there is good reason to believe that whereas exotic hybrids may be suppressed in π production, they are enhanced in photoproduction where essentially no data exist. In the glueball sector, the large samples of glue-rich radiative J/ψ decays should shed light on the spectrum of these gluonic excitations.

2.A.5 Photoproduction of exotic hybrids

Why photoproduction? Based on the arguments presented above, the photon is expected to be particularly effective in producing the *smoking gun* signature for gluonic excitations: hybrids with exotic J^{PC} . In this regard, we will compare the effectiveness of the π or K as a probe with that of the photon. In the former case, the meson is a $q\bar{q}$ with spins anti-aligned ($S = 0$) and in the latter, the photon is a virtual $q\bar{q}$ with spins aligned ($S = 1$). In both cases, the relative orbital angular momentum is zero ($L = 0$) and the flux tube connecting the quarks is in its ground state. Figure 35 illustrates the differences between a π probe and a γ probe. If the scattering results in excitation of the flux tube, one expects exotic hybrid mesons to be suppressed in π -induced interactions and enhanced in photoproduction.

Current phenomenology also supports the notion that photons should be more effective at producing exotic hybrids [Af98, Sz01]. Figure 36 shows an estimate of the photoproduction cross sections at 8 GeV for the $a_2(1320)$ and the exotic $\pi_1(1600)$ [Sz01]. The model uses as input the

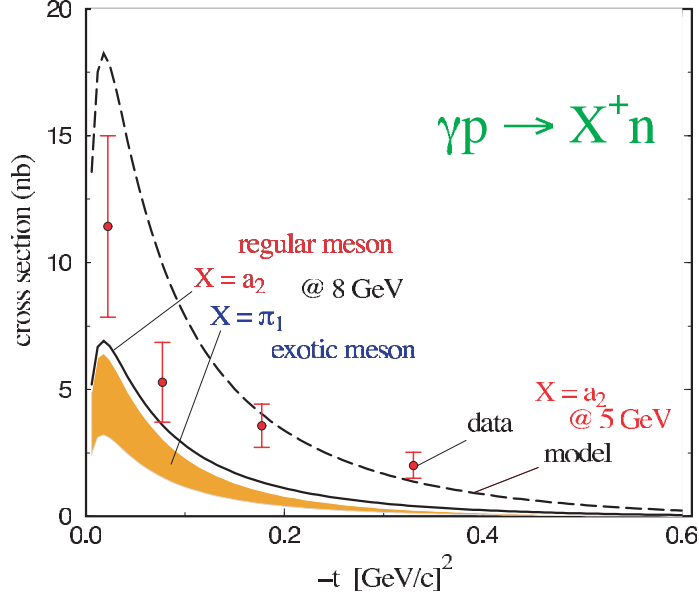


Figure 36: Estimates of the photoproduction cross sections for $a_2(1320)$ and the exotic $\pi_1(1600)$ at 8 GeV based on a phenomenological analysis described in [Sz01]. The model uses as input the ratio of $\pi_1(1600)$ to $a_2(1320)$ as observed in E852. The model is compared with photoproduction of the $a_2(1320)$ at 5 GeV.

ratio of $\pi_1(1600)$ to $a_2(1320)$ as observed in E852. The model is compared with photoproduction of the $a_2(1320)$ at 5 GeV. Whereas in E852, with a π beam, the $\pi_1(1600)$ is produced at about 5% of the rate for $a_2(1320)$, in photoproduction the rates for $\pi_1(1600)$ are expected to be comparable for that of the $a_2(1320)$. In the case of the incident π , the $\pi_1(1600)$ is produced by ρ exchange and the suppression at very low- $|t|$ due to angular momentum – spin 0 in and spin 1 out – decreases the cross section. This is to be compared to photoproduction of the $\pi_1(1600)$ with π exchange where there is no suppression at very low- $|t|$ since now we have spin 1 in and spin 1 out. Furthermore the $N\rho N$ coupling at the baryon vertex in the incident π case is lower by a factor of 4 compared to the $N\pi N$ in the photoproduction case.

To underscore the differences between existing photoproduction and π production, the corresponding largest data sets on 3π production are compared in the plots of Fig. 37. The 3π mass spectrum from the reaction $\pi^- p \rightarrow \pi^+ \pi^- \pi^- p$ at 18 GeV/c from E852 at Brookhaven is shown. Also shown is the 3π mass spectrum from the reaction $\gamma p \rightarrow \pi^+ \pi^+ \pi^- n$ at 19 GeV from SLAC. We note the large difference in statistics between the two and we also note the differences in the structure of the spectra.

Current photoproduction data Table 7 is a partial compilation of known photoproduction cross sections and the numbers of events from the existing experiments. The typical cross sections range from of order $0.1 \mu\text{b}$ up to of order $10 \mu\text{b}$, with most measurements involving rather small numbers of events, typically on the order of a few thousand. The extant data from photoproduction

Table 7: A sample of measured photoproduction cross sections from several references. Note the small numbers of events in any given channel.

<i>Reaction</i>	E_γ GeV	σ (μb)	<i>Events</i>	<i>Ref.</i>
$\gamma p \rightarrow p\pi^+\pi^-$	9.3		3500	[Ba73]
$\gamma p \rightarrow p\pi^+\pi^-$	19.3		20908	[Ab84]
$\gamma p \rightarrow p\pi^+\pi^-\pi^0$	2.8		2159	[Ba73]
$\gamma p \rightarrow p\pi^+\pi^-\pi^0$	4.7		1606	[Ba73]
$\gamma p \rightarrow p\pi^+\pi^-\pi^0$	9.3		1195	[Ba73]
$\gamma p \rightarrow p\pi^+\pi^-\pi^0$	4.7–5.8	$13.5 \pm 1.5 \mu\text{b}$	3001	[Ei72]
$\gamma p \rightarrow p\pi^+\pi^-\pi^0$	6.8–8.2	$11.8 \pm 1.2 \mu\text{b}$	7297	[Ei72]
$\gamma p \rightarrow n\pi^+\pi^+\pi^-$	4.7–5.8	$4.6 \pm 1.4 \mu\text{b}$	1723	[Ei72]
$\gamma p \rightarrow n\pi^+\pi^+\pi^-$	6.8–8.2	$4.0 \pm 1.2 \mu\text{b}$	4401	[Ei72]
$\gamma p \rightarrow n\pi^+\pi^+\pi^-$	16.5–20		3781	[Co93a]
$\gamma p \rightarrow p\pi^+\pi^-\pi^0$	20–70		14236	[At84]
$\gamma p \rightarrow p\pi^+\pi^-\pi^+\pi^-$	4–6	$4.0 \pm 0.5 \mu\text{b}$	~ 330	[Da73]
$\gamma p \rightarrow p\pi^+\pi^-\pi^+\pi^-$	6–8	$4.8 \pm 0.5 \mu\text{b}$	~ 470	[Da73]
$\gamma p \rightarrow p\pi^+\pi^-\pi^+\pi^-$	8–12	$4.5 \pm 0.6 \mu\text{b}$	~ 470	[Da73]
$\gamma p \rightarrow p\pi^+\pi^-\pi^+\pi^-$	12–18	$4.4 \pm 0.6 \mu\text{b}$	~ 380	[Da73]
$\gamma p \rightarrow p\pi^+\pi^-\pi^+\pi^-$	15–20		6468	[Ab85]
$\gamma p \rightarrow p\pi^+\pi^-\pi^0\pi^0$	20–70		8100	[At84a]
$\gamma p \rightarrow p\pi^+\pi^+\pi^-\pi^-\pi^0$	19.5		2553	[Bl97]
$\gamma p \rightarrow \Delta^{++}\pi^-\pi^+\pi^-$	4–6	$1.65 \pm 0.2 \mu\text{b}$	~ 200	[Da73]
$\gamma p \rightarrow \Delta^{++}\pi^-\pi^+\pi^-$	6–8	$1.8 \pm 0.2 \mu\text{b}$	~ 200	[Da73]
$\gamma p \rightarrow \Delta^{++}\pi^-\pi^+\pi^-$	8–12	$1.1 \pm 0.2 \mu\text{b}$	~ 200	[Da73]
$\gamma p \rightarrow \Delta^{++}\pi^-\pi^+\pi^-$	12–18	$1.15 \pm 0.2 \mu\text{b}$	~ 200	[Da73]
$\gamma p \rightarrow p\omega$	4.7–5.8	$2.3 \pm 0.4 \mu\text{b}$	< 1600	[Ei72]
$\gamma p \rightarrow p\omega$	6.8–8.2	$2.0 \pm 0.3 \mu\text{b}$	< 1200	[Ei72]
$\gamma p \rightarrow p\omega$	4.7	$3.0 \pm 0.3 \mu\text{b}$	1354	[Ba73]
$\gamma p \rightarrow p\omega$	9.3	$1.9 \pm 0.3 \mu\text{b}$	1377	[Ba73]
$\gamma p \rightarrow p\phi$	4.7	$0.41 \pm 0.09 \mu\text{b}$	136	[Ba73]
$\gamma p \rightarrow p\phi$	9.3	$0.55 \pm 0.07 \mu\text{b}$	224	[Ba73]
$\gamma p \rightarrow na_2^+$	4.7–5.8	$1.7 \pm 0.9 \mu\text{b}$		[Ei72]
$\gamma p \rightarrow na_2^+$	6.8–8.2	$0.9 \pm 0.9 \mu\text{b}$		[Ei72]
$\gamma p \rightarrow na_2^+$	19.5	$0.29 \pm 0.06 \mu\text{b}$	~ 100	[Co93a]

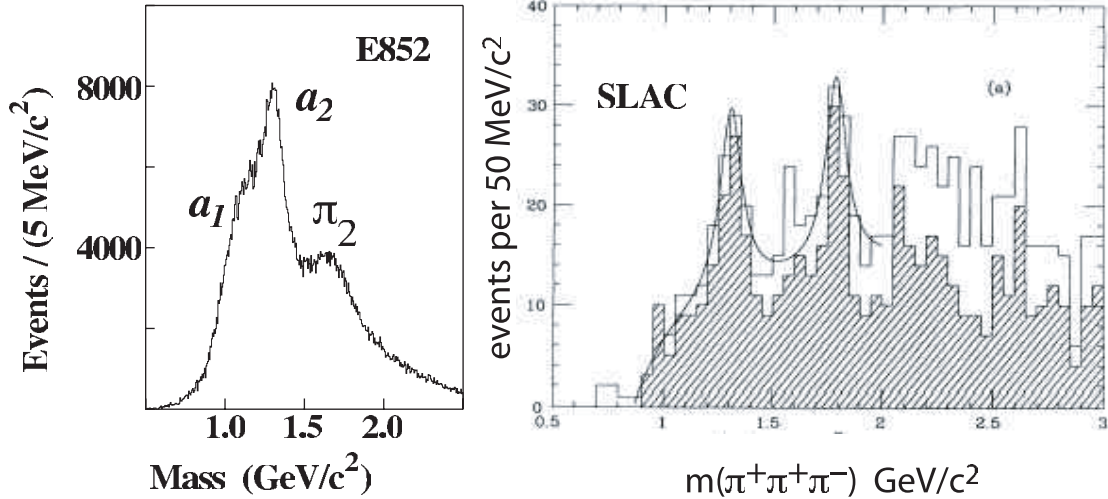


Figure 37: (left) The 3π mass spectrum from the reaction $\pi^-p \rightarrow \pi^+\pi^-\pi^-p$ at 18 GeV/c from E852 at Brookhaven. (right) The 3π mass spectrum from the reaction $\gamma p \rightarrow \pi^+\pi^+\pi^-n$ at 19 GeV from SLAC.

are far too meager to perform the analysis necessary to unambiguously identify gluonic excitations. For example, after one year of low intensity running at 10^7 photons/sec, the yield of $a_2(1320)$ in GLUEX will be five orders of magnitude greater than the same collected in the SLAC photoproduction experiment. The yield of the exotic $\pi_1(1600)$ in the published E852 results will be increased by four orders of magnitude by GLUEX after one year of running.

There are reasonable sized data sets in 2π and 2π photoproduction from the CLAS detector at JLab that are currently under analysis. However, these arise from unpolarized photon beams and are produced from an incoherent bremsstrahlung spectrum that peaks at around 5 GeV.

2.A.6 Complementarity with other searches

Gluonic excitations include both exotic and non-exotic hybrid mesons and glueballs. Hybrid mesons exist in both the light quark (u , d and s) and heavy quark (c and b) sectors. Clearly, existing data collected with incident π beams, central collisions, $p\bar{p}$ annihilations and e^+e^- collisions have not uncovered a wealth of information about these states. As discussed earlier, the focus of the GLUEX project is in the light-quark hybrid sector. The initial benchmark states will be the exotic hybrids, which cannot mix with $q\bar{q}$ and therefore have a *smoking gun* signature. There are good reasons to expect that photoproduction will be particularly effective at uncovering the exotic hybrid mesons. And the existing photoproduction data are meager indeed.

The glueball and heavy hybrid sectors are not accessible to GLUEX. Glueballs are not preferentially produced in photoproduction because they do not couple to photons. Moreover, according to lattice QCD, the lightest exotic glueball has a mass of 4 GeV/c². One fruitful area of investigation

are J/ψ radiative decays since the system recoiling from the photon should be rich in two-gluon states. The planned CLEO-c project at CESR will collect a billion J/ψ radiative decays.

The direct production of exotic hybrids in e^+e^- collisions is complicated by the fact that the angular momentum barrier (the excited flux-tube carries $J = 1$) suppresses this production mode.

Lattice QCD predictions about heavy-quark exotic hybrids are at least as reliable as for the light-quark hybrids but the experimental situation is far more problematic. The photoproduction cross-sections are a few orders of magnitude lower. At the higher energies needed to produce these more massive states many other uninteresting processes can contribute to background. Finally, to unambiguously tag a charm or beauty hybrid one must identify detached vertices, further complicating the experimental challenge.

2.A.7 Production and analysis of hybrid mesons

Kinematics Consider a specific exclusive photoproduction reaction:

$$\gamma p \rightarrow X p \quad (2)$$

The center-of-mass energy squared, s , and the momentum-transfer-squared, t , between the incoming beam and outgoing X are defined in terms of the four-vectors of the particles:

$$s = (p_\gamma + p_p)^2 \quad (3)$$

$$t = (p_\gamma - p_X)^2 \quad (4)$$

The dependence of the cross section on s and t depend on the production mechanism, which is usually described in terms of the particle or particles which can be exchanged as shown in Fig. 38. For example, if the exchange particle is the pomeron (diffractive process) the cross section is nearly constant in s . For meson-exchange processes, cross sections typically fall off with increasing s . The dependence on t is typically exponential:

$$\frac{dN}{dt} \propto e^{-\alpha|t|} \quad (5)$$

For the process (2) at high enough photon beam energy, E_γ , we can make the approximation $s \approx 2 \cdot E_\gamma$ where E_γ is in GeV and s is in GeV^2 . For fixed s and mass of X , m_X , there is a minimum value of $|t|$, or $|t|_{min}$, needed to produce X . This $|t|_{min}$ increases with increasing m_X for fixed E_γ and decreases with increasing E_γ for fixed m_X . Coupled with the steep dependence implied in equation (5), the dependence of $|t|_{min}$ on m_X will affect event yields. In addition, the line shape of a resonance can be distorted if there is too rapid a variation of $|t|_{min}$ across the width of a resonance.

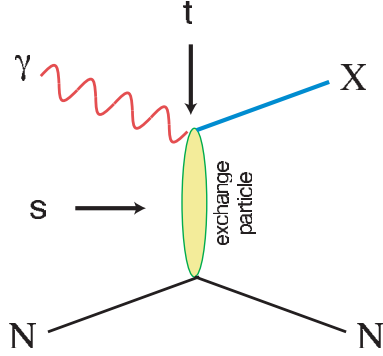


Figure 38: Diagram for the photoproduction of particle X . The variables s and t are the center-of-mass energy squared and the momentum-transfer-squared from incoming photon to outgoing particle X . The process shown here proceeds through the exchange of a particle in the t -channel.

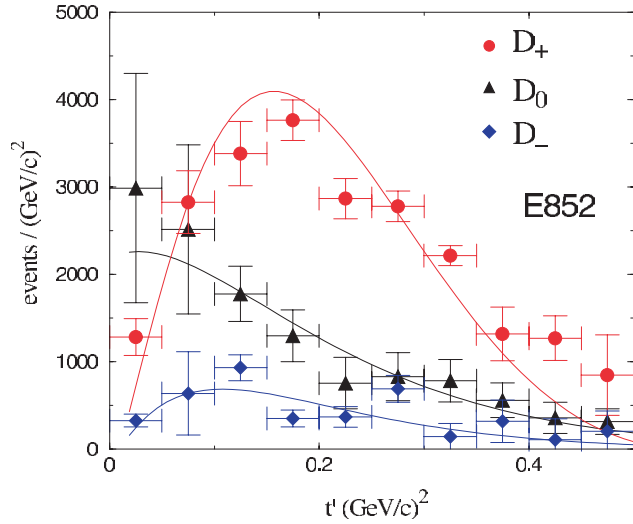


Figure 39: The distribution in $|t'|$ where $t' = t - t_{min}$ for the D -waves after a PWA of the $\eta\pi^0$ system from the reaction $\pi^-p \rightarrow \eta\pi^0n$ at 18 GeV/c. The curves are fits to expected Regge exchanges for the various D -waves.

Figure 39 shows an example of how the dependence in t is correlated with particle exchange. The distribution is in $|t'|$ where $t' = t - t_{min}$ for the D -waves after a PWA of the $\eta\pi^0$ system from the reaction $\pi^-p \rightarrow \eta\pi^0n$ at 18 GeV/c. The curves are fits to expected Regge exchanges for the various D -waves.

PWA requirements The PWA technique is described in a later chapter. It is important to stress here that the detector design focuses on hermeticity and resolution to insure nearly uniform coverage with well-understood acceptance functions for various decay angles for particle X . Kinematic fitting will also be used to identify exclusive processes. The design focuses on the requirements of the PWA. The existence of well established resonances will be used as benchmarks for the PWA. They also provide benchmarks for the phase variation of candidate exotic states. Furthermore, candidate

exotics can appear with multiple decay modes which must give consistent results. As an example, a meson which decays into $\eta\pi$ should be observed in channels where $\eta \rightarrow \pi^+\pi^-\pi^0$, $\eta \rightarrow 3\pi^0$, and $\eta \rightarrow 2\gamma$. Each of these modes leads to different acceptances and systematics. This provides a powerful check on PWA results.

Linear polarization of the beam

Linear and circular polarization We start with a review of the relationship between linear and circular polarization. A right-handed-circularly ($|R\rangle$) polarized photon has $m = 1$ while for a $|L\rangle$ photon $m = -1$. These are related to the linear polarization states, $|x\rangle$ (in production plane) and $|y\rangle$ (perpendicular to production plane) by:

$$|x\rangle = \frac{1}{\sqrt{2}} (|L\rangle - |R\rangle) \quad (6)$$

$$|y\rangle = \frac{i}{\sqrt{2}} (|L\rangle + |R\rangle) \quad (7)$$

States of linear polarization are eigenstates of parity. We will use these relations in several straightforward cases to show how linear polarization:

1. can provide information on decays in lieu of statistics,
2. is essential in isolating production mechanisms, and
3. can be used as an exotics filter if the production mechanism is known.

Linear polarization and statistics To illustrate how linear polarization provides useful information in the PWA, consider the case of the photoproduction of a vector meson which subsequently decays into two pseudoscalar mesons. Possible examples are $\rho \rightarrow \pi\pi$ or $\phi \rightarrow K\bar{K}$. Suppose the production mechanism produces the vector with the same helicity as the incident photon (or *s-channel helicity conservation*). In the rest frame of the vector the two-pseudoscalar wave function is described by

$$Y_1^m(\theta, \phi) \propto \sin\theta \cdot e^{im\phi} \quad (8)$$

For circularly polarized photons (either $m = 1$ or $m = -1$) the square of this amplitude carries no ϕ information while for in-plane photons there is a $\cos^2\phi$ dependence and out-of-plane a $\sin^2\phi$ dependence in the decay angular distribution, since in these cases we have the sum or difference of Y_1^{+1} and Y_1^{-1} according to equations (6) and (7). Although not essential in determining spin, a gain of statistics is needed to recover a drop in the degree of linear polarization. For example, our Monte Carlo simulation studies indicate that when the degree of linear polarization decreases from 0.40 to 0.2 a factor of two increase in statistics is needed to achieve the same relative error in determination of spin amplitudes.

Linear polarization and production mechanism This is best illustrated by considering a specific example. Suppose we produce a vector particle ($J^P = 1^-$) by the exchange of a scalar particle ($J^P = 0^+$ – natural parity exchange) or a pseudoscalar particle ($J^P = 0^-$ – unnatural parity exchange). We wish to determine whether the vector is produced by natural (amplitude A_N) or unnatural (amplitude A_U) parity exchange. In the center-of-mass of the vector particle, the momentum vectors of the beam photon and exchange particle are collinear. For circularly polarized photons, the m of the vector is the same as that of the photon. From parity conservation, the orbital angular momentum between the photon and exchange particle is $L = 0$ or $L = 2$ for natural parity exchange and $L = 1$ for unnatural parity exchange. So for circularly polarized photons, with $m = +1$, the total amplitude is $A_N + A_U$ whereas for $m = -1$, the total amplitude is $A_N - A_U$. This follows simply from the addition of angular momenta. Circularly polarized photons allow us to measure only the sum or difference of the two exchange amplitudes. If however, we have linearly polarized photons along the x -direction, we extract A_N using equation (6) and for polarization along the y -direction, we extract A_U using equation (7).

Linear polarization as an exotics filter Using arguments similar to those above, it has been shown [Af00c] that linear polarization can be used as a tool to filter exotics. For example, a $\rho\pi$ system with $I = 1$ has $C = +$. Suppose that one can determine the naturality of the exchange particle by selecting data within a range of $|t|$. For a produced $C = +$ particle with spin one we can have natural parity ($J^{PC} = 1^{-+}$ – exotic) or unnatural parity ($J^{PC} = 1^{++}$ – non-exotic). In the case of natural parity exchange the in-plane polarization selects the $J^{PC} = 1^{-+}$ wave while out-of-plane polarization selects $J^{PC} = 1^{++}$. For unnatural parity exchange the reverse is true. Note that in this case, we are specifying the naturality of the exchange and using linear polarization to select the naturality of the produced particle. In the previous section, we specified the naturality of the produced particle and used linear polarization to select the naturality of the exchanged particle.

2.B The Fundamental Structure of the Nuclear Building Blocks

The nucleons are the basic building blocks of atomic nuclei. Their internal structure, which arises from their quark and gluon constituents, determines their mass, spin, and interactions. These, in turn, determine the fundamental properties of the nuclei. To make further progress in our understanding of nuclei, it is crucial that we understand in detail how the nucleon’s basic properties are derived from the theory of strong interactions: quantum chromodynamics (QCD).

Over the past half century much progress has been made toward unraveling the structure of the nucleon. However, our understanding is fragmented and incomplete, and many puzzles remain. For example, we only partially understand how the nucleon’s spin is “assembled” from the quark spins and the quark and gluon angular momenta, and we don’t know the details of the spatial and momentum distributions of the quarks and gluons within the nucleon. Our understanding of nucleon structure is, quite simply, very far from the level of our understanding of atomic structure.

The JLab 12 GeV Upgrade will support a great leap forward in our knowledge of hadron structure through major programs in three areas: nucleon form factors at large Q^2 , valence quark structure, and deep exclusive scattering. It will also support important initiatives in a number of other areas of hadron structure. These research programs are described in detail below. The data on hadron structure that will be obtained using the Upgrade can be understood and interpreted coherently, using the theoretical framework of the recently-discovered Generalized Parton Distributions (GPDs), to provide truly remarkable and revealing images of the proton’s structure that will enable us to understand these fundamental “building blocks” of nuclear physics.

2.B.1 Form Factors – Constraints on the Generalized Parton Distributions

Introduction One of the primary goals of nuclear physics is to understand the structure of hadrons in terms of quarks and gluons, the fundamental fields of quantum chromodynamics (QCD). This task is complicated, since confinement, one of the most important features of QCD, is a non-perturbative phenomenon. One strategy has been to incorporate another feature of QCD, asymptotic freedom. This approach was very successful in applications to hard inclusive processes, and made possible the extraction of much information about hadronic structure in terms of quark and gluon longitudinal momentum distributions.

It was anticipated that a similar approach would be applicable to form factors and other exclusive processes at accessible momentum transfer, so that it would be possible to use perturbative QCD (pQCD) together with QCD sum rules to map valence distribution amplitudes of the hadrons. However, several recent experimental results from Jefferson Lab (JLab) involving exclusive form factors [Fr98a, Jo00, Ga02, Na02] have demonstrated unequivocally that pQCD is not applicable at few $(\text{GeV}/c)^2$ momentum transfers.

A recent important breakthrough has been the introduction of the formalism of generalized parton distributions (GPD), which offers a unified framework for accessing the complex structure of hadrons through a variety of exclusive reactions, and promises to yield the first three dimensional description of hadrons. Thus, one of the unique opportunities of JLab at 12 GeV will be to study the structure of hadrons by means of a comprehensive program of exclusive reactions. As described in the following, the measurement of exclusive form factors at high momentum transfer will be an essential part of this program, especially in constraining the GPD based description of the nucleon's short distance structure.

Exclusive form factors are the fundamental measurable quantities in electron scattering, and have direct connection to the charge and current structure of hadronic states. In the past, the measurement of form factors have given a wealth of information about the structure of nuclei. When extended to the highest accessible Q^2 , short distance features of the nucleon's structure have been revealed.

Similarly, the connection of form factors to hadron structure in terms of the quark-gluon distributions has been the subject of a great deal of theoretical study. The recent introduction of the concept of generalized parton distributions within the context of soft-hard factorization is an important breakthrough in connecting exclusive reactions at high momentum transfer with the full complexity of non-perturbative hadronic structure. This is generically illustrated in Fig. 40, where the non-perturbative structure is represented by the lower part of the "handbag", which can be parameterized in terms of four functions, the GPD's. The GPD's are functions of three variables: the longitudinal momentum fraction x of the struck quark, the momentum transfer to the nucleon $-t$, and a *skewedness* parameter ξ . These GPD's correspond to different current structures, H and E for the quark spin-averaged, and \tilde{H} and \tilde{E} for the quark-spin dependent combinations.

The hadronic form factors provide moments of the GPDs, thus offering important constraints on our description of the nucleon's structure. Form factors are complementary to deeply virtual exclusive reactions. In contrast to deeply virtual exclusive reactions (DVE), form factors uniquely access the GPD moments independently of ξ . This offers an additional simplicity compared to the integrals involved in deeply virtual processes. The Fourier transforms of GPDs over t , constrained by form factors, are directly interpretable as the transverse impact parameter dependence b_{\perp} of the hadron's quark charge and magnetic moment distributions [Bu00]. Thus GPDs provide 3-dimensional pictures of hadronic structure which is not obtainable by DIS, as illustrated further in the following.

Another important consideration which makes form factor measurements a necessary complement to DVE is that while deep exclusive reactions access GPD's only at relatively low $-t$, the GPD formalism for form factors is applicable at high $-t$ ($=Q^2$ for form factors), which is specifically necessary to obtain the small b_{\perp} structure of the hadron. Passing to the limits of very high Q^2 or $-t$ the form factors are expected to uniquely access the very simplest short distance valence quark structure of the hadron through the mechanism of pQCD.

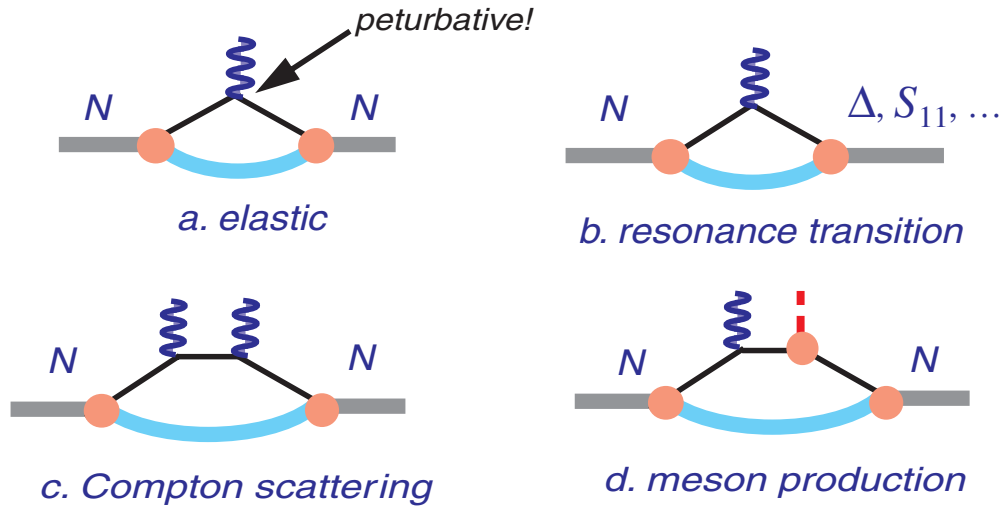


Figure 40: Schematic diagrams of the form factor reactions discussed in the text that can be expressed in terms of the GPD formalism: a) elastic, b) transition, c) Compton scattering, and d) high t meson production.

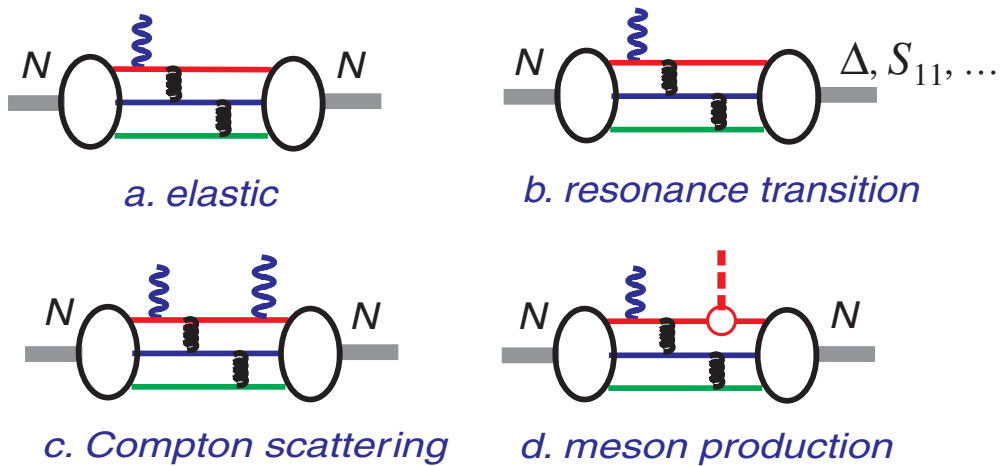


Figure 41: Form factor reactions discussed in the text that can be expressed in terms of the valence pQCD formalism: a) elastic, b) transition, c) Compton scattering, and d) high t meson production.

There exists an immense theoretical literature focused on connection of this short distance meson and nucleon form factors in terms of the quark-gluon structure of the hadron, through the formalism of *valence-pQCD* (pQCD). Analogously to Fig. 40, schematic representations of form factor reactions in the pQCD framework are shown in Fig. 41. Some seminal papers have literally thousands of citations.¹ This leads to the famous constituent Q^2 or s scaling laws, and important relationships between helicity leading and non-leading amplitudes. The great theoretical productivity was matched by considerable experimental effort. Despite the effort, the region of $-t$ or Q^2 where the transition from the soft handbag description to hard pQCD description occurs has not yet been experimentally determined.

In summary, the hadron form factor program at JLab at 12 GeV aims to access the three dimensional structure of the hadron by studying a variety of *form factor like* reactions. The GPD's will serve as the common framework for these studies. At the highest momentum transfers we will try to observe the transition to the simplest small size configurations connected through the valence pQCD formalism. Indeed, some of these measurements have already been started at more moderate momentum transfers and already have a profound affect on how we view the structure of hadrons. In the following sections we briefly describe our experimental program, illustrating where the measurements are today, and pointing out the dramatic increase in momentum transfer made possible with the 12 GeV upgrade.

Form Factors at Large Momentum Transfer Our goal is to observe the evolution with momentum transfer of the non-perturbative hadronic structure from its fully developed complexity at low momentum transfer, through to its simplest small configurations at the highest possible momentum transfers. In the following we describe the reactions we intend to study, and the kinematic ranges in $-t$ that we be able to cover for each.

We will begin by discussing the positive pion form factor F_{π^+} , since this is the benchmark reaction due to its relatively simple structure. We then move to the nucleon case and discuss the various form factors which are accessible, and their specific connection to the GPD's. For example, the elastic nucleon form factors F_1 and F_2 are the zero'th moments $\langle x \rangle^0$ of $H(x, t)$ and $E(x, t)$. For the protons and neutrons these are connected and constrained by isospin invariance. The $N \rightarrow \Delta$ form factor G_M^* is connected to the isovector part of $E(x, t)$, and the $N \rightarrow S_{11}$ to the negative parity member of the nucleon's parity doublet. The real Compton scattering form factors R_V, R_A and R_T provide the $\langle x \rangle^{-1}$ moments of $H(x, t)$, $\tilde{H}(x, t)$, and $E(x, t)$, as well as important polarization observables K_{LL}, K_{LT} and P_N which constrain the GPD's. High $-t$ exclusive meson production involving different mesons access moments of new nucleon form factors which are sensitive to different contributions depending on the meson produced. For example, π^0

¹For example, three papers by Shifman, Zakharov, and Vainshtein [Sh79] on QCD sum rules have been cited almost 5,000 times, two articles by Lepage and Brodsky [Br79a, Br80] on the pQCD formalism, more than 2,000 times, and an article by Chernyak and Zhitnitsky [Ch77] applying the former two to obtain pion and proton elastic form factors more than 600 times, and still counting!

and η production involves $\tilde{H}(x, t)$. Finally, we will discuss the evolution to the highest momentum transfer and the approach of the aforementioned form factors to pQCD. This involves the questions of pQCD constituent scaling and helicity conservation, which are contained in these form factors.

Form Factors and Generalized Parton Distributions Much has been said and written about GPD's during the past several years, and it is not our aim to go into details about the formalism. Rather, after a brief review of the most salient features, and their physical interpretation in terms of the three-dimensional structure of hadrons, we intend to show how a program of form factor measurements at high Q^2 or $-t$ uniquely provides a connection with the various substructures of GPD models which are complementary to deep virtual exclusive reactions. In the GPD picture, the incident real or virtual photon interacts with one of the quarks within the hadron, and is followed by either of two processes: the quark is re-absorbed into the hadron leaving it either intact or in a higher resonant state. The GPD formalism, for the first time, provides us with a unified description of the complex hadronic structure accessed by different exclusive reactions. Because of the correlations of the initial and final parton wave functions in their definition, the GPD's are sensitive to the actual hadron wave functions in a way that traditional inclusive process of deep inelastic scattering (DIS) is not. In particular, while structure functions entering inclusive scattering give information about distribution functions of longitudinal momentum fractions x , GPD's entering exclusive reactions contain information about the longitudinal and transverse momentum distributions, x and k_\perp , and through their correlations give a three dimensional snapshot of the hadronic structure.

The relation between wave functions, form factors and GPD's can be demonstrated through the well known Drell-Yan expression

$$F(t) = \int \Psi^*(x, k_\perp + \bar{x}\Delta_\perp)\Psi(x, k_\perp)\frac{d^2k_\perp}{16\pi^3} \quad (9)$$

where $\xi = 0$ and $\Delta_\perp^2 = -t$. As a simple illustration we choose an effective wave function [Ra98a] with a Gaussian k_\perp dependence

$$\Psi(x, k_\perp) = \Phi(x)e^{-k_\perp^2/2x\bar{x}\lambda^2}, \quad (10)$$

where $\bar{x} \equiv 1 - x$ and λ is a transverse size parameter. This expression for the form factor yields the following GPD

$$H(x, 0; \Delta_\perp) = \frac{x\bar{x}\lambda^2}{16\pi^2}\Phi^2(x)e^{-\Delta_\perp^2\bar{x}/4x\lambda^2} \equiv f(x)e^{-\Delta_\perp^2\bar{x}/4x\lambda^2}. \quad (11)$$

Note that $\xi = 0$ here, although generally it need not be so. GPD's at $\xi = 0$ are sometimes called "nonforward parton densities" [Ra98a]. The correlation of the longitudinal and transverse

momentum distributions is manifestly seen in Eq. 10. As emphasized in Ref. [Bu00], the double Fourier transform with respect to the momentum transfer Δ_\perp

$$H(x, b_\perp) = \int_0^\infty H(x, 0, \Delta_\perp^2) e^{i\Delta_\perp b_\perp} d\Delta_\perp. \quad (12)$$

has the meaning of the parton density distribution in the impact parameter space. The result is shown in Fig. 42. Note, the limits of the integral in eq. 12 require the knowledge of the $-t$ dependence to as high a value of $-t$ possible.

Factorization of the reaction into a hard kernel and soft GPD is a necessary condition for the application of the formalism. For deep virtual reactions this requires *off-forward* kinematics, with simultaneously high Q^2 and low $-t$. A measurement at a particular t , x_B and Q^2 involves an integral over the relevant variables x and knowledge of the skewedness parameter ξ . The great power of this approach is discussed in the physics section on deep virtual reactions. For the present purposes we point out that in the off-forward kinematics the low $-t$ constrains access to rather low k_\perp , or equivalently, large transverse impact parameter b_\perp . Conversely, form factor experiments for which the GPD formalism is applied involve high $-t$, and therefore access large k_\perp , or small transverse impact parameter b_\perp . The price is that a specific measurement always involves an integral (moment) over the full range of x . However, the integrals have a simplicity in that they are independent of skewedness parameter, so that they constrain GPDs at any ξ . Since different form factors access different moments of GPD's, and different structural components of the GPD's, a complete set of measurements will provide the greatest constraints on wave function models.

One of our abiding interests is to obtain a three dimensional mapping of the nucleon structure by modeling the GPD's as a function of x and t , constrained by various form factor measurements as a function of t , and structure functions measurements as a function of x . For illustrative purposes, in the examples which follow, we assume that the handbag can be expressed as an effectively two-body process, as in eq. 11.

The Charged Pion Form Factor F_{π^+} The measurement of F_π will serve as a benchmark reaction for our study of the range of applicability of both the GPD and pQCD formalisms, because the pion has the simplest hadronic structure for which we can measure the form factor at reasonably high $-t$. The pion form factor is related to the pion GPD as [Ra98a, Mu02]

$$F_\pi(t) = \int_{-1}^1 \sum_q H_\pi^q(x, t) dx .$$

One can model the nonforward parton density $H_\pi^q(x, t)$ by an expression similar to Eq.(11) with an exponential t -dependent factor or use an ansatz with a power-law behavior [Mu02]. The current status of the pion form factor is shown in Fig. 43. We note that for elastic scattering $-t = Q^2$, and they are denoted interchangeably. The result of a GPD calculation [Mu02] using a

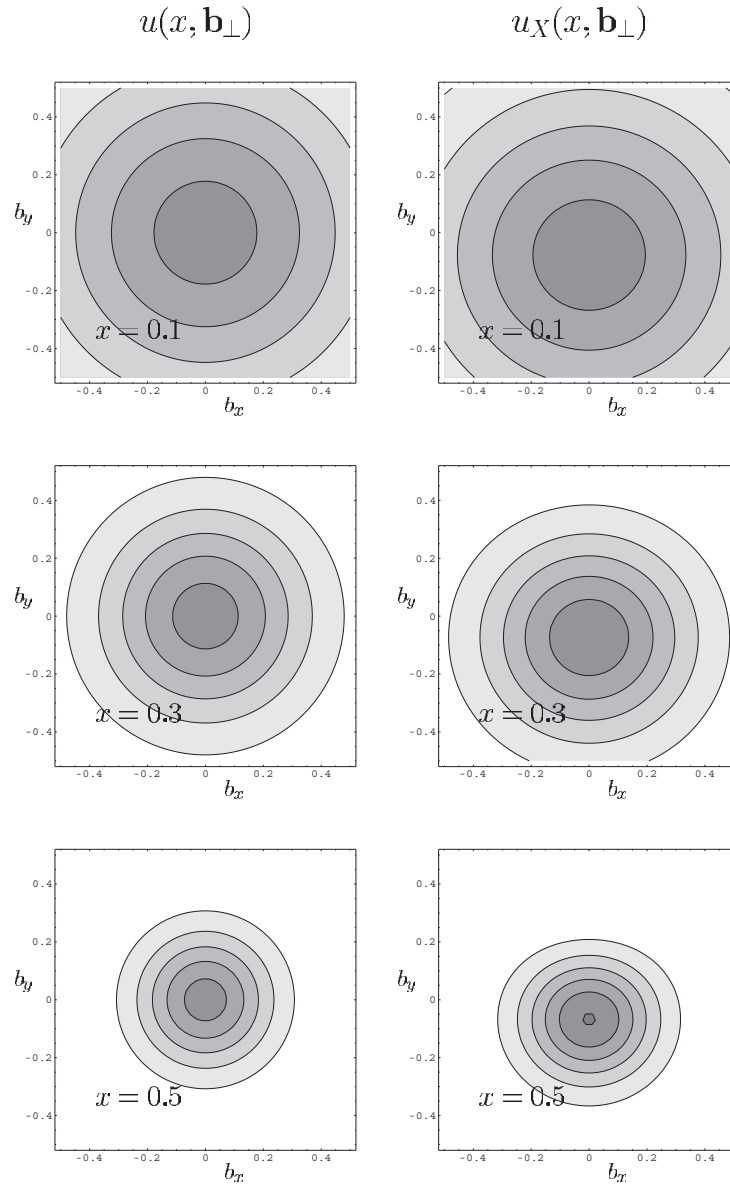


Figure 42: The GPD $H(x, b_\perp) = u(x, b_\perp)$ obtained from the GPD $H(x, 0; \Delta_\perp)$ in eq. 11. Shown are contour plots of transverse density for various slices of longitudinal momentum fraction x . $u_X(x, b_\perp)$ is the probability distribution for the proton polarized in the x direction.

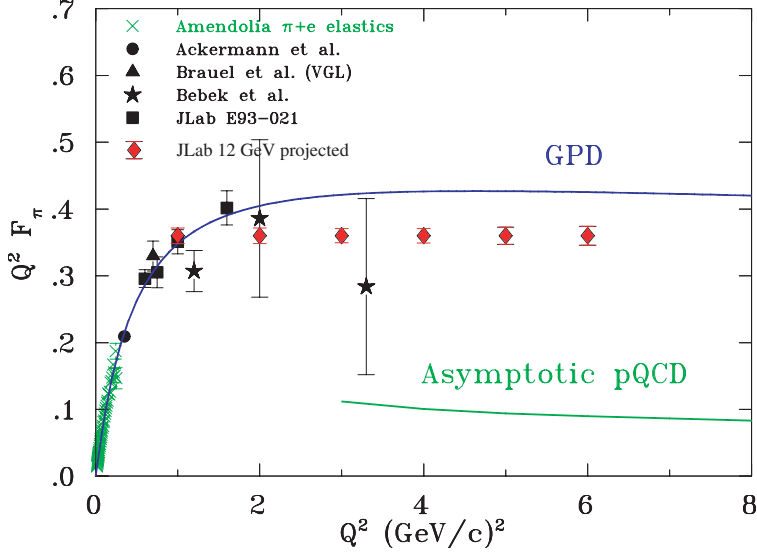


Figure 43: The π^+ form factor. Recent Hall C data are denoted by black squares. Red diamonds denote the Hall C 12-GeV projections. Other available data are shown as well. The curves are the results of theoretical calculations. The GPD based calculation [Mu02] using a power law dependent GPD is shown by a blue curve, and the results of the asymptotic pQCD calculation using an asymptotic valence quark distribution function is shown by the green curve.

simple power-law dependence of $H_\pi^q(x, t)$ is shown together with the asymptotic pQCD prediction and existing experimental data. The recent Hall C results [Vo00], which are the current world standard, reach $Q^2 = 1.6 \text{ (GeV/c)}^2$. The measurement of this form factor to $Q^2 = 6 \text{ (GeV/c)}^2$ is one of the high priority components of the Hall C 12 GeV upgrade program.

Baryon Form Factors and GPDs The description of baryons in terms of GPD's is more complex. In case of the nucleon we have four functions H , E , \tilde{H} and \tilde{E} . Examples of form factor type reactions involving baryons which will be measured are the proton electric to magnetic form factor ratio G_E^p/G_M^p , the $N \rightarrow \Delta$ resonance transition form factors, the $N \rightarrow S_{11}$ transition amplitude $A_{1/2}$, and high $-t$ Compton scattering from the nucleon. In each case, there is a direct relationship between the form factor and a GPD.

Elastic Scattering from the Proton For nucleon elastic scattering, the Dirac (helicity non-flip) and Pauli (helicity flip) form factors are the zero'th moments of the GPD's H and E respectively.

$$F_1(t) = \sum_q F_1^q(t) = \int_{-1}^1 \sum_q H^q(x, \xi; t) dx \quad F_2(t) = \sum_q F_2^q(t) = \int_{-1}^1 \sum_q E^q(x, \xi; t) dx, \quad (13)$$

where q signifies both quark and anti-quark flavors. We take the reference frame in which the momentum transfer is transverse so that $\xi=0$, and denote $H^q(x, t) \equiv H^q(x, 0; t)$, $E^q(x, t) \equiv E^q(x, 0; t)$, etc. There exist also other very important and useful sum rule constraints on the GPDs in eqs. 13. GPD's. They are that in the $-t = 0$ limit, $H^q(x, 0) = f_q(x)$, and $E^q(x, 0) = g_q(x)$, that is, the GPD's coincide with the unpolarized and polarized structure functions which are measured

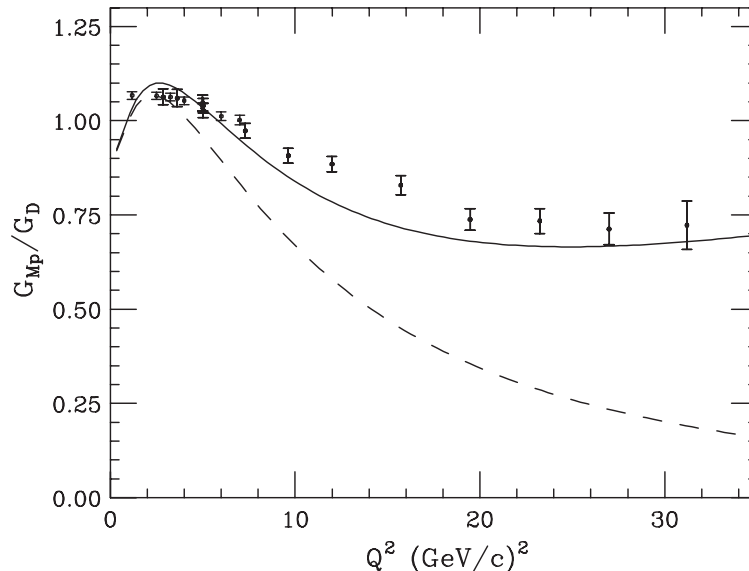


Figure 44: The proton magnetic form factor. The data [Si93], from SLAC, has been adjusted to account for the recent JLab measurements of G_E^p/G_M^p . The dashed curve is obtained [St02] by applying the phenomenological soft wave function of Ref. [Ra98a] of Eq. 10, and the solid curve results from the addition of a power law in k_\perp component to account for the quark high momentum tail.

in deep inelastic scattering. Also, for the proton $F_{1,u}^p(0) = 4/3$ and $F_{1,d}^p(0) = -1/3$, the charges carried by the proton's u and d valence quarks, such that $F_{1,u}^p(0) + F_{1,d}^p(0) = F_1^p(0) = 1$. Also, for F_2^p we have $F_{2,u}^p(0) = \kappa_{p,u}$, and $F_{2p,d}(0) = \kappa_{p,d}$, the anomalous magnetic moments carried by the quarks such that $\kappa_{p,u} + \kappa_{p,d} = k_p \sim 1.79$. Similar constraints hold for neutrons as well.

Experimentally, it has been more convenient to obtain the Sachs form factors, which are linear combinations of the Fermi and Pauli form factors, defined by the relationships

$$G_M(Q^2) = F_1(Q^2) + \kappa F_2(Q^2) \quad G_E(Q^2) = F_1(Q^2) - \tau \kappa F_2(Q^2) . \quad (14)$$

Here, $\tau = Q^2/4M^2$, M is the mass of the nucleon (either proton or neutron) and κ is the nucleon's anomalous magnetic moment. The measurement of either set is equivalent to the measurement of the other.

Of the four nucleon form factors, the magnetic form factor of the proton $G_M^p(Q^2)$ has been the most accessible in the multi GeV range, and had been extracted from ep elastic cross section measurements with rather good accuracy out to high Q^2 . This is shown in Fig. 44.

The proton electric form factor $G_E^p(Q^2)$ is difficult to obtain via a Rosenbluth separation, which is especially subject to systematic errors, and it had previously been obtained with rather poor systematic and statistical accuracy out to about $8(\text{GeV}/c)^2$. Recently, new measurements were performed in Hall A using a recoil polarization technique, which is not as subject to the same systematic errors as the Rosenbluth technique. This result, and its possible interpretations have

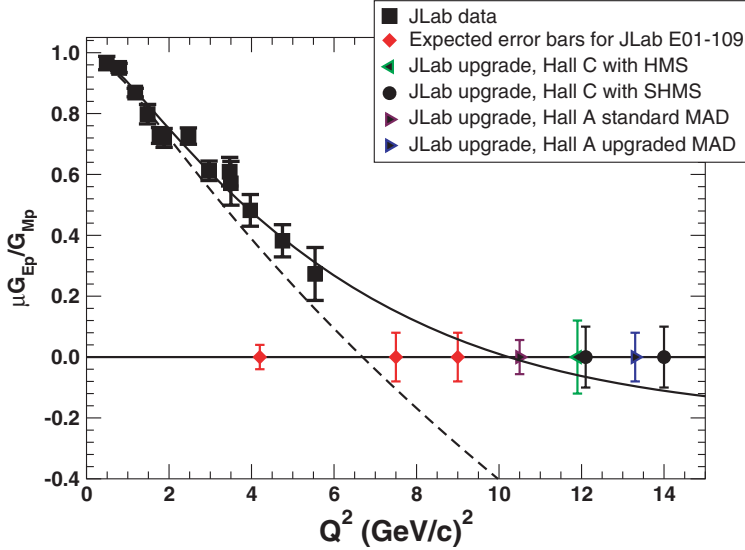


Figure 45: The status of the JLab measurement of G_E^p/G_M^p and the range of the projected measurements with either Hall A or Hall C equipment. The dashed and solid curves are the result of the calculation using a *soft* GPD [Af99, St02] as in eq. 11, and one with additional high momentum components in k_\perp modeled by a power law dependence [St02], respectively.

been the most highly cited and most highly publicized JLab experiment to date, even reaching the popular press. The ratio G_E^p/G_M^p , shown in Fig. 45, actually falls quite dramatically as a function of Q^2 , which contradicts previously held assumptions about the proportionality of G_E^p and G_M^p with Q^2 , and suggests the intuitively baffling idea that the electric charge distribution is spatially softer (larger size) than the magnetic moment distribution. One is naturally led to the question of whether G_E^p/G_M^p will continue to fall with increasing Q^2 (even becoming negative!) It is projected that with the 12 GeV upgrade, G_E^p/G_M^p could be measured up to $Q^2 = 14$ $(\text{GeV}/c)^2$, in either Halls C or Hall A. Projections are shown in Fig 45. This result has also forced us to go back and re-evaluate existing G_M^p data, yielding small modifications in the accepted values.

An initial application of GPD's to nucleon form factors [Ra98a] was for the proton F_{1p} based on nonforward parton density of Eq. 10, with the constraint $H^q(x, 0) = f^q(x)$. With a single parameter λ having the reasonable value around 300 MeV for the average transverse momentum of quarks, a rather good fit was obtained for F_{1p} up to $Q^2 \sim 8$ $(\text{GeV}/c)^2$. With the addition to $\Psi(x, k_\perp)$ of a “hard” component in k_\perp in the form of a power law [St02] a good fit to F_{1p} was obtained over the entire range of Q^2 up to about 32 $(\text{GeV}/c)^2$. A similar application for F_{2p} was made in Ref. [Af99] with the interesting result that, taken together with other data from DIS, it was found that about 50% of the proton spin is carried by the quarks, and half of that (50%) is due to orbital angular momentum. The result of a consistent fit of parameters for F_{1p} and F_{2p} , including high momentum tails [St02] yields the curves for G_M^p , and G_E^p/G_M^p as shown in Figs. 44 and 45.

Elastic Scattering from Neutrons The measurement of form factors of the neutron is vitally

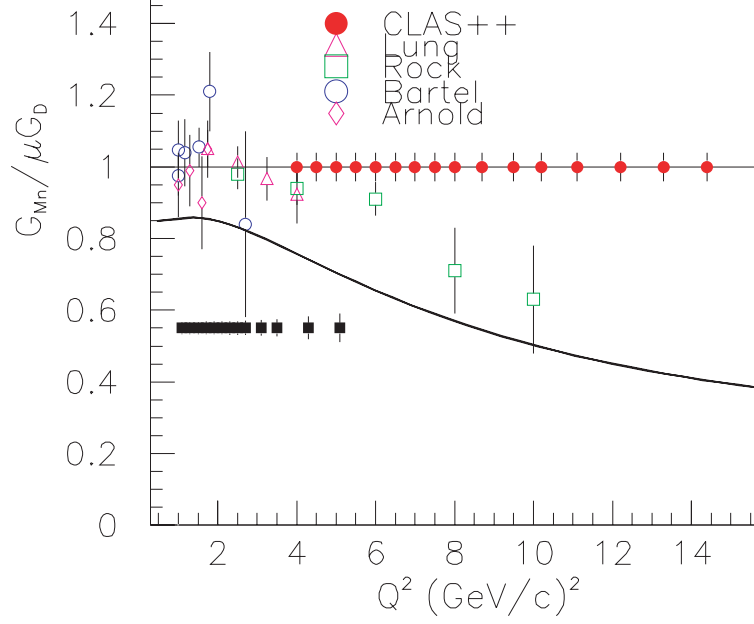


Figure 46: The current status of the data [Lu93, Ro82, Ba73, Ar88] for G_M^n , and the projections, denoted by red circles, for the Hall B program with the 12 GeV upgrade. The open points are existing data and the solid squares are the error projections for data already taken in Hall B. Also shown are the predictions based on the GPD calculations for the proton form factors as in eqs. Figs. 46 and 45 invoking isospin invariance. The meaning of the solid curve is as in Fig. 44.

important because to first order the neutron's quark wave functions are related to those of the proton by simple isospin invariance. Thus, a consistent modeling of all four elastic form factors, G_E^p , G_M^p , G_E^n and G_M^n , is a necessary constraint for any quark based nucleon wave function model. Unfortunately, because the stable neutron only exists within a more complex nucleus, the neutron form factors are much more difficult to measure than those for the proton, and the existing data, even for G_M^n are not in very good shape, plagued by the systematic uncertainty introduced by various assumptions about the relative Q^2 dependences of G_E^n and G_M^n . Thus, there is a major experimental program planning to measure G_M^n in Hall B. Fig. 46 shows the current experimental status of G_M^n , and the projections of the Hall B program for the 12 GeV upgrade.

The neutron electric form factor G_E^n at increasing Q^2 cannot practically be extracted from unpolarized cross sections, and all measurements are obtained from polarization measurements. The two independent sets of JLab measurements in Hall C have been able to extract high quality measurements only up to $Q^2 = 1.5$ (GeV/c)². The results are not final and the expected error bars are shown in Fig. 47. There are plans to extend G_E^n measurements in Hall A to $Q^2 \sim 3.5$ (GeV/c)². Future plans for Hall A with the 12 GeV upgrade call for eventual measurements of G_E^n up to $Q^2 \sim 5$ (GeV/c)². Although it may never be possible to obtain G_E^n at momentum transfers approaching those of the other three elastic form factors, having G_E^n in the proposed range would be extremely valuable as a constraint on the GPD's, and there is no guarantee it will remain very small in comparison to the other form factors at higher Q^2 . The situation is summarized in Fig. 47.

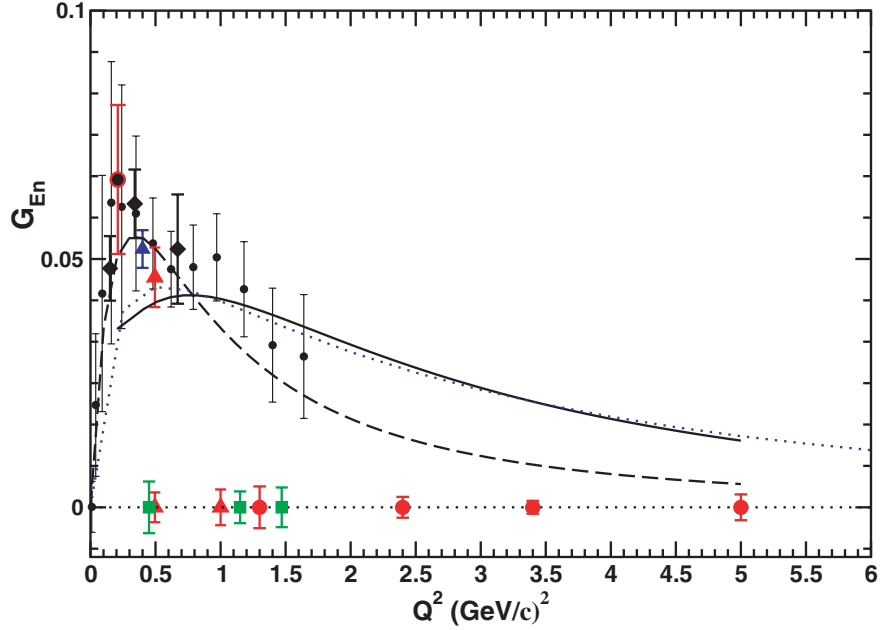


Figure 47: The neutron electric form factor G_E^n . Current data is plotted as open red circle [Pa99], open black diamond [Os99], filled blue triangle [Be99], filled red triangle [Zh01] and filled black diamond [Ro99]. The open circles are En extracted from elastic ed polarization and cross section measurements by Ref. [Sc01]. The points along the baseline (filled green squares [Ma93] and red triangles [Da93]) are the projected errors on G_E^n expected from data already obtained in Hall C, and the two high Q^2 points in red are the errors projected for the approved experiment in Hall A [Ca02]. The projections to higher Q^2 planned for Hall A with the 12 GeV upgrade will extend these measurements to at least $Q^2 \sim 5$ (GeV/c) 2 . The solid black curve is a prediction based on the GPD calculation for the proton form factors invoking isospin invariance as in the previous figures. The curve denoted by black dashes is the Galster [Ga71] parameterization. The blue dotted curve is due to ref. [Mi02].

In Figs. 45, 47 are shown the predictions for G_M^n and G_E^n obtained with the wave functions used to obtain the proton G_M^p and G_E^p curves in Figs. 44 and 45, employing isospin invariance. The curves underestimate the G_M^p data by about 20%. However, the data may be somewhat high due to systematics in the way G_M^p was extracted from the cross section data. The prediction for G_E^n appears to rise to a large value at high Q^2 . One must not over-interpret these curves because they are phenomenological at best, and not based upon rigorous theoretical principles. However, they do illustrate the power of the GPD technique and the need for quality high- Q^2 data.

High $-t$ Compton Scattering and Meson Electroproduction.

High $-t$ Compton Scattering For Compton scattering the appropriate *form factor-like* quantities are the $1/x$ moments of the GPD's

$$R_V(t) = \int_{-1}^1 \sum_q \frac{1}{x} H^q(x, t) dx , \quad (15)$$

$$R_T(t) = \int_{-1}^1 \sum_q \frac{1}{x} E^q(x, t) dx , \quad (16)$$

$$R_A(t) = \int_{-1}^1 \sum_q \frac{1}{x} \tilde{H}^q(x, t) dx . \quad (17)$$

The unpolarized cross section $d\sigma/dt$ at a particular s contains all three form factors, but is sensitive primarily to a combination of $R_V(t)$ and $R_A(t)$. It turns out that the longitudinal and transverse polarization transfer observables K_{LL} and K_{LT} are sensitive to the ratios $R_A(t)/R_V(t)$ and $R_T(t)/R_V(t)$, so that a measurement of $d\sigma/dt$, K_{LL} and K_{LT} are sufficient to determine all three form factors. A polarization transfer measurement [Na02] for the reaction $P(\gamma, \gamma P)$ at $E_\gamma = 3.2$ GeV and $\theta_{p,cm} = 120^\circ$ has been performed, and the quantity K_{LL} was extracted. The result of this experiment is shown in Fig. 48. The data was compared to a number of different theoretical approaches. An important result is that the data is in excellent agreement with a GPD based theoretical calculation [Di99] using wave functions similar to that in eq. 10. This again appears to show the soundness of the GPD approach. Many unpolarized cross section points were also obtained, and a new proposal aims to complete the Hall A experiment by mapping K_{LL} and K_{LT} over a range of $\theta_{p,cm}$ shown in Fig. 49. This will enable one to obtain R_A/R_V and R_T/R_V over a range of $1 \leq -t \leq 5$ (GeV/c)². Plans now exist with the 12 GeV to make a complete set of Compton scattering measurements up to $s = 20$ (GeV/c)² and $-t = 20$ (GeV/c)² making full use of the capabilities of the new detection facilities in Halls A and C. In addition to cross sections, the recoil polarization observables will be obtained over a large range of the available kinematics. The kinematic coverage is illustrated graphically in Fig. 48.

High $-t$ Low Q^2 Meson Electroproduction The cross section for exclusive single meson production can be expressed in terms of form factors analogous to those accessed in Compton scattering. Assuming factorization, the longitudinal cross section corresponding to Fig. 40d. can be written

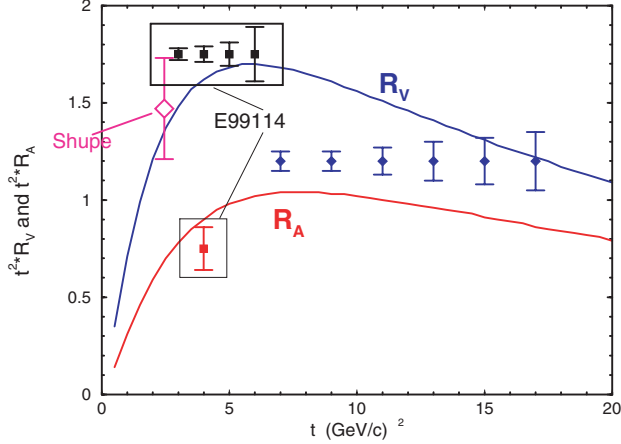


Figure 48: Proposed kinematic coverage of the planned RCS experiments in Halls A and C with the 12 GeV upgrade.

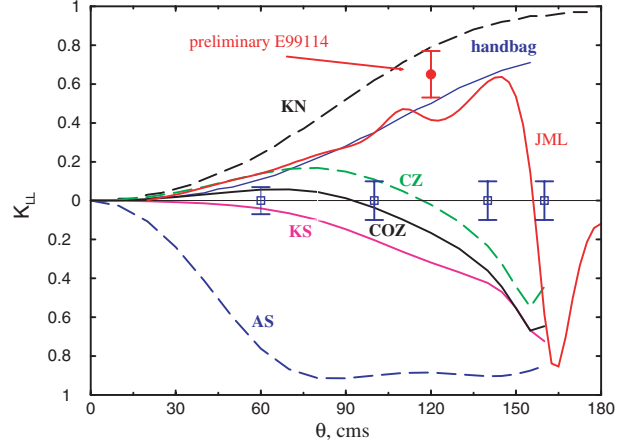


Figure 49: The recoil polarization observable K_{LL} measured in the recent Hall A real Compton scattering experiment, as well as the projected data for the proposed experiment at $E_\gamma = 3.2$ GeV. The solid blue curve is the result of a GPD based calculation [Di99], and the curves at negative K_{LL} are the result of various pQCD based calculation.

as [Di99, Hu00]

$$\frac{d\sigma_L^{\pi^0}}{dt} \sim \left[R_A^{\pi^0}(t) \int_0^1 d\tau \phi_M(\tau) f_0^q(\tau, s, Q^2, t) \right]^2 \quad (18)$$

$$R_A^{\pi^0}(t) = \int_{-1}^1 \sum_q \frac{1}{x} \tilde{H}^q(x, t) dx \quad (19)$$

Technically, only σ_L results in the factorized form in Eq. 18, where the integral represents a convolution over the meson's valence quark momentum fraction τ of the quark distribution function with the pion hard scattering amplitude. At moderate momentum transfer, Ref. [Hu00] finds that σ_L is already dominant, but this needs to be experimentally verified. An important part of the Hall B GPD program is extensive measurements of exclusive π^0 and η at high $-t$. As in the case of the other form factor measurements, this will enable us to obtain information about the short distance (small b_\perp) structure of the GPD's, which is not available from low $-t$ measurements. Figure 50 is an example of the kind of statistical precision on $R_A^{\pi^0}(t)$ anticipated in the Hall B measurement.

Resonance Transition Form Factors Resonance transition form factors access components of the GPD's which are not accessed in elastic scattering or wide angle Compton scattering. The envisaged upgrade program includes high Q^2 measurements of the $P \rightarrow \Delta(1232)$, and $P \rightarrow S_{11}(1535)$. The $\Delta(1232)$, and $S_{11}(1535)$ are to lowest approximation the chiral and parity doublet partners of

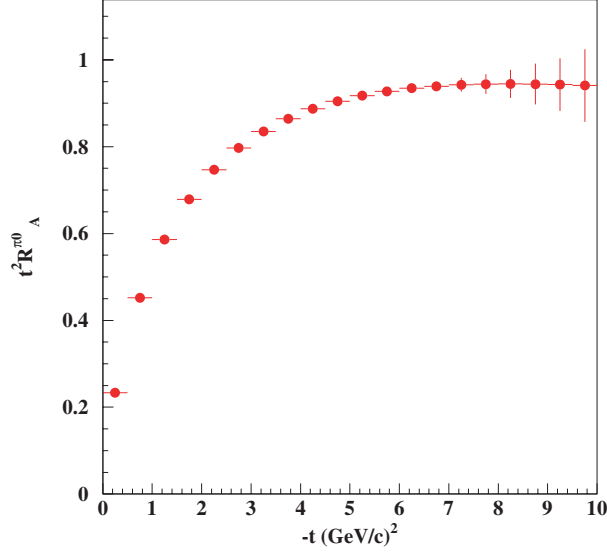


Figure 50: The statistical accuracy of $R_A^{\pi^0}(t)$ anticipated in the Hall B measurement of the exclusive π^0 electroproduction.

the nucleon. The $N \rightarrow \Delta$ form factors are related to isovector components of the GPD's.

$$G_M^* = \int_0^1 \sum_q H_M^q(x, t) dx \quad (20)$$

$$G_E^* = \int_{-1}^1 \sum_q H_E^q(x, t) dx \quad (21)$$

$$G_C^* = \int_{-1}^1 \sum_q H_C^q(x, t) dx \quad (22)$$

where G_M^* , G_E^* and G_C^* are magnetic, electric and Coulomb transition form factors, which are equivalent to the M_{1+} , E_{1+} , and C_{1+} in CGLN multipole notation. H_M^q , H_E^q , and H_C^q are *isovector* GPD's, which can be related to elastic GPD's in the large N_C limit through isospin rotations [Fr00, Go01]. The $N \rightarrow S_{11}$ transition form factor is also important, as it probes fundamental aspects of dynamical chiral symmetry breaking in QCD. If chiral symmetry were not broken, the S_{11} would be the nucleon's parity partner and the N and S_{11} masses would be degenerate.

A major component of the Hall C and B program will be to measure all of these resonance form factors to the highest Q^2 attainable. Figures 51 and 52 show existing data for G_M^*/G_D and G_E^*/G_M^* , respectively, while Fig. 53 shows the existing and G_C^*/G_M^* data. All three figures show projected data from the 12 GeV upgrade.

We note the remarkable falloff of G_M^* relative to the elastic G_M^p . From the GPD formalism, this falloff is related to the falloff of G_E^p/G_M^p (Fig. 45). The black curve [St02] in Fig. 51 is obtained from the same wave functions used to calculate the nucleon form factors, employing isospin rotation. Figure 52 shows the ratio E_{1+}/M_{1+} (or $-G_E^*/G_M^*$). The G_E amplitude is a chiral non-leading

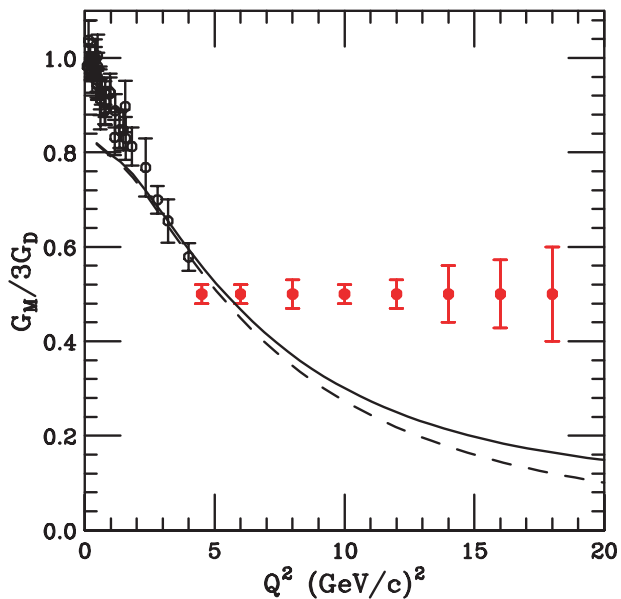


Figure 51: The Delta resonance transition form factor G_M^* , as compared to the dipole G_D . Existing exclusive Hall B and C and other data are in black, with projected 12 GeV upgrade Hall C results are in red. The curves are the result of applying the isovector GPD obtained from the isospin rotated elastic scattering GPD's as discussed in the previous figures and the text.

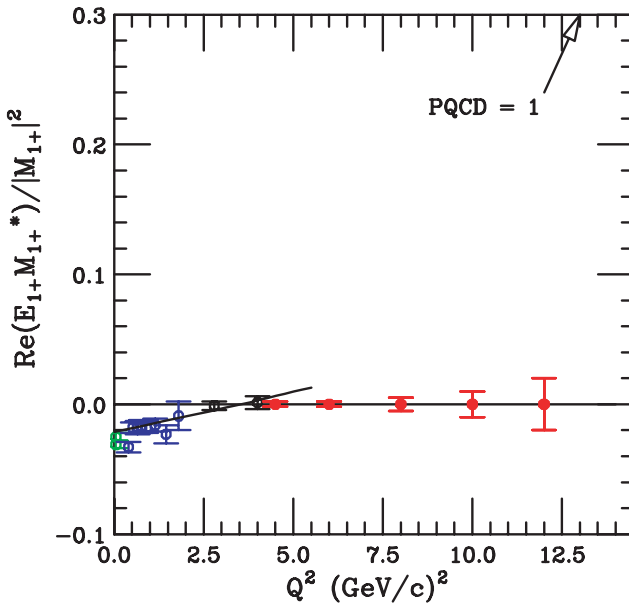


Figure 52: The E_{1+}/M_{1+} (or $-G_E^*/G_M^*$) ratio for Delta excitation, including JLab data from Halls B (blue) and C (black) [Jo02, Fr98a], and projected Hall C 12 GeV upgrade data. The curve below 4 $(\text{GeV}/c)^2$ is the MAID dynamical model fit [Dr99]. In the pQCD limit $G_M^*/G_D \rightarrow \text{const}$ and $E_{1+}/M_{1+} \rightarrow 1$. The dashed curve is due to the soft Gaussian dependent part.

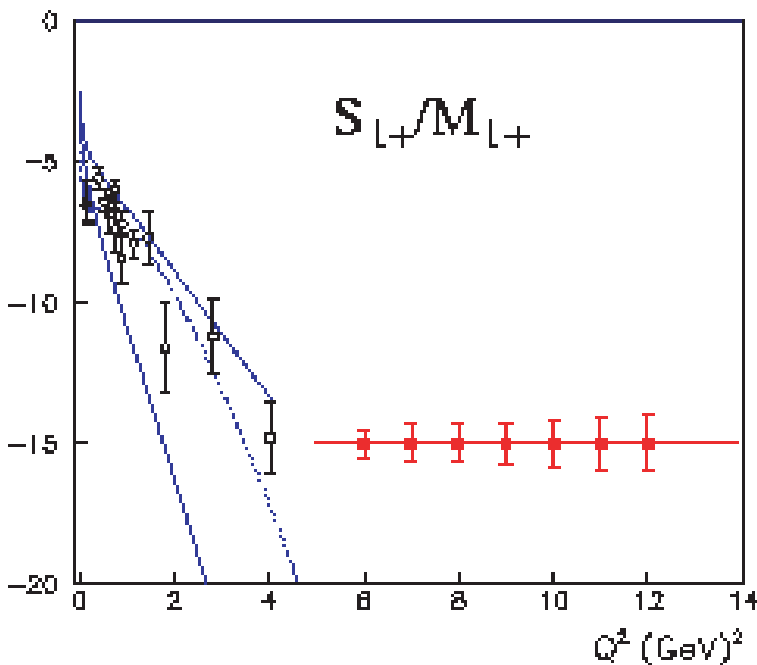


Figure 53: Existing JLab data for S_{1+}/M_{1+} and JLab Hall B 12 GeV projections.

process, and cannot be calculated by simply a naive isospin rotating the nucleon form factor, but requires a more sophisticated approach, which is currently being pursued. The $p \rightarrow \Delta$ form factor G_M^* and the $p \rightarrow S_{11}$ form factors will be measured in Halls B and C, extending the currently maximum Q^2 of 4 (GeV/c)² to almost 18 (GeV/c)², and the ratio E_{1+}/M_{1+} will be extended to about 12 (GeV/c)² (This assumes that ratio stays small. If the ratio grows then higher Q^2 is possible).

pQCD - Constituent Scaling, Helicity Conservation At very high momentum transfer (Q^2 or $-t$), exclusive reactions are expected to access the small but non-perturbative leading Fock state configurations consisting only of the valence quarks, which perturbatively exchange the minimum number of gluons necessary to keep the entire hadron intact. Examples of reactions which have been theoretically studied by means of the pQCD framework are those discussed in regard to GPD's. In analogy with Fig. 40, the same reactions are shown diagrammatically in Fig. 41 a propos of pQCD.

A well known prediction of pQCD is *constituent scaling*: asymptotically the amplitudes have power-law behavior $\sim (1/Q^2)^N$, with the power N determined by the number of valence constituents. Another prediction of pQCD is *hadron helicity conservation*: the amplitudes involving helicity flip are suppressed by powers of $1/Q^2$ compared to non-flip or spin-averaged amplitudes. The crucial question is how large the relevant Q^2 should be to guarantee the dominance of the asymptotic hard scattering mechanism. The power-law behavior with powers close to those given by pQCD was experimentally observed for many form factors and hard exclusive reactions, and that was often considered as evidence that the pQCD mechanism dominates starting from few (GeV/c)² region. The reaction for which pQCD is expected to be applicable at the lowest Q^2 is the neutral pion form factor $F_{\gamma^*\gamma\pi^0}$, which has been measured at CLEO [Gr97] and does indeed exhibit the requisite behavior starting with $Q^2 \sim 2$ (GeV/c)². The theoretical explanation of the early onset of pQCD scaling in this process is the absence of the competing soft mechanism. On the other hand, the charged pion form factor gets contributions both from hard pQCD and soft (or Feynman) mechanisms. In many models, the latter easily fits existing experimental data and, furthermore, imitates the constituent scaling $1/Q^2$ behavior in a wide range of Q^2 . This provides an example that observation of the “correct” power-law behavior may be not sufficient for establishing the reaction mechanism. The pion form factor $F_{\pi^+}(Q^2)$ is a rare case when the normalization of the pQCD term can be estimated with a rather high precision using the $F_{\gamma^*\gamma\pi^0}$ data, the main source of ambiguity being the size of the strong coupling constant α_s . With the (usually accepted) value $\alpha_s \sim 0.4$, the pQCD term is well below the estimates for the soft term. The study of $F_{\pi^+}(Q^2)$ offers the best chance of observing the transition to pQCD at the smallest Q^2 , since the pion has the smallest number of valence quarks.

The most recent theoretical studies of F_{π^+} seem to indicate that hard mechanisms may become important by $Q^2 \sim 5$ (GeV/c)². To date, the most accurate measurements of F_{π^+} have been carried out in Hall C to a maximum Q^2 of around 1.6 (GeV/c)². One of the highest priorities for

the Hall C program is to measure F_{π^+} as accurately as possible to the highest Q^2 possible, which will exceed 6 (GeV/c)^2 . The experimental projections and results of various theoretical calculations are shown in Fig. 43.

For the case of baryons the pQCD mechanism involves two hard gluon exchanges and its dominance for this reason is expected at higher Q^2 than for $F_{\pi^+}(Q^2)$. Experimentally, the proton magnetic form factor $G_M^p(Q^2)$ and Dirac form factor $F_{1p}(Q^2)$ appear to begin to scale at momentum transfers as low as a few $(\text{GeV/c})^2$. The dominance of the pQCD mechanism, however, also implies helicity conservation. It should be experimentally tested before any strong conclusions are made.

Results of four published JLab form factor experiments discussed above have unequivocally shown that at current energies the pQCD regime for nucleons is still elusive. These experiments include 1. the elastic scattering ratio F_{2p}/F_{1p} in Hall A, 2. the transition form factors $P \rightarrow \Delta(1232)$, and 3. the $P \rightarrow S_{11}(1535)$ in Halls B and C, and 4. Compton scattering $P(\gamma, \gamma)P$ in Hall A. With the 12 GeV upgrade, these experiments are expected to greatly increase obtainable momentum transfers, and to involve all three halls; A, B and C.

The Proton Elastic Electric Form Factor pQCD predicts that for elastic scattering the ratio of the helicity non-conserving to helicity conserving form factors are expected to scale as $F_{2p}/F_{1p} \propto \Lambda^2/Q^2$. Within the pQCD scenario, helicity conservation is violated by effects due to quark masses and primordial transverse momentum (Fermi motion) of quarks, hence $\Lambda^2 \sim \langle k_{\perp}^2 \rangle$. The measurements [Jo00, Ga02] in Hall A up to a $Q^2 \sim 5.6 \text{ (GeV/c)}^2$ shows that the ratio $Q^2 F_{2p}(Q^2)/F_{1p}(Q^2)$ is still rising with Q^2 , reaching the value about 1.5 (GeV/c)^2 , which is a huge number compared to $\langle k_{\perp}^2 \rangle \sim 0.1 \text{ (GeV/c)}^2$. The data indicate a $1/Q$ dependence of F_{2p}/F_{1p} (see Fig. 45) which contradicts the pQCD prediction and earlier SLAC data which had indicated a $1/Q^2$ behavior. One is naturally led to the question of where in Q^2 will F_{2p}/F_{1p} begin to approach the pQCD scaling behavior. It is projected that with the 12 GeV upgrade, G_E^p/G_M^p could be measured up to $Q^2 = 14 \text{ (GeV/c)}^2$, in either Hall C or Hall A. Projections are shown in Fig 45.

Resonance Transition Form Factors The leading baryon transition amplitudes are also expected to scale with Q^2 . The $S_{11}(1535)$ is uniquely accessed by its strong η channel via the $p(e, e'p)\eta$, where the η is reconstructed by missing mass. For the $p \rightarrow S_{11}$ transition, the amplitude, which is purely helicity conserving, is expected to scale as $Q^3 A_{1/2} \rightarrow \text{constant}$. In Fig. 54, this is seen not to have occurred yet. However, the shape is beginning to show signs of a possible approach to scaling.

In the $p \rightarrow \Delta(1232)$ transition, as in the case of the nucleon, the magnetic transition form factor is predicted by pQCD to scale as $G_{Mp}^* \rightarrow 1/Q^4$. As seen in Fig. 51, experimental results do not show the onset of constituent scaling up to $Q^2 \sim 4 \text{ (GeV/c)}^2$. In fact, as already noted, $Q^4 G_{Mp}^*$ appears to be decreasing with Q^2 , just as in the case of the elastic G_E^p , which are indicative of related soft processes. Furthermore, helicity conservation, which is a strict criterion for pQCD, requires the ratio of electric to magnetic multipole amplitudes E_{1+}/M_{1+} to approach 1. However,

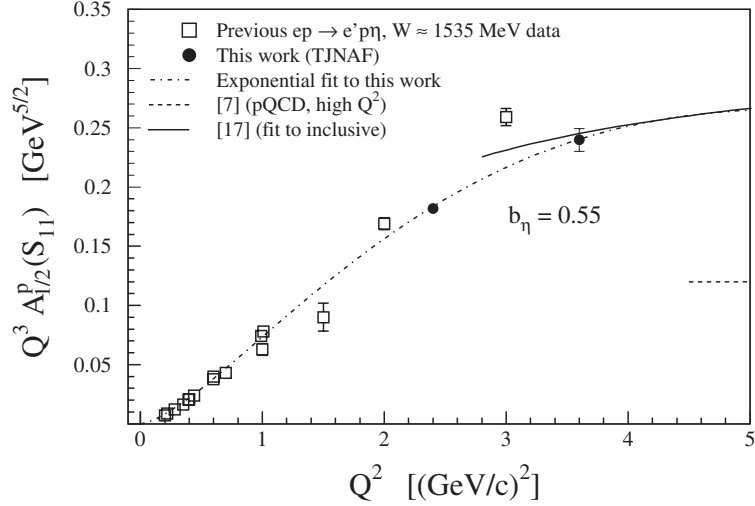


Figure 54: The JLab data for the $p \rightarrow S_{11}$ helicity amplitude $Q^3 A_{1/2}^p$. The lower Q^2 data are from Hall B [Th01], and the higher Q^2 (filled circles) are from Hall C [Ar99]. With the 12 GeV upgrade these measurements can be extended in Hall C to $Q^2 = 18$ $(\text{GeV}/c)^2$.

it is quite apparent from the JLab results shown in Fig. 52 that they remain nearly zero up to $Q^2 = 4$ $(\text{GeV}/c)^2$. Clearly, we would like to see where G_{Mp}^* begins to scale, and E_{1+}/M_{1+} begin to turn over and ultimately increase in the direction required in pQCD. The plans in Halls B and C to extend the Q^2 these quantities by a factor of three to four should help to answer that question.

Compton Scattering Asymmetries Real Compton scattering involves form factors resulting from the *high-t* transverse kick given to the target proton, which remains intact after the reaction. In the pQCD framework it is schematically represented in Fig. 41 by diagram *d*. The results of recent cross section measurements in Hall A over the range $1.5 \leq -t \leq 6.5$ $(\text{GeV}/c)^2$, and $5 \leq s \leq 11$ $(\text{GeV}/c)^2$ are yet to appear. However, the longitudinal recoil asymmetry K_{LL} shown in Fig. 49 strongly disagrees with pQCD. According to pQCD, the Compton form factors R_V , R_T and R_A are also expected to scale with respect to s and $-t$. The planned high s and $-t$ measurements of R_V , R_T , R_A , K_{LL} and K_{LL} in Halls A and C at dramatically increased ranges in s and $-t$ with the 12 GeV upgrade should give us information about the transition to pQCD.

Summary The measurement of exclusive form factors at high momentum transfer will open a new era in which a three dimensional picture of the non-perturbative structure of hadrons can be obtained. Simple models have already demonstrated the value of these experiments, and with high momentum transfer experiments made possible by the 12 GeV upgrade, coupled with the development of a sophisticated theoretical approach, much will be learned about this complex structure. In the extreme high momentum transfer limit, the non-perturbative structure is simplified to three valence quarks, which may be studied with pQCD techniques. The 12 GeV upgrade and associated experimental equipment will give us an excellent opportunity to observe whether the holy grail of the evolution toward pQCD is indeed a practically achievable goal.

2.B.2 Valence Quark Structure and Parton Distributions

One of the most fundamental properties of the nucleon is the structure of its valence quark distributions. Valence quarks are the irreducible kernel of each hadron, responsible for its charge, baryon number and other macroscopic properties. Sea quarks, which at very high Q^2 are largely generated through gluon bremsstrahlung and subsequent splitting into quark-antiquark pairs, represent one source of the nonperturbative “dressing” of the valence quarks at low Q^2 . At higher x values these $q\bar{q}$ contributions drop away, and the physics of the valence quarks is cleanly exposed [Is99].

Experimentally, most of the recent studies of nucleon structure have emphasized the small- x region populated mainly by sea quarks, while the valence quark structure has for some time now been thought to be understood. Starting with the Nobel Prize-winning work of Friedman, Kendall, and Taylor [Bl69] in the 1970s at SLAC, three decades of deep inelastic and other high-energy scattering experiments have provided a detailed map of the nucleon’s quark distributions over a large range of kinematics with one major exception – the deep valence region, at very large x ($x \gtrsim 0.5$). In this region the valence structure of the nucleon can be probed most directly, since sea quark distributions, which must be subtracted from the measured cross sections to reveal the valence structure, are negligibly small beyond $x \sim 0.2 - 0.3$. It is both surprising and unfortunate that the large- x region has been so poorly explored experimentally.

The valence u and d quark distributions are usually obtained from measurements of the proton and neutron F_2 (or F_1) structure functions. At high energy, these functions are defined in leading order perturbative QCD as the charge-squared weighted sums of the quark and antiquark distributions of various flavors ($q = u, d, s, \dots$):

$$F_2(x) = 2xF_1(x) = x \sum_q e_q^2 (q(x) + \bar{q}(x)) . \quad (23)$$

While the u quark distribution is relatively well constrained by the proton F_2^p data for $x < 0.8$, the absence of free neutron targets has left large uncertainties in the d quark distribution beyond $x \sim 0.5$ arising from incomplete understanding of the nuclear medium modifications in the deuteron, from which the neutron F_2^n is extracted. For instance, depending on how one corrects for Fermi motion and binding (off-shell) effects in the deuteron, the extracted ratio $R^{np} \equiv F_2^n/F_2^p$ of neutron to proton structure functions can differ by $\sim 50\%$ already at $x \sim 0.75$ [Wh92, Me96] (see Fig. 55).

These large uncertainties have prevented answers to such basic questions as why the d quark distribution at large x appears to be smaller (or “softer”) than that of the u , softer even than what would be expected from flavor symmetry. Furthermore, since the precise $x \rightarrow 1$ behavior of the d/u ratio is a critical test of the mechanism of spin-flavor symmetry breaking, the large errors on the current data preclude any definitive conclusions about the fundamental nature of quark-gluon dynamics in the valence quark region. From another perspective, knowledge of quark distributions

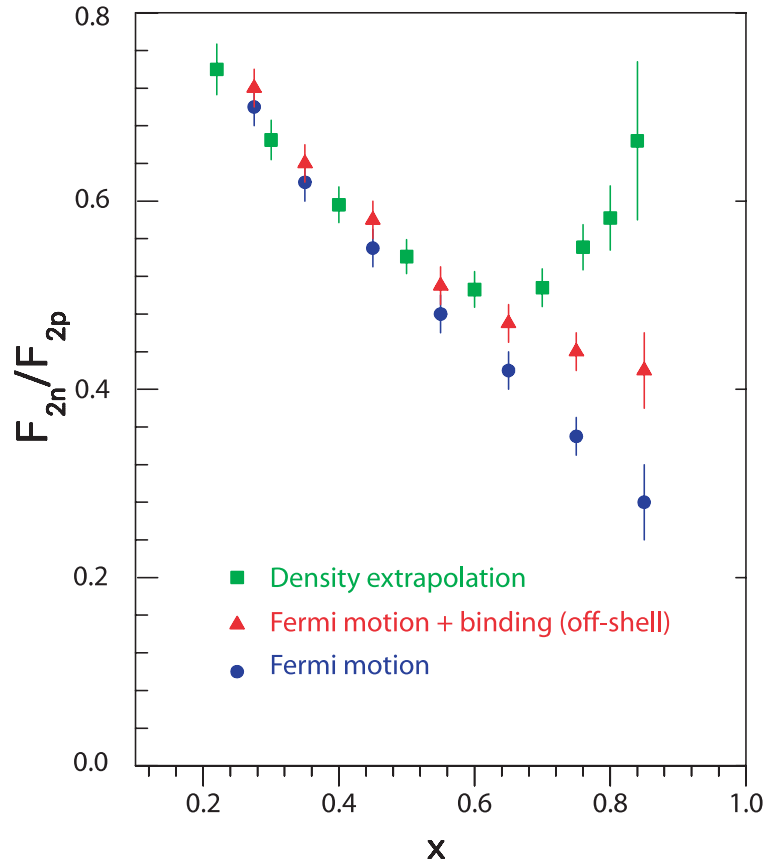


Figure 55: Ratio R^{np} of neutron to proton structure functions as a function of x , extracted from the SLAC data on the deep inelastic proton and deuteron structure functions. The three sets of data points represents R^{np} extracted from the *same* data according to different prescriptions for treating nuclear effects in the deuteron: Fermi smearing only [Bo81, Wh92] (blue circles), Fermi motion and nuclear binding (off-shell) corrections [Me96] (red triangles), and assuming the nuclear EMC effect in the deuteron scales with nuclear density [Fr88] (green squares).

at large x is also essential for determining high-energy cross sections at collider energies, such as in searches for the Higgs boson or for new physics beyond the Standard Model [?, Ku00], where structure information at $x \sim 0.6 - 0.8$ feeds down to lower x at higher values of Q^2 through perturbative Q^2 evolution.

The need for reliable large- x data is even more pressing for the spin-dependent quark distributions. Spin degrees of freedom allow access to information about the structure of hadrons not available through unpolarized processes. Spin-dependent quark distributions are usually extracted from measurements of the spin-polarization asymmetry, A_1 , which is approximately given by the ratio of spin-dependent to spin-averaged structure functions:

$$A_1(x) \approx \frac{g_1(x)}{F_1(x)}, \quad (24)$$

where, to leading order,

$$g_1(x) = \frac{1}{2} \sum_q e_q^2 (\Delta q(x) + \Delta \bar{q}(x)), \quad (25)$$

with Δq defined as the difference between quark distributions with spin aligned and anti-aligned with the spin of the nucleon, $\Delta q = q^\uparrow - q^\downarrow$. The first spin structure function experiments at CERN [As88] on the moment, or integral, of g_1 suggested that the total spin carried by quarks was very small, or even zero, prompting the so-called “proton spin-crisis”. A decade of subsequent measurements of spin structure functions using proton, deuteron, and ^3He targets have determined the total quark spin much more accurately, with the current world average value being $\sim 20\text{--}30\%$ [La00], which is still considerably less than the value expected from the most naïve quark model in which valence quarks carry all of the proton spin.

While the spin fractions carried by quarks and gluons (or generically, partons) are obtained by integrating the spin-dependent parton momentum distributions, the distributions themselves, as a function of the momentum fraction x , contain considerably more information about the quark-gluon dynamics than their integrals do. Furthermore, the spin-dependent distributions are generally even more sensitive than the spin-averaged ones to the quark-gluon dynamics responsible for spin-flavor symmetry breaking. Considerable progress has been made in measuring spin-dependent structure functions over the last decade, especially in the small- x region. However, relatively little attention has been paid to the polarized structure functions in the pure valence region at large x . The lack of data in the valence region is particularly glaring in the case of the neutron, where there is no information at all on the polarization asymmetry A_1^n for $x \geq 0.4$. (The only exception is the recent preliminary Hall A A_1^n data which extend to $x \approx 0.6$; recent Hall B data on A_1^p and A_1^d have also been extended to a maximum of $x \approx 0.6$.)

Theoretical predictions for large- x distributions The simplest model of the proton, polarized in the $+z$ direction, has three quarks described by a wavefunction that is symmetric in spin and flavor [C173]:

$$\begin{aligned}
 |p^\uparrow\rangle &= \frac{1}{\sqrt{2}} |u^\uparrow(ud)_{S=0}\rangle + \frac{1}{\sqrt{18}} |u^\uparrow(ud)_{S=1}\rangle - \frac{1}{3} |u^\downarrow(ud)_{S=1}\rangle \\
 &\quad - \frac{1}{3} |d^\uparrow(ud)_{S=1}\rangle - \frac{\sqrt{2}}{3} |d^\downarrow(ud)_{S=1}\rangle,
 \end{aligned}
 \tag{26}$$

where $q^{\uparrow\downarrow}$ represents the active quark that undergoes the deep inelastic collision, and $(qq)_S$ denotes the two-quark configuration with spin S that is a spectator to the scattering. (The neutron wavefunction can be obtained by simply interchanging the u and d quarks in this expression.) On the basis of exact spin-flavor symmetry, which is described by the group $SU(6)$, the $S = 0$ and $S = 1$ “di-quark” states contribute equally, giving rise to simple relations among the quark distributions, such as $u = 2d$ and $\Delta u = -4\Delta d$, which in terms of the structure functions correspond to:

$$R^{np} = \frac{2}{3}; \quad A_1^p = \frac{5}{9}; \quad \text{and} \quad A_1^n = 0.
 \tag{27}$$

In nature the spin-flavor $SU(6)$ symmetry is, of course, broken. It has been known for some time that the d quark distribution is softer than the u quark distribution, reflecting the fact that the ratio R^{np} (shown in Fig. 55) deviates strongly from the $SU(6)$ expectation beyond $x \sim 0.4$. On the other hand, the data for the polarization asymmetries A_1^p and A_1^n (shown in Fig. 56) are so poor in the valence region that it is presently not possible to discern whether the $SU(6)$ predictions are borne out for the spin-dependent distributions.

A number of models have been developed for quark distributions that incorporate mechanisms for the breaking of the $SU(6)$ symmetry; some of these models can be linked directly to phenomena such as the hyperfine splitting of the baryon and meson mass spectra. Feynman and others [Fe72, C173, Ca75a] observed that there was a correlation between the nucleon and Δ mass difference and the suppression of R^{np} at large x . A quark hyperfine interaction, such as that due to one-gluon exchange, instantons or pion exchange (which can induce a higher energy for the $S = 1$ spectator “di-quark” in Eq. (26)) will necessarily give rise to a larger mass for the Δ since the quark wavefunction for the Δ has all “di-quark” configurations with $S = 1$. If the $S = 0$ states are dominant at large x , Eq.(26) implies that the d quark distribution will be suppressed relative to that of the u . This expectation has, in fact, been built into most phenomenological fits to the parton distribution data [Ei84, Di88, Ma94a, La95].

This mechanism also leads to specific predictions for the polarization asymmetries as x becomes large and close to unity. The ratio R^{np} is expected to decrease to a value of $1/4$, while A_1 will increase to a positive limiting value of unity for both the proton and neutron.

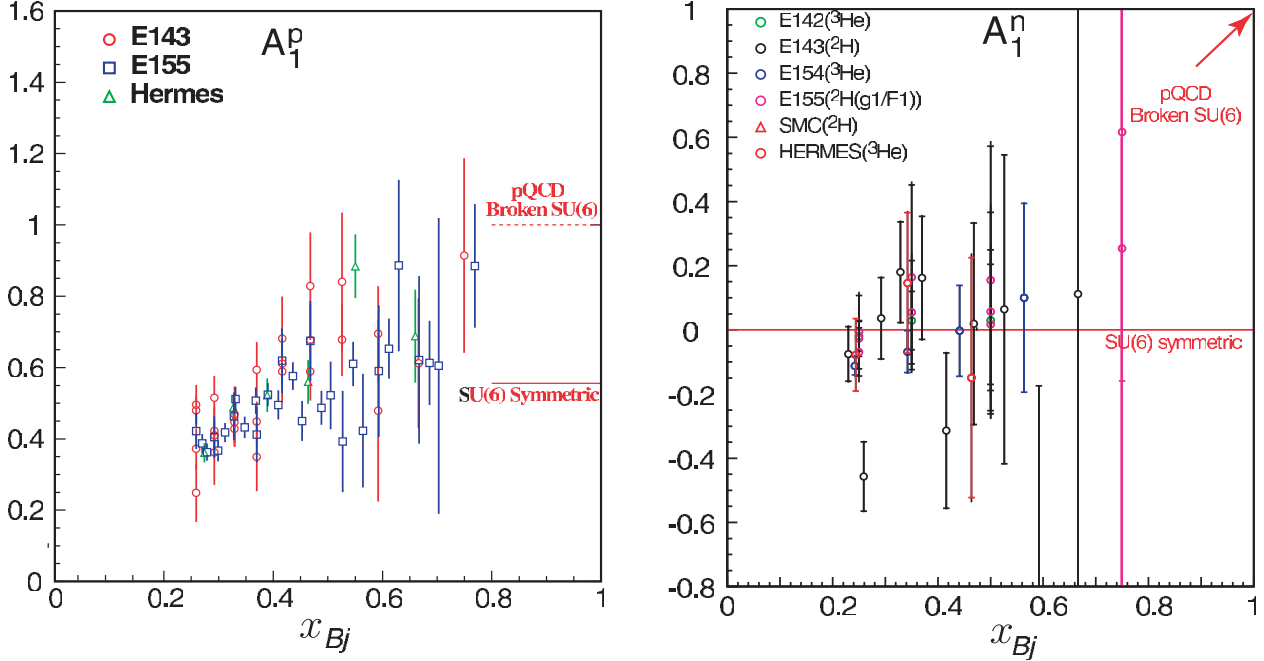


Figure 56: Sample of large- x data for A_1^p (left) and A_1^n (right). The predictions of SU(6) and models based on broken SU(6) for $x \rightarrow 1$ are indicated.

More radical nonperturbative models of SU(6) breaking, such as those which include instantons as important degrees of freedom, predict dramatically different behavior for A_1 as x approaches 1; *i.e.*, that it goes to a limiting of -1 for the proton and a value close to zero for the neutron[Ko97].

Arguments based on hadron helicity conservation (HHC) within perturbative QCD, on the other hand, predict that the dominant components of the proton valence wavefunction at large x are those associated with states in which the total “di-quark” helicity, or spin projection, S_z , is zero [Fa75]. Consequently, scattering from a quark polarized in the opposite direction to the proton polarization is suppressed relative to the helicity-aligned configuration. This leads to a stronger x dependence in the ratio R^{np} , with a limiting value of $3/7$ as $x \rightarrow 1$, and a faster approach to unity for the asymmetries A_1^p and A_1^n .

The novelty of the hadron helicity conservation predictions, especially for A_1^p and A_1^n , is that they can be related to the large Q^2 behavior of elastic form factors, whose detailed Q^2 dependence can provide information about the role of orbital angular momentum of quarks in the nucleon [Ra03, Ji03a]. Furthermore, because A_1 depends weakly on Q^2 we expect these predictions to still be valid in the Q^2 range accessible experimentally. However, it is not clear *a priori* at which x the transition from the nonperturbative dynamics, embodied in the above predictions, to perturbative QCD takes place, so experimental guidance on this issue is essential.

While the trend of the existing R^{np} data is consistent with models with broken SU(6) symmetry, they cannot discriminate between the competing mechanisms of SU(6) breaking (as evident from

Fig. 55) because of uncertainties in the extraction procedure associated with nuclear corrections. For the asymmetries A_1^n and A_1^p , while we do not expect the SU(6) predictions to be accurate, the existing measurements at high x lack the precision to even distinguish any of the predictions from the naïve SU(6) result.

The structure of the free neutron If the nuclear EMC effect (the modification of the free nucleon structure function in the nuclear environment) in deuterium were known, one could apply nuclear smearing corrections directly to the deuterium data to obtain the free neutron F_2^n . However, the EMC effect in the deuteron requires knowledge of the free neutron structure function itself, so the argument becomes cyclic. As seen in Fig. 55, the current experimental impasse has prevented a full understanding of the structure of valence quarks in the nucleon. The 12 GeV Upgrade will finally provide a solution to this 30-year old problem.

“Tagged” neutron structure function The cleanest way to obtain the free neutron structure function is with a novel method currently being pioneered at Jefferson Lab in Hall B, in which a recoil detector is used to tag scattering events on a nearly on-shell neutron in a deuteron target. By detecting slow protons emitted in the backward hemisphere in coincidence with the scattered electron, the initial four-momentum of the struck neutron can be inferred from the observed spectator proton.

A newly designed time-projection-chamber-like recoil detector, in combination with sufficiently thin targets, will allow protons to be detected down to momenta around 70 MeV/c, where the bound neutron is only around 7 MeV away from its mass-shell. The choice of backward kinematics for the spectator proton serves to suppress effects from final state interactions (rescattering of the spectator proton by the deep inelastic remnants of the scattered neutron) [Me97, Ci02], as well as independent target fragmentation [Ci93, Bo94], while the restriction to small proton momenta mostly eliminates uncertainties associated with the deuteron wave function and on-shell extrapolation [Me94].

This new technique will allow the structure of the free neutron to be accessed with unprecedented accuracy over the range $0.2 \leq x \leq 0.82$, and with a minimum of uncertainty associated with nuclear corrections. It opens up a completely new program of measurements on the neutron, in analogy with those which have been carried out in the past on the proton. Figure 57 illustrates the expected errors on the ratio R^{np} extracted from such a measurement. Note that this method can be used to study not only the deep inelastic structure functions of the neutron, but also the structure of neutron resonances, and neutron elastic form factors, essentially free of nuclear effects.

Deep inelastic scattering from $A = 3$ nuclei An alternative, independent method to reliably determine R^{np} , free of the large uncertainties associated with nuclear corrections at large x , is through simultaneous measurements of the inclusive ${}^3\text{He}$ and ${}^3\text{H}$ structure functions, maximally

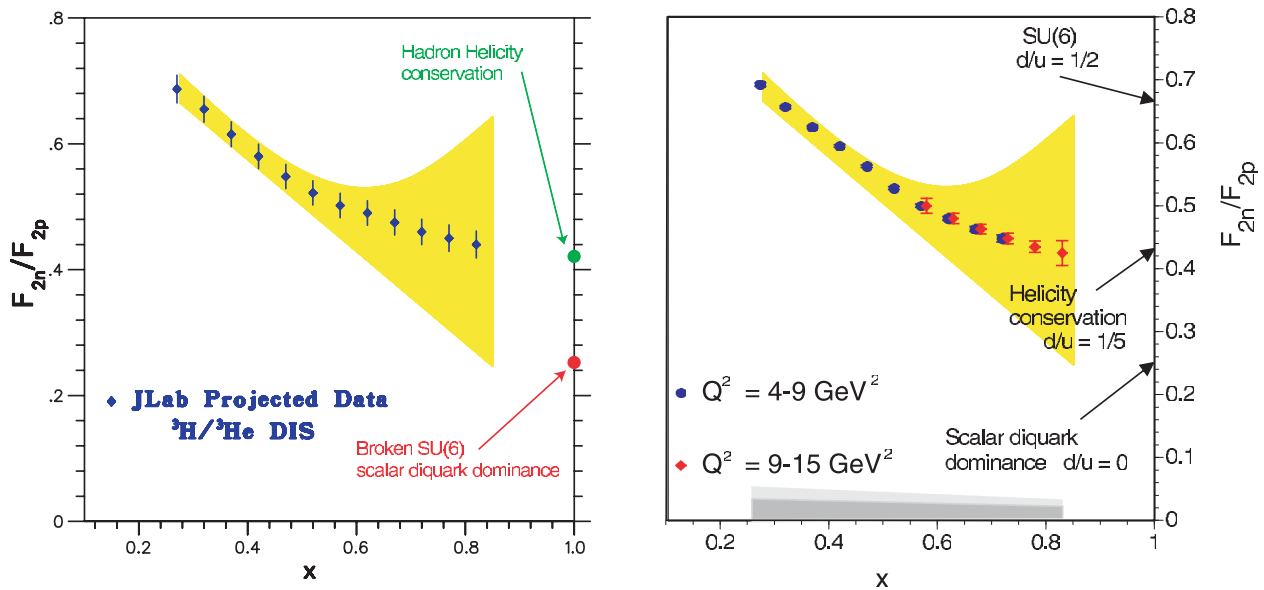


Figure 57: The ratio F_{2n}^n/F_{2p}^p versus x by two techniques. *Left figure:* Using the ${}^3\text{He}/{}^3\text{H}$ ratio, with total (statistical, systematic, and theoretical) errors indicated. *Right figure:* Using spectator proton tagging from a deuteron target. Estimated systematic errors due to experimental and theoretical uncertainties are indicated by the bands at the bottom (light shade for total systematic error, darker shade for point-to-point error after normalization at low x). The arrows indicate the different possible approaches to the limit $x \rightarrow 1$. The yellow shaded area indicates the range of uncertainty from existing data due to different treatment of nuclear effects (see Fig. 55).

exploiting the mirror symmetry of $A = 3$ nuclei. Regardless of the absolute value of the nuclear EMC effect in ${}^3\text{He}$ or ${}^3\text{H}$, the differences between the EMC effects in these nuclei will be small (on the scale of charge symmetry breaking in the nucleus). The advantage of this method is that by measuring a ratio of cross sections, most of the systematic and theoretical errors cancel.

In the absence of a Coulomb interaction, and in an isospin-symmetric world, the properties of a proton (neutron) bound in the ${}^3\text{He}$ nucleus would be identical to those of a neutron (proton) bound in the ${}^3\text{H}$ nucleus. If, in addition, the proton and neutron distributions in ${}^3\text{He}$ (and in ${}^3\text{H}$) were identical, the neutron structure function could be extracted with no nuclear corrections, regardless of the size of the EMC effect in ${}^3\text{He}$ or ${}^3\text{H}$ separately.

In practice, ${}^3\text{He}$ and ${}^3\text{H}$ are not perfect mirror nuclei (*e.g.*, their binding energies differ by some 10%) and the proton and neutron distributions are not quite identical. However, the $A = 3$ system has been studied for many years, and modern realistic $A = 3$ wavefunctions are known to rather good accuracy. Using these wavefunctions, together with a nucleon spectral function, the difference in the EMC effects for the ${}^3\text{He}$ and ${}^3\text{H}$ nuclei has been calculated [Uc88, Ci90, Af00b, Pa01, Sa01] to be less than 2% for $x < 0.85$. More importantly, the actual model dependence of this difference is less than 1% for all x values accessible experimentally with an 11 GeV beam.

By performing the tritium and helium measurements under identical conditions, the ratio of the deep inelastic cross sections for the two nuclei can be measured with 1% experimental uncertainty in Hall A with the MAD (Medium Acceptance Device) spectrometer (SLAC Experiments E139 [Go94] and E140 [Da94, Ta96] have quoted 0.5% uncertainties for measurements of ratios of cross sections). Deep inelastic scattering with the proposed 11 GeV electron beam can therefore provide precise measurements for the $F_2^{{}^3\text{He}}/F_2^{{}^3\text{H}}$ ratio, from which R^{np} can be extracted essentially free of nuclear corrections at the 1% level over the entire range $0.10 \leq x \leq 0.82$. In addition, it will for the first time enable the size of the EMC effect to be determined in $A = 3$ nuclei, which to date has been measured only for $A \geq 4$ nuclei. The key issue for this experiment will be the availability of a high-density tritium target, comparable with the previously used Saclay [Am94] and MIT-Bates [Be89] tritium targets. The quality of the projected data is highlighted in Fig. 57.

Longitudinal–transverse separation While the relation between the F_1 and F_2 structure functions in Eq. (23) is exact for scattering off free, spin-1/2 quarks or anti-quarks, at finite Q^2 small differences between these arise due to gluon radiation and multiparton correlation effects in QCD. These give rise to a non-zero value for the ratio of longitudinal to transverse cross sections, $R = \sigma_L/\sigma_T$. Unfortunately, the difficulty in separating the longitudinal and transverse components of the cross sections via the usual Rosenbluth separation method has resulted in a paucity of data on R , particularly at larger x . Current extractions of the F_2 structure function are therefore hampered by poor knowledge of the longitudinal corrections, and often model-dependent assumptions must be made.

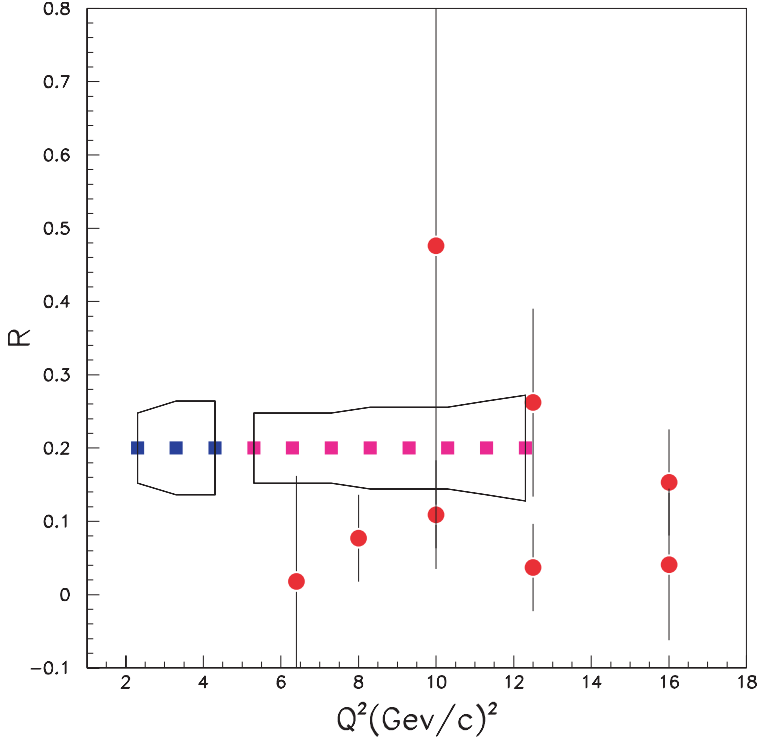


Figure 58: Projected measurements for $R = \sigma_L/\sigma_T$ at $x = 0.8$ (blue for 6 GeV, pink for 11 GeV). The surrounding lines indicate the total uncertainty, compared to the existing data (red).

With a 6 GeV beam, the measurement of separated transverse and longitudinal structure functions is limited to $Q^2 < 6$ (GeV/c)². With an 11 GeV beam, this range can be doubled and separated cross sections obtained out to $Q^2 = 12$ (GeV/c)². Moreover, the precision possible for $4 < Q^2 < 6$ (GeV/c)² can be significantly improved by the larger beam energy available. Projected measurements of R with the HMS and SHMS Hall C spectrometers are shown in Fig. 58 for $x = 0.8$ (in blue for 6 GeV and pink for 11 GeV). The surrounding lines indicate the total statistic and systematic uncertainties possible, a substantial improvement to the existing data set shown in red. Data of this quality would be obtained for numerous such bins in x , allowing for the experimental extraction of all unpolarized structure function moments out to $Q^2 = 10$ (GeV/c)². This is of particular interest since these moments are now calculable from QCD using lattice techniques. In addition, the measurement of the Q^2 dependence of R will be highly sensitive to gluons, and can provide another means for probing the gluon distribution in the nucleon.

Moments of structure functions A high luminosity 11 GeV beam complemented with well matched detectors will make accessible the broad kinematic region required to map out both the resonance and deep inelastic regimes requisite to precision structure function studies. The wide range of scattered electron energy and angle provided by the HMS and SHMS spectrometers in Hall C for instance will allow measurement of the F_1 and F_2 structure functions over a large range of x at a constant value of Q^2 . In combination with the existing inclusive scattering data, typically

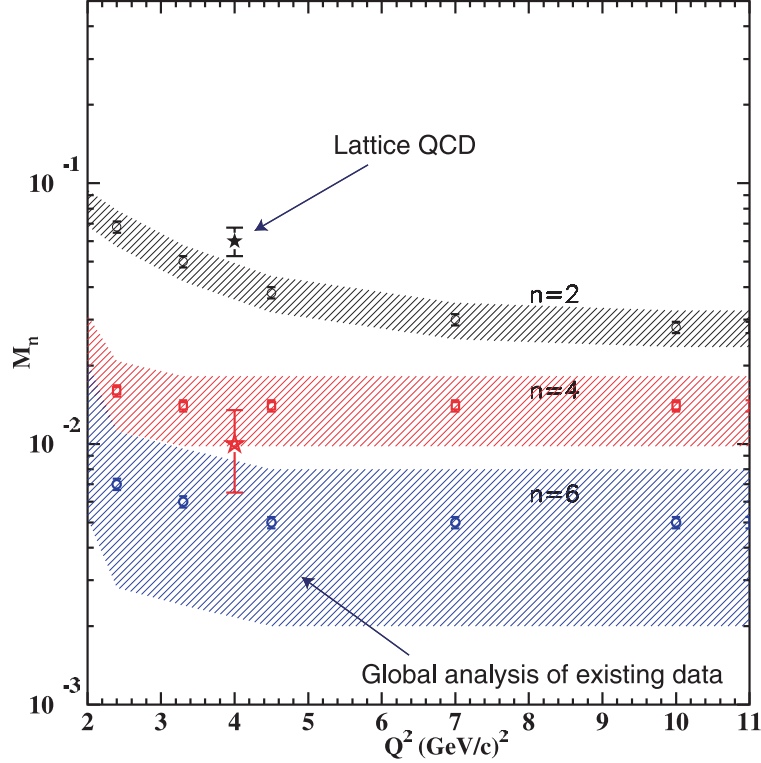


Figure 59: Lowest moments $M_n^2(Q^2)$ of the proton–neutron F_2 structure function difference, for $n = 2$ (black), 4 (red), and 6 (blue), as a function of Q^2 . Experimental moments without including JLab data are indicated as hatched areas. The 12 GeV program will obtain precise moments for $Q^2 \leq 10$ (GeV/c) 2 for all structure functions. Lattice QCD calculations (stars) are shown at $Q^2 = 4$ (GeV/c) 2 for $n = 2$ (black) and 4 (red).

emphasizing lower values of x , the 11 GeV data can be used to obtain moments of all unpolarized structure functions, defined as

$$M_n^i(Q^2) = \int_0^1 dx x^{n-2} F_i(x, Q^2), \quad i = 1, 2, \quad (28)$$

with unprecedented precision, up to $Q^2 \simeq 10$ (GeV/c) 2 . The virtue of these moments is that they can be compared directly with first principles calculations in lattice QCD.

The operator product expansion in QCD allows the moments of structure functions to be expanded in powers of $1/Q^2$, with the coefficients of each of the terms given by matrix elements of local operators of a given twist (where “twist” is defined as the difference between dimension and spin of an operator), which can be calculated numerically on the lattice.

Figure 59 shows the quality of data for the lower moments of $F_2^p - F_2^n$ that will be accessible in Hall C, compared with recent lattice QCD simulations [De02]. Note that because of the x^{n-2} weighting, the higher moments are more sensitive to the large- x behavior of the structure functions, the currently poor knowledge of which will be significantly improved with the 12 GeV Upgrade. In particular, the technique of spectator proton tagging or $^3\text{He}/^3\text{H}$ structure function

measurements discussed above will lead to a dramatic improvement in the accuracy of the neutron structure function, F_2^n . The relatively large error bars on the calculated moments are associated with extrapolation of the lattice moments from the large values of quark mass at which they are currently calculated to the physical values [De01]. The realization of multi-Teraflops computing facilities in the next few years will allow the moments of the structure functions to be computed at the 5% level, providing critical benchmarks for the planned 12 GeV experiments [Ne00].

The spin structure of the nucleon While the behavior of the spin-averaged quark distributions at large x still awaits definitive resolution, our lack of understanding of the spin-dependent distributions at large x is even more striking.

Neutron spin structure functions Although data on R^{np} and A_1^p in Figs. 57 and 56 give some indication of the large- x behavior of the valence quark distributions at $x \lesssim 0.5$, the experimental situation for the neutron A_1^n at large x is totally unclear. The statistical precision of the data available does not even allow a meaningful statement about the qualitative behavior of A_1^n for $x > 0.4$. The experiment proposed here will use the 11 GeV electron beam to perform a precision measurement of A_1^n , utilizing the Hall A polarized ^3He target and the proposed MAD spectrometer. Because the neutron in ^3He carries almost 90% of the nuclear spin, polarized ^3He is an ideal source of polarized neutrons [Fr90].

The experiment involves measurement of the ^3He polarization asymmetry,

$$A_1^{^3\text{He}}(x) \approx \frac{1}{D} \frac{d\sigma^{\uparrow\downarrow} - d\sigma^{\uparrow\uparrow}}{d\sigma^{\uparrow\downarrow} + d\sigma^{\uparrow\uparrow}}, \quad (29)$$

where $d\sigma^{\uparrow\uparrow}$ ($d\sigma^{\uparrow\downarrow}$) is the cross section for scattering polarized electrons from a polarized ^3He target with the beam and target helicities parallel (antiparallel), and D is a kinematic factor relating the virtual photon polarization to that of the electron. The neutron asymmetry A_1^n is extracted from $A_1^{^3\text{He}}$ after correcting for residual nuclear effects in ^3He associated with Fermi motion and binding, using modern three-body wavefunctions [Wo89, Ci93a, Sc93, Bi01], similar to those used in correcting for nuclear effects in $F_2^{^3\text{He}}$. Furthermore, because the asymmetry is a ratio of nuclear structure functions, the nuclear effects on A_1^n will be considerably smaller than those associated with absolute structure functions. In addition to the use of the polarized ^3He target, other polarized targets (ND_3 and NH_3) will be used for cross checks and for the investigation of the nuclear effects.

An example of the kinematics relevant for this experiment is given in Table 8. To illustrate the improvement of the projected results obtainable with JLab at 11 GeV compared with previously measured data from other facilities, we introduce a figure of merit ($\text{FOM} = D^2 \times \text{Rate} \times f$), which allows a meaningful comparison between different laboratories. Here “Rate” takes into account the use of the proposed MAD spectrometer, and f is the dilution factor defined as the ratio of polarized nucleons to the total number of nucleons in the target. Table 8 shows the comparison

Table 8: Comparison of the figure of merit (FOM) for large x measurements of the A_1^n structure function at HERA, SLAC, and JLab.

Expt. name	E_i (GeV)	E' (GeV)	θ (deg.)	x bin	Q^2 (GeV/c) ²	D	f	Rate (Hz)	FOM (10^{-4})
HERMES	35.0	17.0	5.2	0.60-0.70	9.1	0.22	0.3	0.05	7
SLAC E154	48.3	34.1	5.5	0.50-0.70	15	0.29	0.16	?	?
JLab	11.0	4.4	25	0.60-0.70	8.5	0.67	0.3	2.7	370

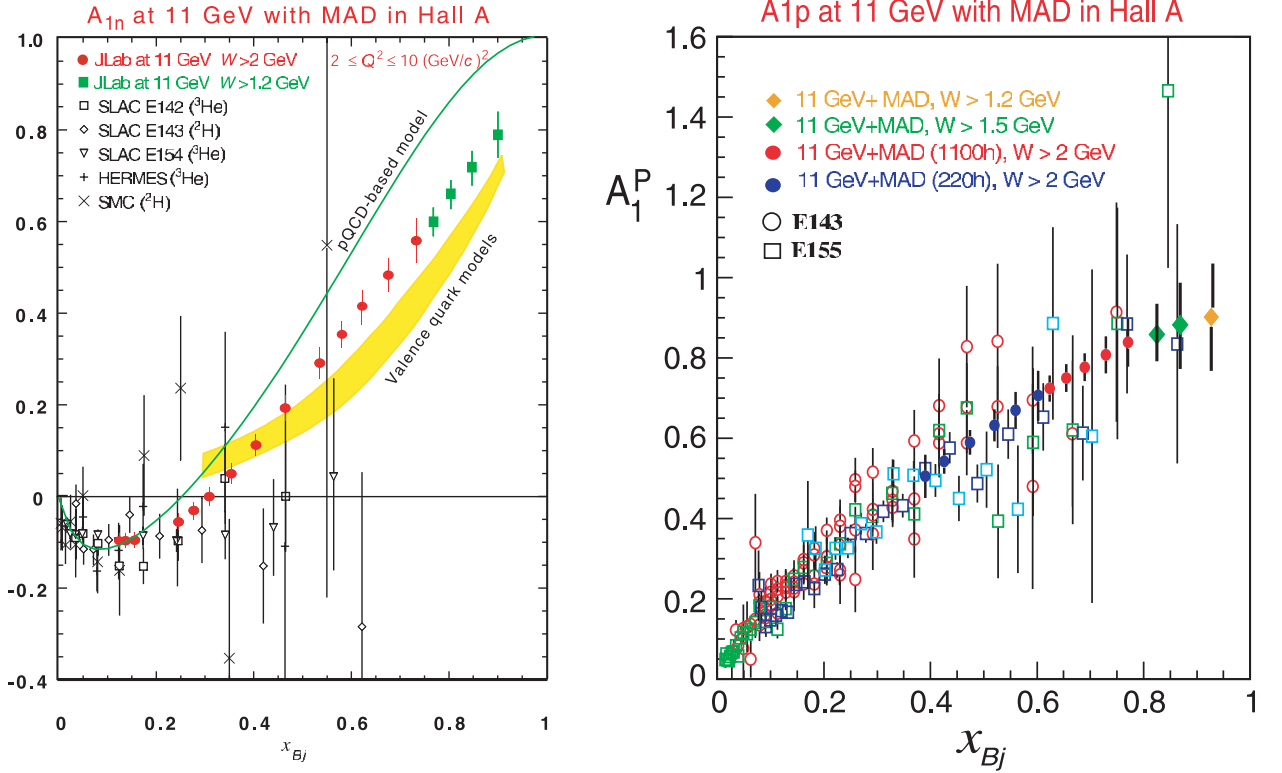


Figure 60: Projected errors for measurements of asymmetries A_1 in the large- x region made possible by the proposed 12 GeV Upgrade. *Left panel:* Neutron A_1^n in Hall A, compared with existing data from SLAC, HERMES and SMC. The red circles correspond to the DIS region ($W > 2$ GeV), while the green squares illustrate the possibility of extending the measurement to higher x in the resonance region ($W > 1.2$ GeV). *Right panel:* Proton A_1^p for Hall A (solid circles), compared with existing data from the SLAC E143 and E155 experiments (open symbols). Statistical errors only are shown. Extensions into the resonance region are denoted by diamonds. Theoretical $x \rightarrow 1$ limits are indicated by red lines on the right side of the graph.

between the relevant parameters at competitive existing laboratories at comparably large x and Q^2 . Note that with increasing beam energy the depolarization factor decreases. The lowest beam energy, therefore, which guarantees access to the large- x region in the Bjorken limit is optimal. The anticipated data are shown in Fig. 60 (left panel). Jefferson Lab at 11 GeV would enable access to $x \lesssim 0.8$ at $W \approx 2$ GeV.

While the cut in W would allow the deep inelastic continuum to be cleanly accessed, one may extend the measurements of A_1^n to even larger x by using quark-hadron duality in the resonance region, $W < 2$ GeV. If duality is observed to hold for the spin-dependent g_1 structure function as well as it does for the unpolarized F_2 structure function [Ni00], averaging over small regions of W will suppress the high twist ($\sim 1/Q$) contributions associated with the low-lying resonances, and enable the dominant scaling component of A_1 to be measured out to $x \simeq 0.95$. This will be discussed in more detail below.

In addition to providing unprecedented access to the spin structure of the neutron at large x , the 12 GeV Upgrade will allow significant improvements in our knowledge of the proton and deuteron spin structure. At low and medium x ($x < 0.4$) the various data sets for A_1^p are consistent with each other and show a definite rise with x . At higher x ($x > 0.4$), however, the errors become significantly larger, and the trend is no longer clear: the current data cannot distinguish between a pure SU(6) symmetric scenario, in which $A_1^p \rightarrow 5/9$, and the SU(6) breaking predictions in which $A_1^p \rightarrow 1$. With an 11 GeV beam, Jefferson Lab will provide a unique facility for closing this gap in our knowledge of A_1^p .

Figure 60 (right panel) illustrates the improvement in the measured proton asymmetry A_1^p at large x with the MAD spectrometer in Hall A. The precision that can be achieved for A_1^p with the CLAS⁺⁺ detector in Hall B is illustrated in Fig. 61 (left panel). These data will clearly distinguish between the SU(6) various models, and dramatically improve our knowledge of the proton's spin structure at high x . The difference between these predictions is even more striking for the deuteron, where one will also be able to significantly improve on existing data, as shown in Fig. 61 (right panel) for CLAS⁺⁺ kinematics. The high precision data on all three targets (³He, proton and deuteron) that will be collected at fixed x , but in several bins in Q^2 , will constrain the logarithmic and $1/Q^2$ scaling violations of the spin structure functions g_1 , and determine their higher moments, as well as allow duality for spin structure functions to be studied in detail. The accurate determination of the Q^2 dependence of g_1 at fixed x may also enable the poorly-known polarized gluon distribution, $\Delta G(x)$, to be constrained at large x .

One should note that in order to unambiguously extract the A_1 asymmetry from data, two beam-target asymmetries must be measured: one with the target polarization oriented longitudinally with respect to the electron beam (A_{\parallel}) and one oriented transversely (A_{\perp}):

$$A_{\parallel} = \frac{d\sigma^{\downarrow\uparrow} - d\sigma^{\uparrow\uparrow}}{d\sigma^{\downarrow\uparrow} + d\sigma^{\uparrow\uparrow}} \quad \text{and} \quad A_{\perp} = \frac{d\sigma^{\downarrow\rightarrow} - d\sigma^{\uparrow\rightarrow}}{d\sigma^{\downarrow\rightarrow} + d\sigma^{\uparrow\rightarrow}}, \quad (30)$$

where $d\sigma^{\downarrow\rightarrow}$ ($\sigma^{\uparrow\rightarrow}$) is the cross section for scattering an electron polarized parallel (anti-parallel)

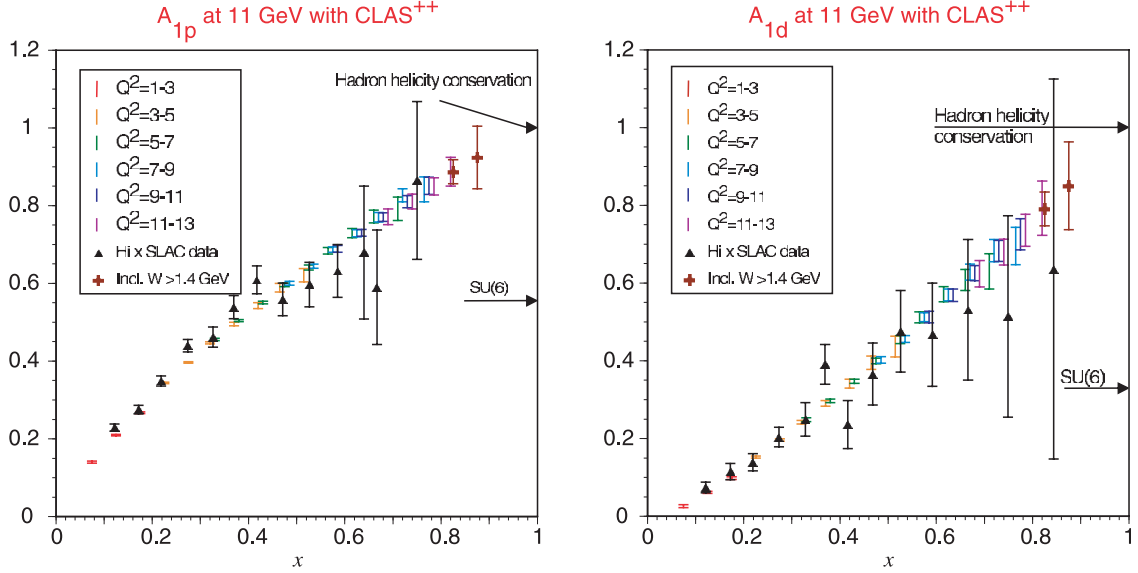


Figure 61: Expected data with CLAS⁺⁺ in Hall B for the polarization asymmetries of the proton (left panel) and deuteron (right panel) with statistical errors from 40 days of running. Several bins in Q^2 (in units of $(\text{GeV}/c)^2$) are indicated by slightly offset error bars. Existing SLAC data (from E130, E143 and E155) are shown for comparison. The predicted approach to the limit $x = 1$ for two different models is indicated.

to the beam direction from a transversely polarized target. These observed asymmetries can then be related to the virtual photon-absorption asymmetries, and structure functions, g_1 and g_2 , the latter which is discussed below. Longitudinally and transversely polarized ^3He targets have been used routinely in Hall A in many experiments, allowing the direct extraction of g_1 and g_2 from the measured spin-dependent cross sections. Transversely polarized targets can be used straightforwardly in Hall A and Hall C, and future installation of a transversely polarized target is also planned for CLAS⁺⁺. An illustration of the quality of the data on the A_{\parallel} asymmetry for a proton target at $Q^2 = 8 (\text{GeV}/c)^2$ is shown in Fig. 62, representing the results of a two-week experiment in Hall C. A measurement of A_{\perp} to minimize the uncertainty in A_{\parallel} due to the A_2 component of A_{\parallel} ($= D(A_1 + \eta A_2)$, where D and η are kinematic factors) requires only a small amount ($\approx 10\%$) of this beam time.

Higher-twist effects Unlike the g_1 structure function, which has a simple interpretation in the quark-parton model in terms of quark helicity distributions, and has been the focus of extensive experimental programs over the last decade, there have been few dedicated experimental studies of the g_2 structure function. The g_2 structure function is related to the transverse polarization of the nucleon, and although it does not have a simple quark-parton model interpretation, it contains important information about quark-gluon correlations within the nucleon.

In QCD the quark-gluon correlations are associated with higher twist operators, which are suppressed by additional factors of $1/Q$ relative to the leading twist contribution (which corresponds

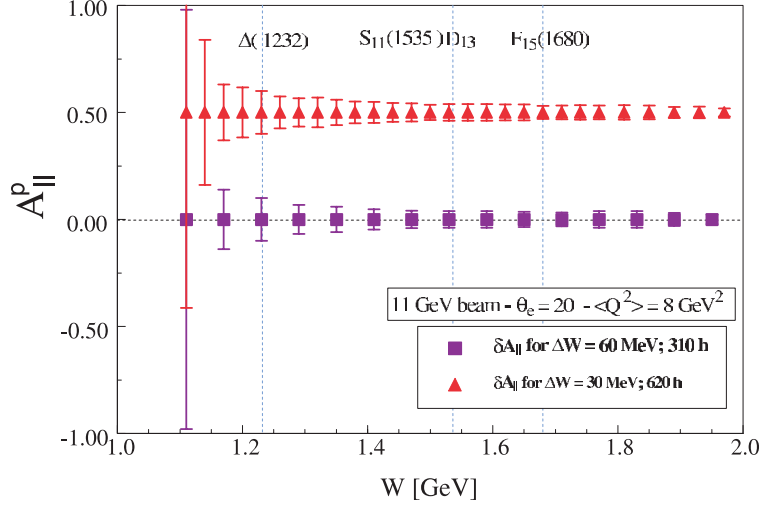


Figure 62: Longitudinal beam-target polarization asymmetry of a proton versus W , for an 11 GeV measurement at $Q^2 = 8 \text{ (GeV/c)}^2$ in Hall C.

to free quark scattering). At large values of Q^2 , QCD allows one to relate moments of spin structure functions to the matrix elements of operators of given twist. The simplest twist-3 matrix element that contains information on quark-gluon correlations is given by:

$$d_2(Q^2) = \int_0^1 dx x^2 \left[2g_1(x, Q^2) + 3g_2(x, Q^2) \right]. \quad (31)$$

Note that because of the x^2 weighting in the integral, d_2 is dominated by the large- x behavior of g_1 and g_2 . The physical significance of d_2 is that it reflects the response of a quark to the polarization of the gluon color field in the nucleon, $d_2 = (2\chi_B + \chi_E)/8$, with χ_B (χ_E) the gluon-field polarizability in response to a color magnetic (electric) field \vec{B} (\vec{E}) [St95].

Published data for g_2 were obtained from experiments E143-E155x at SLAC [Ab96, An03] and the SMC experiment at CERN [Ad93]. Using results from the most recent experiment at SLAC [An03], which measured g_2 for the proton and deuteron, values for g_2 are shown in Fig. 63 for the neutron (left panel) and proton (right panel). Note that the SLAC data vary in Q^2 from 0.8–8.4 GeV^2 over the measured x range. The curve labeled “ g_2^{WW} ” for the neutron represents the leading twist contribution to g_2 [Wa77] at fixed $Q^2 = 3 \text{ GeV}^2$, calculated from a fit to world data on g_1 [An03]. Using these data, a nonzero positive value for d_2^m has been extracted that is in disagreement with all of the theoretical calculations [Ba90, St93a, Ji94, Eh95, St95, So96, We97]. However, in most cases, the disagreement is less than 1σ , and the size of the experimental error does not allow one to make a conclusive statement about the importance of higher-twist effects in the nucleon. On the other hand, considerable progress has been made recently in calculating matrix elements from first principles in lattice QCD. The lattice results from the QCDSF Collaboration [?] are in agreement with the better determined proton d_2^p , but underestimate somewhat the neutron data. For the neutron, the d_2^p lattice results have an error that is significantly smaller than the current experimental error, and will become even smaller with the next generation of lattice

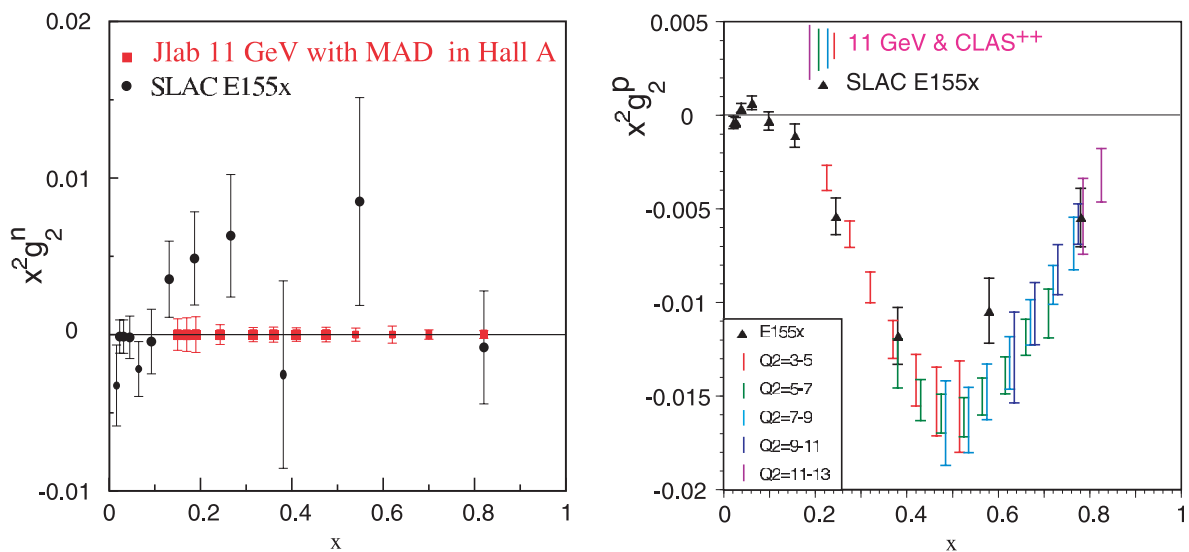


Figure 63: Projected errors for $x^2 g_2(x)$ for the neutron (left panel) and proton (right panel) from 11 GeV JLab measurements, compared with values from the SLAC experiment E155x.

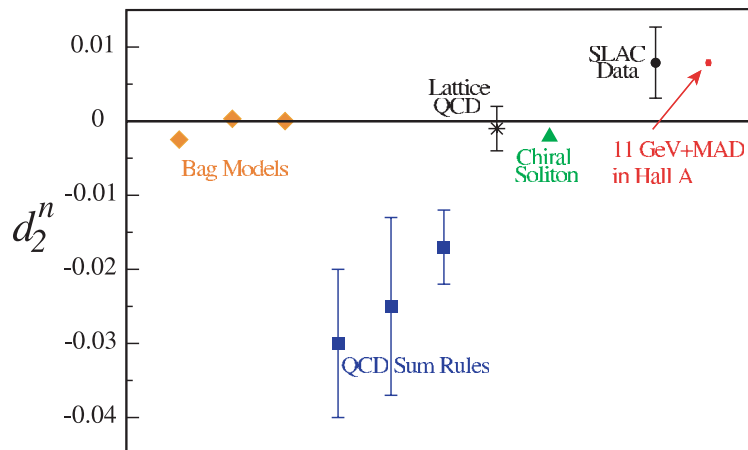


Figure 64: Neutron twist-3 matrix element d_2^n : projected error from a 12 GeV JLab measurement in Hall A compared with existing data from SLAC, and several theoretical calculations.

simulations which will be performed over the next 2–3 years [Ne00].

A 12 GeV JLab experiment will make a factor of 10 statistical improvement in the error on d_2^n , by taking advantage of the high-luminosity 11 GeV polarized beam and the large-acceptance MAD spectrometer. Precision data for g_1^n and g_2^n will be obtained by direct measurements of longitudinal and transverse polarized cross sections in the range $0.15 < x < 0.9$ at fixed $Q^2 = 3 \text{ GeV}^2$, with special focus on the high- x region which dominates d_2 . Projected statistical errors for $x^2 g_2^n$ and d_2^n are shown in Figs. 63 and 64. The expected statistical error on d_2^n for this experiment is 2.5×10^{-4} for 100 hours of beam. Precision data are also planned at fixed x values for several values of Q^2 in the range $2 \leq Q^2 \leq 10 \text{ (GeV/c)}^2$. Installation of a transversely polarized target in Hall B will improve significantly on the existing SLAC data for the proton g_2^p structure function, with smaller error bars and finer binning in x and Q^2 . This will allow the Q^2 dependence of g_2^p to be studied and d_2^p extracted with three times smaller statistical error than the current world data allow. In addition, the proposed 6 GeV experiment in Hall C with the BETA detector [Wa03] could improve the SLAC result by a factor of 2–3 in both statistical precision and resolution in x , which will improve even more at 11 GeV.

Semi-inclusive scattering The production of mesons (M) in semi-inclusive electron scattering, $eN \rightarrow e'MX$, offers a tremendous opportunity for determining the spin and flavor structure of the nucleon, as well as extracting information on new distributions which are not accessible in inclusive scattering. At asymptotic energy the scattering and production mechanisms factorize into a parton distribution function and a quark \rightarrow meson fragmentation function,

$$\frac{d\sigma}{dx dz} \propto \sum_q e_q^2 q(x) D_q^M(z), \quad (32)$$

where $D_q^M(z)$ gives the probability that a quark q hadronizes into a meson M with a fraction z of the virtual photon energy. The extent to which this factorization applies at lower energy is an open question (see the material on semi-inclusive duality below). Nonetheless, confirmation of factorization at lower energies would open the way to an enormously rich semi-inclusive program, allowing unprecedented spin and flavor decomposition of quark distributions.

The probability that the observed meson originated from the struck quark, and not from a $q\bar{q}$ pair produced from the vacuum, can be maximized by restricting measurements to large values of z . In this way high momentum fragments of deep inelastic nucleon breakup statistically tag the underlying quark structure. On the other hand, semi-inclusive cross sections at large values of x and z are small, requiring the highest possible luminosity, while the detection of two particles in the final state requires an electron beam with a high duty cycle. These factors make the 12 GeV Upgraded CEBAF a unique facility for studying semi-inclusive electroproduction reactions.

The large x behavior of spin dependent distributions dictates the $x \rightarrow 1$ limit of the inclusive polarization asymmetries A_1^n and A_1^p . As discussed above, measurements of the asymmetries A_1^n

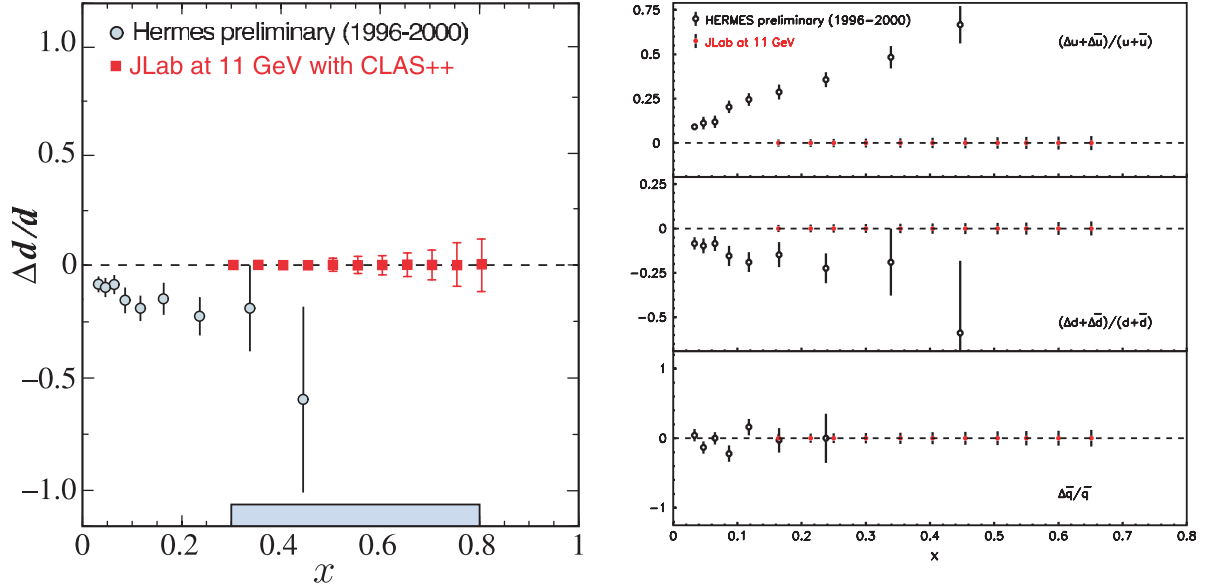


Figure 65: Projected errors for the ratio of polarized to unpolarized quark distribution functions at a 12 GeV CEBAF, compared with HERMES data. *Left panel:* d quark ratio from an 80 day measurement in Hall B. The solid curve uses wavefunctions from a constituent quark model, while the dashed uses pQCD-constrained fits to the world data. *Right panel:* Ratios for various flavors from 1000 hours of beam time on polarized NH_3 and ${}^3\text{He}$ targets in Hall A. Error bars are statistical only.

and A_1^p at $x \leq 0.8$ at 11 GeV will enable one to clearly establish where the deviations from SU(6) symmetry appear. On the other hand, nonperturbative models which incorporate SU(6) breaking typically lead to a suppression of d quarks relative to u [Cl73, Ca75a, Is99]. Consequently, these models also predict that $A_1^{n,p} \rightarrow 1$ as $x \rightarrow 1$, making it difficult to discriminate for instance between the broken SU(6) and HHC behaviors from inclusive measurements alone. This is unfortunate, since the behavior of the polarized d quark distribution is predicted to be qualitatively different: $\Delta d/d \rightarrow 1$ in HHC, but $\Delta d/d \rightarrow -1/3$ in broken SU(6) with hyperfine interactions, so that even the sign is unknown. By tagging π^\pm mesons in the final state at large z , one can disentangle the individual Δu and Δd distributions at large x . There are indications from HERMES data of a positive trend for $\Delta u/u$ with increasing x , while $\Delta d/d$ appears to stay below zero out to $x \sim 0.4$, as shown in Fig. 65. Semi-inclusive data will enable measurements to be extended to $x \sim 0.8$, and definitively test whether Δd stays negative, or turns positive as expected from HHC arguments.

The expected precision of the extracted $\Delta d/d$ ratio for an 80 day measurement in Hall B is indicated in Fig. 65 (left panel). Using the MAD spectrometer in Hall A, the projected statistical errors for the individual polarized to unpolarized quark distribution ratios are shown in Fig. 65 (right panel), compared with the HERMES data [Ac99]. The errors are based on 1000 hour measurements with polarized NH_3 and ${}^3\text{He}$ targets.

The semi-inclusive scattering on unpolarized nucleons could provide an independent check on

the methods for d/u extraction discussed above. Detection of π^+ or π^- mesons produced from a hydrogen target at large z would preferentially tag u and d quarks in the proton, respectively [Me98].

In addition to determining the large- x behavior of the valence u and d flavor distributions, measurement of semi-inclusive cross sections will also allow an accurate reconstruction of the spin and flavor dependence of the $q\bar{q}$ sea. One of the most important and exciting discoveries of the past decade concerning the structure of the nucleon came with the observation that the sea quarks in the proton are not symmetric, but that there is a significant excess of \bar{d} antiquarks over \bar{u} in the proton [Am91, Ba94, Ac98, Ha98]. Naive expectations from gluon radiation into $q\bar{q}$ pairs, which is the dominant process of sea quark creation at high Q^2 , were that this perturbatively generated sea would be equally populated by $u\bar{u}$ and $d\bar{d}$ pairs. The large asymmetry observed between \bar{u} and \bar{d} highlighted the crucial role played by nonperturbative physics in both the valence and sea structure of the proton. Many theoretical explanations of this effect focused on the role of dynamical chiral symmetry breaking and the associated pion cloud of the nucleon [Ku98, Sp98, Th00, Ga01].

On the other hand, the magnitude and x dependence of the $\bar{d} - \bar{u}$ asymmetry is more difficult to understand from QCD, especially at larger x ($x \sim 0.2 - 0.4$), where the asymmetry becomes smaller and the error bars larger. In particular, the downward trend of the \bar{d}/\bar{u} ratio observed in the Fermilab E866 Drell-Yan data [Ha98] in Fig. 66 presents a serious challenge to theoretical models [Pe98], and other mechanisms may be necessary to accurately describes the shape of the asymmetry [Me99]. For example, because there are more valence u quarks than d in the proton, the Pauli Exclusion Principle would suggest that creation of $u\bar{u}$ pairs should be suppressed relative to $d\bar{d}$ [Fi77, Sc91].

A study of the light quark sea flavor asymmetry in the high x region with precision significantly exceeding the Drell-Yan measurement is achievable with a 12 GeV CEBAF. Though the incident electron energy is lower than that available at HERMES, the larger scattering angle allows an exploration of a similar Q^2 range with higher precision. The projected uncertainties in the extraction of \bar{d}/\bar{u} are shown in Figure 66, for a sixty-day measurement period in Hall A, compared with the existing Drell-Yan data.

To fully disentangle the pion cloud and Pauli blocking effects on the antiquark distributions one needs to consider the spin dependence of the $\bar{d} - \bar{u}$ asymmetry. Since pions have spin zero, scattering from a virtual pion cloud of the nucleon will not contribute to the helicity distributions $\Delta\bar{u}$ or $\Delta\bar{d}$. Effects of quark antisymmetrization, on the other hand, are expected to be as large or larger in the spin-dependent asymmetry $\Delta\bar{u} - \Delta\bar{d}$ as in the unpolarized $\bar{d} - \bar{u}$ asymmetry [Di97, Gl00, St02]. Preliminary data from HERMES [We02] shows that the distributions $\Delta\bar{d}$ and $\Delta\bar{u}$ are rather small, and consistent with zero within overall errors, suggesting that the dominant mechanism underlying the generation of the proton sea may be that associated with dynamical chiral symmetry breaking [Do77, Ro79, St97]. However, the errors on the difference $\Delta\bar{u} - \Delta\bar{d}$, which is most sensitive to nonperturbative effects such as meson clouds, are rather large, and better quality data in the range

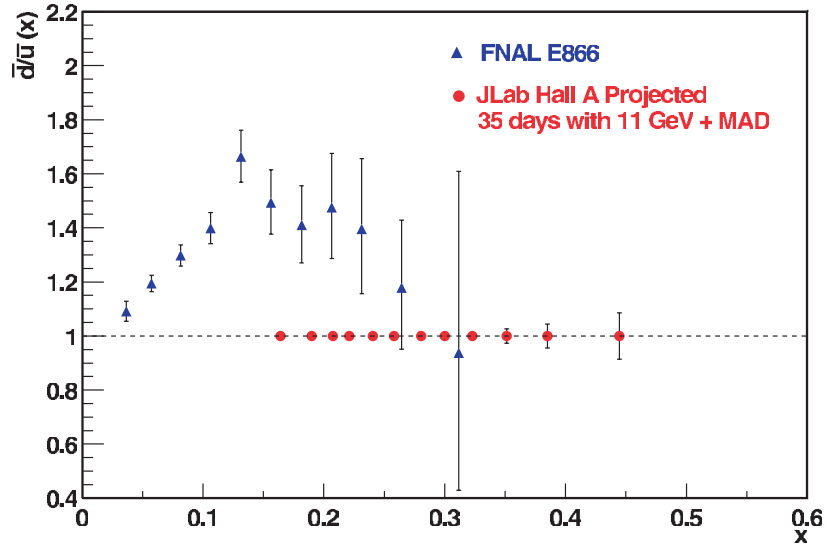


Figure 66: The projected precision of \bar{d}/\bar{u} extractions assuming factorization with strict Q^2 and z cuts, and an 11 GeV JLab beam energy in Hall A, compared with the FNAL E866 Drell-Yan [Ha98] measurements. Statistical uncertainties are shown only.

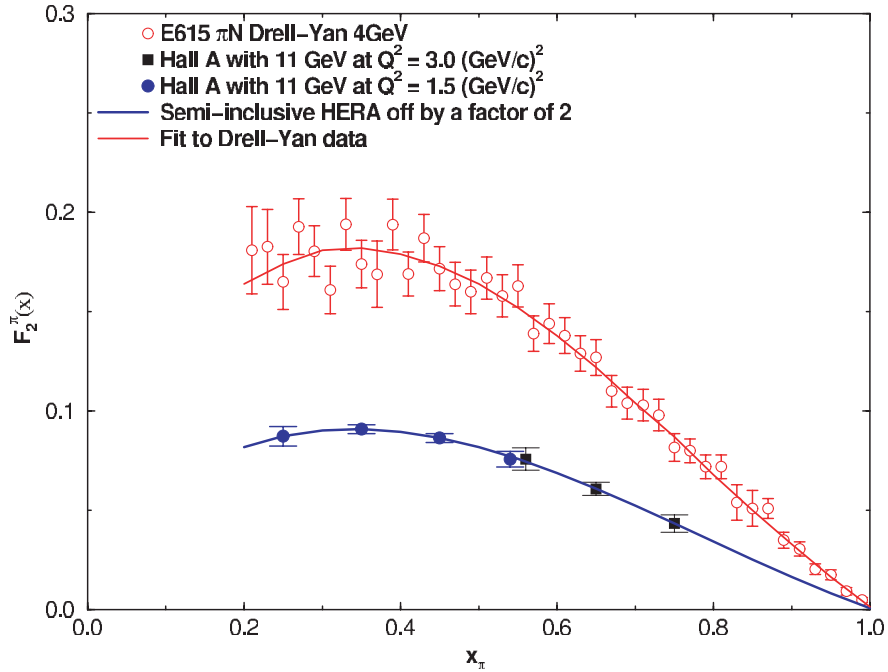


Figure 67: Simulated data for the pion structure function at $Q^2 = 1.5$ (filled circles) and 3.0 $(\text{GeV}/c)^2$ (squares) using the MAD spectrometer in coincidence with a low energy neutron detector at 11 GeV beam in Hall A, for a 25-day run period. Existing data from the Fermilab E615 experiment [Co89] are shown for comparison (open circles).

$0.1 < x < 0.4$ would be crucial for drawing firm conclusions. The quality of the data on the antiquark polarization attainable with a 11 GeV beam in Hall A is illustrated in Fig. 65 (right panel). Clearly, measurement of semi-inclusive production of π^\pm with unpolarized and polarized electron beam and target at 11 GeV JLab kinematics will significantly improve our knowledge of the x dependence of both the flavor asymmetry \bar{d}/\bar{u} and the polarization asymmetries $\Delta\bar{u}$ and $\Delta\bar{d}$.

Finally, a more direct test of the role of the pion cloud in spin-flavor asymmetries can be made by measuring the structure function of the pion in the semi-inclusive charge exchange reaction, $ep \rightarrow en\pi^+$, a technique that was recently used at HERA at small x [Le02]. These measurements revealed that the $q\bar{q}$ sea in the pion was about 1/2 that which was expected based on current theoretical models. With the 12 GeV upgrade at Jefferson Lab measurements could be made in the valence region, and compared with existing pion Drell-Yan data, which would verify the technique used by the HERA experiments to measure the pion structure function. The key to the experimental technique is to measure the low-energy outgoing neutron in coincidence with the scattered electron. A simulation of a possible experiment in Hall A with the 11 GeV beam and the MAD spectrometer with an unpolarized beam is shown in Fig. 67.

2.B.3 The Generalized Parton Distributions as Accessed via Deeply Exclusive Scattering

The Physics of the Generalized Parton Distributions In the past five decades of electron-nucleon scattering, experiments dedicated to studying the substructure of the nucleon have mainly focused either on the measurements of electromagnetic form factors in exclusive processes or on measurements of deep inelastic structure functions in inclusive processes. Inelastic exclusive reactions, such as pion or eta electroproduction, played a role mostly in the study of nucleon resonances [Bu03]. This situation, however, is now changing. The 12 GeV upgrade at Jefferson Lab allows a first dedicated study of a whole new class of hard exclusive processes which are capable of probing the quark-gluon dynamics of the nucleon in unprecedented details.

Elastic processes measure the electromagnetic form factors as a function of the invariant momentum transfer $t = -Q^2$. The physical interpretation of the form factors is the simplest when the nucleon travels at the speed of light or in the infinite momentum frame (IMF): the Fourier transformation of the charge form factor with respect to t yields a two-dimensional distribution of electric charges in the transverse plane. Inclusive processes probe deep inelastic structure functions which again have a simple interpretation in the IMF: they are quark density distributions as a function of longitudinal momentum fraction x . Taking together, form factors and deep inelastic structure functions measure the proton structure in two orthogonal sub-spaces. While it is clear that the two pictures must be part of the big one, the actual framework unifying the two has only been discovered recently with the Generalized Parton Distribution (GPD) functions [Mu94, Ji97, Ra97]. The GPDs encode both the transverse spatial dependence and the longitudinal momentum dependence. A few review articles on the subject can be found in Ref. [Ji98, Go01b, Ra01].

A generalized parton distribution depends on three kinematic variables: the invariant momentum transfer to the proton $t = (p - p')^2$ just like the form factors do, the momentum transfer projected along the light cone: $\xi = (p - p')^+ / P^+ \rightarrow x_{Bj} / (2 - x_{Bj})$ where $P = (p + p') / 2$, and finally the quark momentum fraction x as in the Feynman parton distributions. At the twist-2 level, for each quark species there are eight GPDs. The experiments at JLab can make a detailed study of at least four of them:

- $H(x, \xi, t)$, $\tilde{H}(x, \xi, t)$ the helicity conserving and helicity flip, respectively, matrix elements of the vector current; and
- $E(x, \xi, t)$, $\tilde{E}(x, \xi, t)$, the helicity conserving and helicity flip, respectively, matrix elements of the axial-vector current.

The other four are related to the transverse polarization of quarks and are still under theoretical investigation. The first moments of the GPDs in x are related to the proton's form factors [Ji97],

$$\begin{aligned} \int dx H(x, \xi, t) &= F_1(t), & \int dx E(x, \xi, t) &= F_2(t), \\ \int dx \tilde{H}(x, \xi, t) &= G_A(t), & \int dx \tilde{E}(x, \xi, t) &= G_P(t) \end{aligned} \quad (33)$$

where $F_1(t)$, $F_2(t)$, $G_A(t)$ and $G_P(t)$ are Dirac and Pauli form factors of the vector current, and pseudo-vector and pseudo-scalar form factors of the axial current, respectively. At $t = \xi = 0$, the GPDs H and \tilde{H} reduce to the quark momentum $q(x)$ and helicity distributions $\Delta q(x)$,

$$\begin{aligned} H(x, 0, 0) &= q(x)\theta(x) - \bar{q}(-x)\theta(-x) \\ \tilde{H}(x, 0, 0) &= \Delta q(x)\theta(x) + \Delta \bar{q}(-x)\theta(-x) \end{aligned} \quad (34)$$

The forward limit of $E(x, \xi, t)$ is related to the angular momentum distributions of partons (see below).

As an example of the GPDs, a model of $H(x, \xi, t)$ distribution with factorized t -dependence [Go01b] is shown in Fig. 68. At $\xi = 0$, we have the usual parton distribution, and thus at very small x , the distribution becomes singular. The distribution is negative at negative x because the antiquark distribution is positive. For non-zero ξ , the distribution in $|x| > \xi$ is markedly different from that in $|x| < \xi$. The former is a smooth continuation of the ordinary parton distributions, whereas the latter describes the amplitude for the proton to emit or absorb a meson, mimicking the meson light-cone distribution amplitude.

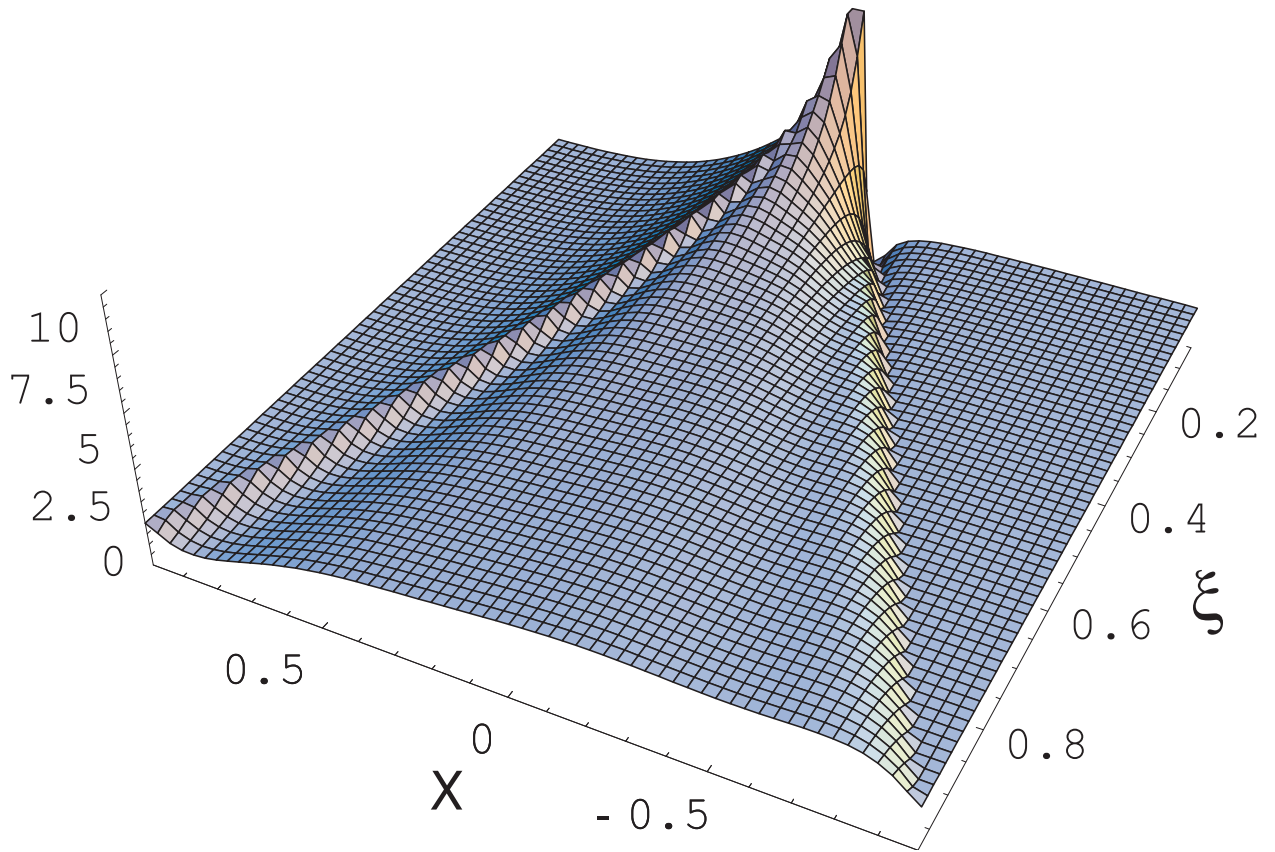


Figure 68: Two dimensional image of $H(x, \xi, t)$ from a model with factorized t -dependence. The dramatic change in the shape of the surface reflects the change in the underlying physics. As ξ increases, the correlations between the quarks and anti-quarks increase leading to meson-like distributions at large ξ .

The joint probability distribution, represented by the GPDs, contains much more of the physics of partons than forward parton distributions and form factors. Mapping out the GPDs will allow, for the first time, to construct “tomographic” images of the nucleon’s charge and quark helicity distributions in transverse impact parameter space [Be02, Bu00, Ra02], in some analogy to the way tomographic images of macroscopic objects are assembled. Some highlights of the *new physics* involved in GPDs are as follows:

Spin Structure of the Nucleon In the simple quark model of Gell-Mann and Zweig, the spin of the nucleon comes just from the spin of the three valence quarks which carry no orbital angular momentum. This picture has been challenged recently by the data from polarized deep-inelastic scattering. Through a global analysis of the EMC, SMC, E142, E143, E154, E155, and HERMES data, it has been found that the fraction of the nucleon spin carried by the quark is about 25%, falling far short of the quark model prediction [Fi01]. The remaining part of the nucleon spin must be carried by the quark orbital motion and the gluon angular momentum.

Indeed, a quark having a momentum fraction x also carries some angular momentum. The angular momentum distribution $J_q(x)$ can be obtained from the GPDs [Ho99]:

$$J_q(x) = \frac{1}{2}x[H_q(x, 0, 0) + E_q(x, 0, 0)] , \quad (35)$$

which involves the forward limit of E . After integrating over the momentum fraction, we have the fraction of the nucleon spin carried by quarks [Ji97]

$$J_q = \frac{1}{2} \int_{-1}^1 x dx [H_q(x, \xi, 0) + E_q(x, \xi, 0)] . \quad (36)$$

Given the result of the polarized DIS, an experimental determination of J^q allows extraction of the quark orbital angular momentum. Here an extrapolation of the GPDs from finite t to the $t = 0$ point is needed.

Gravitational Form Factors If gravitons were available in the laboratory just like photons, they could be used to measure the mass and momentum distributions in the nucleon. [The notion of these distributions is usually considered only for macroscopic systems.] With GPDs, one can obtain the gravitational form factors without graviton scattering! Indeed, the second x -moment of the GPDs [Ji97a],

$$\begin{aligned} \int dx x H(x, \xi, t) &= A(t) + \xi^2 C(t) , \\ \int dx x E(x, \xi, t) &= B(t) - \xi^2 C(t) , \end{aligned} \quad (37)$$

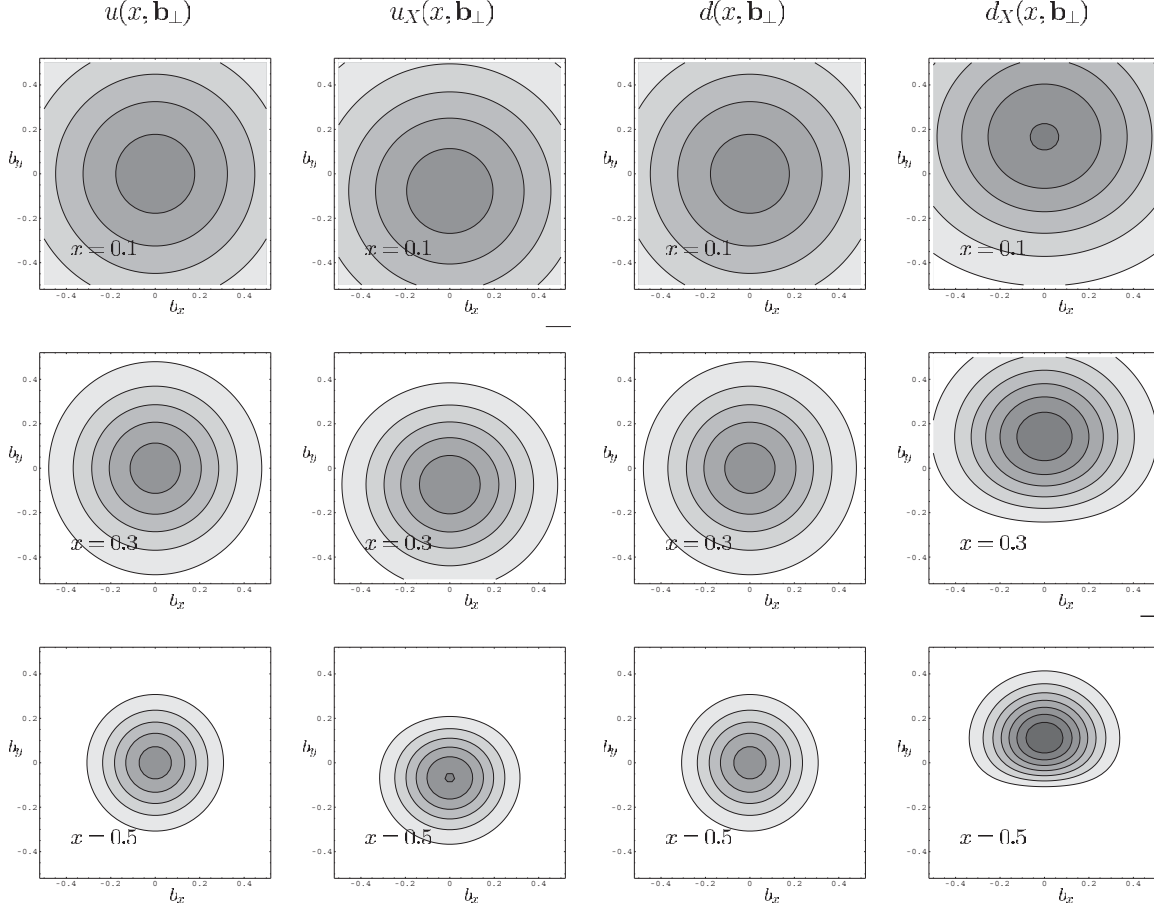


Figure 69: Model “tomographic” images of quarks in the transverse plane in an unpolarized and polarized nucleon in the IMF. The left panels show the u quark distribution at fixed x in unpolarized and polarized proton, and the panels on the right show the corresponding images for the d quarks. The right columns in each panel show the quark distributions in a transversely polarized proton. u and d quarks exhibit a strong and opposite spatial asymmetry generating a strong spin-flavor polarization, especially prominent at high x .

where $A(t)$, $B(t)$ and $C(t)$ are gravitational form factors. In the infinite momentum frame, the Fourier transformation of $A(t)$ gives the mass distribution in the transverse plane and that of $t(A(t) + B(t))$ the momentum distribution. It would be very interesting to compare these distributions with electromagnetic charge and current distributions.

“Tomographic” Images of the Nucleon Knowledge of the x and t dependence of GPDs for specific quark flavors provides the basis for the construction of a 3-dimensional representation of the proton’s quark content in the transverse plane and in longitudinal momentum space [Bu00, Be02, Ra02]. This may be seen in some analogy to the way images of macroscopic objects can be assembled in tomography.

In GPDs, we expect that t and x dependences are correlated. The physical significance of these correlations at finite ξ is discussed in [Di02]. At $\xi = 0$, a particularly simple interpretation is possible [Bu00]. A simple model of H , incorporating the general properties of the correlations between t and x is as follows [Bu00].

$$H_f(x, 0, t) \sim q_f(x) e^{-a|t|(1-x)\ln\frac{1}{x}}$$

where $q_f(x)$ is the forward parton distribution of flavor f and a is a scale parameter characterizing the transverse size. Figure 69 illustrates these correlations in this model. The graphs show a strong correlation between the t -dependence (its Fourier conjugate is the transverse size, or impact parameter b_\perp) and the x -dependence (longitudinal momentum). According to the uncertainty principle, t is related to b_\perp approximately through $b_\perp \sim 1/\sqrt{-t}$. For a spin-averaged nucleon, the panels show the dramatic change in transverse profile as a function of x , while the image remains isotropic.

For small x , the proton has a large transverse size, and it becomes very dense at large x . A strong spatial anisotropy is observed for the quark density in a polarized proton. The tomographic image shows the very strong spin-flavor polarization between the u quarks and d quarks for a proton polarized in the transverse plane, with the u and the d quark spin distribution spatially separated from each other, especially in the valence quark domain at high x . This regime can be accessed in deeply exclusive processes at JLab beginning at 6 GeV, and will be more fully accessible after the 12 GeV upgrade. Thus, *the knowledge of GPDs will provide the most fundamental insights into the internal quark-gluon dynamics of the nucleon, unimaginable just five years ago.*

Modeling GPDs Theoretical studies of the GPDs fall in two categories. In the first category, the nucleon models are used to calculate the GPDs. For example, the MIT bag model was used first to calculate GPDs [Ji97a]. Later the chiral soliton model was also used to compute the new distributions [Go01b, Pe00a]. In these calculations, the constraints on the GPDs are automatically satisfied. In the second category, GPDs are parameterized and the parameters are fitted by the constraints of the GPDs from the elastic form factors and parton distributions [Go01b]. Moreover, the moments of the GPD as a function of ξ must satisfy the polynomial condition [Ji98, Ji97a]. This later condition can be satisfied if one models the double distributions directly [Ra01, Ra99]. Additional constraint on the GPDs come from bounds derived from various inequalities [Po02].

Probing GPDs Through 12 GeV Upgrade One of the striking findings associated with GPDs is that they can be measured through a new class of "hard" exclusive processes: Deeply Virtual Compton Scattering (DVCS) and Deeply Virtual Meson Production (DVMP), both are part of deep inelastic scattering with special exclusive final states [Ji97, Ra97, Co97]. The basis for getting access to GPDs is the "handbag" mechanism for deeply virtual exclusive process shown in Fig.70. The electron knocks a quark out of the proton by exchanging a deeply virtual (massive) photon. The quark then emits a high energy photon and is put back into the proton (DVCS). Alternatively,

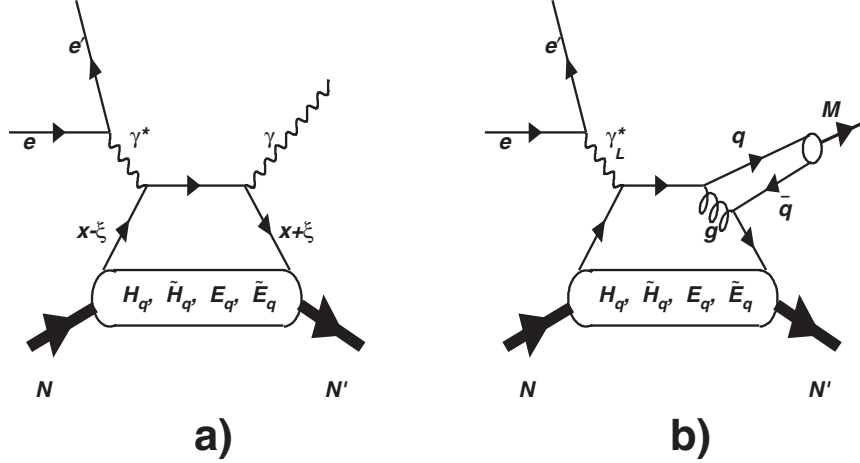


Figure 70: Representative handbag diagrams for deeply virtual Compton scattering a), and for deeply virtual meson production b).

a $q\bar{q}$ pair is created, and a quark is returned into the proton while the \bar{q} recombines with the struck quark to form a meson. At sufficiently high energy and virtuality of the exchanged photon (Bjorken regime) these hard processes can be described by perturbative QCD, and the cross section can be used to extract the “soft” information of the nucleon which is just the GPDs.

In the handbag approximation the cross sections for DVCS and for meson production at fixed t follow a $1/Q^4$ and $1/Q^6$ dependence, respectively. Predicted cross sections are shown in Fig. 71 for deeply virtual productions of photons, pseudoscalar mesons, and vector mesons at $t = t_{min}$ [Go01b].

In the scaling regime, the production of photons will dominate over the production of π^0 's and η 's already at relatively low Q^2 , and become the dominant exclusive channel at very high Q^2 . Due to the absence of any gluon propagator, DVCS is likely to enter the Bjorken regime at relatively low photon virtuality, Q^2 . This expectation has to be quantified experimentally. Until recently, the main evidence in support of this expectation came from the CLEO data on the $\gamma\gamma^*\pi^0$ transition form factor measurement [Gr98]. The pQCD predictions for $F_{\gamma\gamma^*\pi^0} \sim 1/Q^2$ seem valid for $Q^2 > 2 \text{ GeV}^2$. With additional quark transverse momentum corrections, this limit may even be as low as 1 GeV^2 (see Fig. 73).

The $\gamma\gamma^*\pi^0$ vertex (for a virtual pion) can also be measured on a fixed-target machine, in which case it is just part of the DVCS amplitude corresponding to the $\tilde{E}(x, \xi, t)$ GPD. Hence, CLEO data indicate that DVCS may be handbag dominated for Q^2 as low as $1 - 2 \text{ GeV}^2$.

At the energies currently available at JLab, the DVCS process is masked by the more copious production of photons from the Bethe-Heitler (BH) process. However, using polarized electron beams allows to isolate the DVCS/BH interference term, which gives direct access to the imaginary part of the DVCS amplitude T^{DVCS} . The BH term depends only on the well known electromagnetic form factors, and is used here to “boost” the much smaller DVCS term which depends on the

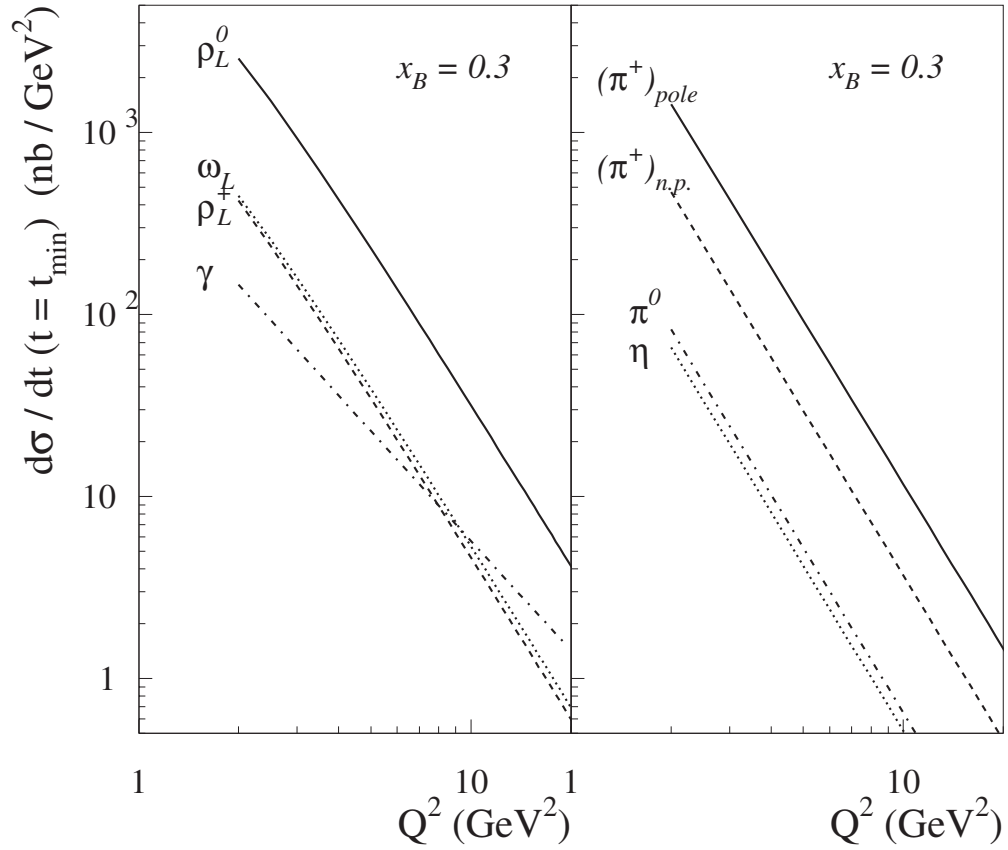


Figure 71: Scaling cross sections for the production of photons (DVCS), pseudoscalar mesons, and vector mesons. For meson production, the longitudinal cross sections are shown. For charged pion production there are two contributions, one related to the pion form factor (pole), the second one is due to knock out of quarks from the nucleon's quark core.

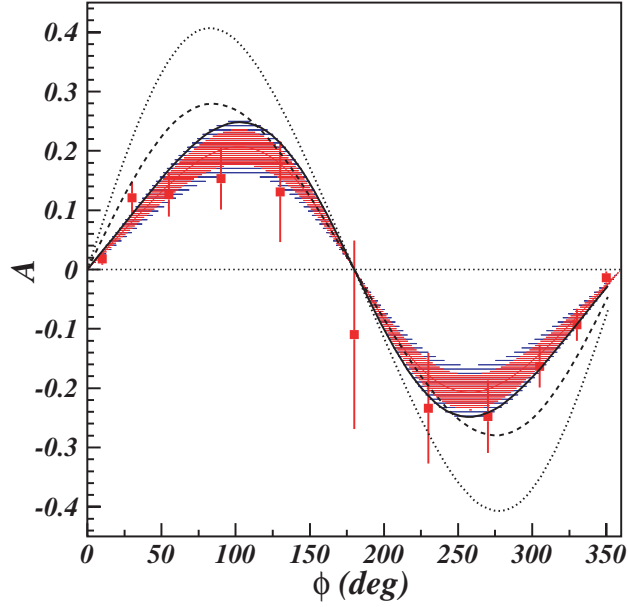


Figure 72: Beam spin asymmetry measured with CLAS. The shaded band shows the systematic uncertainties. The dashed and dotted curves are early predictions, while the solid curve is a more recent calculation.

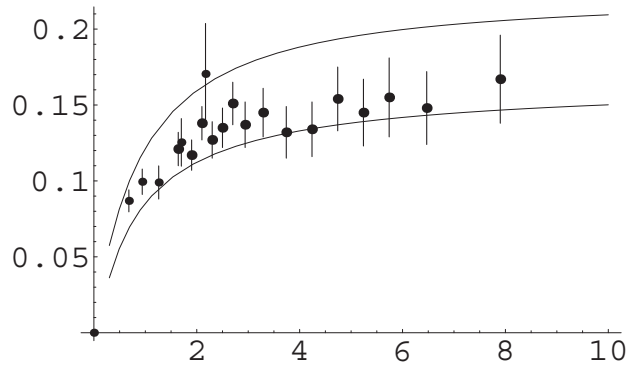


Figure 73: Comparison of data on the Q^2 dependence of the $\gamma\gamma^*\pi^0$ form factor with quark transverse momentum power-corrected pQCD predictions using asymptotic shape for the pion distribution amplitudes (lower-curve) and the Chernyak-Zhitnitsky model (upper curve). The quantity $Q^2 \cdot F_{\pi^0\gamma\gamma^*}$ is plotted versus Q^2 (GeV^2).

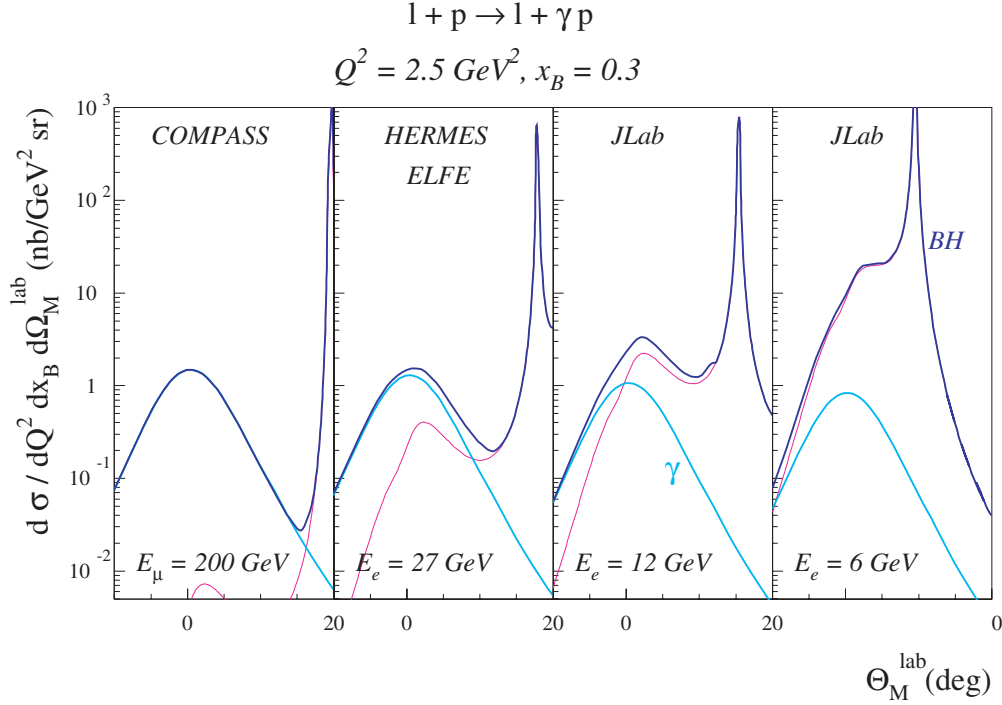


Figure 74: DVCS (cyan) and Bethe-Heitler (magenta) cross section for different beam energies.

unknown GPDs. The asymmetry, which is due to the DVCS/BH interference term, has recently been measured at CLAS [St01] and at HERMES [Ai01]. Figure 72 shows the CLAS result. The asymmetry data have been predicted within the GPD framework using cross section data from HERA [Ad01, Sa03] measured at very small x_B values as input [Fr03]. Excellent agreement with the CLAS data is obtained in LO, lending strong support to the assumption of dominance of the handbag diagram.

Despite these recent successes, a direct demonstration of “scaling” of the DVCS amplitude is currently lacking, and is one of the objectives of two experiments currently in preparation at JLab. A set of new detectors for a complete measurement of all final state particles (e, γ, p) are currently under construction for CLAS and Hall A, which will also be used for DVCS experiments after the Upgrade. These experiments will directly measure the Q^2 dependence of the $\Im(T_{DVCS})$ as well as the ξ and t dependences.

DVCS at JLab with 12 GeV Electrons At the energies achieved with the Upgrade the DVCS and BH cross section become comparable in size in a broader kinematics domain, as shown in Fig.74. This will allow measurement not only of beam asymmetries but access to the DVCS cross section will also be possible. Beam asymmetries give access to the imaginary part of the DVCS amplitude, and are especially sensitive to the GPD $H(\xi, \xi, t)$. The DVCS cross section determines the x -integral, and is sensitive to the real part of a combination of GPDs, therefore

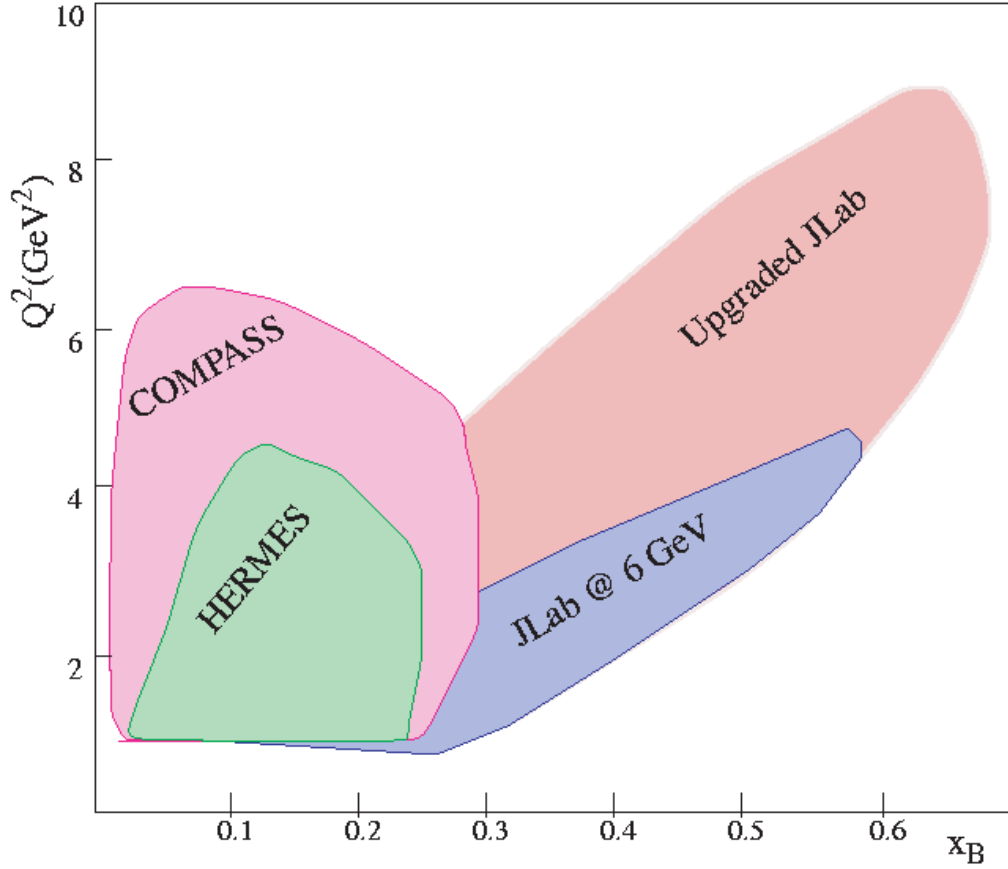


Figure 75: Kinematics coverage for deeply virtual exclusive processes for experiments at various laboratories. Not shown are the HERA experiments which cover a domain at very small x_B values.

providing independent information.

The energy Upgrade, in conjunction with the unprecedented luminosity that will be available, will allow a much broader kinematic coverage to be accessed in deeply virtual exclusive processes. Figure 75 shows the expected coverage in Q^2 and x_B . Although the energy is lower for JLab experiments than for HERMES or COMPASS, the luminosity that can be utilized is several orders of magnitudes greater than for the higher energy experiments. This makes exclusive experiments at JLab competitive to the higher energy experiments in kinematics for which there is kinematic overlap, i.e. at $x_B = 0.1 - 0.3$, and unique in the range $x_B > 0.3$. For processes requiring $Q^2 > 4-5 \text{ GeV}^2$ to reach the Bjorken regime, e.g. vector mesons or pseudoscalar meson production, they can only be accessed efficiently with the high luminosities achievable with the 12 GeV Upgrade.

DVCS using polarized electrons Use of polarized beams at 11 GeV will be the most effective way of extracting information on the GPD H which is kinematically favored in the cross section

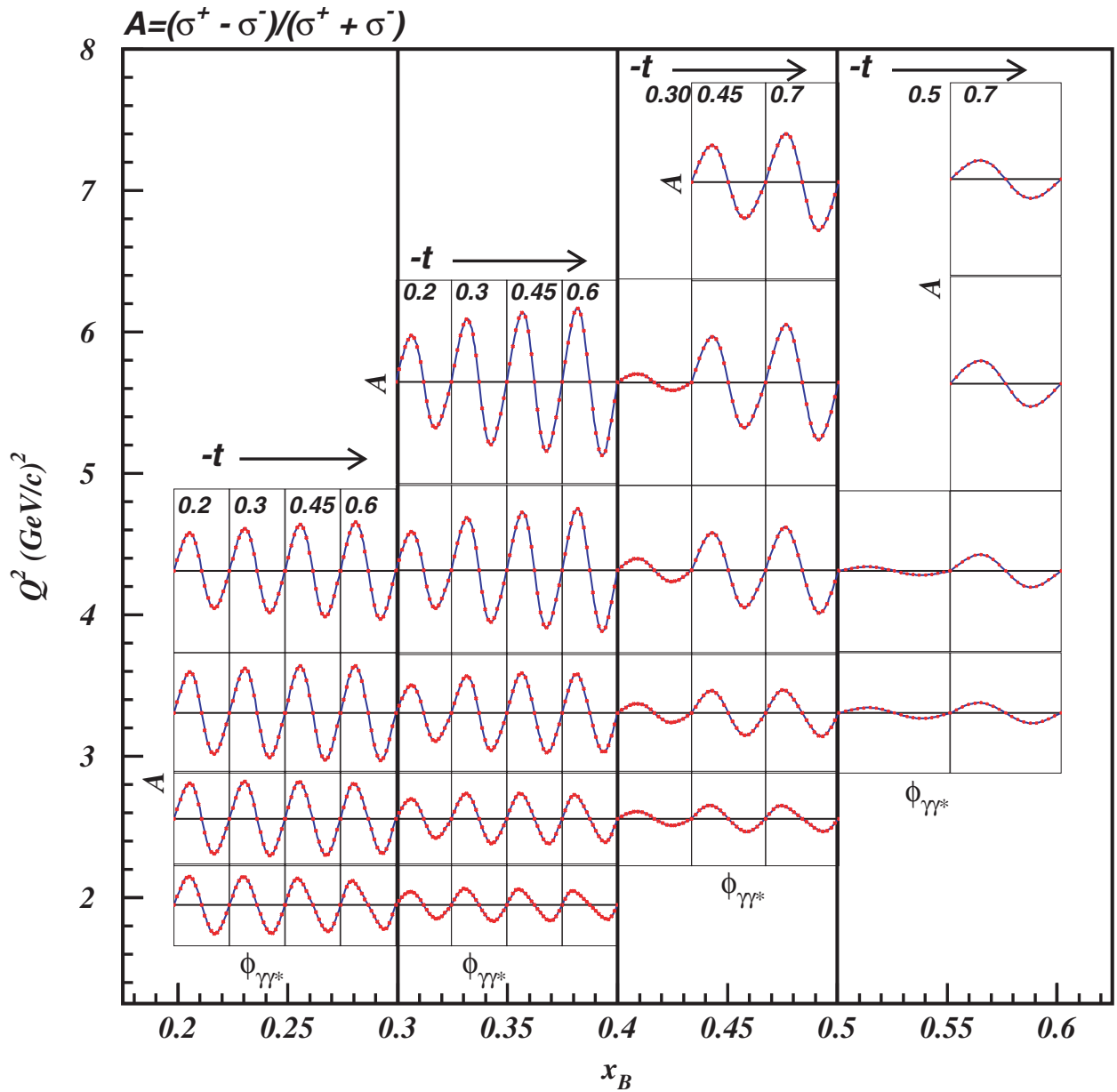


Figure 76: Kinematics for DVCS beam asymmetry measurements at 11 GeV. Only the bins for lower t values are shown. With CLAS $^{++}$ all bins will be measured simultaneously.

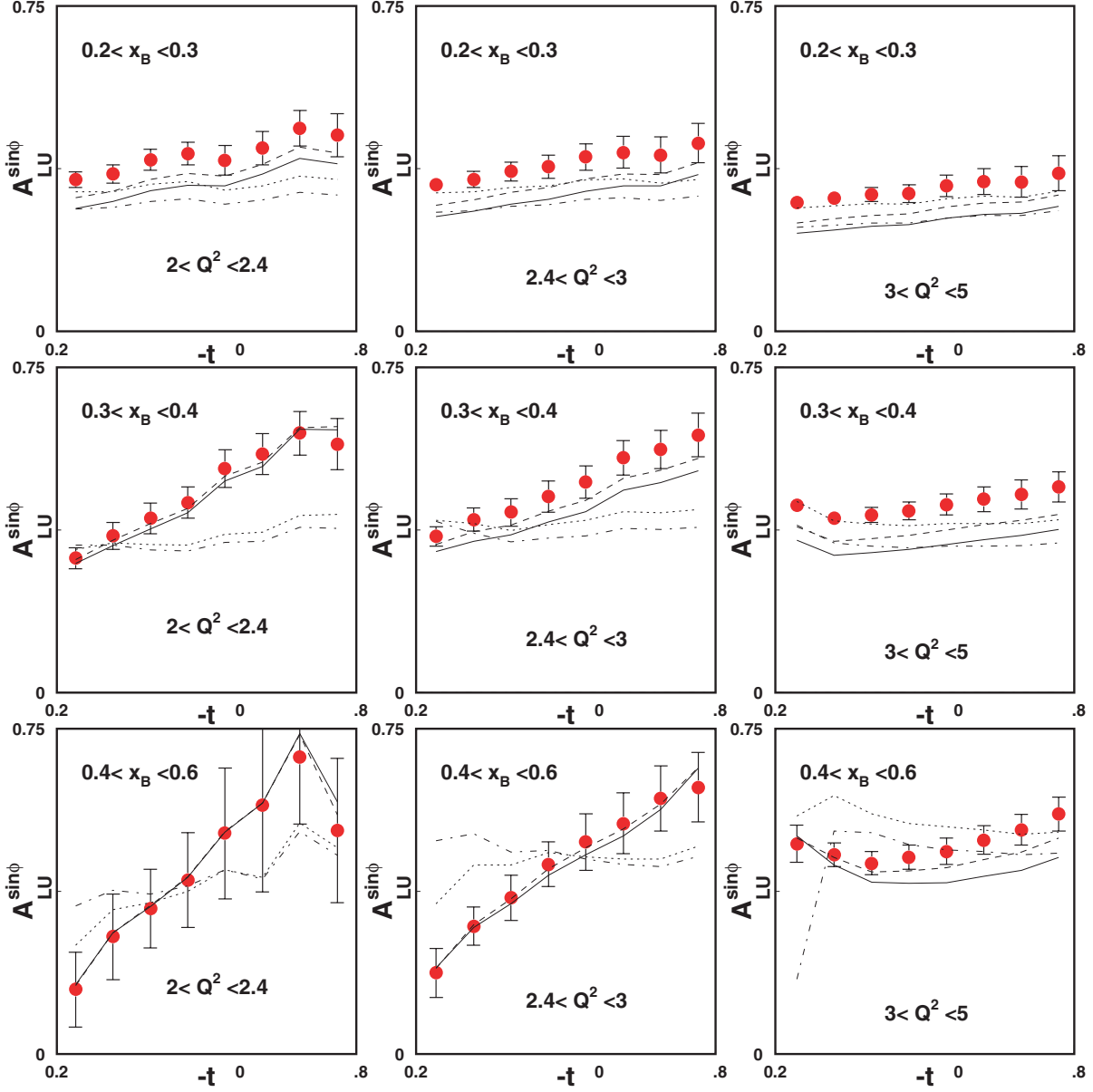


Figure 77: Projected data for the $\sin \phi$ moment $A_{LU}^{\sin \phi}$ of the DVCS/BH asymmetry. The curves and data points represent predictions of the GPD model with five different input parameter sets.

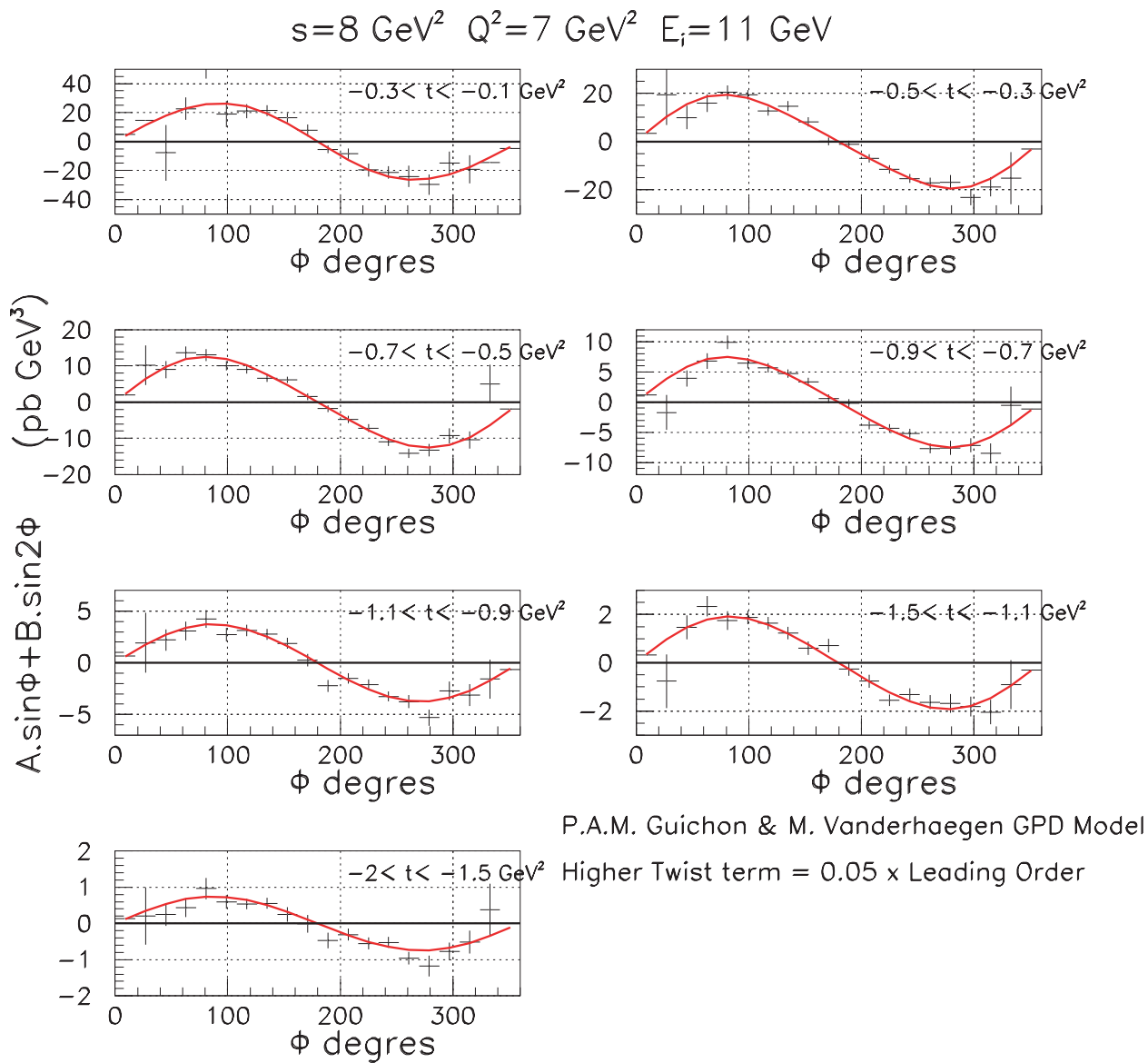


Figure 78: Projected Hall A data for the beam-helicity dependent cross section weighted by Bethe-Heitler denominator: $-(k \cdot q')(k' \cdot q')\Delta\sigma$ at $Q^2 = 7 \text{ GeV}^2$.

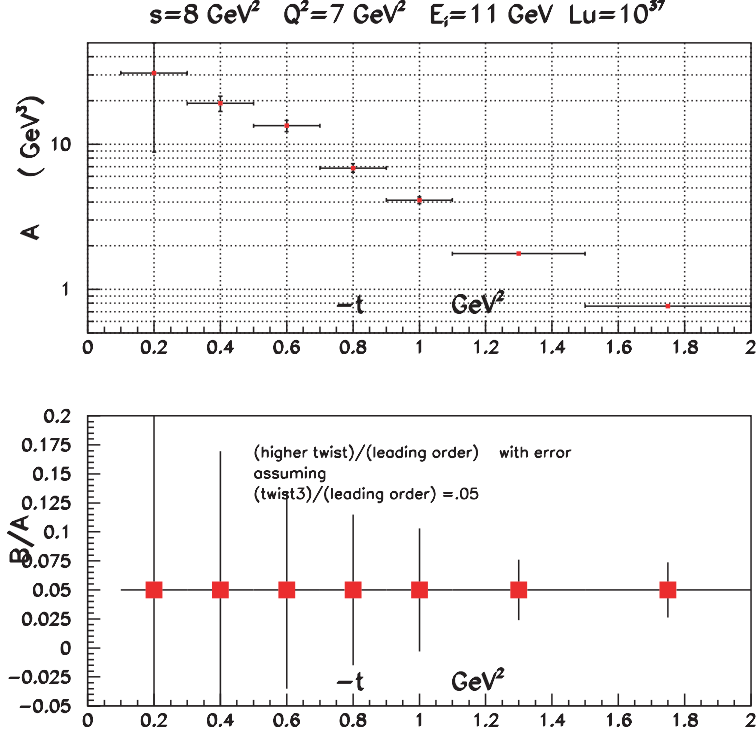


Figure 79: Projected results for the separation of $\sin \phi$ and $\sin(2\phi)$ terms in Fig. 78.

difference. For $Q^2 \gg -t$, $4x_B^2 M^2$, the beam helicity dependent cross section difference is [Be02a]:

$$\frac{\Delta^5 \sigma}{dx_B dQ^2 dt d\phi_e d\phi_{\gamma\gamma}} \rightarrow \frac{\sin \phi_{\gamma\gamma} \alpha^3}{-s'u'} \frac{2-y}{\pi^2} \frac{\sqrt{1-x_B} \sqrt{t_{\min}-t}}{\sqrt{Q^2}} \left[F_1(-t)H + \frac{x_B}{2-x_B} G_M(-t)\tilde{H} + \frac{t}{4M^2} F_2(-t)E \right], \quad (38)$$

where $y = p \cdot q / p' \cdot k$ is the electron inelasticity and $-s'u' = -4(q' \cdot k)(q' \cdot k')$ is the product of the $\phi_{\gamma\gamma}$ -dependent BH propagators. The GPD's in Eq. 6 are $H(\xi, \xi, t) - H(-\xi, \xi, t)$, $E(\xi, \xi, t) - E(-\xi, \xi, t)$ and $\tilde{H}(\xi, \xi, t) + \tilde{H}(-\xi, \xi, t)$.

At small to modest values of x and t both \tilde{H} and E are kinematically suppressed, allowing direct access to the GPD $H(\xi, \xi, t)$. For the upgraded CLAS (CLAS⁺⁺) an operating luminosity of $10^{35} \text{ cm}^{-2} \text{ sec}^{-1}$ is anticipated. Figure 76 shows the projected coverage of the beam spin asymmetry measurement. These measurements will produce high precision DVCS data for $Q^2 = 1.0 - 7.5 \text{ GeV}^2$, $x_B = 0.1 - 0.65$, and $-(t - t_{\min}) < 1.5 \text{ GeV}^2$. Figure 77 shows the $\sin \phi$ moments for the projected CLAS data. At the same time the beam helicity dependent cross section differences will be extracted as well.

A complementary DVCS program in Hall A will focus on measurements of the helicity-dependent cross section difference at the highest Q^2 . Projections of a 400 hours measurements of $\Delta\sigma$ at a luminosity of $10^{37} \text{ cm}^{-2} \text{ sec}^{-1}$ are shown in Fig. 78 at $Q^2 = 7 \text{ GeV}^2$. The projected data were fitted to a form $\Delta\sigma = A \sin \phi + B \sin(2\phi)$, where A and B correspond to the twist-2 and

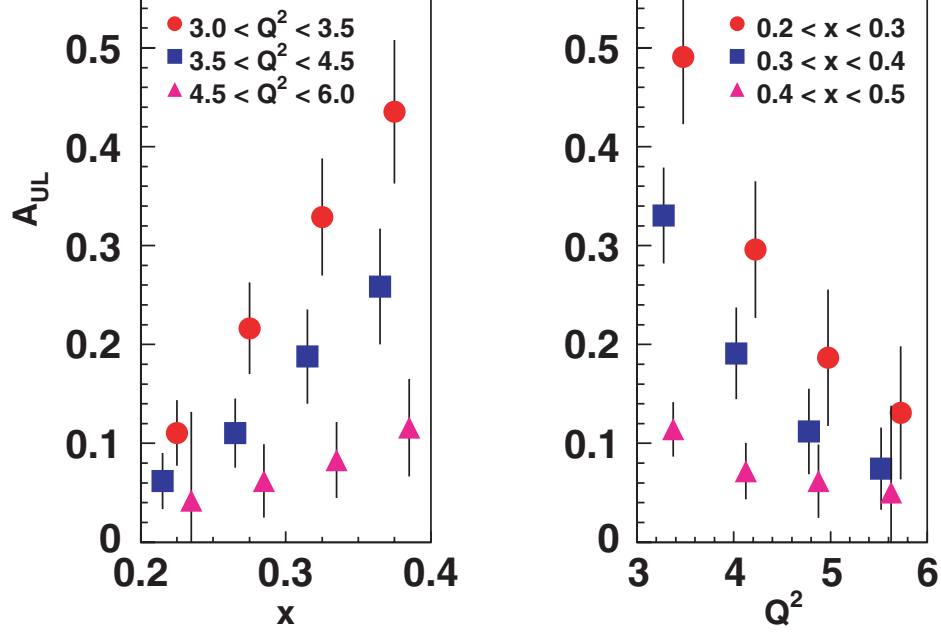


Figure 80: Projected data for longitudinal target asymmetry measured in CLAS⁺⁺ for a 2000 hrs run at a luminosity of $10^3 5\text{cm}^{-2}\text{sec}^{-1}$. The t-dependences will be obtained simultaneously.

twist-3 terms, respectively. The size of the twist-3 term will give an indication of the convergence of the series, but it also contains information on the twist-3 GPDs which are of interest in their own rights. Figure 79 shows projections of the errors on the twist-2 and twist-3 contributions extracted from fitting the cross section differences.

DVCS with polarized targets The use of polarized nucleon targets will provide independent information on the GPDs. The longitudinal polarized target polarization dependent cross section is (in the same kinematic limits as Eq. 6 [Be02a]):

$$\frac{\Delta^5 \sigma}{dx_B dQ^2 dt d\phi_e d\phi_{\gamma\gamma}} = \frac{1}{-s'u'} \frac{\alpha^3}{\pi^2} \frac{2 - 2y + y^2}{y} \frac{\sqrt{1 - x_B} \sqrt{t_{\min} - t}}{(-t) \sqrt{Q^2}} \left[\frac{x_B}{2 - x_B} G_M(-t) \left(H + \frac{x_B}{2} E \right) + F_1(-t) \tilde{H} + \frac{x_B}{2 - x_B} \left(\frac{x_B}{2} F_1(-t) + \frac{t}{4M^2} F_2(-t) \right) \tilde{E} \right], \quad (39)$$

As in Eq. 6, the GPDs are evaluated at $x = \pm\xi$.

In contrast to the beam asymmetry (6), \tilde{H} is not kinematically suppressed, but H , E , \tilde{E} are. The longitudinal target asymmetry will give the most direct information on the GPD $\tilde{H}(\xi, \xi, t)$ in the lower x and lower t range where H , E and \tilde{E} are kinematically suppressed. Figure 80 shows projections of the target asymmetry for the CLAS⁺⁺ detector for different models of \tilde{H} .

DVCS on Neutron Targets DVCS on protons is the most promising and cleanest way of

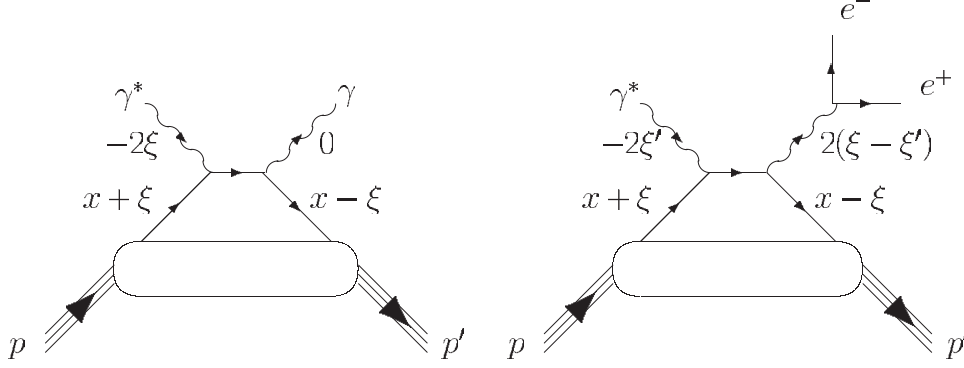


Figure 81: The handbag diagrams for DVCS (left) and DDVCS (right). The presence of two kinematic quantities ξ and ξ' in the case of DDVCS allows to access the kinematic region outside of $x = \xi$ directly.

accessing GPDs. However, photons have no flavor sensitivity and the observables contain contributions of both u -quarks and d -quarks. In DVCS on protons, the GPDs for each flavor enter in the combination

$$H_{DVCS}^p = \frac{4}{9}H^u + \frac{1}{9}H^d + \frac{1}{9}H^s \quad (40)$$

and similarly for \tilde{H} , E , and \tilde{E} . For neutrons one has different weighting factors for the different flavors:

$$H_{DVCS}^n = \frac{1}{9}H^u + \frac{4}{9}H^d + \frac{1}{9}H^s \quad (41)$$

and similarly for \tilde{H} , E , and \tilde{E} . This, in principle, opens up the possibility of studying the flavor dependence of the dominant GPD H . Unfortunately, the form factor F_1 is small for the neutron, and Eq. (6) shows that this causes a suppression of the GPD H , which makes the flavor separation very difficult. However, this may open up the possibility to access the GPD E . DVCS measurements on neutrons can, in principle, be done using ${}^2\text{H}$ or ${}^3\text{He}$ targets. These possibilities of DVCS measurements at 11 GeV on neutrons are currently being evaluated.

Double Deeply Virtual Compton Scattering (DDVCS) The DDVCS process is the extension of DVCS to the regime where the final state photon is time-like and decays into a lepton pair (Fig. 81).

This process gives *direct* access to the GPDs in a wider kinematic range. While DVCS with real photons gives access to GPDs integrated over x , or to GPDs at fixed kinematics $x = \xi$, DDVCS accesses GPDs directly in a large kinematic range as the kinematics of the two photons is now described by two variable ξ and ξ' that can be independently varied. The beam asymmetry depends on both variables and the GPD is measured at $H(2\xi', \xi, t)$. Since ξ and ξ' can be varied independently this allows to map out an extended area on the surface in Fig. 68 rather than a line. The rates for this process are suppressed by a factor of two to three orders of magnitude compared to DVCS. Any measurement of DDVCS will therefore be restricted to a much smaller number of bins and will yield larger statistical errors. Nevertheless the process has been seen in CLAS data taken

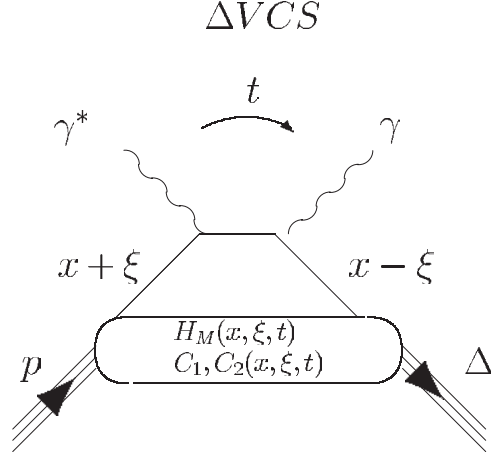


Figure 82: The handbag diagram for Δ DVCS

at 4.3 GeV, showing the feasibility of the measurement. With the higher luminosity available with the upgraded equipment, these processes will become accessible with modest statistical accuracy.

DVCS in $N \rightarrow \Delta$ and Resonance Transitions. Inelastic deeply virtual Compton scattering can provide a new avenue of resonance studies at the elementary quark level. The process of interest is $ep \rightarrow e\gamma\Delta^+(N^{*+})$. Varying ξ and the momentum transfer t to the recoil baryon probes the “transition” GPDs from the ground state nucleon to the excited Δ or N^* . The handbag diagram is shown in Fig. 82.

That this process is indeed present at measurable levels can be seen in the preliminary data from CLAS [Gupc] shown in Fig. 83. The recoiling baryon system shows the excitation of resonances. Besides the $\Delta(1232)$, the $N^*(1520)$ and $N^*(1680)$ are seen. While these are well known s-channel resonances, they are here excited in t-channel processes. This has the advantage that the photon virtuality Q^2 is decoupled from the momentum transfer to the baryon system. As in the case of elastic DVCS, Q^2 can be chosen sufficiently high, such that the virtual photon couples to an elementary quark, while the momentum transfer to the baryon system can be varied from small to large values, allowing to access the resonance transition GPDs as a function of t . Similar to the elastic DVCS, the Bethe-Heitler process interferes with the DVCS process producing an asymmetry for the $N\Delta(1232)$ transition. In general the beam asymmetry for the Delta production is expected to be smaller than for the elastic process as shown in Fig. 84

Deeply Virtual Meson Production at JLab with 12 GeV Electrons DVCS is the most promising and cleanest way of accessing GPDs, however, as discussed earlier, it is difficult to perform a flavor separation. Moreover, a separation of the spin-dependent GPDs from the spin-independent GPDs requires use of a polarized target, and may be limited to accessing the GPD \tilde{H} . Vector meson and pseudoscalar meson production, in principle, allow to accomplish both objectives. Measurements of exclusive vector mesons isolates the helicity-independent GPDs. If one measures

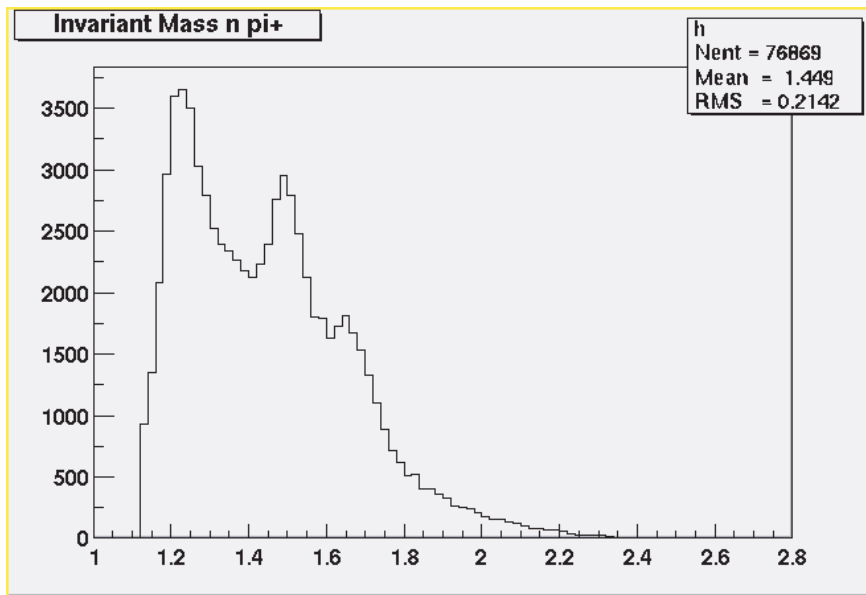


Figure 83: Inelastic DVCS as measured at 4.3GeV. The scattered electrons, π^+ , and neutron are detected. The recoil system clearly shows the excitation of the $\Delta(1232)$ and higher mass states. Single γ and π^0 were not fully separated in this measurement.

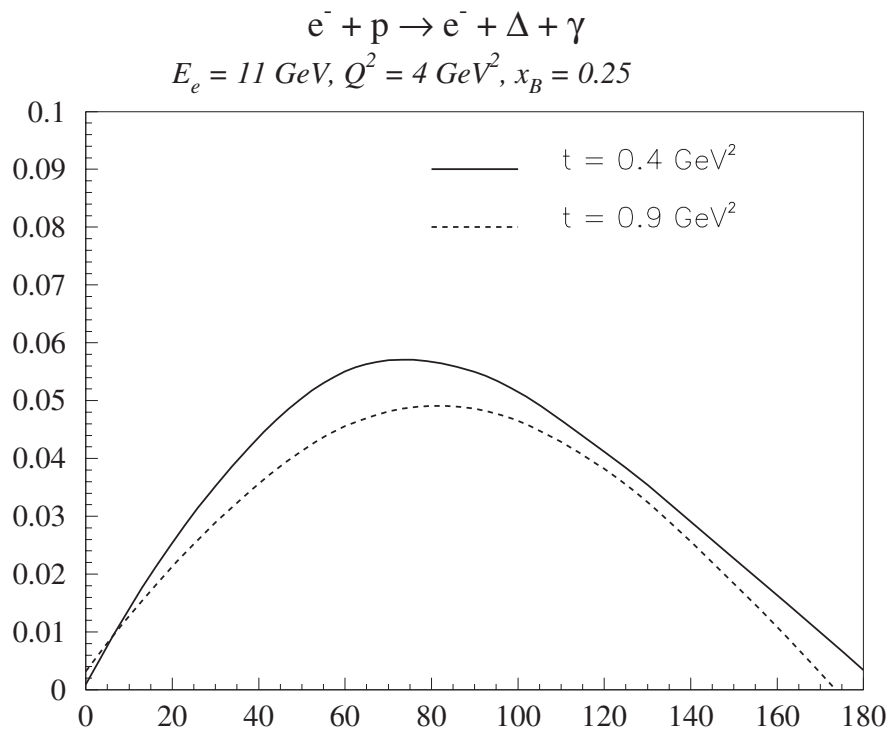


Figure 84: Asymmetry predicted for the Δ DVCS at 11 GeV.

both ρ 's and ω 's production one can separate the u -quark and d -quark contributions in the GPDs. The electroproduction amplitudes for ρ° and ω contain terms with a different sign:

$$\rho : e_u H^u - e_d H^d \quad \omega : e_u H^u + e_d H^d \quad (42)$$

Measurement of pseudoscalar meson production isolates the helicity-dependent GPDs \tilde{H} and \tilde{E} . However, there is a price one pays for using the meson channel in the study of GPDs. Compared to DVCS, higher values of the photon virtuality Q^2 are required to reach the domain where the GPD formalism is controlled by pQCD. The exact Q^2 value where this will be the case is not currently well understood and needs to be studied experimentally in more detail. It will depend also on the specific kinematics being studied. This aspect is currently under intense investigation.

The $ep \rightarrow epp^\circ$ Channel An experimental program to study GPDs in hard meson production must begin by identifying the longitudinal part of the cross section for which the factorization theorem applies and the connection with the GPD formalism can be made. Longitudinal ρ_L° 's can be identified through the angular distribution of the vector meson decay. Assuming s-channel helicity conservation (SCHC), the desired cross section: $\gamma_L^* p \rightarrow p\rho_L^\circ$ can be extracted by analyzing the angular distribution ² of the $\rho \rightarrow \pi^+\pi^-$ decay distribution, which reflects its polarization state. Assuming the outgoing electron and proton are detected, measurement of only one decay pion is sufficient to determine the decay angular distribution. The decay pion defines an angle, θ_{cm} , which is the polar angle relative to the direction opposite to the recoiling target in the ρ center-of-mass frame. The $\cos(\theta_{cm})$ distribution follows the form:

$$W(\cos(\theta_{cm})) = \frac{3}{4}[1 - r_{00}^{04} + (3r_{00}^{04}) \cos^2(\theta_{cm})]. \quad (43)$$

The matrix element r_{00}^{04} depends on Q^2 and W , and is linked to the longitudinal polarization state of the ρ . For example, $r_{00}^{04} = 1$ (0) correspond to pure longitudinal (transverse) polarization of the ρ , respectively, and, in terms of angular distribution, to $\frac{3}{2} \cos^2 \theta_{cm}$ ($\frac{3}{4} \sin^2 \theta_{cm}$), respectively. Using SCHC, the ρ polarization can be linked to the virtual photon polarization by defining:

$$R = \frac{\sigma_L}{\sigma_T} = \frac{1}{\epsilon} \frac{r_{00}^{04}}{1 - r_{00}^{04}},$$

where ϵ defines the degree of longitudinal polarization of the virtual photon. R has been measured at low and at high Q^2 , but only recently at moderately high Q^2 . Figure 85 shows the world data including preliminary CLAS data. For $W > 2$ GeV, the data show a consistent pattern of R rising steeply with Q^2 in, what appears, an approximately linear fashion. Should σ_L become strongly dominant, an L/T separation may not be necessary at high Q^2 , and one might be able to use σ_{tot} to extract information on GPDs by simply applying corrections for σ_T . This will only be possible as long as ϵ is sufficiently large that the contribution of σ_L is dominant.

²The SCHC hypothesis can actually be tested by considering the interference response functions R_{TT} and R_{TL} , which are accessible with a large-acceptance detector such as CLAS⁺⁺.

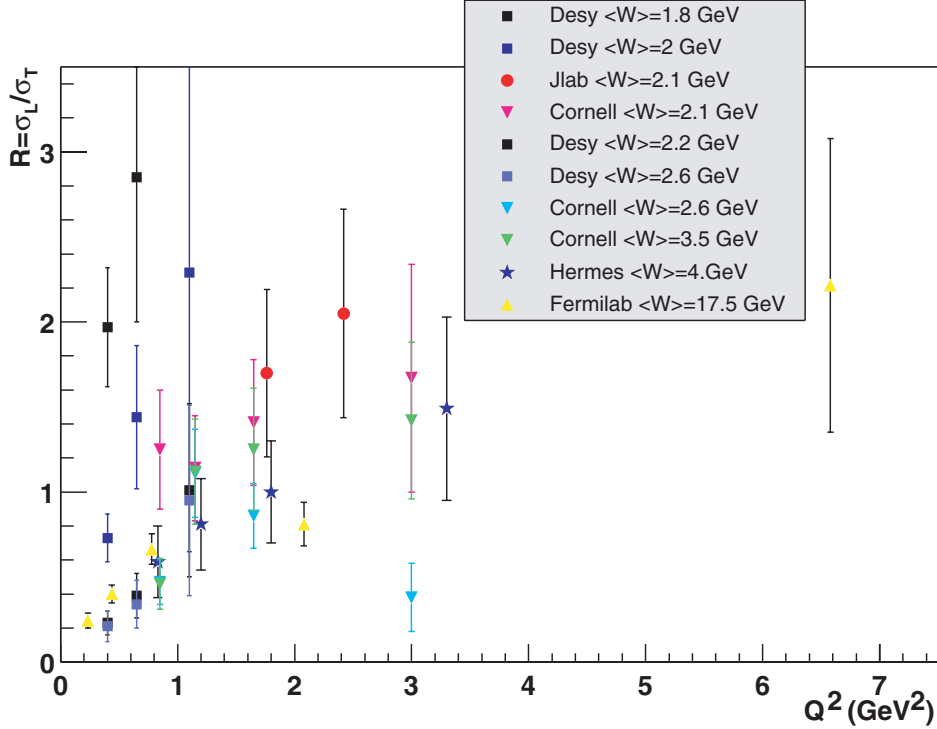


Figure 85: World data for $R = \sigma_L/\sigma_T$ as a function of Q^2 (assuming SCHC).

Recent results from CLAS and HERMES on ρ production indicate that modestly high Q^2 values may be sufficient for the GPD formalism to be applicable. Figures 86 and 87 show preliminary CLAS and HERMES data, respectively, for ρ^0 production with longitudinal photons compared with calculations in the GPD framework using a “frozen” α_s [Gupc]. The various curves correspond to different assumption on the input GPDs. The quite good agreement with the data in the range $x_B < 0.4$ gives some indication that the handbag diagram dominance may set in for longitudinal ρ^0 production at $Q^2 > 2 - 5$ GeV 2 , dependent on the exact kinematics being probed. These recent findings provide support for the GPD program with vector meson final states with the Upgrade.

While these data support the expectation that the handbag mechanism may become dominant already at modestly high photon virtualities, such expectations need to be tested at higher energies. Some of this can already be achieved at JLab using the 6 GeV [Ga99] beam.

At the energy of the upgraded CEBAF significantly higher Q^2 will be achieved. In meson production, only the longitudinal component can be used for the direct extraction of GPDs. In the case of vector meson production the longitudinal contribution can be isolated by analyzing the decay distribution of the $\pi^+\pi^-$ system for the ρ^0 , or the 3-pion system in the case of ω production, by using the s-channel helicity conservation for small-t vector meson production. Figure 88 shows the projected data for the total ρ^0 cross section and for the longitudinal and transverse pieces separately. The longitudinal cross section can be extracted for Q^2 up to 7 GeV 2 at this particular x_B and t kinematics. Other kinematics will be measured, simultaneously.

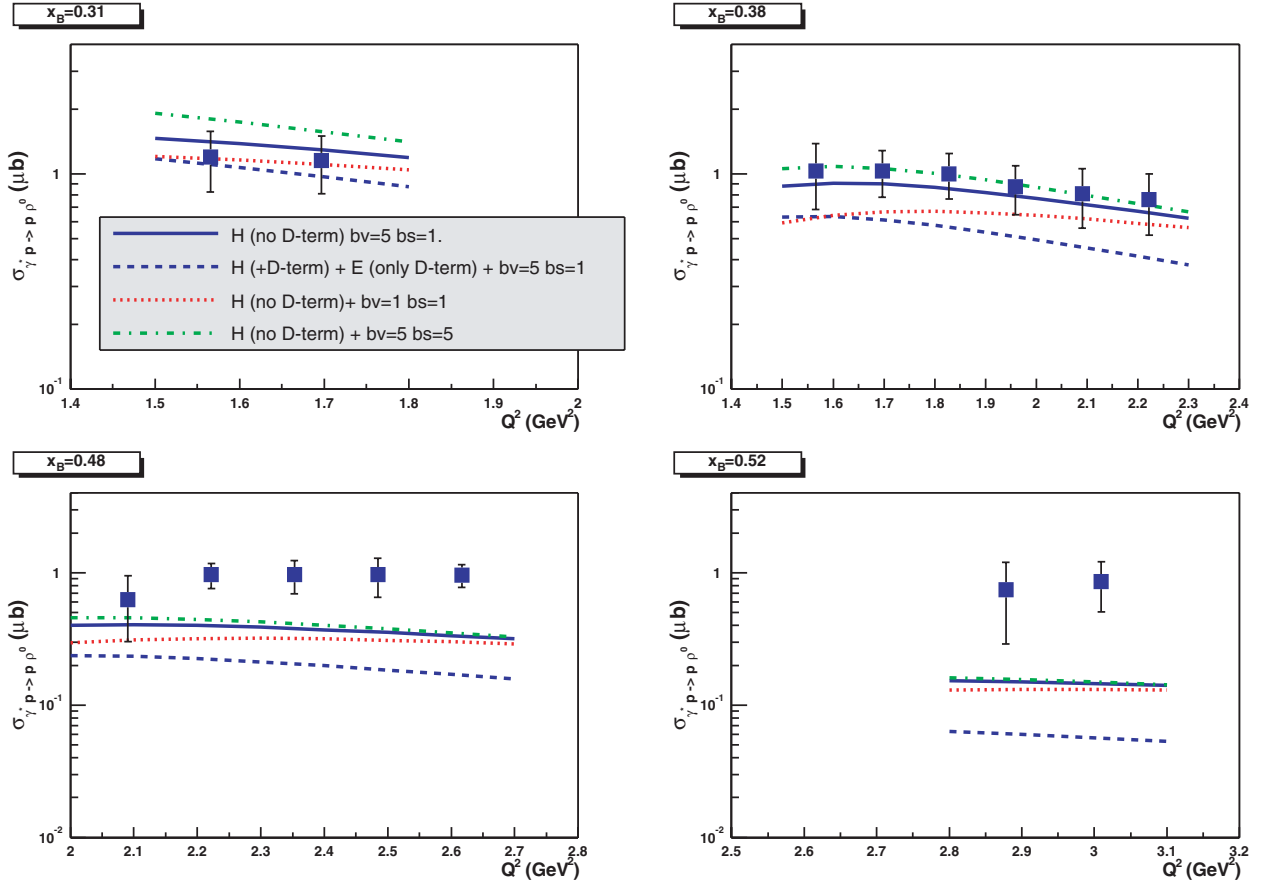


Figure 86: Preliminary data from CLAS on the longitudinal cross section for ρ production at 4.3 GeV beam energy. The curves represent predictions based on the GPD formalism with “frozen” α_s . Different GPD ingredients are used as input.

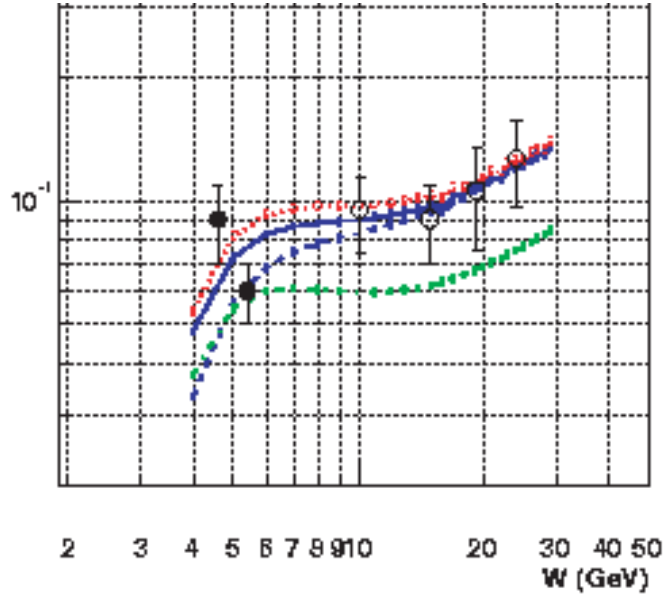


Figure 87: Data from HERMES on longitudinal cross sections for ρ^0 production from protons at a beam energy of 27 GeV. The curves represent predictions based on the GPD formalism with “frozen” α_s . Different GPD models are used as input.

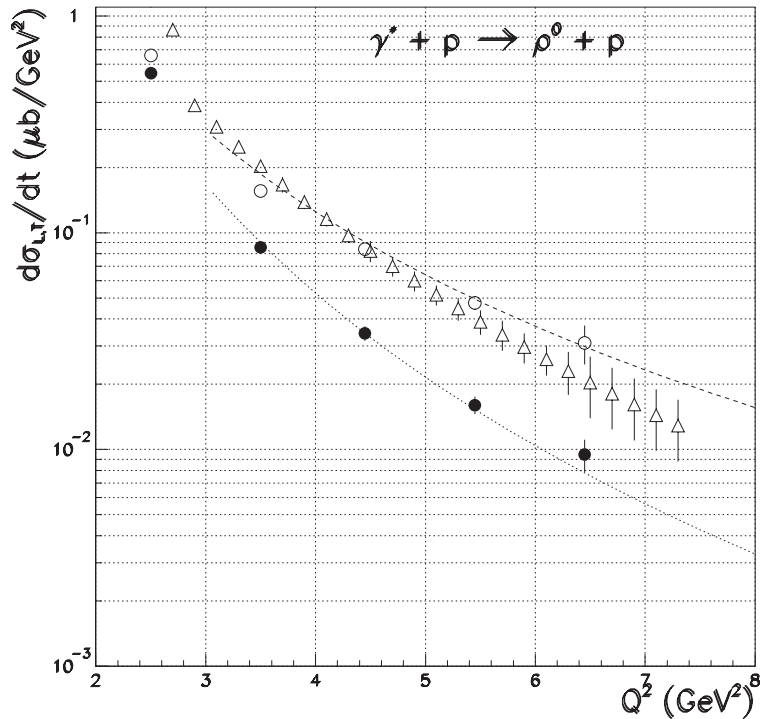


Figure 88: Projected data on ρ^0 production from protons using CLAS⁺⁺. The projected errors for the unseparated cross section and the separated longitudinal and transverse pieces are shown for the 2000 hours of data taking at a luminosity $L = 10^{35} \text{ cm}^{-2} \text{ sec}^{-1}$. Kinematic bins of $x_B = 0.3-0.4$, $-t = 0.2-0.4 \text{ GeV}^2$ were chosen. Other bins in x_B and t will be measured simultaneously, and with similar statistics.

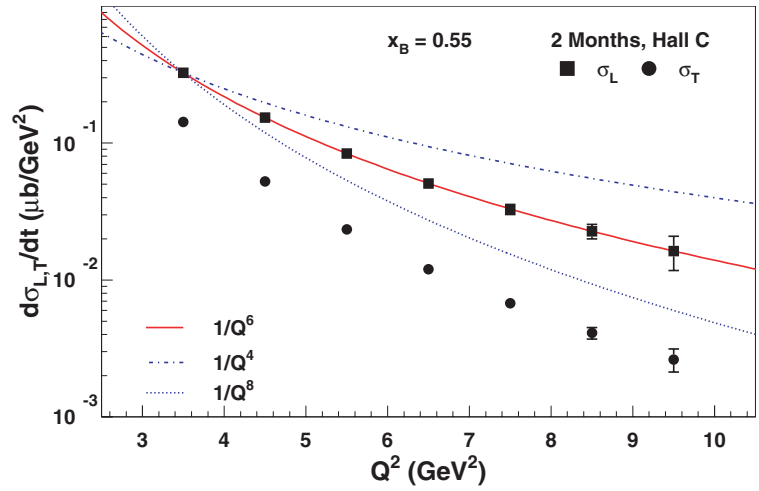


Figure 89: Projected data for a Rosenbluth separation of $ep \rightarrow en\pi^+$ in Hall C at $t = t_{min}$, $x_B = 0.55$.

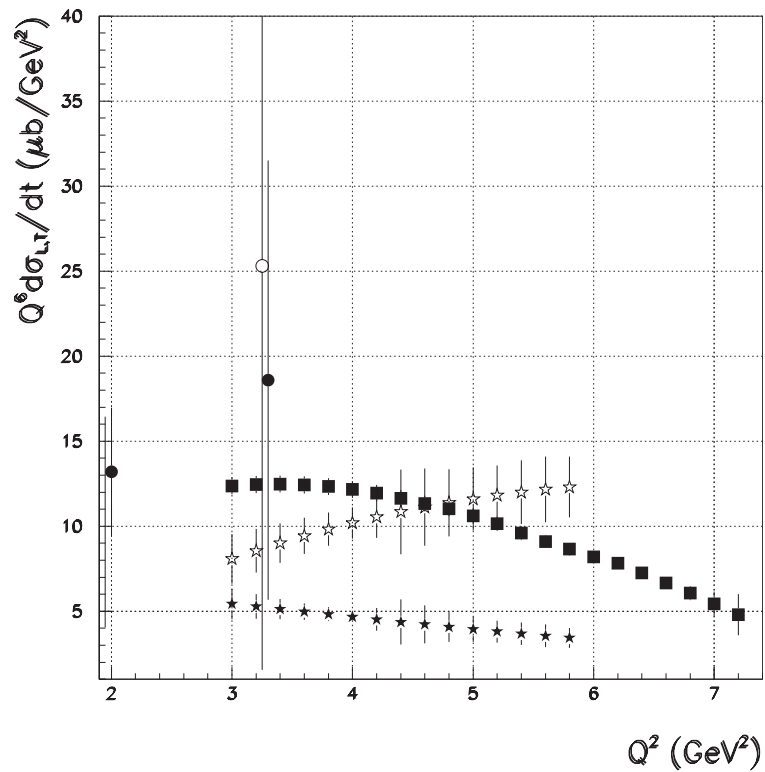


Figure 90: Projected CLAS⁺⁺ data for a Rosenbluth separation of $ep \rightarrow en\pi^+$ for $x_B = 0.45$, $-t = 0.5 \text{ GeV}^2$.

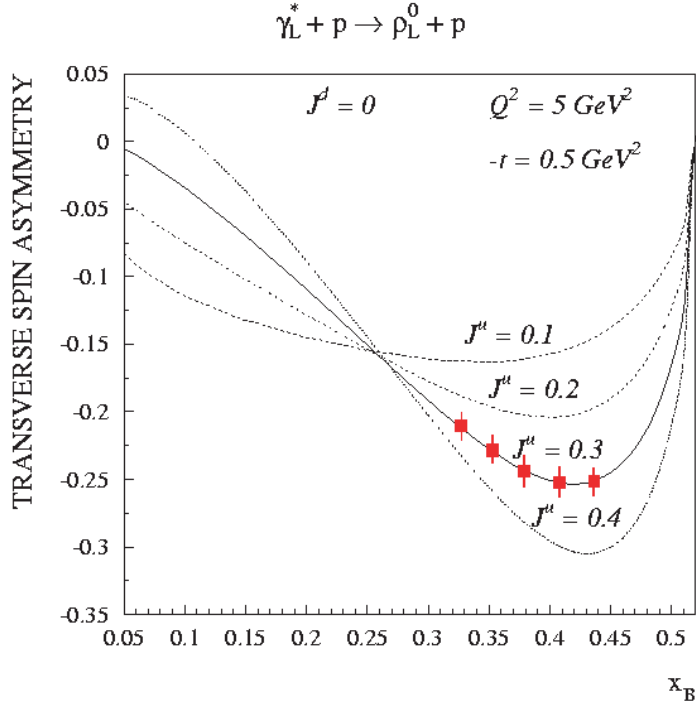


Figure 91: Projected CLAS⁺⁺ data on the transverse target asymmetry for ρ^0 production on protons. σ_L dominance in the cross section is assumed.

Hard pseudoscalar meson electroproduction Production of pseudoscalar mesons $\pi^{\circ\pm}$, η , $K^{\circ,\pm}$ access the helicity-dependent GPDs $\tilde{H}^{u,d,s}$ and $\tilde{E}^{u,d,s}$. The neutral channels are generally expected to reach the Bjorken regime earlier than the charged channels, and asymmetries or ratios of cross sections may even scale at a relatively low Q^2 value. However, it is still important to study the charged channels as well. They can usually be more easily accessed experimentally. The process $ep \rightarrow e\pi^+n$ is of special interest as it contains two contributions, one related to the well known pole-term scattering of the nucleon's pion cloud, and has sensitivity to the pion form factor F_π , the second relates to the usual handbag diagram in Fig. 70. Both terms should exhibit the same asymptotic Q^2 -dependence, however they have different dependences on the kinematic quantities x_B and t . In order to separate the longitudinal contribution a Rosenbluth separation is necessary. This can be accomplished using the combination of HMS-SHMS spectrometers in Hall C for parallel kinematics ($t = t_{min}$). Figure 89 shows projected data of a Rosenbluth separation for the $n\pi^+$ channel. A maximum Q^2 can be achieved using the Hall C spectrometers for this kinematics allowing to test the Q^2 dependence to the highest possible values. With CLAS⁺⁺ a somewhat lower Q^2 is achieved with access to a broad t -range allowing to map out the entire transverse impact parameter space, simultaneously. This allows to have different sensitivity to the two contributions in the cross section. Using Rosenbluth separation σ_L can be measured up to $Q^2 = 6 \text{ GeV}^2$ using beam energies of 6, 8, and 11 GeV. Figure 90 shows the Q^2 -dependent separation at $-t = 0.5 \text{ GeV}^2$.

Transversely polarized target asymmetry Of special interest in the study of GPDs is their

connection to the quark angular momentum contribution to the total nucleon spin as formulated in Ji's spin sum rule [Ji97]. It contains the two GPDs H and E . While H is accessible through the beam asymmetry accessed in DVCS, E may be accessed in vector meson production from a transversely polarized target. In leading order the asymmetry is given by [Go01b]:

$$A_{UT} = -\frac{2t\text{Im}(AB^*)/\pi}{|A|^2(1-\xi^2) - |B|^2(\xi^2 + t/4m^2) - 2\text{Re}(AB)\xi^2} \quad (44)$$

with

$$A \sim (e_u H^u - e_d H^d) \quad , \quad B \sim (e_u E^u - e_d E^d) \quad . \quad (45)$$

The asymmetry depends linearly on the GPD E . As shown in Fig. 91, the asymmetry A_{UT} has strong sensitivity to the u -quark angular momentum contribution to the proton spin. Similar sensitivity is predicted for the ω channel. The model curves are labeled by the value of the u -quark contribution to the angular momentum sum rule: Eq. (3).

From Observables to GPDs Extracting GPD information from asymmetries and cross section measurements is not an easy task, and, unless additional conditions are imposed, may not give unambiguous results. However, one can make use of important constraints given by form factors as well as the parton distribution functions measured in DIS experiments. Moreover, the GPDs are strongly constraint by certain polynomial conditions.

Currently, at least three avenues are being investigated on how to obtain most direct information on the GPD content of exclusive reactions.

(1) As is clear from the relations (2) and (3), approximations may be made for certain kinematics allowing to directly extract individual GPDs from asymmetry or from cross section differences at $x = \xi$. For example, the GPD H may be extracted from the beam asymmetry measurements for $x_B < 0.25$ values [Do02]. Similar approximations are possible for the GPD \tilde{H} using asymmetry data from longitudinally polarized targets. The GPD E may be accessible in polarized beam measurements on neutrons.

(2) Global information on GPDs can be obtained from fits to large sets of data where constraints from elastic form factors, meson distribution amplitudes, forward parton distributions, and polynomiality conditions are imposed[Fr03, Be02b]. With increasing experimental information, this method may provide the strongest constraints on GPDs in the future.

(3) A new technique has recently been proposed [Po03] that makes use of partial wave analysis techniques where the GPDs are expanded in infinite sums over t -channel exchanges. The range of convergence of such a procedure still remains to be explored. In summary, GPDs uniquely connect the charge and current distributions of the nucleon with the forward quark distributions measured in DIS, in a fundamental and hitherto experimentally unexplored way. Recent results demonstrate

the applicability of the GPD framework at currently achievable values of Q^2 for DVCS and possibly for ρ meson production. A broad program of DVCS and DVMP has been proposed for the 12 GeV Upgrade, that will provide a solid basis for the extraction of GPDs from exclusive processes.

2.B.4 Other Topics in Hadron Structure

Transverse parton distributions The origin of the spin of the proton has become a topic of considerable experimental and theoretical interest ever since the EMC [As88] measurements implied that the constituent quarks account for only a fraction of the nucleon spin. The gluon polarization and the orbital momentum of partons have been of central interest.

Transverse momentum of quarks is a key to orbital angular momentum. In recent years parton distribution functions were generalized to contain information not only on the longitudinal but also on the transverse distributions of partons in a fast moving hadron. Much of the interest in Generalized Parton Distributions (GPDs) [Ji97, Ra96] has been triggered by their potential to help unravel the spin structure of the nucleon, as they contain information not only on the helicity carried by partons, but also on their orbital angular momentum (OAM).

Another important, complementary to GPDs, class of nonperturbative functions that carry information not only on the longitudinal but also on the transverse hadron structure are the transverse momentum dependent (TMD) parton distributions [Ra79, Mu96, Ko95]. They provide rich and direct information on the orbital motion of quarks. If the transverse momentum k_T of partons is included into consideration, the number of independent distribution functions at leading twist (see Table 9) increases to eight [Mu96, Ko95]. While distribution functions describe the *confinement* of partons inside hadrons, another analogous set of non-perturbative functions describe the transition of partons to hadrons or *hadronization*. Three diagonal elements (in bold), f_1, g_1 and h_1 reduce to well known one dimensional, longitudinal momentum dependent parton distribution functions $q(x), \Delta q(x)$ and $\delta q(x)$ when integrated over k_T . This new degree of freedom makes possible studies of transitions of nucleons with one polarization state to a quark with another. Off diagonal elements of table 9 describe those transitions. In particular the f_{1T}^\perp known as the Sivers function [Si91, An98, Br02, Co02, Ji03b, Be03] describes unpolarized quarks in the transversely polarized nucleon. It is *time-reversal odd* (T-odd) and requires final state interactions and interference between different helicity states. The counterpart of the Sivers function in the hadronization process is the Collins T-odd fragmentation function H_1^\perp [Co93] describing fragmentation of transversely polarized quarks to unpolarized hadrons. As shown recently in Ref.[Be03], the interaction between the active parton in the hadron and the target spectators [Br02, Co02, Ji03b] (see Fig.92) leads to gauge-invariant TMD parton distributions.

The interference of wavefunctions with different orbital angular momentum responsible for the non-zero Sivers functions [Si91, An98, Br02, Co02, Ji03b, Be03] also yields the helicity-flip Generalized Parton Distribution (GPD) E [Br02a, Ji03a] which enters Deeply Virtual Compton

Table 9: Leading twist transverse momentum dependent distribution functions. The U,L,T stand for transitions of unpolarized, longitudinally polarized and transversely polarized nucleons (rows) to corresponding quarks (columns).

N/q	U	L	T
U	\mathbf{f}_1		h_1^\perp
L		\mathbf{g}_1	h_{1L}^\perp
T	f_{1T}^\perp	g_{1T}	$\mathbf{h}_1, h_{1T}^\perp$

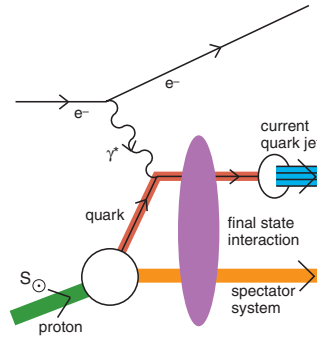


Figure 92: Interaction of struck quark and the target spectators[Br02].

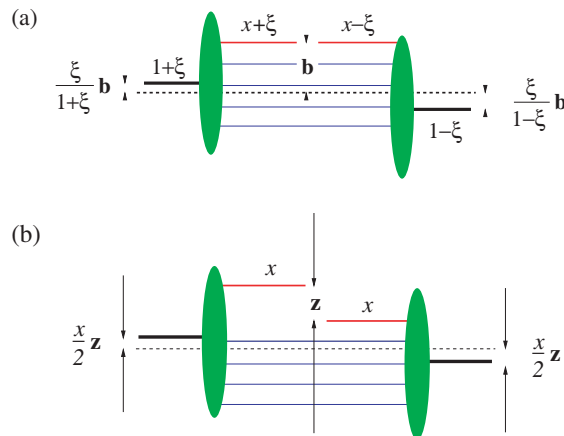


Figure 93: Representation of a GPD (a) and TMD (b) in impact parameter space [Di02a].

Scattering [Ji97, Ra96] and the Pauli form factor F_2 . Relations of GPDs and TMDs become particularly intuitive after a Fourier transform from transverse momentum transfer to impact parameter, both for GPDs [Bu03a, Di02a] and TMDs [Di02a]. The impact parameter gives the location where a quark or antiquark is pulled out of the proton and put back. The center of momentum of the target is defined by the sum $\sum_{i \in q, g} x_i \mathbf{b}_{\perp, i}$ over the transverse positions $\mathbf{b}_{\perp, i}$ of all quarks and gluons in the target, and the weight factors x_i being the momentum fraction carried by each parton [Bu03a]. GPDs at nonzero longitudinal momentum transfer ξ correlate hadronic wave functions with both different momentum fractions and different transverse positions of the partons. However, the difference in transverse positions is a *global* shift in each wave function; the *relative* transverse distances between the partons in a hadron are the same before and after the scattering. In contrast to impact parameter dependent GPDs in TMD distributions (see Fig. 93b) describing the correlation in transverse position of a single parton, the struck quark has a different transverse location *relative* to the spectator partons in the initial and the final state wave functions, in addition to the overall shift of the proton center of momentum.

It was recognized long time ago, that non-zero transverse momenta of partons (a consequence of being confined by strong interactions) is accessible in measurements of azimuthal distributions of final state hadrons [Ge78, Ca78, Be80]. Combined with spin asymmetries, which were a major testing ground for QCD, measurement of azimuthal distributions of final state particles provides a new important class of measurements: so-called spin-azimuthal asymmetries.

Both TMDs and impact parameter dependent GPDs are sensitive to the orbital momentum of partons and lead to predictions of spin-azimuthal asymmetries in hard scattering processes [Si91, Co93, Mu96, Ko95, Br03, Bu03a]. The connection between Single-Spin azimuthal Asymmetries (SSAs) and GPDs has also been discussed in terms of the transverse distribution of quarks in nucleon [Bu03a].

Measurement of asymmetries in azimuthal distributions of final state photons and hadrons in semi-inclusive DIS thus allows access to the transverse momentum distributions of quarks [Co93, Br02, Bu03a] providing a window to the physics of final and initial state interactions at the parton level. It is also argued that in both semi-inclusive [Ba02] and in hard exclusive [Fr99, Fr00a] pion production, scaling sets in for cross section ratios and, in particular, for spin asymmetries at lower Q^2 than it does for the absolute cross section. There are quite a few examples of remarkable agreement between spin asymmetries measured at different beam energies over a wide Q^2 range. Very good agreement was observed in single-spin asymmetries in ep scattering at HERMES [Mi02a] and CLAS [Av02, CLAS03], both for target and beam SSA measurements. Figure 94 shows that beam SSA measurements, providing also important information on the Collins fragmentation function, performed at very different energies are in fact consistent. All this makes spin-asymmetries a major tool for the measurement of different parton distribution functions (GPDs, TMDs) in the Q^2 domain of a few GeV^2 .

SSA in semi-inclusive DIS are recognized now as a major tool to measure the leading twist

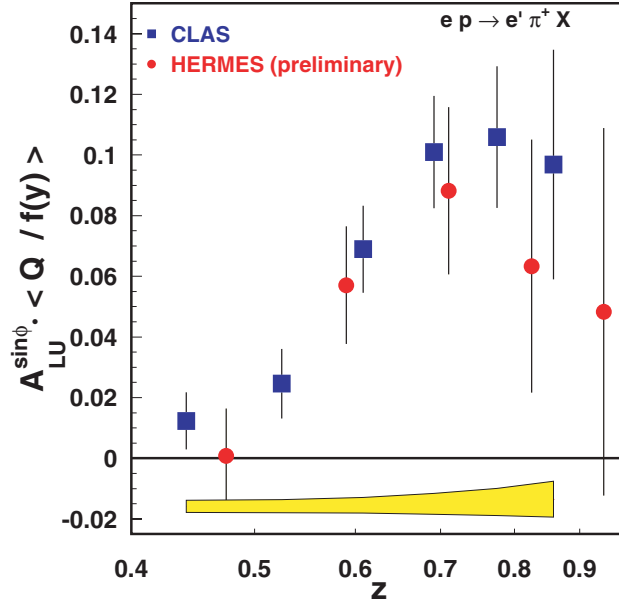


Figure 94: Beam SSA: HERMES vs CLAS. Analyzed in fragmentation terms $A_{LU}(z)$ depends on the ratio of the Collins function and unpolarized fragmentation function. The $f(y)$ is the kinematic factor, depending on the fraction of the initial energy of electron carried by the virtual photon.

TMD distributions and in particular Collins function and quark transversity [Co93]. The chiral-odd transversity distribution $\delta q(x)$ which in combination with the number density $q(x)$ and the helicity distribution $\Delta q(x)$ completes the list of leading-twist parton distribution functions is essentially unexplored.

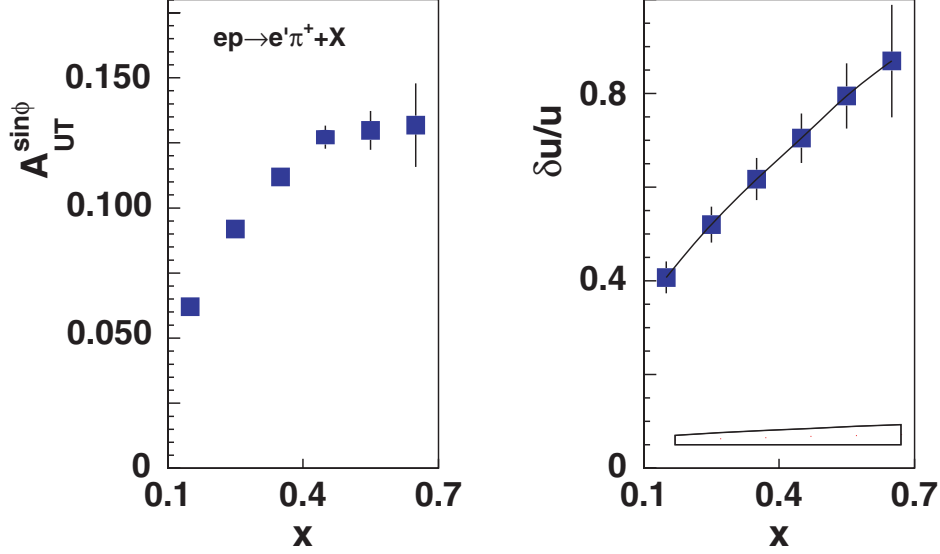


Figure 95: Projected transverse spin asymmetry ($A_{UT}^{\sin\phi}$) in single π^+ production with CLAS at 12 GeV (left plot) and expected precision of the extracted $\delta u/u$ (right plot). The line is the Monte Carlo generated $\delta u/u$.

For transversely polarized case, however, several SSA arise at leading order[Co93, Mu96, Ko95, Br02, Ji03b, Ko96]:

$$\sigma_{UT}^{\sin\phi} \propto S_T(1-y+y^2/2)\sin(\phi-\phi_S)\sum_{q,\bar{q}}e_q^2x\delta q(x)H_1^{\perp q}(z), \quad (46)$$

$$+ S_T(1-y)\sin(\phi+\phi_S)\sum_{q,\bar{q}}e_q^2xf_{1T}^{\perp q}(x)D_1^q(z), \quad (47)$$

where ϕ_S is the azimuthal angle of the transverse spin in the photon frame, $D_1^q(z)$ is the spin-independent fragmentation function, $f_{1T}^{\perp q}(x)$ and $H_1^{\perp q}(z)$ are T-odd Sivers and Collins functions, respectively. Contributions to transverse SSAs from T-odd distributions of initial quarks (or Sivers effect) and T-odd fragmentation of final quarks (or Collins effect) could be separated by their different azimuthal and z -dependencies. The program of transverse asymmetry measurements is under way at HERMES[Mi02a] and COMPASS[CO96]. JLab at 12 GeV will provide measurements a The effect of transversity is a valence quark effect and JLab measurements at 12 GeV will provide unique access to transverse spin effects at large x (see Fig. 95).

The interpretation of these experiments, and extraction of transversity in particular, will require a detailed knowledge of the Collins fragmentation function, $H_1^{\perp}(z)$. To reveal the source of SSA and accomplish the separation of Collins and Sivers contributions measurements with different target polarizations and with detection of different final state particles may be required. One

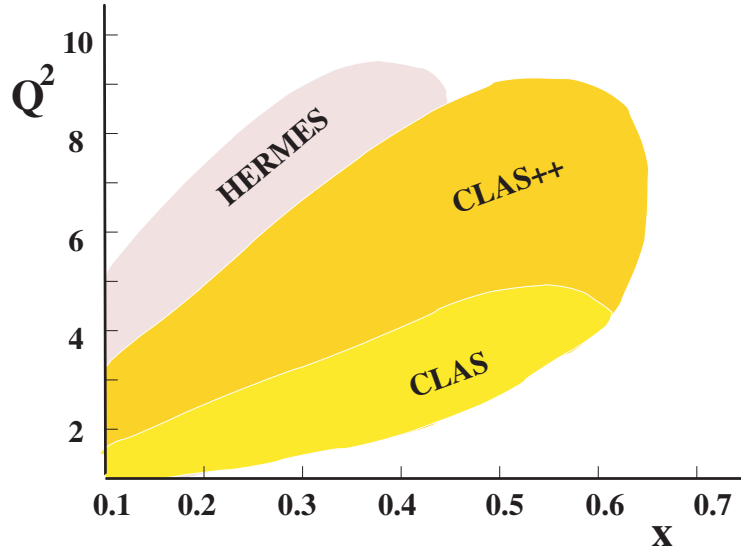


Figure 96: Kinematic coverage at JLab at 12 GeV.

important feature of Collins mechanism is the presence of $\sin 2\phi$ dependent SSA, arising for the longitudinally polarized target. Sufficiently large effect was predicted only at large x , the region well covered by JLab at 12 GeV (see Fig. 96). The Fig. 97 shows the prediction for the SSA arising only due to the Collins mechanism. JLab measurement will pin down the corresponding transverse momentum distribution function, describing transition of longitudinally polarized nucleon to transversely polarized quarks.

In conclusion, the SSA observables are most sensitive to the orbital motion of quarks and provide direct access to transverse momentum dependent distributions. Model calculations indicate that SSA are not very sensitive to scale and higher order corrections making them especially appropriate at low beam energies. SSA measured at JLab already at 4-6 GeV are consistent with partonic picture and can be described by a variety of theoretical models. The significantly higher statistics of JLab at 12 GeV data, in simultaneous measurements of SSAs for different final state particles as shown in Table 2, especially in the large x region, will enable the extraction of the x and Q^2 dependencies for different azimuthal moments in a wide kinematical range. The key goal of this program will be the study of transitions between the nonperturbative and perturbative regimes of QCD in measurements of spin-azimuthal asymmetries with unpolarized, longitudinally polarized, and transversely polarized targets enabling access to orbital motion of quarks.

The extended GDH integral and sum rule The extended GDH integral, $I(Q^2)$, is a quantity that can be measured from arbitrarily small Q^2 , where behavior is dominated by hadronic degrees of freedom, to arbitrarily large values of Q^2 , where behavior is dominated by quark degrees of freedom.

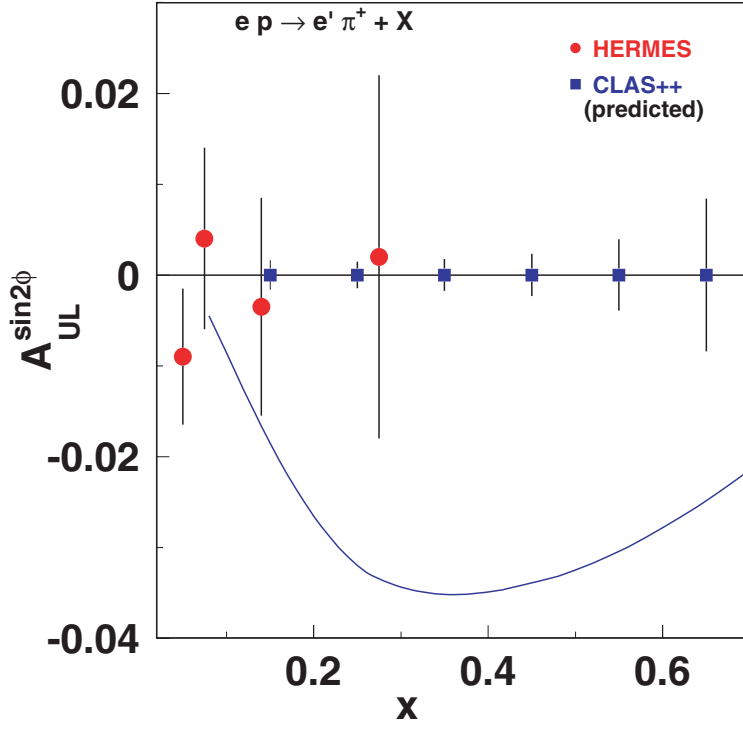


Figure 97: Target SSA: The shape of the $A_{UL}^{\sin 2\phi}(x)$ measured with longitudinally polarized target depend only on the ratio of the TMD distribution h_{1L}^\perp and f_1 , providing a direct access to h_{1L}^\perp . The curve is the theory prediction based on the Collins mechanism [Ef01]

Table 10: CLAS⁺⁺ Program Summary - Quark Transverse Momentum and Nucleon Orbital Angular Momentum in Semi-inclusive DIS

REACTIONS	OBSERVABLES	REQUIREMENTS
$\vec{e}p \rightarrow e\pi^+X$		
$\vec{e}p \rightarrow e\pi^0X$		
$\vec{e}p \rightarrow e\gamma X$		
$\vec{e}p \rightarrow eK^+X$		
$\vec{e}\vec{p} \rightarrow e\pi^+X$	PDF, TMD, \bar{d} , \bar{u}	Large t coverage
$\vec{e}\vec{p} \rightarrow e\pi^0X$	Frag. distribution fun.	Low $L \rightarrow$ large acc.
$\vec{e}\vec{p} \rightarrow e\gamma X$	Transversity	pol. targets
$\vec{e}\vec{p} \rightarrow eK^+X$		Improved Particle ID
$\vec{e}p^T \rightarrow e\pi^+X$		
$\vec{e}p^T \rightarrow e\pi^0X$		
$\vec{e}p^T \rightarrow e\gamma X$		
$\vec{e}p^T \rightarrow eK^+X$		

As such, the extended GDH integral provides a window on the transition from perturbative to non-perturbative regimes. The integral involves a sum over energy loss ν from the pion threshold to infinity, however, so there will always be a limit to the range over which the integral can be measured. Existing measurements at JLab have made accurate measurements of $I(Q^2)$ through the resonance region, but not much higher[Am02]. An upgraded JLab will be capable of measurements at much higher ν over a wide range of Q^2 values. Among the exciting new possibilities will be studying the high energy piece of the extended GDH integral.

The extended GDH integral can be written[Dr00]

$$I(Q^2) = \int_{\nu_0}^{\infty} \frac{d\nu}{\nu} (1-x) [\sigma_{1/2}(\nu, Q^2) - \sigma_{3/2}(\nu, Q^2)] = 2 \int_{\nu_0}^{\infty} \frac{d\nu}{\nu} (1-x) \sigma'_{TT} \quad , \quad (48)$$

where $\sigma_{1/2(3/2)}(\nu, Q^2)$ is the total *virtual* photoabsorption cross section for the nucleon with a projection of $\frac{1}{2}$ ($\frac{3}{2}$) for the total spin along the direction of photon momentum, ν_0 is the pion production threshold, $x = Q^2/2M\nu$ is the Bjorken scaling variable, M is the mass of the nucleon, and σ'_{TT} is the transverse-transverse interference cross section. Stringent theoretical constraints make $I(Q^2)$ a quantity that can be used to test our understanding of hadronic structure. At $Q^2 = 0$, $I(Q^2)$ is anchored by the GDH sum rule[Ge66, Dr66]:

$$I(0) = -\frac{2\pi^2\alpha}{M^2}\kappa^2, \quad (49)$$

where α is the fine structure constant and κ is the nucleon's anomalous magnetic moment. At small values of $Q^2 > 0$, $I(Q^2)$ can be computed using chiral perturbation theory[Ji01, Be93a, Ji00, Be02d]. At high Q^2 , $I(Q^2)$ is related to the moments of the spin structure functions, and is thus constrained by various results from OPE techniques including the Bjorken sum rule[Bj66, El74]. The extended GDH integral can even be related to the forward virtual Compton amplitudes, thus establishing a true extended GDH sum rule[Ji01].

With the 12 GeV upgrade, an important door will be opened to new kinematic windows that, among other possibilities, will make accessible the high-energy piece of the extended GDH integral. Recent results from Mainz on the original GDH sum rule have made it clear that the high-energy piece of the integral is critical to convergence[Ah01]. We remark more generally that with the upgrade, high- ν low- Q^2 physics will become accessible, and the high-energy piece of the extended GDH integral may well be the first of a new class of measurements[Ba01]. The upgrade is thus very central to both GDH physics, as well as to exploring a kinematic regime that is certain to provide important new insights.

Quark-Hadron Duality While at present we cannot describe the structure and interactions of hadrons directly utilizing the quark and gluon degrees of freedom of QCD, we know that in principle it should just be a matter of convenience in choosing to describe a process in terms of quark-gluon or hadronic degrees of freedom. This fact is referred to as *quark-hadron duality*, and means that one can use either set of complete basis states to describe physical phenomena. At high energies,

where the interactions between quarks and gluons become weak and quarks can be considered asymptotically free, an efficient description of phenomena is afforded in terms of quarks; at low energies, where the effects of confinement make strongly-coupled QCD highly non-perturbative and the final state is guaranteed to be made of hadrons, it is more efficient to work in terms of collective degrees of freedom, the physical mesons and baryons. The duality between quark and hadron descriptions reflects the relationship between confinement and asymptotic freedom, and is intimately related to the nature of the transition from non-perturbative to perturbative QCD.

Although the duality between quark and hadron descriptions is formally exact in principle, how this reveals itself specifically in different physical processes and under different kinematical conditions is the key to understanding the consequences of QCD for hadronic structure. The phenomenon of duality is in fact quite general in nature and can be studied in a variety of processes, such as $e^+e^- \rightarrow$ hadrons, or semi-leptonic decays of heavy quarks. Duality in electron–nucleon scattering, historically called Bloom-Gilman duality, links the physics of resonance production to the physics of deep inelastic scaling.

It has been said that (short of the full solution of QCD) understanding and controlling the accuracy of the quark-hadron duality is one of the most important and challenging problems for QCD practitioners today [Sh01]. Jefferson Lab at 11 GeV is uniquely poised to provide a wealth of data which can accurately answer where duality works, in what structure functions, in what reactions, and at what kinematics. While duality has been well-verified for the proton F_2 structure function, significant progress can be made in a variety of experiments, for instance in the longitudinal and transverse separated unpolarized structure functions, on nucleons and in nuclei, in polarized structure functions, and in semi-inclusive reactions.

Measuring the complete set of unpolarized structure functions (F_L , F_1 , F_2 , R) in inclusive electron nucleon scattering requires a separation of the cross section into longitudinal and transverse strengths. The cleanest way to do this separation experimentally is via the Rosenbluth technique, where the cross section is measured at multiple values of ϵ , or relative longitudinal virtual photon polarization, for fixed x and Q^2 . The precision obtainable for measuring the longitudinal structure function depends on both the precision of the individual data points and the range in ϵ over which the measurements are made. Given the typical point-to-point systematic uncertainties on precision cross section measurements in Hall C of $\approx 1.2\%$, the minimum ϵ range required to perform a separation of the cross section is $\Delta\epsilon \approx 0.3$. Figure 98 shows the ϵ range verses Q^2 which is accessible at $x = 0.8$ for a maximum JLab beam energy of both 6 GeV (red squares) and 11 GeV (blue diamonds). For a 6 GeV beam, the measurement of separated structure functions is limited to $Q^2 < 6$ (GeV/c)², but with an 11 GeV beam this range can be doubled. In addition, with the higher beam energy, the precision possible for $4 < Q^2 < 6$ (GeV/c)² can be significantly improved due to the extended ϵ range which is opened up at the higher energy.

Figure 99 depicts the substantial kinematic range enhancement made possible by the SHMS spectrometer and the 11 GeV beam over a range in x . This data will serve a variety of purposes,

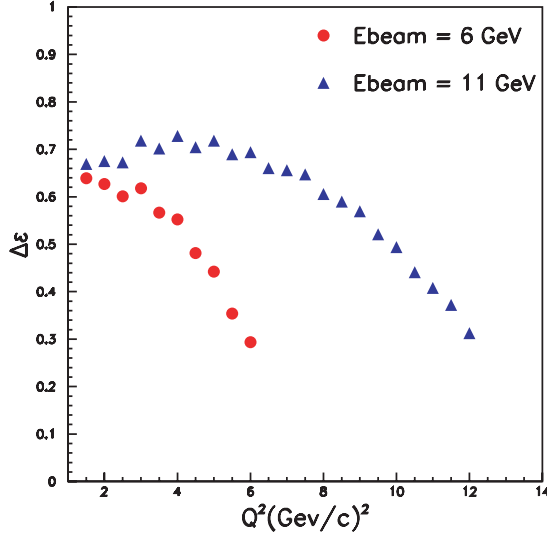


Figure 98: The $\Delta\epsilon$ range (left) accessible at $x = 0.8$ in Hall C as a function of Q^2 for beam energies of 6 GeV (red circles), and 11 GeV (blue diamonds).

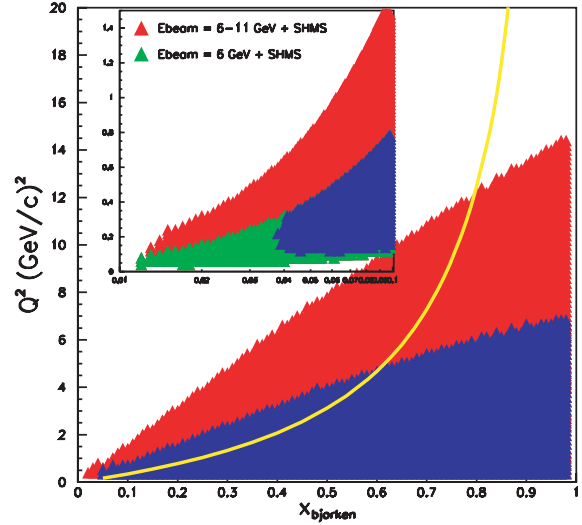


Figure 99: The (x, Q^2) ranges available with the SHMS and HMS spectrometers for $\Delta\epsilon$ ranges above 0.3. The yellow line represents fixed $W^2 = 4 \text{ GeV}^2$.

including addressing for instance long-standing questions regarding structure function behavior at low Q . Perhaps most importantly, the range of the data will allow for accurate moments of the structure functions to be obtained. To obtain a structure function moment, it is necessary to integrate over the full range in x at a fixed value of Q^2 . These moments are calculated in lattice QCD without higher twist contributions. If duality is shown to hold, the proposed structure function moment data may be directly compared to lattice QCD calculations.

Bloom-Gilman duality can be formulated in the language of an operator product expansion (OPE) of QCD moments of structure functions, in which contributions are organized according to powers of $1/Q^2$. The leading terms are associated with free quark scattering, and are responsible for the scaling of the structure function. The $1/Q^2$ terms involve interactions between quarks and gluons and hence reflect elements of confinement dynamics. Duality measurements have been explained in terms of a weak Q^2 dependence of the low moments of F_2 . This is interpreted within the OPE as indicating that the non-leading, $1/Q^2$ -suppressed, higher twist interaction terms do not play a major role even at low Q^2 ($\approx 1 \text{ GeV}^2$). It is this interpretation that facilitates comparison to lattice calculations.

Large x (resonance region) data become increasingly important for higher order moments. At $n=6$, for example, the resonance and large x region above $x = 0.7$ make up 70% of the Cornwall-Norton moment of F_2 at $Q^2 = 10 \text{ (GeV/c)}^2$. There exist little to no inclusive spectra in the resonance region above $Q^2 \approx 8 \text{ (GeV/c)}^2$, data which will be easily obtainable in Hall C at 11 GeV where cross sections can be measured to $Q^2 > 15 \text{ (GeV/c)}^2$ and L/T separated data will be available at least out to $Q^2 = 12 \text{ (GeV/c)}^2$. This latter can be used to obtain moments of all

unpolarized structure functions.

While the OPE formalism allows us to organize hadronic observables in terms of an asymptotic expansion, it does not tell us *a priori* why certain matrix elements are small or cancel. This can only be addressed via numerical solutions of QCD, or from experiment. Since the details of quark-hadron duality are process dependent, there is no reason to expect the accuracy to which it holds and the kinematic regime where it applies to be similar for different observables. In fact, there could be qualitative differences between the workings of duality in spin-dependent structure functions and spin-averaged ones, or for different hadrons — protons compared with neutrons, for instance.

Because of the absence of free neutron targets, deuterons are typically employed as effective neutron targets. However, at large x , theoretical uncertainties in the treatment of nuclear corrections has led to substantial ambiguity in extracted neutron structure functions. In particular, inclusion of Fermi motion and nuclear off-shell corrections in the deuteron can lead to F_2^n values which differ by 50% at $x = 0.75$. These differences are even greater if F_2^n is extracted on the basis of a nuclear density model. Therefore, while there exists a large body of data on nucleon structure functions over a wide range of x and Q^2 , the region above $x = 0.6$ is poorly explored. This is precisely both the regime necessary to duality studies and the regime which an 11 GeV beam at Jefferson Lab can optimally explore.

To overcome this problem, a program is proposed in Hall B to measure the inclusive electron scattering cross section on an almost free neutron using a novel recoil detector with low momentum threshold for protons and high rate capability. This detector will allow tagging of slow backward-moving spectator protons with momentum as low as 70 MeV/c in coincidence with the scattered electron in the reaction $D(e, e'p_s)X$. This will ensure that the electron scattering took place on an almost free neutron, with its initial four-momentum inferred from the observed spectator proton spectrum. This technique will allow for measurements in the neutron resonance region up to $x > 0.95$ and Q^2 14 (GeV/c)².

Close and Isgur refCloseIsgur suggest that the onset of duality may occur later for the neutron as higher W states are averaged than the proton. Furthermore, the existing lattice QCD calculations are for non-singlet only, and therefore the proton- neutron difference moment is the best entity for comparison (given the minimal or cancelling higher twists from duality) with experiment. In all, the proposed 11 GeV neutron measurements will provide an “acid test” for duality.

While the phenomenon of quark-hadron duality has been precisely determined in the F_2 structure function, it has not yet been established for the spin-dependent structure functions. The structure function g_1 , for example, is an intriguing case; the workings of duality may be more intricate for g_1 than for the spin-averaged structure functions. It is given by a difference of cross sections, which need not be positive. Unlike the unpolarized case, spin 1/2 and 3/2 resonances contribute with opposite phase. For fixed Q^2 values less than 1 (GeV/c)² the $\Delta(1232)$ resonance pulls the g_1 structure function from its large and negative value at $Q^2 = 0$ (where it is related

to the GDH sum rule) to a positive value at large Q^2 (where it is related to the deep inelastic sum rules such as the Bjorken sum rule). Yet, duality may yet be realized at low Q here and in other polarized structure functions if one averages over a complete set of resonances or performs a moment analysis. It is vital for our understanding of duality and its practical exploitation that both the spin and flavor dependence of duality be established and carefully quantified empirically. There are robust programs of spin structure function measurements proposed for Halls A, B, and C at 11 GeV, which will provide the extensive kinematic range necessary to precise quark-hadron duality tests.

It is important to point out that a revolutionary application of duality, if one understands the workings of the resonance—deep-inelastic interplay, would be to allow access to the region of very high x , which has not been possible in any other experiment. The region of $x \approx 1$ is an important testing ground for mechanisms of spin-flavor symmetry breaking in the valence quark distributions of the nucleon. In addition, with nuclear targets it would permit measurement of the nuclear medium modification of the nucleon structure function (nuclear EMC effect) at large x , where the deviation from unity of the ratio of nuclear to nucleon structure functions is largest, and sensitivity to different nuclear structure models greatest.

While the phenomenon of duality in inclusive scattering is under investigation, duality in the related case of semi-inclusive meson electroproduction has not been experimentally tested. Here, the reaction is typified by $\gamma + p \rightarrow \pi + X$, where the photon may be real or virtual. One can substitute a pion for a kaon, with a loss in rate of order 10. The interesting kinematic region for this purpose is one where the pion is directly produced at short range and exits the reaction in kinematic isolation from other exiting particles. The cross section for hard pion photoproduction can be written as a kinematic factor times a scaling function, where the latter is a function that in general depends on several variables but in the limit of large t and large m_X depends only on the variable x (up to logarithmic corrections). A goal here is to see what happens at smaller recoiling mass m_X , particularly in the resonance region. The scaling curve will become bumpy at low m_X , and we may ask, Will the resonances averaged over their own width reproduce the scaling curve already (by that time) established? Will the resonance peak to background ratio remain constant for a given resonance as $|t|$ increases?

The scaling region where m_X is large and direct pion production is dominant must be defined. One problem when the energy or transverse momentum is not high is a background coming from soft processes, which can be estimated using vector meson dominance (VMD) ideas. One can reduce the VMD background by having the photon off shell. For an 11 GeV incoming beam, preliminary estimates based on earlier work indicate that, with photons spacelike by 1 GeV², there is a significant scaling region with m_X between 2 and 3 GeV and with direct pion production dominating both fragmentation or VMD processes. There is also a resonance region with m_X between 1 and 2 GeV. Thus, an 11 GeV beam in Hall C, using the HMS / SHMS for electron and pion identification in coincidence, would undeniably allow this category of semi-inclusive duality

experiment to be performed.

Semi-inclusive deep inelastic scattering in parallel kinematics can also be measured. Here, a parton exits the fundamental reaction, and then at some distance fragments into a jet of hadrons, one of which is the observed pion. This is in contrast to the process described above, where, at very high transverse momentum, short-range direct production dominates. Here again duality would manifest itself with an observed scaling in the meson plus resonance final state. Assuming one is in a kinematics region that mimics single-quark scattering, in analogy with the inclusive scattering case, the question here is whether the remaining part of the process can be described in terms of a process where the struck quark hadronizes into the detected meson. Assuming such a factorization approach, where the cross section decomposes into a part, $f_i(x, Q^2)$, dependent on the photon-quark interaction, and another part described by the quark fragmentation functions $D_{q_i}^h(z, Q^2)$ (or the probabilities that a quark of flavor q_i hadronizes into a hadron h). This approach is strictly valid at asymptotic energies only, as at low energies there may not be clear separation of target and current fragmentation regions. However, as in the inclusive case where the nucleon resonances average at low energies to the scaling curve, the nucleon resonances remaining in the final state after having produced a fast meson may average to the fragmentation function.

The importance of understanding the onset of factorization for our understanding of the flavor content of the nucleon can not be underestimated. Should factorization (and duality) hold at JLab energies, unprecedented spin-flavor decomposition of the nucleon will become possible.

2.C The Physics of Nuclei

A great deal of nuclear properties and reactions over a wide energy range — from the few keV of astrophysical relevance to the MeV regime of nuclear spectra to the tens to hundreds of MeV measured in nuclear response experiments — can be quantitatively understood by describing nuclei as assemblies of individual nucleons interacting among themselves via effective interactions.

The dominant two-body interaction has a component at large inter-nucleon distances (≥ 2 fm) due to pion exchange, which is theoretically well understood. The main feature of this one-pion-exchange component is its tensor character, which leads to a strong coupling between the nucleons' spatial and spin degrees of freedom. Indeed, these spin-space correlations make nuclei markedly different from other systems where the dominant interaction is independent of the particles' internal degrees of freedom (spin and isospin), such as the Coulomb interaction in atoms and molecules or the van der Waals interaction in liquid Helium. At short inter-nucleon distances, the two-body interaction is presumably influenced by heavy-meson and quark-exchange mechanisms, and the excitation of nucleon resonances. It is, in fact, poorly understood, although it is well constrained phenomenologically, at least below the pion production threshold, by the large body of pp and np elastic scattering data. It is predominantly characterized by a strong repulsion.

The interplay between these two outstanding aspects of the nucleon-nucleon interaction—its short-range repulsion and long-range tensor character—have profound consequences for the spatial and spin structure of nuclei [Fo96]. For example, the deuteron, the simplest nucleus consisting of a proton and neutron bound together, has a toroidal shape when the proton’s and neutron’s spins are opposite, and a dumbbell shape when their spins are aligned. This picture of the deuteron has been confirmed experimentally, in its broad outlines, by the recent measurement of the deuteron tensor polarization at Jefferson Lab [Ab00].

These short-range and tensor correlations are reflected in many nuclear properties. For example, the density distributions in nuclei of two-nucleon states with deuteron-like quantum numbers are very small at small inter-nucleon separations and exhibit strong anisotropies depending on the relative orientation of the two nucleons’ spins; in the region $r \leq 2$ fm, they are found to differ from those in the deuteron only by an overall scale factor depending on the mass number of the nucleus (e.g. [Fo96]). Another example of the impact of correlations is the increase in the relative probability of finding, within the nucleus, a nucleon with very large momenta.

As mentioned above, the nucleon-nucleon interaction is mediated at large distances by pion exchange. There were attempts to describe the nucleon-nucleon interaction at short and intermediate distances by an exchange of heavier (vector) mesons, with phenomenologically determined couplings and short-range cut-offs. Although this method described some set of experimental data, the paradox is in the fact that QCD justifies only the existence of pseudoscalar (Goldstone) meson exchange as a result of spontaneously broken chiral symmetry of the QCD Lagrangian.

While the description of nuclei based on nucleon-meson picture outlined above provides a description of nuclear properties at average internucleon distances in nuclei, the lack of the knowledge of the strong interaction dynamics at short and intermediate distances generates several questions that need to be answered:

- To what extent is the quark substructure of nucleons and mesons modified in the nuclear medium?
- Down to what distance scale does the short-range structure of nuclei implied by the interactions based on the nucleon-meson degrees of freedom remain valid?
- How does the transition from the nucleon-meson to the quark-gluon based description of nuclei occur and what are its signatures?

A large portion of the experimental program of the 12 GeV upgrade is aimed at an understanding of the structure of isolated hadrons through a comprehensive study of their form factors, valence quark distribution functions, and generalized parton distribution functions. The 12 GeV upgrade will also provide unique opportunities for the investigation of possible modifications of this structure in the nuclear medium and the identification of the QCD mechanisms responsible for

these modifications, through studies of the phenomenon of color transparency in exclusive processes, color van der Waals-type interactions in J/ψ -meson photoproduction, and quark propagation and hadronization in the nuclear medium.

Our current knowledge of nuclear structure and reactions in terms of interactions and rearrangements of unperturbed nucleons, as succinctly outlined above, has been derived by probing nuclei “gently”, namely by measuring their response to hadronic and electroweak probes at low and moderate energies. However, an obvious question to ask is what happens when very high energies (comparable to or larger than the nucleon mass) are transferred to a nucleus and when nucleons are emitted at large angles. This must involve short-range mechanisms where nucleons overlap and where interactions between their constituents become relevant—the regime of short-range correlations. One expects that, in this regime, the notion of meson exchanges breaks down and direct constituent interactions like quark exchanges between nucleons, or “kneading” of the constituents of bound nucleons, becomes important. Clearly, the distance scale at which this occurs and the dynamical mechanisms responsible for short-range correlations need to be identified experimentally.

Finally, the hadron to parton transition region is another interesting and important open question in nuclear physics. Low energy nuclear physics has been described successfully using effective interactions among nucleons, i.e. in terms of hadronic degrees of freedom. On the other hand, at sufficiently high energy, perturbative QCD (pQCD) describes hadronic reactions in terms of quark and gluon degrees of freedom. Very little is known about the transition between these two regimes, in particular there are no clear indications from theory as to the energy range in which it should occur. Thus it must be mapped out by experiment.

An important search for this elusive transition region will be carried out with the 12 GeV Upgrade envisioned for Jefferson Lab. The strategy outlined below is to search for it in the simplest systems, i.e. in the pion and nucleon, since these are the hadronic building blocks of nuclei at low energy, and in the deuteron and helium isotopes, since these nuclei are particularly amenable to theoretical interpretation. Some proposed signals for the transition region are observation of scaling, hadron helicity conservation, color transparency and nuclear filtering. The proposed high-current 12-GeV electron beam coupled with relatively large acceptance detectors will be essential tools in searching for these exotic effects.

2.C.1 Hadron Structure in the Nuclear Medium

One of the key goals of modern nuclear physics is to connect the properties of hadrons to their underlying degrees of freedom. Hadrons are bound states of quarks and gluons, whose interactions are described by QCD. While QCD is convincing in the description of quarks interacting weakly at short distances (perturbative QCD) and standard meson-nucleon models are successful in reproducing the overall picture of hadrons interacting at large distances, our understanding of the connection between these regimes is extremely limited. While QCD is well established in

the perturbative regime, properties of hadrons cannot be calculated perturbatively. Lattice QCD (non-relativistic) allows calculations of simple bound systems and is making significant progress in providing glimpses of the nucleon structure, but we are far from being able to calculate more complicated systems (e.g. nuclei or even nucleons) or the interactions of hadrons in terms of the underlying strong interaction of quarks and gluons. What we do know is that QCD leads to confinement of the fundamental constituents within hadrons, and that it is possible to describe nuclear structure in terms of these effective hadronic degrees of freedom at least in the limited energy range explored so far at Jefferson Lab.

As described above, the 12 GeV upgrade will allow us to probe in great detail the structure of nuclei, both in terms of the meson-nucleon model and the underlying quark structure. However, with the upgrade it also becomes possible to use the nucleus itself as a laboratory to study some of the central features of QCD which do not appear in traditional hadronic descriptions of nuclei. Studies of the strong interaction at short distance scales, where the meson-exchange model should break down, can help us understand how hadronic interactions are built up from the underlying interactions of quarks. Modification of nucleon structure as we approach the phase transition connected to chiral restoration and deconfinement at high densities will allow us to start mapping out the transition from hadronic degrees of freedom to the underlying quark degrees of freedom in the intermediate region between confinement and asymptotic freedom. We can also look for color transparency, a prediction of QCD that is related to the underlying color degrees of freedom, which is absent in traditional nuclear physics models.

In addition, with the energy upgrade we will cross the charm production threshold (8.3 GeV on free nucleons). The large mass of the charmed quark guarantees a perturbative treatment of its interaction with nuclear matter which may reveal 'exotic configurations' at short distances: J/ψ -N or J/ψ -A bound or quasi-bound states, as well as multi-quark, gluonic, or hidden color correlations in nuclei. The study of threshold and sub-threshold J/ψ production will also allow us to probe the creation mechanism and hadronic interactions of an exotic, intrinsically small-sized hadron. This will allow us to study the interaction of a small color dipole object, providing yet another window on the microscopic (QCD) origins of hadronic interactions. Finally, because of the lack of c -quarks in nucleons, the production is dominated by multi-gluon exchanges, allowing us to access the Van der Waals part of the color interaction.

While these may appear to be largely unrelated topics, they all use the nuclear medium to look for effects absent in purely hadronic models of nuclear physics to establish QCD as the underlying theory of nuclear physics. They also give additional insight into the behavior of QCD in the non-perturbative regime. Currently, we study the non-perturbative behavior using effective degrees of freedom in QCD-inspired models and compare the predictions of these models to our knowledge of hadronic structure. As in the search for hybrid mesons, the goal is to probe the structure and interactions of new 'exotic' (non-hadronic) bound states of QCD to give us new windows on the non-perturbative behavior. The ultimate goal is to answer the fundamental question: How are the

structure and interactions of hadrons built up from their underlying constituents?

Nuclear Matter at High Densities High energy studies of hadrons in the nuclear medium will provide important opportunities to study the structure of nuclear matter at high density and characterize the nucleon-nucleon interaction at sub-fermi separations. The proton electromagnetic radius is ~ 0.86 fm, and in the ground state of infinite nuclear matter the average spacing of nucleons is ~ 1.7 fm. In dense nuclei, nucleons are closely packed and nearly overlapping. As the nucleons are not at rest, and in fact have strong interactions that generate significant momenta, there will be fluctuations in the nucleon separations. Thus, the nucleus is a natural place to investigate several questions regarding nuclear structure at high densities:

- What happens during the brief time intervals when two or more nucleons overlap in space?
- What is the mechanism of the exchange forces in sub-fermi distances? Can one continue to account for the interactions using meson-exchanges or will explicit quark-exchange forces start to play a dominant role?
- Does new physics emerge in these states where the densities can be several times the standard nuclear density as one approaches the phase transition from hadronic to quark matter?

If there is some modification to the confinement for overlapping nucleons, then a nucleus should deviate from a collection of closely packed nucleons. These deviations should increase for heavier nuclei, where the average density is larger and where there should be a larger component of overlapping nucleons. This should manifest itself in a density-dependence of the nucleon, or nuclear, structure beyond those predicted in meson-nucleon models. Such density-dependent effects have been seen in the past and these studies can be extended with the energy upgrade, in order to better understand their origins. More significantly, the upgrade will allow a new avenue of investigation into the behavior of matter at high densities. If we can isolate high density fluctuations in nuclei, we can probe these high density configurations, rather than just measuring the influence of this small component of the nuclear wavefunction on the overall structure of nuclei.

Investigating these questions will help us address the more general question of what is the role of quantum chromodynamics in the microscopic structure of nuclei. Figure 100 shows the phase diagram for hadronic matter. The high-density configurations in nuclei can have instantaneous densities several times higher than ordinary nuclear matter. Such densities approach the phase transition to a quark-gluon plasma, and effects from the onset of deconfinement and chiral restoration may significantly modify hadronic structure. These studies of high-density matter will provide complementary information to RHIC studies of the same phase transition at high temperature. In addition, these high-density fluctuations are the only forms of super-dense matter accessible in terrestrial laboratories, and what we learn in nuclei may provide additional insight into matter at similar densities in neutron stars and other compact astronomical objects.

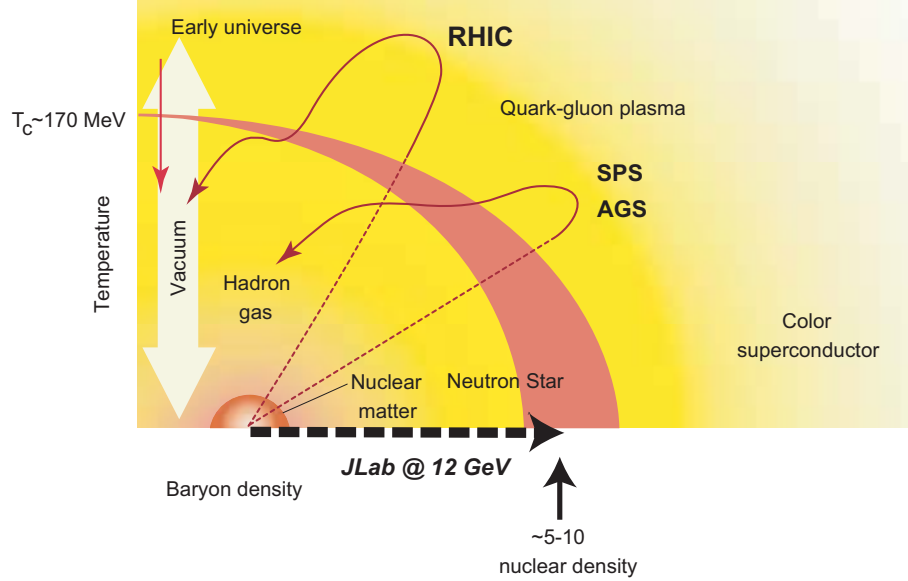


Figure 100: Phase diagram for hadronic matter.

Modification to Hadron Structure in Nuclei The EMC collaboration first measured the nuclear dependence of the F_2 structure function by comparing DIS scattering from heavy nuclei to deuterium. While these and subsequent measurements provided a clear observation of density-dependence to nuclear structure, there is not yet an accepted explanation of the effect. Some have tried to explain the effect within meson-nucleon models while others require modification to the hadronic structure. The exact origin of the nuclear dependence of the structure function is not known, although recent works [Sm02] indicate that a non-hadronic component is required to explain the data.

The shape (x -dependence) of the heavy nucleus to deuterium ratio is independent of A and fairly well known for heavy nuclei, while the magnitude of the modification depends on the nucleus, and can be described in terms of either an A - or ρ -dependence. With the 12 GeV upgrade, Jefferson Lab can improve data at large x and in light nuclei. Data on ^3He and ^4He will allow us to determine if the EMC effect scales with A or with ρ , since while they are both very light nuclei, ^4He has an anomalously large density ($\rho_{^4\text{He}} \approx \rho_{^{12}\text{C}}$). If the EMC effect is related to a two-body effect (e.g. modification to nucleon structure in overlapping nucleons), then the EMC effect may have a very different x -dependence in few-body nuclei than in heavy nuclei [Sm99, Be99]. Measuring the EMC effect in light nuclei, especially at large x , will clearly differentiate such models from those which have a fixed x -dependence.

One other possibility is to determine the EMC ratio for the separated structure functions F_1 and F_2 . While existing DIS data show no nuclear dependence to $R = \sigma_L/\sigma_T$, the uncertainties are too large to determine if the separated structure functions might have different nuclear dependence, especially in the region where the EMC effect is large. While coverage in the DIS region is limited for separated structure functions, coverage to larger x is possible in the resonance region. Even

with 4 GeV beam, we see that the nuclear dependence in the resonance region (for $Q^2 \gtrsim 4 \text{ GeV}^2$) is identical to the EMC effect observed in the DIS region. At larger beam energies, any deviation from this behavior due to the (much smaller) resonance contributions should be greatly reduced. The difficulty may be in extending the measurements to adequately large Q^2 , as the ratio of σ_L/σ_T is expected to become quite small at large Q^2 .

High-Density Configurations in Nuclei As discussed earlier, scattering from nuclei at $x > 1$ can provide a great deal of information about the high momentum components of the nuclear wave function which are sensitive to short-range correlations (SRC's) in the nucleus. These correlated nucleons are an important part of nuclear structure and represent local high-density nuclear configurations. The minimum separation of the nucleons is determined by the short-range repulsive core of the N-N potential (at $\sim 0.4 \text{ fm}$). By measuring at the highest Q^2 values possible, we can isolate and probe the quark structure of these high-density configurations. This will allow us to look for new physics at high matter density (several times nuclear matter densities in the region where two nucleons overlap). At high enough densities, as at high temperatures, hadrons should be deconfined and hadronic matter undergoes a phase transition to a quark-gluon plasma. While these high-density fluctuations in nuclei will not lead to deconfinement, the structure of hadrons may be dramatically changed during the brief periods when the nucleons have significant overlap. The observations of the EMC effect as well as more recent measurements that indicate the form factors of a nucleon are modified [St02] when in a bound nucleus, already hint that confinement may be weakened at densities found inside of a nucleus. By probing the quark structure of correlated nucleons, we can look directly for modification to hadron structure at high density.

The energy upgrade will allow us to expand the Q^2 range for inclusive scattering at $x > 1$. This provides access to the DIS regime, even for $x > 1$, allowing us to probe the internal structure of two-nucleon correlations. A measurement in the DIS regime at $x > 1$ would lead to a determination of the distributions of super-fast quarks in nuclei, where the momentum carried by the struck quark is greater than what one would expect for an entire nucleon. These quark distributions are related to the quark structure of the two-nucleon correlations which dominate for $x \gtrsim 1.1$ and large Q^2 . The EMC effect demonstrates that the quark structure of a nucleus is more than just a convolution of the quark structure of its nucleons. If this comes from density-dependent modifications to nucleon structure, then similar, but much larger, effects should be seen when one examines the quark distributions at large x , where the strength comes almost entirely from pairs of overlapping nucleons (Fig 117). The x -dependence from a convolution of the nucleon momentum distribution with the nucleon parton distribution functions will be very different from the quark distribution (*e.g.* 6-quark bags or nucleon deformations in the region of overlap). Such an exotic configuration would allow the quarks in the two nucleons to share momentum directly, rather than sharing momentum just by nucleon interactions. The direct interaction of quarks in the two nucleons will lead to a dramatically increased probability of finding quarks at $x > 1$, and such an observation will give a clear indication of deviations from a purely hadronic picture of nuclear structure.

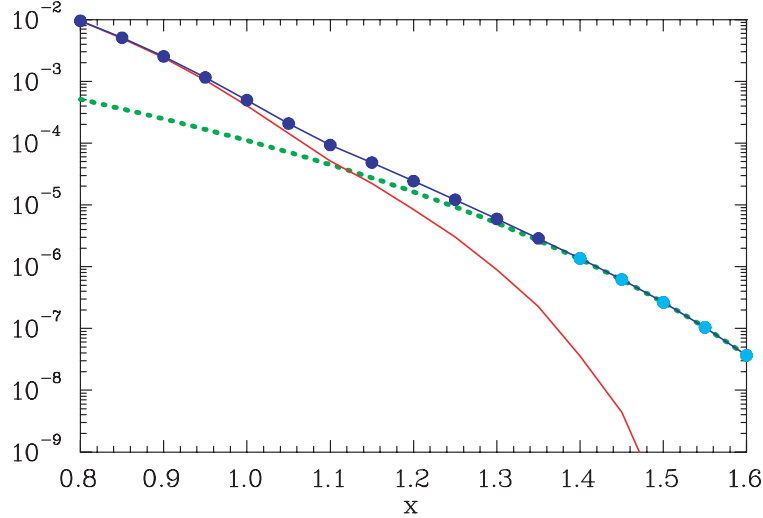


Figure 101: Distribution of super-fast quarks for deuteron assuming just two nucleons (red curve), or assuming a 5% contribution from a 6-quark bag (blue line).

There is little data available for structure functions of nuclei at $x > 1$. Measurements of muon scattering from Iron [Be94] have only upper limits above $x = 1.1$, and show a rapid falloff in the structure function near $x = 1$ ($F_2(x) \propto \exp(-16.5x)$). Measurements of neutrino scattering from Carbon [Va00] also have a limited x range ($x < 1.2$), but indicate significantly more strength at large x ($F_2(x) \propto \exp(-8.3x)$). With the increase in Q^2 possible with the JLab energy upgrade, high precision measurements of the structure function can be made over a wide range in x , allowing us to cleanly map out the distribution of super-fast quarks. The energy upgrade will allow us to reach $Q^2 > 20 \text{ GeV}^2$, where the inelastic contributions dominate the cross section up to $x = 1.4$. Figure 101 shows the difference in the distribution of super-fast quarks in deuterium in the presence of a small (5%) six-quark bag component to the deuteron. Measurements on deuterium will allow us to look for deviations from the purely hadronic model, without the need to model the effects of multi-nucleon correlations. Measurements on heavier nuclei (*e.g.* Carbon) will have much larger signals from two-nucleon SRC's, which can be separated from the effects of multi-nucleon correlations, as described in section 2.C.2.

The second step in understanding the structure of high-density configurations will be to study tagged structure functions [Fr81, Fr88, Ci93] in order to compare directly the parton structure of the bound and free nucleon. This will start with the $e + {}^2\text{H} \rightarrow e + \text{backward nucleon} + X$ reaction in the kinematics where the momentum fraction carried by the struck quark in the moving nucleon (\tilde{x}) is sensitive to the EMC effect [$0.3 \leq \tilde{x} \leq 0.7$ (CEBAF at 11 GeV covers all of this region; see Fig. 102)] and continue to a similar reaction with ${}^3\text{He}$ and the tagging of two backward nucleons to consider deformations in the three-nucleon correlations. In contrast to the case of the inclusive EMC effect, different models predict [Fr88, Ca91, Ca95, Me97] a qualitatively different dependence of the experimental results on the modifications of the bound nucleon wavefunction, which range

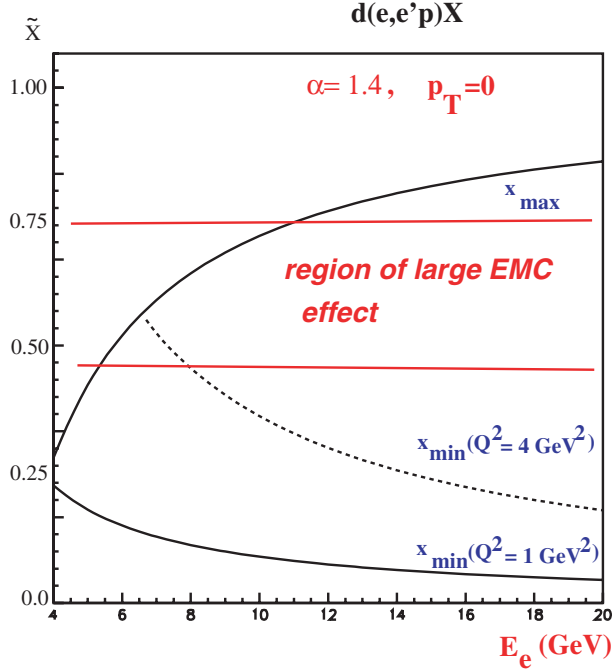


Figure 102: The scaling window for $\alpha = 1.4$, where α is the light-cone fraction of the knocked-out nucleon. The upper curve is defined by the requirement that the mass of the produced final hadronic state $W \geq 2$ GeV.

from a complete absence of modification to an effect comparable to the EMC effect for heavy nuclei in the color screening model, for tagged nucleon momenta $p_N \geq 300$ MeV/c. If the EMC effect for the bound nucleon is observed, one would be able to check whether the theoretical account of such deformations together with a realistic light-cone nucleon density (measured in the $A(e, e'p)$ processes) would reproduce $F_{2A}(x, Q^2)/F_{2D}(x, Q^2) > 1$ in the scaling region.

The two-step strategy described above requires related studies that are important to cross-check all aspects of these studies:

- *Investigation of the reaction dynamics at $Q^2 \geq 4$ GeV².* The reaction dynamics of $(e, e'p)$ at GeV energy and momentum transfers have only just begun due to limited beam energy. These dynamic will be quite different from low energy, due to the diffractive nature of the high-energy NN interaction and the role of relativity. With the energy upgrade, one can study, for example, the reaction $e + {}^2H \rightarrow e + p + n$ in parallel kinematics for recoil nucleon momenta $p_N = 400 - 500$ MeV/c up to $Q^2 \approx 8$ GeV². A study of this type is essential for our understanding of the baseline color transparency calculations and of short-range structures in the nucleus.
- *A test of the binding models of the EMC effect,* by measuring the position of the quasielastic peak at large Q^2 . In these models, a shift of the nucleon spectral function to $\alpha < 1$ is expected, leading to a significant asymmetry in the cross section of the $(e, e'p)$ process in

parallel kinematics near the quasielastic peak [Fr92].

- *Studies of special modes of deuteron breakup at high Q^2 using the upgraded CLAS* would be sensitive to meson-exchange currents, *e.g.*, $e + {}^2\text{H} \rightarrow$ two forward protons + leading π^- , and processes such as production of backward Δ 's off the deuteron and ${}^3\text{He}$ that are especially sensitive to the presence of Δ -isobar-like color-singlet clusters and six-quark clusters.
- *Probing quark degrees of freedom in large-angle electrodisintegration of the deuteron* will be a natural extension of the CEBAF photodisintegration experiment [Bo98]. This was the first case of a high-energy nuclear physics reaction for which descriptions based on the quark degrees of freedom and on the assumption that *the short-range NN forces are due to quark exchange* quantitatively agree with the data, while all theoretical descriptions invoking hadronic degrees of freedom qualitatively disagree with the data [Fr00]. Study of deuteron electrodisintegration and similar exclusive real photon reactions at high energies will allow a significant extension of the range of the observed energy scaling. A crucial prediction of the quark-exchange picture is that for a wide range of photon virtualities the cross section should depend on the photon virtuality as the point-like Mott cross section.

In summary, the increase of electron energy to 11 GeV will significantly expand the possibilities for systematic studies of high-momentum-transfer processes with nuclei. The ultimate result will be a detailed understanding of the hadronic and quark degrees of freedom in nuclear matter at extremely high densities.

Color Transparency While color transparency (CT) as a direct consequence of QCD in hard exclusive processes is not questionable, its applicability and its manifestation in specific processes remain open problems. Indeed, a non-ambiguous evidence of CT not only requires the selection of a small size configuration but also a clear signature of the subsequent reduced interaction. The main parameter that governs the CT phenomenon is the momentum transfer of the virtual photon that controls the transverse size and part of the coherence length of the mini-hadron. The latter corresponds to the distance required for the mini-hadron to evolve from its minimal valence state toward its asymptotic wave function. There are several ways to look for CT effects: $A(e,e'p)$ reactions in both heavy and few-body nuclei, and meson electro- and photo-production.

Color Transparency in $A(e,e'p)$ The study of quasiexclusive hard reactions $A(p,2p)$ and $A(e,e'p)$ can shed light on the range of Q^2 's necessary for the wavefunctions of nucleons to be dominated by point-like configurations (PLC) [Br82, Mu82]. If Q^2 is large enough, one expects both the scattered particle and the projectile (for $(p,2p)$) to travel through the nucleus in point-like configurations. A straightforward way to look for CT is to determine the transparency ratio $T = \sigma_{exp}/\sigma_{PWIA}$ in $A(e,e'p)$ reactions as a function of Q^2 and various nuclei A . Experiments at SLAC [Ne95] and JLab [Ab98, Ga02] exclude sizable CT effects up to $Q^2 = 8.1 \text{ GeV}^2$. The 12 GeV

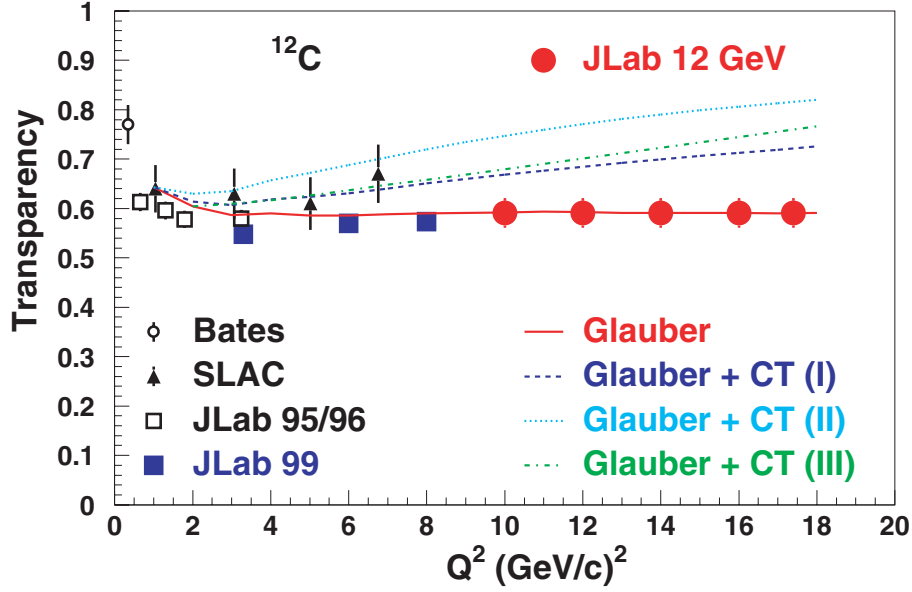


Figure 103: The Q^2 -dependence of nuclear transparency. The data are from Refs. [Ga92, Ne95, Ab98, Ga02], while the circles are projected uncertainties for a one week run at 12 GeV.

upgrade will improve the situation by more than doubling the accessible Q^2 region. This will allow measurements to be made where the CT predictions diverge appreciably from the predictions of conventional calculations. In addition, the Brookhaven (p,2p) data establish a definite increase in transparency for nucleon momenta above 7 GeV^2 . If this is a signature of CT, then $A(e,e'p)$ measurements at $Q^2 > 12 \text{ GeV}^2$, corresponding to comparable momenta of the ejected nucleon, would also be expected to show CT. Figure 103 shows both the present status and projected uncertainties of CT in the measurements feasible with 11 GeV beams.

Color Transparency in Few-Body Systems A more sensitive way to observe the onset of CT in nuclei, feasible only with higher beam energies, is to look for processes where the ejectile interacts with other nucleons after the interaction with the virtual photon [Fr91, Eg94, Fr95b, La98a]. A large portion of the $(e,e'p)$ cross section beyond $p_m \geq 300 \text{ MeV}/c$ originates from recoil nucleons with lower momenta rescattering. With the onset of CT, this rescattering should decrease as a function of increasing Q^2 , and produce a more significant effect than just measuring the transparency ratio T , even at low values of Q^2 . Another important advantage of studying this reaction process is that the effect can be studied even in the lightest nuclei ($^2\text{H}, ^3\text{He}, ^4\text{He}$) for which wave functions are known much better and the eikonal approximation which accounts for all orders of rescattering [Eg94, Fr95, La98a] can provide a reliable base line calculation.

A suitable measure of this effect can be studied in the $(e,e'p)$ reaction as a ratio R of the cross section in kinematics where this rescattering term is dominant ($p_{recoil} \sim 400 \text{ MeV}/c$) to the cross section in kinematics where single scattering is dominant ($p_{recoil} \leq 200 \text{ MeV}/c$) and Glauber screening is important. Figure 104 shows these regions clearly in the recent $^3\text{He}(e,e'p)d$ reaction

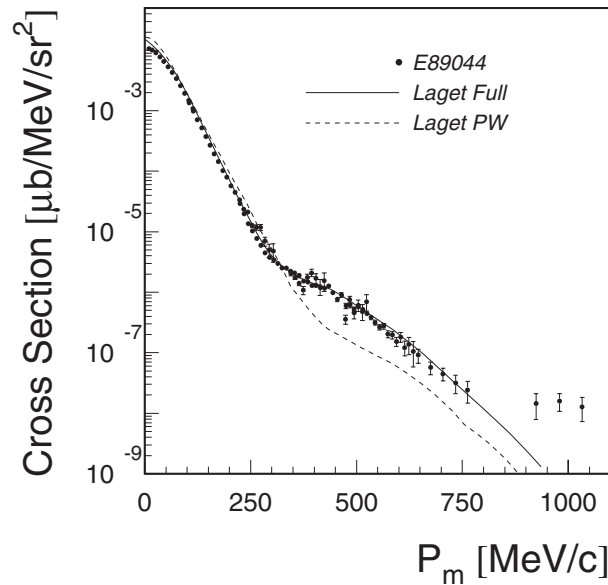


Figure 104: Data from the Hall A ${}^3\text{He}(e, e'p)d$ experiment [E89044] shown with the calculations of Jean-Marc Laget show that the region around 400 MeV/c is dominated by FSI.

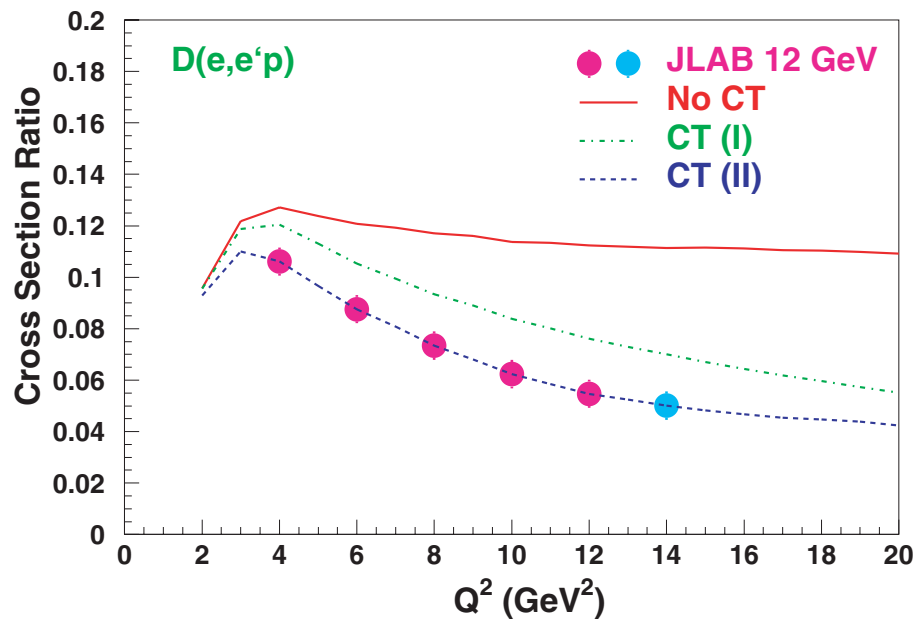


Figure 105: Ratio $R = \sigma(p_m = 400 \text{ MeV}/c)/\sigma(p_m = 200 \text{ MeV}/c)$ for $D(e, e'p)$ reaction. CT(I) and CT(II) corresponds to Color Transparency calculations with $\Delta M^2 = 0.7$ and 1.1 GeV^2 respectively in the QDM Model [Fa88, Sopc]

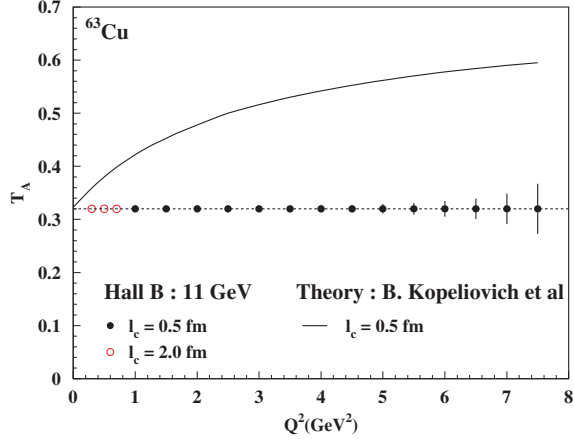


Figure 106: Projected uncertainties for a measurement of transparency in ρ -electroproduction in Hall B .

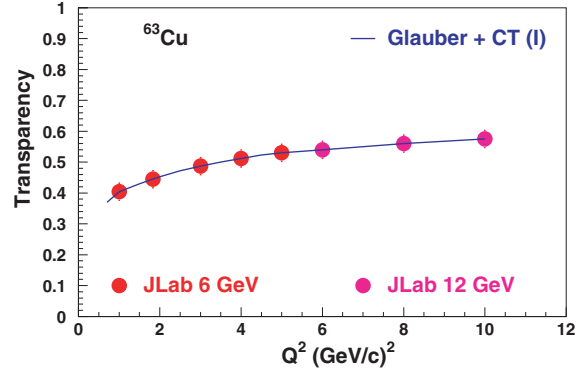


Figure 107: Projected uncertainties for measurement of transparency in pion electroproduction in Hall C.

cross section as a function of the missing momentum [E89044] for a low value of $Q^2 = 1.55 \text{ GeV}^2$. The predicted value of this ratio $R = \sigma(p = 400 \text{ MeV}/c)/\sigma(p = 200 \text{ MeV}/c)$ for the case of $D(e, e'p)$ and the effect of color transparency is quite dramatic even at low values of Q^2 (Fig. 105). In all cases, the CT effects are estimated within the quantum diffusion model (QDM) of Ref. [Fa88] utilizing two values for the expansion parameter $\Delta M^2 = 0.7$ and 1.1 GeV^2 , which characterize the time development of the PLC during the propagation in the nuclear medium. These two values of ΔM^2 give the upper and lower limit of CT predictions within the QDM model. The predicted signal is much larger than in the attenuation measurement, and by measuring the Q^2 -dependence of the *ratio*, uncertainties in the reaction mechanism become much less important.

Color Transparency in Meson Production Meson production should provide an even clearer process for observing CT phenomenon. Intuitively, one expects an earlier onset of CT for meson production, as it is much more probable to produce a small transverse size in a $q\bar{q}$ system than in a three quark system. Direct measurements of nuclear transparency can be performed with pion and rho-meson electroproduction, as well as pion photoproduction. As in the case of the direct measurements of nuclear transparency in proton knock-out reactions, the increased beam energy will allow for a significant increase in the momentum transfer of these reactions compared to the measurements that can be made with 6 GeV beams. Figures 106 and 107 show projected uncertainties for measurements of ρ and π electroproduction. Color transparency in pion photoproduction is also discussed in a later section, along with the closely related topic of nuclear filtering, whereby the formation of a small size hadron configuration reduces not only the interaction of pions as they traverse the nucleus, but also the long-distance amplitudes which may lead to oscillations in the pion photoproduction cross section.

With the availability of high energy and high intensity electron beams, one can combine the advantages of rescattering measurements with those of meson production. Such experiments will be less sensitive to the formation of the PLC and its subsequent evolution back to a normal hadron, and should allow the cleanest test for color transparency. Electroproduction of vector mesons off a deuteron in a fully exclusive reaction is one such reaction:

$$e + d \rightarrow e' + V + d' \quad (50)$$

where “ V ” is the ρ , ω , or ϕ vector meson. The electron, recoiling deuteron, and decay products of the vector meson are all detected in the final state.

Coherent production of vector mesons off deuterium can be described by single- and double-scattering mechanisms. In the single-scattering case, only one nucleon participates in the interaction and so the t -dependence will follow the deuteron form factor. In the double-scattering (rescattering) mechanism, dominant at $-t > 0.6 \text{ GeV}^2$, the photon interacts with one nucleon to form an intermediate hadronic state that subsequently rescatters from the second nucleon before forming the final state vector meson. This process has a harder t -dependence than the first one, and this is where evidence of CT will manifest itself.

The key point in the investigation of CT phenomena is measuring the re-interaction process at different Q^2 values. The reduction of the transverse size of the intermediate hadronic state with increasing Q^2 will lead to a diminished reinteraction, and thus a change in the t -dependence at high t . Differential cross sections will be measured at the same Q^2 and coherence length, $l_c = 2\nu/(m_V^2 + Q^2)$, but at different t values. At low $-t$, the single scattering process dominates, while at high $-t$, the rescattering dominates. The ratio of these cross sections, with and without the inclusion of CT effects, is plotted in Fig. 108. This ratio is sensitive to the effects of CT while being insensitive to systematic uncertainties.

The above series of attenuation and rescattering measurements for both protons and mesons will allow us to separate the necessary ingredients: formation of the small sized configuration, the reduced color interaction of these configurations, and the evolution of these exotic configurations back into ordinary hadrons. The observation of color transparency and characterization of the non-perturbative evolution of a mini-hadron to its physical size will lead to a better understanding of the dynamics of confinement.

J/ψ Photoproduction Near Threshold The threshold production of charmonium and open charm production opens up a new window into QCD dynamics; in particular, these reactions are sensitive to multiquark, gluonic and hidden color correlations in nucleons and nuclei. In contrast to diffractive charm production at high energy, which tests the behavior of the gluon structure functions at small x , charm production near threshold tests the structure of the target near $x = 1$ and its short-range behavior.

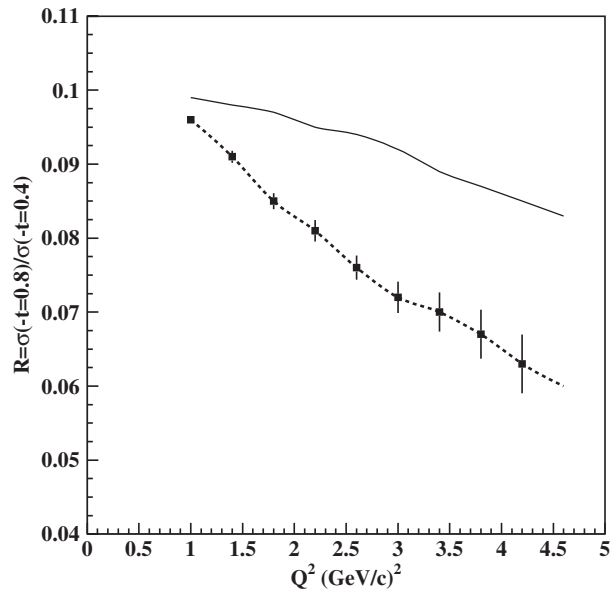


Figure 108: Projected uncertainties on the ratio of cross sections at transferred momenta $0.4 \text{ GeV}/c^2$ and $0.8 \text{ GeV}/c^2$ for 2000 hours of running on CLAS with 11 GeV beam. The solid curve assumes no color transparency effects, the dotted curve is with color coherent effect. Events in each point are integrated in the bins of $\Delta Q^2 = 0.4 \text{ GeV}/c^2$ and $\Delta l_c = 0.2$.

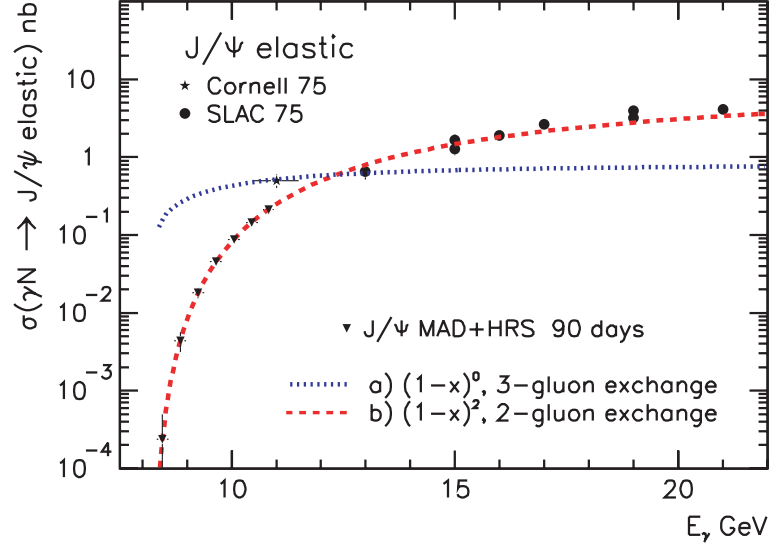


Figure 109: Variation of the cross sections of J/ψ photoproduction near threshold, for two or three gluon exchange mechanisms. The inverted triangles show the expected accuracy using the Hall A MAD and HRS spectrometers with 11 GeV beam.

This difference results from the kinematics of the reaction products. For J/ψ production on nucleon, the threshold energy is $E_\gamma = 8.20$ GeV, and due to the large mass of the charmed quark ($m_c \approx 1.5$ GeV) the $c\bar{c}$ fluctuation of the photon travels over the coherence length $l_c \cong 2E_\gamma/4m_c^2 = 0.36$ fm. The large mass of the charmed quark also imposes a small transverse size $r_\perp \sim 1/m_c = 0.13$ fm of this fluctuation as well as a small impact parameter $b \sim 1/m_c = 0.13$ fm. All five valence quarks (the two heavy charm quarks in the probe and the three light quarks in the target) must be in the same small interaction volume. As a consequence, all the quarks must be involved in the reaction mechanism. For nucleon targets, this implies that three-gluon exchange may take over two-gluon and one gluon exchange, and open the way to the study of correlations between valence quarks [Bro01]. As depicted in Fig. 109, such a conjecture is consistent with the limited data that are available [Ca75, Gi75, An77] on a nucleon target. Clearly higher energy beams from an upgraded CEBAF will allow a more comprehensive determination of the J/ψ photoproduction cross section between threshold and 12 GeV.

On few-body targets each exchanged gluon may couple to a colored quark cluster and reveal the hidden color part of the nuclear wave function, a domain of short-range nuclear physics where nucleons lose their identity. These hidden color configurations are predicted by the QCD evolution equations [Br83]. It is striking that in $\gamma d \rightarrow J/\psi pn$ the $|B_8\bar{B}_8\rangle$ hidden color state of the deuteron couples naturally by two gluons to the $J/\psi pn$ final state [La94] (see Fig. 110). Such a contribution may dominate subthreshold production, since the high momentum of the nucleon suppresses quasisfree mechanisms. The threshold for J/ψ production on deuterium is 5.65 GeV, while on heavy nuclei the threshold approaches 3.1 GeV, the J/ψ mass.

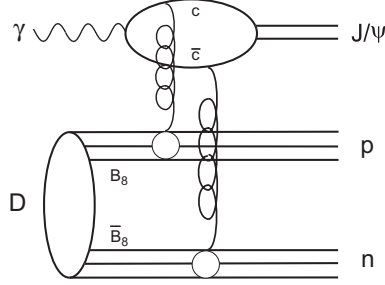


Figure 110: The simplest diagram to reveal hidden color state in deuterium [La94].

Even though the $c\bar{c}$ pair is created with rather high momentum at threshold, it may be possible to observe reactions where the pair is captured by the target nucleus, forming “nuclear-bound quarkonium” [Br90, Wa91]. This process should be enhanced in subthreshold reactions. There is no Pauli blocking for charm quarks in nuclei, and it has been estimated that there is a large attractive van der Waals potential binding the pair to the nucleus [Lu92]. The discovery of such qualitatively new states of matter would be a major achievement.

The formation length, l_F , over which the $c\bar{c}$ pair evolves into a J/ψ after its interaction with a nucleon, is given by:

$$l_F \cong \frac{2}{m_{\psi'} - m_{J/\psi}} \left[\frac{E_{J/\psi}}{2m_c} \right] \cong 0.22E_\gamma \quad (51)$$

Near threshold l_F is around 1 fm, closer to the size of the nucleon than the size of the nucleus. This is the ideal situation for determining the scattering cross section of a full sized charmed meson on a nucleon, in contrast to the situation at higher energies, where the cross section is sensitive to the interaction of a compact $c\bar{c}$ pair with the entire nucleus. The study of the A -dependence of the J/ψ photoproduction cross section at SLAC at 20 GeV [An77b] gave $\sigma_{J/\psi} = 3.5 \pm 0.8 \pm 0.5$ mb. Unfortunately the need to subtract a large calculated background and the lack of information on the J/ψ kinematics makes it impossible to disentangle coherent and incoherent photoproduction in this experiment. The study [Ge92] of hadron production gave $\sigma_{J/\psi} \approx 7$ mb. However, after correction [Hu98] for energy loss of the incoming hadron and for coherence effects this value went down to $\sigma_{J/\psi} \approx 3.6$ mb. On the theoretical side, QCD calculations [Kr99] predict that $\sigma_{J/\psi} \approx 0.3$ mb at 20 GeV, and that it falls rapidly as the energy is reduced. In contrast, a calculation by Brodsky [Br97] based on the van der Waals potential yielded $\sigma_{J/\psi} \approx 7$ mb at low energies.

This situation calls for a new measurement of J/ψ photoproduction on several nuclei for $E_\gamma \approx 10$ GeV, with a good identification and determination of the J/ψ momentum. The systematic error of such a measurement will be better than in the previous SLAC measurement [An77b]. The nuclear transparency $T = \sigma_{\gamma A}/(A \cdot \sigma_{\gamma N})$ and the expected statistical accuracy are given in Table 11.

Besides possible applications in connected domains (for instance, the knowledge of the J/ψ - N scattering in the search for signatures of Quark-Gluon plasma), all these studies select *gluonic*

Table 11: The values of nuclear transparencies for J/ψ propagation, calculated in the model used by the SLAC measurement [An77b], for 3 values of $\sigma_{\psi N}$. The last column presents the expected statistical error, $\delta\sigma_{\psi N}$ for a $\sigma_{\psi N}$ measurement at CEBAF using 11 GeV beam, assuming a statistical error of 3% for the yields on every target.

A	9	12	27	63	108	207	$\delta\sigma(\sigma_{\psi N})$, mb
T for $\sigma_{\psi N}=1.0$ mb	0.982	0.980	0.974	0.963	0.952	0.929	0.28
T for $\sigma_{\psi N}=3.5$ mb	0.938	0.931	0.908	0.870	0.833	0.751	0.24
T for $\sigma_{\psi N}=7.0$ mb	0.876	0.863	0.816	0.740	0.665	0.502	0.17

exchange mechanisms between hadrons or quark clusters. The observation of a gluonic potential between color neutral states is of utmost importance as it would open up the possibility to trace part of the nucleon-nucleon interaction at short range to such a color van der Waals force. Only the high intensity and duty factor of the beams that will be available from an upgraded CEBAF make it possible to realize the new experiments that are essential for the exploration of this frontier of our knowledge.

Space-Time Characteristics of Hadronization Due to the property of confinement, a struck quark in a hard process will evolve in space-time to produce multiple hadrons through the complex process of hadronization. This behavior is a unique distinctive of QCD. By studying the properties of the hadrons emerging from deep inelastic scattering (DIS) on a range of nuclei, important information on the characteristic time-distance scales of hadronization can be determined as a function of several variables.

The physical picture of hadronization in a nucleus begins with a hard interaction on a bound quark within the nuclear volume. This is illustrated in Fig. 111. For large Q^2 and ν the initial interaction is localized to a very small volume and results in an energetic quark propagating through the nuclear medium. Ultimately this quark emerges bound in a hadron, accompanied by other hadrons generated in the process. The time interval between the γ^*-q interaction and the hadron being fully reconstituted is often referred to as the *formation time*. If the formation time is much smaller than the nuclear transit time, then the hadron that carries the struck quark will strongly interact with the nuclear medium. This hadron will then be 'lost' in the sense that the event shifts to higher multiplicity and lower particle momenta relative to the same interaction on a smaller nucleus. If, on the other hand, the formation time is much longer than the nuclear transit time, then the formed hadron will not interact with the nuclear medium. In this way, hadron absorption by nuclei can be used to estimate the time scales of the hadronization process.

The observable that is used to quantify this absorption is the *hadronic multiplicity ratio* R_M^h . This quantity is defined as



Figure 111: Artist's concept of the hadronization process in the valence quark regime. In the upper right corner, a quark undergoes a hard interaction with a virtual photon; in the middle picture the struck quark separates rapidly from the other quarks, forming a region of high energy density in which several proto-hadrons begin to form; in the bottom left-hand corner the struck quark emerges as part of a newly-formed hadron. In the upper left corner of the figure, this process is visualized implanted in a nucleus; by varying the nuclear size, the distance scales involved can be probed, since the fully formed hadron will interact with the nuclear medium.

$$R_M^h = \left\{ \frac{N_h(z, \nu)}{N_e^{DIS}(\nu)} \right\}_A / \left\{ \frac{N_h(z, \nu)}{N_e^{DIS}(\nu)} \right\}_D \quad (52)$$

In this expression, N_h is the number of hadrons produced in DIS events and N_e^{DIS} is the number of associated DIS electrons. The numerator corresponds to target nucleus A, and the denominator corresponds to deuterium. ν is the energy transferred by the electron, and z is the hadron energy divided by ν ($0 < z < 1$). In the QCD-improved parton model, R_M^h is given by ratios of sums over products of the quark distribution functions with fragmentation functions.

There are several scientific issues surrounding the hadronization distance scale studies. An important example is the fundamental process of gluon emission. The present understanding of gluon emission by the propagating quark is that it occurs both in vacuum and within the nuclear medium; within the nuclear medium it is additionally stimulated by multiple scattering from the nuclear partons. The propagating quark loses energy as a result. In a hot nuclear medium an additional dynamic of thermally stimulated gluon absorption and emission comes into play, while this is irrelevant in the cold nuclear medium. At some point the propagating quark evolves into a hadron, and the copious production of gluons ceases. The balance between gluon emission and hadronization, and the relationships between the two, are not established theoretically or experimentally, and this is a major theme addressed by the measurements identified here. Most experimental efforts, as will be discussed below, have focused on formation of either pions or protons; the proposed JLab measurements will address a much broader spectrum of nearly twenty hadrons.

Exploratory studies of R_M^h have been carried out at HERMES using 12 and 27 GeV positron beams on nitrogen and krypton targets; the higher energy nitrogen data have been published to date [Air01, Nat02]. These studies have been interpreted as being dominated by hadronization, and characteristic formation times for negative and positive pions, and protons, have been derived. The HERMES nitrogen analysis employed a phenomenological formalism [Bi83] that characterizes the hadronization process by a single time constant, the formation length, which is the characteristic parameter of a decaying exponential $P_q(x_1 - x_2) = \exp[(x_1 - x_2)/\tau_f]$ representing the probability that the propagating object struck at coordinate x_1 is still a quark at coordinate x_2 . The probability that the object is a hadron is then $1 - P_q$. The propagating object interacts with a quark-nucleon cross section σ_q while it is a quark, and a hadron-nucleon cross section σ_h while it is a hadron. The ν - and z -dependence of τ_f is not known from a fundamental theory, and several have been proposed. The HERMES analysis tested three basic forms and was able to eliminate two of the three based on the observed z -dependence. Within the above phenomenological framework, the form that most closely represented their data was $\tau_f = c_h(1 - z)\nu$, where c_h is a constant depending on the hadron type. Figure 112 shows a schematic example of what the upgraded JLab would be able to measure.

While many assumptions necessarily go into such an analysis, the HERMES pioneering studies offer tantalizing hints concerning the nature of hadronization. There are still numerous outstanding

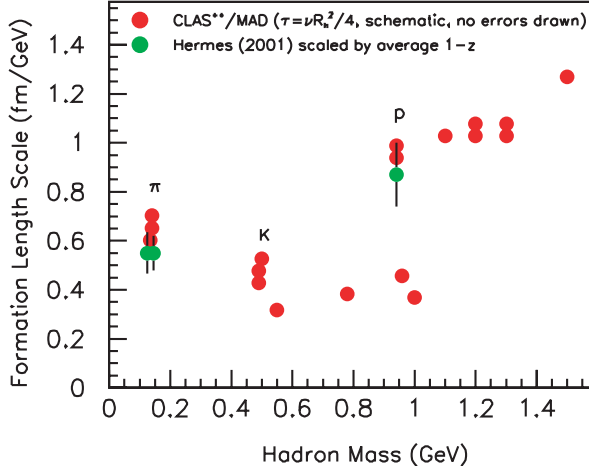


Figure 112: Schematic example of possible results for hadronization length scales. The meson band is in the lower half of the plot, the baryon band in the upper half.

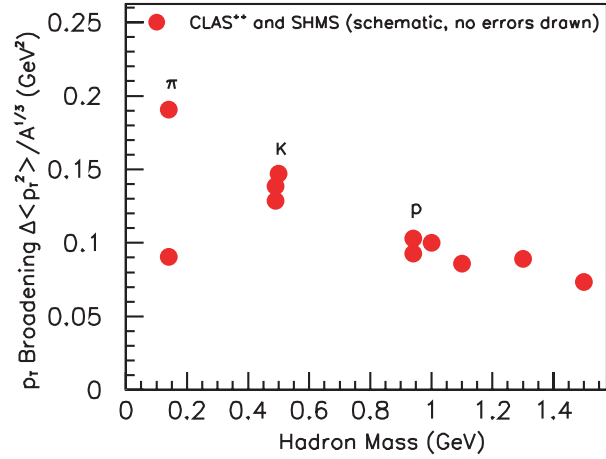


Figure 113: Schematic example of possible results for transverse momentum broadening. Many such plots will be available, in multivariable bins in, e.g., Q^2 , ν , z , helicity.

questions. For instance, is this a mass effect or a size effect? Is there contamination from knocked-out protons or pions rather than particles created through a fragmentation process? Are there other reaction mechanisms contaminating the event sample? What is the flavor dependence of the formation time? How realistic is the relatively simple picture of hadronization within the nucleus on which these analyses are based?

These questions can be well-addressed by an upgraded JLab in a natural extension to an approved 6 GeV measurement [E02104]. The limited information available on the Q^2 -dependence of R_M^h will be easily remedied by the high luminosity available after the upgrade. The issue concerning contamination from potentially knocked-out protons (or pions) can be addressed by studying particles of a similar mass which were not pre-existing in the nucleus, such as Λ particles or neutral kaons. The flavor and mass dependence can be further studied by using a wide array of particles that are known to be stable over a distance scale much larger than nuclear dimensions. Accessible hadrons include $\pi^{+,-,0}$, η , ω , η' , ϕ , $K^{+,-,0}$, p and \bar{p} , Λ and $\Lambda(1520)$, $\Sigma^{+,0}$, and $\Xi^{0,-}$. A quite impressive advance in understanding formation lengths can be attained by systematically studying the production of all of these particles for a series of nuclei, providing strong constraints on model calculations.

The hadrons that decay into multiple particles will be measured by CLAS⁺⁺. Measurements for the lowest-rate hadrons, or out to highest p_T or Q^2 , can be performed by the SHMS and MAD. Because of the high luminosity, the dependence on multiple variables can be studied even for the particles that have a low production cross section or for which the acceptance is small. The ability to carry out studies on a number of different particles will help to evaluate if this simple picture of hadronization within nuclei is adequate. If a consistent picture emerges, then one can have confidence in that picture; if not, a more sophisticated framework can be developed.

In conclusion, the opportunity exists to thoroughly and systematically study the space-time characteristics of hadronization by determining the variable dependences of the formation length. The studies can be carried out as a function of Q^2 , ν , p_T , z , helicity, hadron mass and size, and quark flavor. This large program is expected to yield a wealth of new insights into the nature of the gluon emission process and hadronization, which is a direct manifestation of confinement.

Transverse Momentum Broadening As a struck quark traverses the color field presented by a nucleus, it scatters off the partons in the medium, losing energy primarily by radiation of gluons. The gluon emission, which is a fundamental prediction of QCD, may have a coherent character similar to that of the Landau-Pomeranchuk-Migdal (LPM) effect [Lan53, Mig56, An97] in the QED energy loss of charged particles passing through atomic matter. This coherence, in combination with the non-Abelian nature of QCD radiation, predicts that the energy loss will be *quadratic* in the distance the quark travels through a nuclear medium, in strong contrast to the energy loss in quantum electrodynamics.

A number of theoretical studies have linked the broadening of the transverse momentum to the energy loss due to gluon radiation [Ba00, Wan95]. Specifically, if the transverse momentum broadening through a nuclear medium of thickness L is expressed as $\langle p_T^2 \rangle_L$, then the energy loss per unit length $-dE/dx$ is given approximately by

$$\frac{-dE}{dx} = \frac{\alpha_s}{\pi} N_c \langle p_T^2 \rangle_L \quad (53)$$

where N_c is the number of colors and α_s is the strong interaction coupling constant. Further, the broadening is expected to be proportional to L , i.e., to vary for nuclei as $A^{\frac{1}{3}}$. As a result, the total energy loss is predicted to scale as L^2 , a novel behavior quite unlike the QED energy loss of particles traveling through ordinary atomic matter. An observation of the quadratic energy loss would be a striking confirmation of the importance of coherence behavior in these processes, such as the LPM effect.

Transverse momentum broadening has also been theoretically linked to a correlation function between hard quarks and soft gluons [Guo00]. Therefore, these studies offer one avenue for studying partonic correlations. All of these simple interpretations depend on the assumption that the quark travels independently in the medium, which in turn requires an understanding of the hadronization time scales discussed in the previous section.

A further interest in this study is to gain a greater understanding of the ‘‘Cronin effect’’, the overabundance of high p_T events in heavier nuclei relative to light nuclei [Cro75, Kop02]. This effect, while seen most prominently in hadron-nucleus scattering, is also seen in DIS studies on nuclei [Muc01]. An advantage of DIS for these studies relative to hadron beam studies is that the probe does not multiple scatter or otherwise interact before undergoing the interaction being studied. The primary limitation of the study of this phenomenon in DIS to date is statistical accuracy, since the events of interest are for $p_T > 0.5$ GeV, where the rate is correspondingly low.

Since JLab brings high luminosity to these studies, it should be possible to determine the kinematic dependences that accompany the effect, such as the dependence on the coherence length [Kop02]. In general, p_T broadening will ultimately be predictable within the context of quark propagation models, and therefore will provide further discrimination power to differentiate among them. Experimentally, the determination of transverse momentum broadening for channels including only charged particles will be straightforward. A substantial body of new information will clearly become available from this data, as illustrated in Fig. 113.

2.C.2 Short-Range Correlations in Nuclei

Observing short-range correlations (SRC) in nuclei has been an important goal of experimental nuclear physics for decades [Be99, Be67]. Not that these correlations are small – calculations of nuclear wavefunctions with realistic NN potentials consistently indicate that in heavy enough nuclei about 25% of the nucleons have momenta above the Fermi surface [Pa97]. This corresponds to about 50% of the kinetic energy being due to SRC. The experimental problem has been the unavailability of the high-momentum-transfer kinematics that could discriminate decisively between the effects of SRC in the initial- and final-state interactions. Though the final-state interactions in nucleon knockout do not disappear at large Q^2 , two important simplifications occur which make extraction of the information about the short-range nuclear structure possible. First, in high-energy kinematics a “hidden” conservation law exists – the light-cone momentum fractions of slow nucleons do not change if the ejected nucleon elastically scatters off slow nucleons [Fr97]. Second, the rescatterings of a high-energy nucleon can be described by the generalized Glauber approximation, which takes into account a difference in the space-time picture of proton-nucleus scattering (a proton coming from $-\infty$) and the $A(e, e'p)$ process (a proton is produced inside the nucleus) and also accounts for the nonzero Fermi momenta of rescattered nucleons [Fr97].

There is a general consensus that Glauber theory is the appropriate tool for describing final state interactions for proton kinetic energies $\gtrsim 1$ GeV, which corresponds to $Q^2 \geq 2$ (GeV/c)². On the other hand, pushing to Q^2 values that are too high is not optimal for the study of nucleon degrees of freedom in nuclei as at $Q^2 \geq 4$ (GeV/c)² one may encounter new phenomena related to the EMC effect [Fr88, Fr96]. Hence the optimal range for probing nucleonic degrees of freedom is $1.5 \leq Q^2 \leq 4$ (GeV/c)². CEBAF at 6 GeV reaches the lower end of this range and can provide limited access to its upper part, but at the cost of low counting rates, especially at the higher missing momenta, p_m , crucial for observing SRC. Studies of the $(e, e'N)$ and $(e, e'NN)$ reactions with 11 GeV will allow us to probe missing momenta up to 500–700 MeV/c, and will also provide information on how these momenta are balanced in nuclei: two- and three-nucleon short-range correlation contributions versus those of the mean field. Inclusive $A(e, e')$ processes at deep inelastic kinematics are also sensitive to multi-nucleon correlations.

Electrodisintegration of the Deuteron Current NN interaction models, while tightly constrained by the large body of NN elastic scattering data, do not explicitly account for the quark-gluon substructure of the interacting nucleons. Indeed, it is an open question whether this rich substructure is correctly and/or adequately represented in these models at short internucleon separations. It is also unclear whether the short range structure in nuclei implied by these interactions is correct. The deuteron, being the simplest nucleus, is the necessary first nuclei for carrying out the systematic study of these issues with the possibility to extend these measurements at high missing momentum to few-body systems (such as $A=3$ and 4) which are amenable to accurate calculations.

The $e + {}^2H \rightarrow e'pn$ reaction is ideally suited for this purpose, particularly in view of the fact that a high energy beam allows measurements to very high missing momenta (p_m) where one is sensitive to the very short-range NN interaction. Though one has to rely on reaction models in order to extract information on the deuteron's structure, the kinematical flexibility afforded by beams of 8–11 GeV would allow extreme tests of the model assumptions. Finally, this same flexibility provides an opportunity to select kinematics where various reaction effects, which would otherwise frustrate the extraction of structure information, are likely to be small. Here we discuss two main components of the ${}^2H(e, e'p)n$ program.

The first component of the ${}^2H(e, e'p)n$ program would involve “perpendicular” kinematics at $x_{bj} \approx 1$ where a separation of the R_{LT} interference response function would be carried out. This response function is predicted to be highly sensitive to relativistic effects and final state interactions. It should be pointed out that the NN potential models alluded to above were constructed from non-relativistic versions of 1-body and 2-body operators and based on relatively low energy data. The second component would involve measurements in parallel kinematics (where protons are detected along the three-momentum transfer direction) for $x_{bj} > 1$. In this configuration, non-nucleonic effects (virtual isobars and meson-exchange currents), as well as FSI, are expected to play a minimal role, whereas relativistic effects are expected to be quite large. This kinematics offers the greatest promise of constraining models of the deuteron structure, especially when combined with the R_{LT} measurements and resulting constraints on the relativistic aspects of the theory.

Although quite extreme kinematics can be accessed with 6 GeV beam energies, higher energies would reduce the beam time requirement significantly since the same Q^2 could be reached with smaller scattering angles and commensurately larger cross sections. This can be seen from Fig. 114 which shows the statistical uncertainty per day of beam time as a function of beam energy for $Q^2=6$ (GeV/c)² at various missing momenta. The kinematics are parallel with $x_{bj}>1$. The uncertainties are into each bin: ± 50 MeV/c in p_m , ± 1.0 (GeV/c)² in Q^2 and ± 0.2 in x_{bj} . For this analysis, the Hall C spectrometers, SHMS and HMS, were assumed for the detection of electrons and protons respectively. It is evident that a maximum beam energy of 11 GeV would allow measurements of the ${}^2H(e, e'p)n$ reaction to very high Q^2 and p_m (*i.e.* missing momentum). An analysis assuming the Hall A spectrometers, HRS and MAD, gives very similar counting rates for a beam energy of

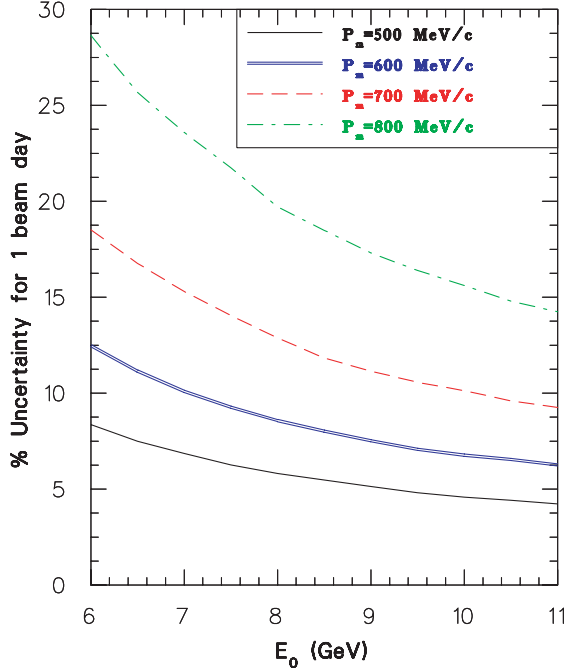


Figure 114: Statistical error per day of beam time as a function of beam energy for $Q^2=6$ $(\text{GeV}/c)^2$ at various recoil momenta. The kinematics are parallel with $x_{bj}>1$.

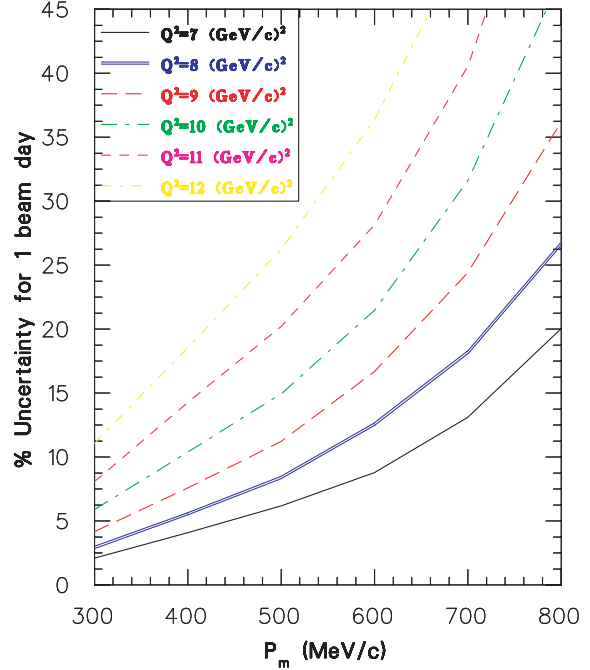


Figure 115: Statistical error per day of beam time for a beam energy of 11 GeV as a function of missing momenta for a variety of values of Q^2 . The kinematics are parallel with $x_{bj}>1$. See the text for details.

8 GeV. Here, the maximum usable beam energy of 8 GeV is dictated by the momentum limits of these spectrometers. The relatively larger acceptances of the Hall A spectrometer pair very nearly compensate for the lower cross sections at the lower beam energy.

Given an 11 GeV beam energy, and the SHMS and HMS spectrometer configuration, Figure 115 shows the statistical uncertainty per day of beam time as a function of missing momentum for Q^2 up to 12 $(\text{GeV}/c)^2$ (the bin sizes are the same as given above) for the high x_{bj} parallel kinematics case. For $Q^2=12$ $(\text{GeV}/c)^2$, a missing momentum of 500 MeV/c could be measured with 10% uncertainty with one week of beam time. For $Q^2=8$ $(\text{GeV}/c)^2$, the same uncertainty could be obtained in the same running time for a missing momentum of 800 MeV/c.

The progress in constructing tensor-polarized deuteron targets will make it feasible to study the same reaction using polarized targets at sufficiently large Q^2 . In this case a separation of S - and D -wave contributions is possible. Since the D -wave is expected to play a key role over a wide range of nucleon momenta both in ^2H and in heavier nuclei [Fr81, Fo96], this process will provide a crucial test of our understanding of the short-distance NN interactions.

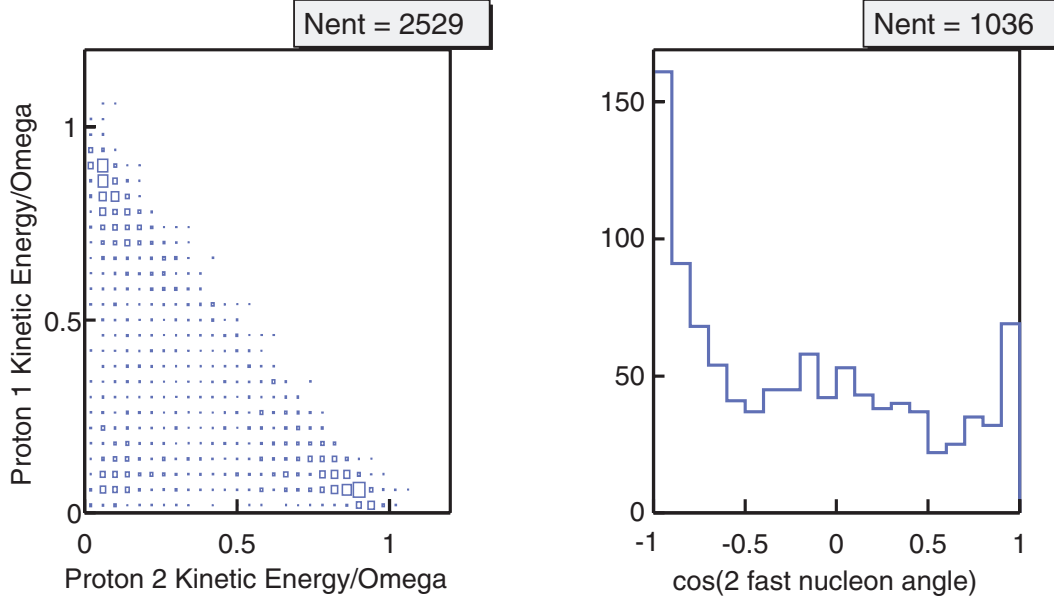


Figure 116: ${}^3\text{He}(e, e'pp)n$ measured with CLAS in one day at $E_0 = 4.4$ GeV. Left: Kinetic energy balance of the three nucleons for $p_N > 0.25$ GeV/c (ie: a lab frame Dalitz plot). Note the large peaks in the corners where one ‘leading nucleon’ carries most of the kinetic energy the other two ‘fast nucleons’ share the remainder. Right: The cosine of the fast nucleon pair opening angle where the leading nucleon is a proton and the remaining p and n are ‘fast’. Note the very large back-to-back peak, indicative of the presence of short range correlations.

$A(e, e'pN)$ **Processes** Triple coincidence experiments of the type $A(e, e'pN)$ offer the opportunity to study directly short range correlations by measuring both ejected nucleons and directly determining the total (p_{tot}) and relative (p_{rel}) momenta of the final state NN pair and the excitation energy and momentum of the unobserved $A - 2$ recoil. We then need to connect the NN pair final state with the NN pair initial state (within a model). We can do this either with theoretical guidance or, hopefully, through judicious choice of kinematics.

One possibility is to measure $A(e, e'N_f N_b)$ with N_f the forward- and N_b the backward-going nucleons. If, as expected, the dominant contribution is from two-nucleon correlations, N_b should carry most of the excitation energy and the $A - 2$ recoil should be almost at rest in a low energy state. Comparing (pp) , (pn) , and (nn) cross sections will check the reaction mechanism and possibly allow us to compare the isospin zero and one NN SRC wavefunctions. However, one needs to properly include the effects of FSI and two body currents to extract any information about the wavefunction.

A much more promising technique for measuring NN momentum distributions is to study ${}^3\text{He}(e, e'pp)n$ events in CLAS where one nucleon absorbs the virtual photon and the correlated pair is a spectator. This has been achieved in kinematics where all three nucleons have momenta $p > 0.25$ GeV/c.[We02a] In this case, there are peaks in the kinetic energy distribution with one leading nucleon ($T_N > 0.6 * \omega$) and two ‘fast’ nucleons ($T_f < 0.2 * \omega$). These peaks in the kinetic

energy distribution become much more pronounced at $E_0 = 4.4$ GeV ($1 \leq Q^2 \leq 2$ GeV²) than at $E_0 = 2.2$ GeV ($0.5 \leq Q^2 \leq 1$ GeV²) (Fig. 116). The opening angle of the two fast nucleons has a pronounced peak at 180° for both fast pn and fast pp pairs. This back-to-back peak is not due to kinematics (we do not see it in a fireball phase space simulation) or to the CLAS acceptance (since we see it for both pn and pp pairs).

Restricting the perpendicular momentum of the leading/struck nucleon (relative to \vec{q}) to be less than 0.3 GeV/c (to minimize FSI) selects primarily NN pairs with very large opening angles. These pairs have the momentum component parallel to \vec{q} , $p_{tot}^{\parallel} \ll |\vec{q}|$, and total momentum ($\vec{p}_{tot} = \vec{p}_1 + \vec{p}_2$) smaller than their relative momentum ($\vec{p}_{rel} = \frac{1}{2}(\vec{p}_1 - \vec{p}_2)$). The shape of the momentum distributions is very similar for pp and for pn pairs at both beam energies measured ($E_0 = 2.2$ and 4.4 GeV). The shapes of the distributions are comparable to a Plane Wave Impulse Approximation calculation by M. Sargsian, but a factor of about 6 smaller. Calculations by Glockle [Glo97] at much lower energy indicate that the cross section is very strongly reduced by the continuum interaction between the nucleons of the fast pair and that meson-exchange currents (MEC) and final state interactions (FSI) of the leading nucleon are negligible. Calculations by Laget [La88] for leading proton and fast pn pair events at $E_0 = 2.2$ GeV describe the data very well when he includes just the rescattering of the fast pair from each other. The FSI of the leading proton and MEC contributions are negligible.

Thus, these measurements appear to have measured distorted correlated NN momentum distributions in ^3He by striking the third nucleon and observing the spectator pair. These measurements will benefit tremendously from CEBAF at 12 GeV:

- Cleaner signal: The peaks in the three-nucleon kinetic energy distribution are much more pronounced as Q^2 increases.
- Larger momentum range: Since most of the events of interest have $x_B \approx 1$, increasing Q^2 increases the average ω and therefore increases the maximum relative momentum of the fast nucleon pair (since $T_{fast} \leq 0.2 * \omega$).
- More data: increased CLAS⁺⁺ luminosity, smaller minimum scattering angle, fewer acceptance holes.

Although SRC are expected to be predominantly two-nucleon, three or more-nucleon SRC are also significant; they are likely to constitute $\sim 20\%$ of all SRC. Their probability can be measured in the ratio of $A(e, e')$ cross sections at $x > 1$ and $x > 2$ at large Q^2 . They can be best measured through the $A(e, e'N_fN_b)$ reaction and in processes with two backward-ejected nucleons [Fr88].

Inclusive $A(e, e')X$ Processes The ‘EMC effect’ from measurements of the parton densities in nuclei (\bar{q}_A/\bar{q}_N , etc.), unambiguously demonstrated that on the parton level a nucleus cannot be viewed as merely a collection of nucleons. Practically all the mechanisms suggested to explain

the EMC effect address the question of the quark-gluon structure of SRC and/or the origin of the nuclear forces. These include:

- a. Various patterns of mixing quarks (gluons) from different nucleons ranging from the deformation of the bound nucleon wavefunctions to “kneaded” (multiquark) states [Cl83, Ca83, Na84, Ja84, Fr85, Fr96].
- b. A loss of momentum by nucleons to some fields that bind *undeformed* nucleons together [Er83, Fr83, Be84, Ak85, Ku89, Du85, Ju88, Ci89, Ka90, Me93, Bi89, Me94, Ku94].
- c. The presence of Δ -isobars, N^* 's in nuclei, especially in the SRC [Fr83].

However, inclusive experiments at $x \leq 0.8$ have not allowed us to discriminate between such models. The broad (x, Q^2) range available at 11 GeV and the feasibility of correlation experiments suggest a strategy that will work. Deep inelastic scattering off nuclei at $x \geq 1$ in the scaling limit is a first step to establish in a model-independent way (*i.e.*, not sensitive to the final-state interactions) the presence of superfast quark components in nuclei – quarks that carry a larger momentum fraction than a whole nucleon.

Theoretical estimates indicate that for $x \leq 1.5$ this will require $Q^2 \leq 20$ (GeV/c)², so experiments will be feasible with $E_e = 11$ GeV. Several features of CEBAF and its experimental facilities (the good acceptance and high resolution of the CEBAF spectrometers, and the high intensity and small energy spread of the electron beam) are crucial for performing these measurements. Through a study of the Q^2 -dependence of the cross section at fixed x it will be possible to observe for the first time the onset of scaling at $x \geq 1$ (Fig. 117), which will be the definitive signature for the existence of superfast quarks in nuclei.

Comparing the cross sections for $A = 2, 3$, and 4 and for heavy nuclei will allow the model-independent separation of contributions of two-, three-, or more-nucleon SRC. The two-nucleon correlations are expected to dominate for $1.3 \geq x \geq 1$, leading to quark structure functions for $A \geq 12$ nuclei a factor of 5–6 larger than in the deuteron [Fr81, Fr88]. This ratio should be similar to the cross-section ratio for quasielastic scattering:

$$R_{A/D}(x, Q^2) \equiv \frac{2}{A} \frac{\sigma_{eA}(x, Q^2)}{\sigma_{e^2H}(x, Q^2)}$$

observed at $x \sim 1.5$, $4 \geq Q^2 \geq 1$ (GeV/c)² at SLAC [Fr93a]. Local nuclear densities probed in this case are three to four times larger than the average value, $\rho_0 \sim 0.17$ fm⁻³. For larger $x \sim 1.5$ higher order correlations are expected to dominate, leading to an increase of $R_{A/D}(x \sim 1.5, Q^2 \sim 50$ (GeV/c)²) [Fr81]. At the same time the local nature of generating $x \geq 1$ quarks will manifest itself experimentally through the same shape and probability per nucleon of the $x \geq 1$ component in ⁴He and heavy nuclei. In this kinematics we expect to observe densities at least five times larger than ρ_0 . Detailed studies of the A -dependence of $q_A(x, Q^2)$ at $1 \leq x \leq 1.5$ will provide important

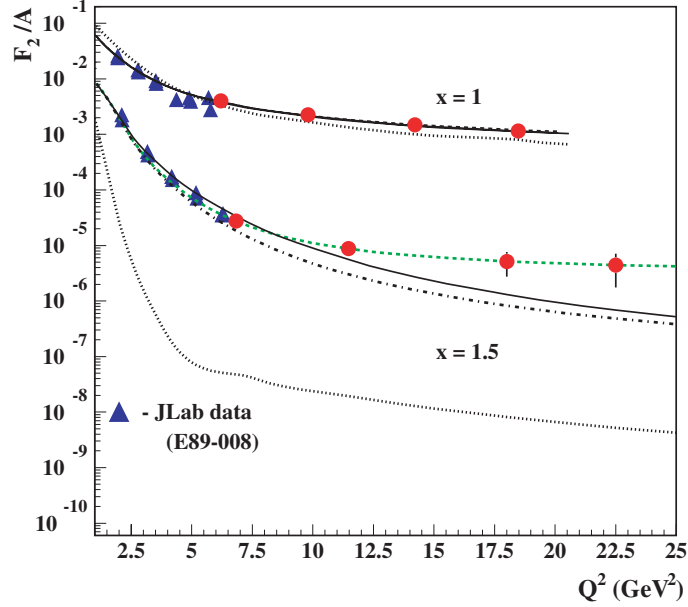


Figure 117: Prediction of the onset of scaling for the $^{56}\text{Fe}(e, e')X$ reaction. The solid line and the dash-dotted line are predictions with 2 nucleon correlation, without and with the EMC modification of the nucleon elastic form factor, respectively. In both cases, one includes the EMC effect in the inelastic structure function to have agreement with EMC data at DIS for ^{56}Fe . The dashed line is the prediction with multinucleon correlation with EMC effects included, and the dotted line is the prediction of mean-field approximation. The data shown are from Ref. [Ar99]

information about fluctuations of the local nuclear density as a function of average nuclear density as well as of the isospin of the correlations.

Measurement of the quark distribution at $x \geq 1$, in combination with the measurements of the light-cone nucleon density matrix (ρ_A^N), will allow a check of whether $F_{2A}(x, Q^2) > 1$ can be described as a convolution of ρ_A^N and the *free* nucleon structure function. At the same time these measurements will establish in a model-independent way the relative importance of two- and three-nucleon SRC by comparing $F_{2A}(x, Q^2)$ for light and heavy nuclei and show the dependence of SRC on nuclear density. Figure 117 shows prediction of the onset of scaling for the $^{56}\text{Fe}(e, e')X$ reaction. The solid line and the dash-dotted line are predictions [Fr93a] with two nucleon correlation, without and with the EMC modification of the nucleon elastic form factor, respectively. In both cases, one includes the EMC effect in the inelastic structure function to have agreement with EMC data at DIS for ^{56}Fe . The dashed line is the prediction with multinucleon correlation [Sa03a] with EMC effects included, and the dotted line is the prediction of mean-field approximation. The data shown are from Ref. [Ar99]. With the 12 GeV upgrade data, measurements can be made to above $Q^2 = 20 \text{ (GeV}/c)^2$, where the dash-dotted line and dashed line will have separated by more than an order of magnitude for $x = 1.5$.

2.C.3 The Parton-Hadron Transition in Nuclei

Mapping the transition from strongly interacting, non-perturbative Quantum Chromodynamics (QCD), where nucleon-meson degrees of freedom are effective, to perturbative QCD (pQCD), is one of the most fundamental and challenging tasks in nuclear and particle physics. Scaling¹ in the differential cross section $d\sigma/dt$ and hadron helicity conservation have been pursued experimentally as signatures of this transition for decades.

Quark counting rules were originally obtained based on dimensional analysis [Br73], and were later confirmed by a short-distance pQCD approach up to calculable powers of the running coupling constant [Le80]. While global scaling behavior has been observed in many exclusive processes [An76], no experimental evidence supports hadron helicity conservation, which was predicted in the same approach, in similar energy- and momentum-transfer regions. Hadron helicity conservation arises from the vector coupling nature of the quark-gluon interaction, quark helicity conservation at high energies, and the neglect of the non-zero quark orbital angular momentum state in the nucleon. The parton orbital angular momentum was considered for the first time by Chernyak and Zhitnitsky [Ch77] for form factors. Recently, Ji, Ma and Yuan [Ji03] derived a generalized counting rule for exclusive processes at fixed angles involving parton orbital angular momentum and hadron helicity flip. This generalized counting rule opens a new window for probing the quark orbital angular momentum inside the nucleon. A natural connection between the study of the parton-hadron transition through exclusive processes and generalized parton distributions probed through deeply virtual processes is therefore established.

The elastic form factor of charged pions is extremely important since the pion has the simplest valence quark structure and is therefore amenable to both nonperturbative and pQCD calculations. Based on those calculations we know where to expect the transition to scaling – it should occur at relatively low momentum transfer. Measurements of the pion form factor will confirm our understanding and delineate the transition from nonperturbative to perturbative QCD. Measurements of the form factors of light nuclei at large momentum transfers provide analogous information on another important transition in nuclear physics – the transition from the traditional meson-nucleon description of nuclei to the underlying (and more fundamental) quark-gluon description.

Exclusive processes such as proton-proton elastic scattering, meson photoproduction, and deuteron photodisintegration have been measured extensively at many laboratories over the years in the search for such a transition, particularly at Jefferson Lab in recent years, taking full advantage of the high luminosity capability of the CEBAF facility. Early onset of the transition from hadronic degrees of freedom to partonic degrees of freedom is also expected in nuclear transparency measurements due to nuclear filtering and color transparency. Nuclear filtering refers to the suppression of nonperturbative amplitudes involving large quark separations inside the nuclear environment. Nuclei are therefore often employed as laboratories in the search for this transition.

¹Scaling in this context implies a dependence on a reduced set of kinematic variables.

While a coherent picture of this transition is on the verge of emerging, the Jefferson Lab 12 GeV energy upgrade will allow the exploration of this transition region with detail and precision. In the remaining section, we will discuss the planned measurements of the charged pion form factor, form factors of light nuclei, deuteron photodisintegration and photopion productions at Jefferson Lab with energy upgraded CEBAF and upgraded instrumentation.

Elastic Form Factor of Charged Pion A well known signature for the onset of pQCD is *constituent counting* scaling, where the cross sections are sensitive to short range valence quark distribution amplitudes. The reaction for which pQCD is expected to manifest itself at the lowest momentum transfers is in the elastic scattering from the charged pion, since the pion has the simplest valence quark structure. There have been a large number of calculations [Br00, Ja90, Ti92, It92, Ma00] of the pion form factor, F_π , which predict its magnitude and Q^2 dependence. In one extreme the calculations involving purely perturbative mechanisms utilize simple valence quark distributions which have either their asymptotic shapes or those based upon QCD sum rules. Other calculations add higher non-leading configurations in various ways. The most recent theoretical studies of the charged pion form factor F_π seem to indicate that these hard exclusive processes may be expected to become important by $Q^2 \sim 5 \text{ (GeV/c)}^2$. To date, the most accurate measurement of F_π has been carried out in Hall C from the $p(e, e\pi^+)n$ process to a maximum Q^2 of around 1.6 (GeV/c)^2 [Vo01]. Not surprisingly, these results do not exhibit the $1/Q^2$ scaling predicted by pQCD. Thus it is crucial to measure F_π as accurately as possible to the highest Q^2 possible to approximately 6 (GeV/c)^2 with the CEBAF upgrade. The goal is to observe the transition to constituent scaling, and also to pin down the magnitude of the cross section, which constrains valence non-perturbative models, and their higher twist corrections. Since F_π is manifested in the longitudinal cross section, one must carry out a Rosenbluth separation, and project as closely as possible to the *non-physical* pion pole. The combination of the SHMS and HMS spectrometers in Hall C is ideal for such a separation. High momentum pions will be detected at very forward angles by the SHMS spectrometer, in coincidence with electrons detected in the HMS spectrometer. Results of various theoretical calculations are shown in Fig. 118 together with the 12 GeV projection on the F_π measurement.

While one expects pQCD to set in early in the elastic form factor of the charged pion because of its simple $q\bar{q}$ valence quark structure, the pion form factor at a few $(\text{GeV/c})^2$ is still dominated by non-perturbative effects. However, when one forms the charged pion photoproduction differential cross-section ratio, $\frac{d\sigma}{dt}(\gamma n \rightarrow \pi^- p) / \frac{d\sigma}{dt}(\gamma p \rightarrow \pi^+ n)$, such non-perturbative effects may cancel out to first order. If this is the case, the π^-/π^+ ratio could give the first indication of the simple pQCD prediction [Hu00]. Experiment E94-104 provides data on the charged pion ratio up to a momentum transfer $|t|$ value of 5.0 (GeV/c)^2 , the highest $|t|$ value ever achieved for this quantity. The highest $|t|$ results are already in agreement with the perturbative value; however, the measurements must be extended to higher energy to confirm this finding. With an 11 GeV beam, this ratio measurement can be extended to $|t| \approx 11 \text{ (GeV/c)}^2$, significantly higher than the projected charged pion form

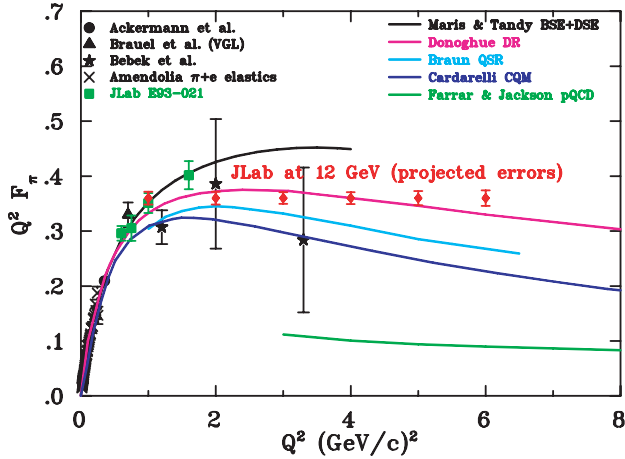


Figure 118: The π^+ form factor, with recent Hall C data denoted by filled squares and previously obtained Cornell data indicated by filled stars. The curves are the results of theoretical calculations.

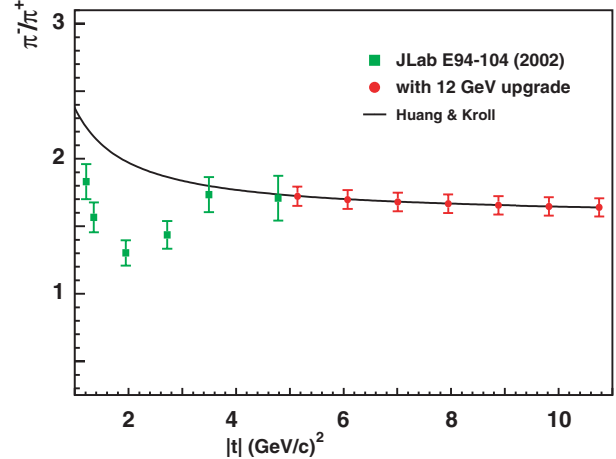


Figure 119: The charged pion photoproduction differential cross-section ratio at a C.M. angle of 90° , as a function of $|t|$ (GeV/c) 2 from experiment E94-104 (blue) along with the projected measurements for JLab at 11 GeV (red). The solid curve is a prediction by Huang and Kroll [Hu00].

factor measurement at $Q^2 \leq 6$ (GeV/c) 2 . Figure 119 shows the E94-104 results on the charged pion ratio, the projected results at 11 GeV, and the pQCD prediction by Huang and Kroll [Hu00].

Few-Body Form Factors Measurements of the elastic form factors of the deuteron and the helium isotopes are of crucial importance in understanding their electromagnetic structure and testing the “standard model” of light nuclei that is based on the meson-nucleon framework, the impulse approximation (IA), and meson-exchange currents (MEC) [Ca97]. Such measurements offer unique opportunities for studying the short-range nucleon-nucleon interaction, few-body wavefunctions, isobar and three-body force contributions, and effects from possible quark-cluster admixtures. Large-momentum-transfer measurements can also test “nuclear chromodynamics” predictions based on quark dimensional scaling (QDS) and pQCD [Ca97].

The starting point of the conventional theoretical approach of elastic scattering from few-body systems is the impulse approximation, where the incident electron interacts with one of the nucleon constituents of deuterium or helium. The form factors of light nuclei are then convolutions of the nuclear wavefunction with the form factors of the constituent nucleons. At large momentum transfers the effects of relativity cannot be ignored, and either corrections must be made to the IA or fully relativistic approaches developed (as has been done in the case of the deuteron [Hu90]). It has long been understood and overwhelmingly supported by the available data that the few-body form factors are sensitive to the presence of meson-exchange currents and isobar configurations that augment the IA picture [Ca98].

At distances much less than the nucleon size, the underlying quark substructure of the nucleons cannot be ignored. This has led to the formulation of so-called hybrid quark models [Di89] that treat few-body nuclei as quark clusters when the internucleon separation becomes smaller than ~ 1 fm. At sufficiently “large” momentum transfers, the few-body form factors are expected to be calculable in terms of only quarks and gluons within the framework of pQCD. The first attempt at a quark-gluon description of the few-body elastic form factors was based on the dimensional-scaling quark model (DSQM) [Br73], where the underlying dynamical mechanism during elastic scattering is the hard rescattering of the constituent quarks via exchange of hard gluons. The Q^2 -dependence of this process is then predicted by simply counting the number n of gluon propagators ($n = 5$ for deuterium, 8 for ${}^3\text{He}$, and 11 for ${}^4\text{He}$), which implies that the elastic structure functions $A(Q^2)$ of the few-body systems should follow the power law: $\sqrt{A(Q^2)} \sim (Q^2)^{-n}$. This prediction was later substantiated, for the deuteron case, in the pQCD framework, where it was shown [Br83] that to leading order:

$$\sqrt{A(Q^2)} = \left[\alpha_s(Q^2) / Q^2 \right]^5 \sum_{m,n} d_{mn} \left[\ln \left(\frac{Q^2}{\Lambda^2} \right) \right]^{-\gamma_n - \gamma_m},$$

where $\alpha_s(Q^2)$ and Λ are the QCD strong coupling constant and scale parameter, and $\gamma_{m,n}$ and d_{mn} are QCD anomalous dimensions and constants.

The 12 GeV energy upgrade of the JLab electron beam and the proposed spectrometer upgrades will be ideal for improving and extending the existing elastic structure function measurements of light nuclei to higher momentum transfers. These measurements will test the limits of the standard model of few-body nuclei, and may uncover a possible transition to a quark-gluon description of the few-body form factors, as predicted by quark dimensional scaling and perturbative QCD.

Figure 120 shows the recent JLab Hall A and older SLAC and Saclay data [Al99] on the deuteron form factor, $F_d(Q^2) \equiv \sqrt{A(Q^2)}$, multiplied by $(Q^2)^5$. It is evident that the data show an approach to a scaling behavior consistent with the power law of DSQM and pQCD. Although several authors have questioned the validity of QDS and pQCD at the momentum transfers of this experiment [Is84], similar scaling behavior has been reported in deuteron photodisintegration at moderate photon energies (see next section). It is extremely important to test this apparent scaling behavior by extending the deuteron $A(Q^2)$ measurements to higher momentum transfers. Higher JLab beam energies in the range of 9–11 GeV are essential for such measurements. To separate elastic from inelastic scattering and to suppress backgrounds, recoil deuterons should be detected in coincidence with scattered electrons. A possible scenario would be to use the proposed Medium-Acceptance Device (MAD) to detect recoiling deuterons and a segmented electromagnetic calorimeter (ECAL) to detect scattered electrons. Assuming a 20-cm-long liquid-deuterium target and beam current of 70 μA , $A(Q^2)$ can be measured up to ~ 10 $(\text{GeV}/c)^2$ in one month of beam time, as shown in Fig. 120. Such an experiment will double the Q^2 range of the existing data, which have been acquired over a period of 40 years. The observation of a diffractive structure (which cannot be ruled out from the existing data) would settle in the negative the question of the applicability of the QDS ideas at moderate momentum transfers once and for all.

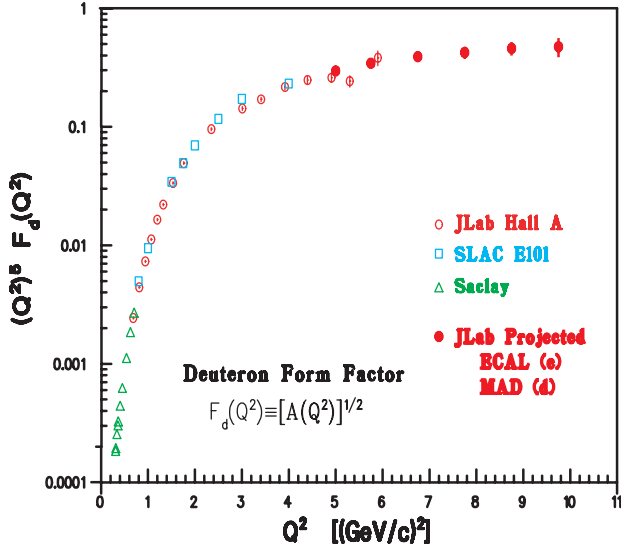


Figure 120: Projected data for the deuteron form factor $F_d(Q^2)$ with an 11 GeV JLab beam. Also shown are existing JLab, SLAC, and Saclay data.

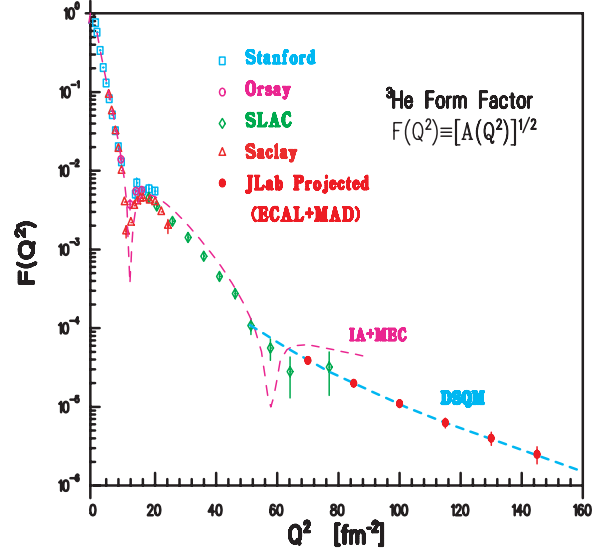


Figure 121: Projected data for the ${}^3\text{He}$ elastic form factor $F(Q^2)$ with an 11 GeV beam. Also shown are existing data and predictions of the standard model (IA+MEC) [Sc91] and the dimensional-scaling quark model (DSQM) [Ch78].

The existing data [Am94] on the ${}^3\text{He}$ form factor, $F(Q^2) \equiv \sqrt{A(Q^2)}$ (shown in Fig. 121), are in good agreement with the standard model (IA+MEC) calculations [Sc91] at low Q^2 but are fairly inconclusive at the largest momentum transfers. They are consistent with a change in slope at $\sim 55 \text{ fm}^{-2}$, indicative of an onset of quark scaling [Ch78], but, at the same time, cannot exclude the presence of a second diffraction minimum as predicted by conventional meson-nucleon theory. As in the case of the deuteron, more measurements at higher Q^2 would be crucial in testing the quark-scaling prediction and a possible breakdown of the meson-nucleon framework. The energy upgrade of JLab will also allow new ${}^3\text{He}$ measurements that could double the Q^2 range of the existing data (taken also over a period of 40 years) in a single experiment with a tenfold better sensitivity. As in the case of the deuteron, recoiling nuclei will be measured with the MAD spectrometer and scattered electrons with a calorimeter. Assuming a 20-cm-long ${}^3\text{He}$ gas cryogenic target and an electron beam of 11 GeV with current of $70 \mu\text{A}$, the ${}^3\text{He}$ $F(Q^2)$ can be measured up to $\sim 150 \text{ fm}^{-2}$ in one month of beam time, as shown in Fig. 121. It is evident that this experiment will be able to show whether the apparent change in slope of the SLAC data can be attributed to a classical diffraction minimum, or a quark-scaling approach as argued in Ref. [Ch78].

Deuteron Photodisintegration The deuteron photodisintegration reaction, $\gamma d \rightarrow pn$, is one of the simplest reactions for studying explicit quark effects in nuclei. In recent years, extensive studies of deuteron photo-disintegration have been carried out at SLAC and JLab [Na88, Bo98, Sc01].

Figure 122 shows the scaled differential cross-section ($s^{11} \frac{d\sigma}{dt}$) from deuteron photodisintegration as a function of photon energy. The data seem to show scaling at 70° and 90° , and suggest the onset of scaling at higher photon energies at 52° and 36° . The threshold for this scaling behavior corresponds to a transverse momentum slightly over 1 GeV/c. Also shown in Fig. 122 are the QCD rescattering calculation [Fr00] (shaded region), the quark-gluon string model calculation (dashed line) [Ko93, Gr01], and an estimate from Raydushkin [Ra01a] (dash-dotted line) based on a quark-exchange picture. While none of the theories agree with all of the data as well as one would like, they do indicate that quark models can approximately reproduce the cross section data, therefore establishing the importance of deuteron photodisintegration process in the study of the transition region.

A recent polarization measurement on deuteron photo-disintegration [Kr01] disagrees with hadron helicity conservation at kinematics where quark counting behavior is observed in the differential cross section. This is also supported by $^1H(\vec{\gamma}, \vec{p})\pi^0$ [Kr02], $d(e, e'\vec{d})$ deuteron tensor polarization T_{20} measurement [Ab00], and the $p(\vec{e}, e'\vec{p})$ measurement of the proton electric to magnetic form factor ratio [Jo00].

At this point, it is extremely difficult to extend either the cross section or polarization measurements to higher energies at JLab with existing equipment. Experimental considerations for measurements of $\gamma d \rightarrow pn$ are dominated by the small cross sections and by the high momentum of the outgoing proton, relative to other reaction products. The increased solid angle of the proposed MAD spectrometer in Hall A would allow cross sections and polarization to be measured at higher energies, if backgrounds are low, as they have been for existing Hall A experiments. The MAD spectrometer will allow cross section measurements to photon energies near 8 GeV, which is a straightforward extension of the latest Hall C measurements [Sc01]. The Hall A polarization data can be extended to about 4 GeV. Figures 122 and 123 show the projected differential cross-section and induced polarization measurements for the deuteron photodisintegration with MAD together with existing data, respectively.

Nucleon Photopion Production Because of the simple valence quark structure of the pion, its photoproduction from nucleon ($\gamma n \rightarrow \pi^- p$, $\gamma p \rightarrow \pi^+ n$, $\gamma p \rightarrow \pi^0 p$) is an essential probe of the transition from meson-nucleon degrees of freedom to quark-gluon degrees of freedom. The relatively large cross-section at high energies (quark counting rule predicts a s^{-7} -dependence for the differential cross-section) not only will allow the investigation of the t and p_T dependence of the scaling behavior in addition to the s dependence, but also will allow studies of possible QCD oscillation². In nuclei, photoreactions allow the search for QCD nuclear filtering of those oscillation as well as color transparency.

Apart from the early onset of scaling and departure from hadron helicity conservation rule, several other striking phenomena have been observed in pp elastic scattering –one of the prime cases

²QCD oscillation refers to oscillatory scaling behavior around the quark counting rule prediction

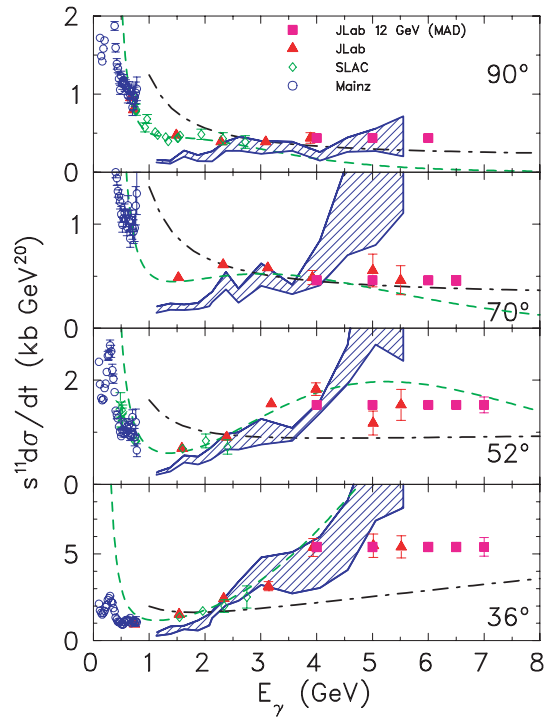


Figure 122: High energy deuteron photodisintegration differential cross sections scaled by s^{11} . The projected results with MAD are shown as purple solid squares.

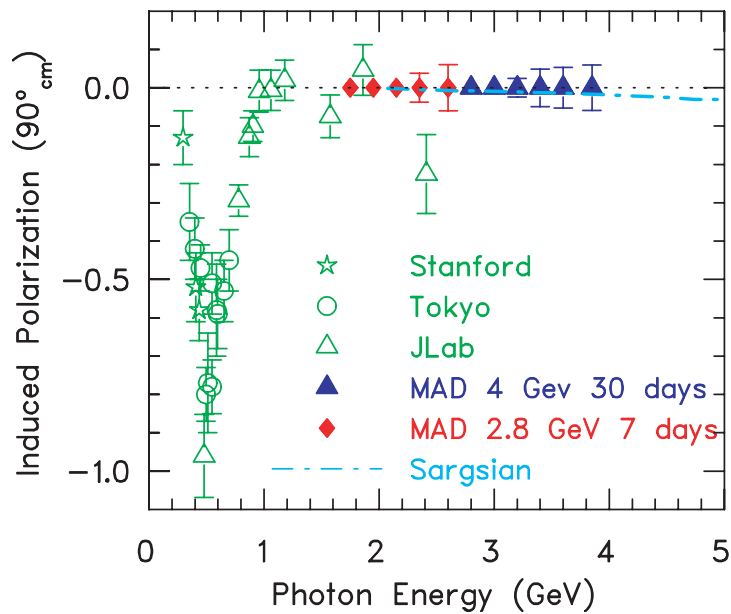


Figure 123: Projected results for deuteron photodisintegration polarizations with MAD.

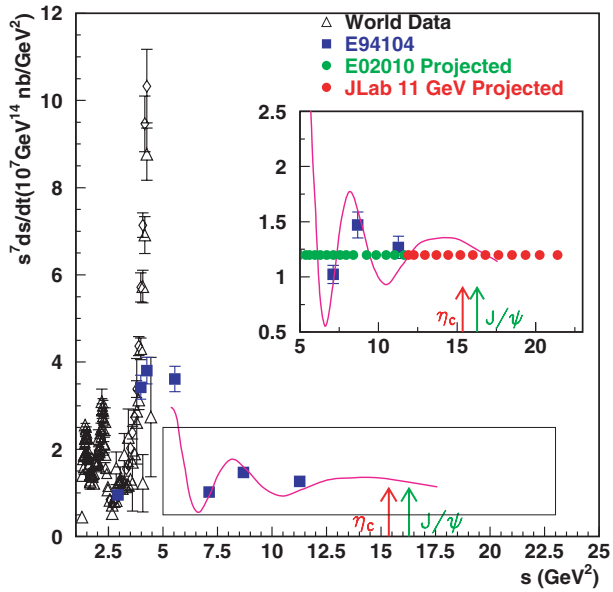


Figure 124: The scaled differential cross-section for the $n(\gamma, \pi^- p)$ process at a C.M. angle of 90° , as a function of C.M. energy squared s in GeV^2 along with the projected measurements for JLab at 11 GeV (red). The green points are the projected results from E02-010 and the blue points show the completed E94-104 data points.

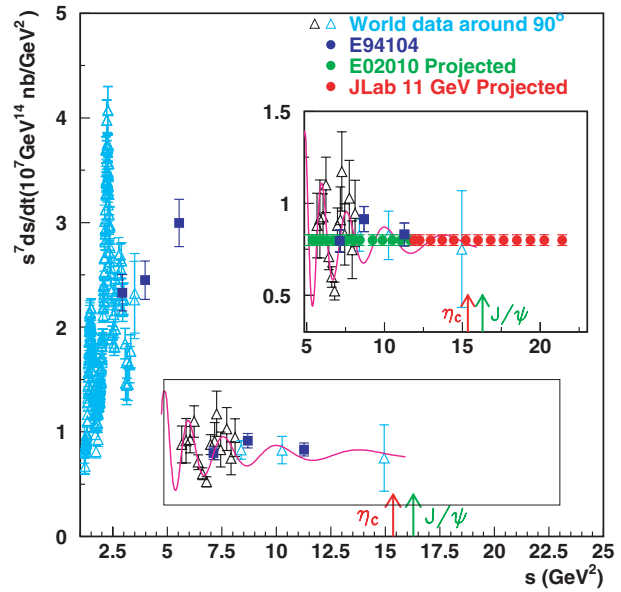


Figure 125: The scaled differential cross-section for the $p(\gamma, \pi^+ n)$ process at C.M. angle of 90° , as a function of cms energy squared s in GeV^2 along with the projected measurements for JLab at 11 GeV (red). The green points are the projected results from E02-010 and the blue points show the completed E94-104 data points.

establishing the experimental support of the constituent quark counting rule. This includes: the oscillation of the differential cross-section about the scaling behavior predicted by quark counting rules (s^{-10} for pp elastic scattering) and the anomalous spin correlation coefficient A_{nn} observed in pp elastic scattering [Cr78, Co86]. Theoretical interpretation for such an oscillatory behavior and the spin-correlation in pp elastic scattering was attempted [Br79] within the framework of quantum chromodynamic quark and gluon interactions, where interference between hard pQCD short-distance and long-distance (Landshoff [La74]) amplitudes was discussed for the first time. This QCD process is analogous to the QED effect of Coulomb-nuclear interference observed in low energy charged particle scattering. Lastly, Carroll *et al.* [Ca88] reported the anomalous energy dependence of the nuclear transparency from the quasi-elastic $A(p, 2p)$ process: the nuclear transparency first rises followed by a decrease. This intriguing result was confirmed recently at Brookhaven [Ma98a] with improved experimental technique. Ralston and Pire [Ra02] explained the free pp oscillatory behavior in the scaled differential cross section and the $A(p, 2p)$ nuclear transparency results using the ideas of interference between the short-distance and long-distance amplitudes and QCD nuclear filtering. Carlson, Chachkhunashvili, and Myhrer [Ca92] have also applied such an interference concept to pp scattering and have explained the pp polarization data. On the other hand, Brodsky and de Teramond [Br88] proposed that the structure seen in $s^{10} \frac{d\sigma}{dt}(pp \rightarrow pp)$, A_{nn} spin correlation [Cr78, Co86], and the $A(p, 2p)$ transparency result can be attributed to new $c\bar{c}uuduu$ resonant states.

Whether similar phenomena occur in pion production is an open problem. The results from E94-104, at 90° c.m. angle, suggest an onset of scaling behavior around a center-of-mass energy of 2.5 GeV and show very interesting hints of possible oscillation in the scaled differential cross-section for the $\gamma n \rightarrow \pi^- p$ and $\gamma p \rightarrow \pi^+ n$ channels. Precision measurements of these fundamental cross-sections would be a timely guide for theoretical efforts on this subject (see for instance [Is01, Zh03]) and would help understand the exact mechanism behind the scaling behavior observed in exclusive processes. An experiment (E02-010) to perform a fine scan of the region between $2.3 \text{ GeV} < \sqrt{s} < 3.4 \text{ GeV}$ with photo-pion production from nucleons was recently approved. With the upgrade of JLab energy to 12 GeV, these measurements will be extended up to $\sqrt{s} = 4.6 \text{ GeV}$, above the charm production threshold.

Coincidence measurements from deuterium, $d(\gamma, \pi^- p)$, are necessary in order to study the fundamental $\gamma n \rightarrow \pi^- p$ process. The combination of HMS and the planned Super-HMS spectrometers in Hall C makes this experiment feasible. Figure 124 shows the projected result as a function \sqrt{s} for the $\gamma n \rightarrow \pi^- p$ process together with a 3% point-to-point systematic uncertainty and a 2% statistical uncertainty. For the $\gamma p \rightarrow \pi^+ n$ process, the detection of the π^+ particle alone is sufficient. Figure 125 shows the projected result as a function \sqrt{s} for the $\gamma p \rightarrow \pi^+ n$ process together with a 3% point-to-point systematic uncertainty and a 2% statistical uncertainty, when the π^+ is detected in the Hall A Medium Acceptance Spectrometer (MAD).

Polarization measurements can play a crucial role in understanding reaction mechanisms of

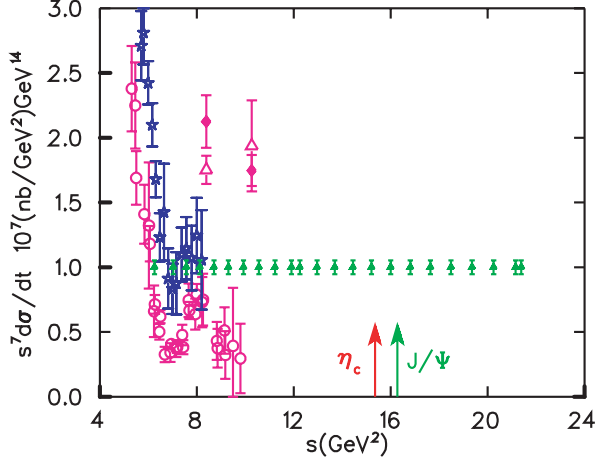


Figure 126: The scaled differential cross-section for the $p(\gamma, \pi^0)p$ process at C.M. angle of 90° , as a function of cms energy squared s in GeV^2 along with the projected measurements for JLab at 11 GeV (green).

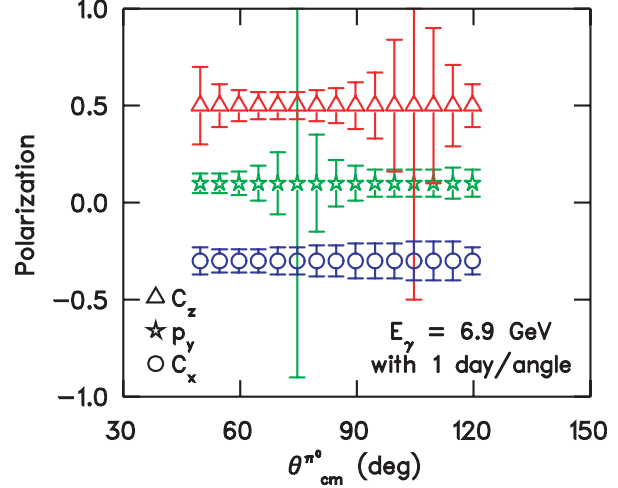


Figure 127: Estimated uncertainties for the induced polarization in $\vec{\gamma}p \rightarrow \vec{p}\pi^0$ for $E_\gamma = 6.9$ GeV, as a function of π^0 angle. The value chosen for the polarizations is arbitrary. One day of beam time at each angle is assumed. Similar quality angular distributions would be obtained at the same time for several additional 200 MeV bins in photon energy. See text for further details.

wide angle meson photoproduction at high energy. The scattering amplitude at asymptotic energies is dominated by multi-gluon exchange within the minimal Fock-state of the nucleon and meson. The soft overlap process that likely dominates in Real Compton Scattering at energies below the asymptotic limit is also expected in the meson production case. These two mechanisms predict large, but opposite sign, polarization transfer observables.

Recoil polarimetry of the proton, in neutral pion photoproduction, allows a determination of the induced polarization p_y and the polarization transfers C_x and C_z , for a longitudinally polarized electron beam. Recent Hall A experiments, G_{Ep} (E99-007) and RCS (E99-114), have demonstrated the feasibility of using a calorimeter for coincidence measurement of the two photons from the π^0 decay, allowing a clean measurement of $\vec{\gamma}p \rightarrow \vec{p}\pi^0$. Fig. 126 shows the projected result for the differential cross section measurement for the $\gamma p \rightarrow \pi^0 p$ process together with a 5% point-to-point systematic uncertainty and a 2% statistical uncertainty. Figure 127 shows estimated uncertainties for the recoil polarization that could be obtained with a polarimeter installed in MAD, and a coincident π^0 detection to reduce background.

Pion Photoproduction in the Nuclear Medium In the nuclear medium, it has been suggested that these long distance amplitudes are suppressed (nuclear filtering) by the strongly interacting nuclear environment [Ra90]: The oscillation phenomena arising from their interference

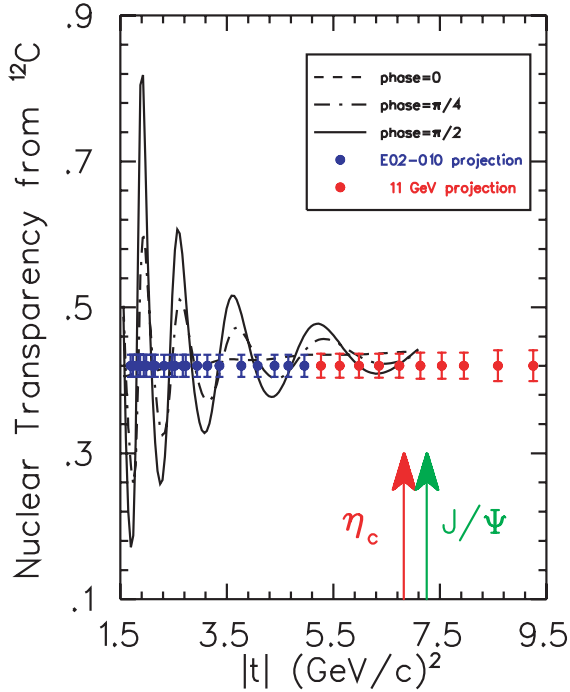


Figure 128: The projected results for nuclear transparency for photo-pion production from a ^{12}C target. The lines are calculations from Ref [Ja02].

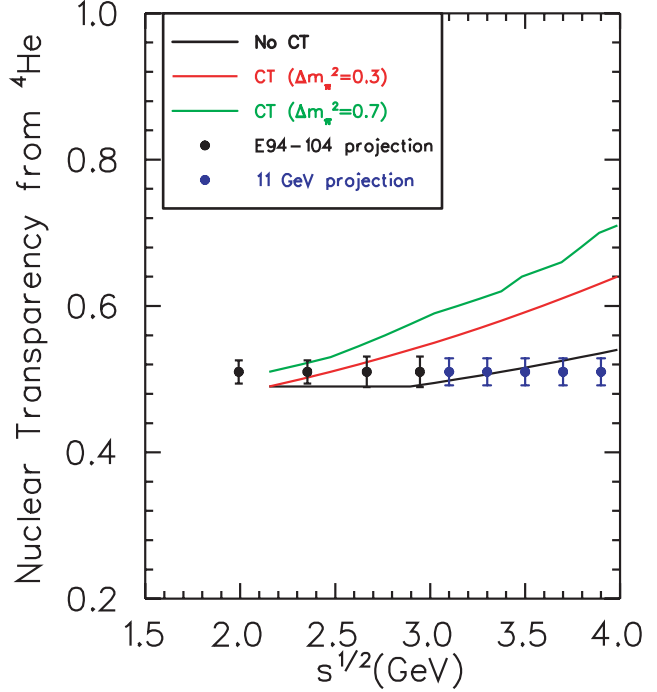


Figure 129: The projected results for nuclear transparency for photo-pion production from a ^4He target. The lines are color transparency calculations from Ref [Ga96].

with the short distance amplitude is expected to disappear in nuclear medium. The experimental manifestation of this effect is predicted to be in the form of oscillations in nuclear transparency³, which are 180° out of phase with oscillations in the scaled free differential cross-section. The nuclear filtering effect can be studied with photo-pion production from nuclei such as ^{12}C . The preliminary results from the exploratory data taken on a ^4He target during E94-104 demonstrated the experimental technique. With JLab at 12 GeV, search of nuclear filtering will be extended beyond the charm threshold. Figure 128 shows the projected results on the ^{12}C nuclear transparency measurement of the $\gamma n \rightarrow \pi^- p$ process, in which a 3% point-to-point systematic uncertainty along with a 2.0% statistical uncertainty are shown. Different curves shown in Fig. 128 correspond to different phase angles in the two-component model by Jain and Ralston [Ja02], which explains the Brookhaven A(p,2p) [Ca88, Ma98a] nuclear transparency data.

Color Transparency (CT), discussed previously in Section 2.C.1, is another phenomenon which will be studied with pion photoproduction in the nuclear medium. While nuclear filtering uses the nuclear medium actively, in CT large momentum transfers select out the short distance amplitude which are then free to propagate through the passive nuclear medium. The preliminary E94-104

³Nuclear transparency is defined as the ratio of the cross-section for a specified physical process from a nuclear target to a modeled cross-section based on the specified process from a free nucleon target within the plane-wave impulse approximation normalized by the number of nucleons in the nuclear target.

^4He nuclear transparency results from the $\gamma n \rightarrow \pi^- p$ process at a 90° center-of-mass angle up to a center-of-mass energy of 3.0 GeV show a very intriguing momentum transfer dependence of the nuclear transparency. With a 12 GeV CEBAF and the upgraded detection system, the nuclear transparency of the $\gamma n \rightarrow \pi^- p$ process from ^4He can be extended to a $|t|$ value of ~ 10 (GeV/c) 2 . Such an extension allows detailed investigation of the onset of color transparency. The projected results are shown in Fig. 129, in which a 3% point-to-point systematic uncertainty along with a 2.0% statistical uncertainty are shown.

With the 12 GeV energy upgrade and the planned upgrade of instrumentation, the transition region can be studied systematically using the simplest system: pion, nucleon, deuteron and helium with precisions, which allow definitive statements about the onset of the transition. This study is also important and coupled closely to other important nuclear physics questions which are discussed previously.

2.D Symmetry Tests in Nuclear Physics

Precision parity-violating electron scattering experiments made feasible by the 12 GeV Upgrade have the sensitivity to search for deviations from the Standard Model that could signal the presence of new gauge bosons Z' s, the existence of leptoquarks, or particles predicted by supersymmetric theories, *i.e.* physics beyond the Standard Model. Planned studies of the three neutral pseudoscalar mesons, the π^0 , η and η' , will provide fundamental information about low energy QCD, including certain critical low energy parameters, the effects of SU(3) and isospin breaking by the u , d , and s quark masses, and the strengths of the two types of chiral anomalies. These two programs are described briefly below, and in detail in below.

2.D.1 Standard Model Tests

Tests of fundamental symmetries have been an important area of study in nuclear physics for decades. Studies of parity-violation in β -decay and electron scattering, time-reversal violation in nuclear decays and electromagnetic interactions, and lepton number violation in neutrinoless $\beta\beta$ -decay—to mention a few examples—have contributed in significant ways to our understanding of the structure of the Standard Model of the electroweak interaction. Now, attention is focused on what may lie beyond the Standard Model (SM). There exist numerous theoretical and phenomenological reasons for believing that the SM is only part of a larger, more fundamental framework. Uncovering the structure of the “new” Standard Model will require a concerted effort involving both experiment and theory. On the experimental side, important information will be gleaned from both high-energy collider studies as well as highly precise, low-energy measurements. In this respect, precision electroweak nuclear physics will continue to play an important role. Indeed, this fact was highlighted in the April 2002 NSAC Long Range Plan [NS02], which identified “What is to be the new Standard Model?” as one of the five scientific questions that would drive nuclear science for the next decade.

Tests of fundamental symmetries are also helping to elucidate presently poorly understood aspects of the strong interaction in the non-perturbative domain. The parity-violating electron scattering (PVES) program currently underway at Jefferson Lab represents an excellent example of using a symmetry violation to study novel aspects of non-perturbative nucleon structure. The parity-violating weak, neutral current electron-quark interaction provides one of the only tools we have for probing the $s\bar{s}$ sea over distance scales where a valence quark description of the nucleon has been assumed to be adequate. It remains a mystery as to why the valence quark model should work so well, given what we know about the role played by sea quarks and gluons in high-energy scattering processes. The use of parity-violation in electron scattering is shedding new light on this fundamental problem.

There exists a powerful synergy between these two uses of symmetry violation in nuclear physics. For example, the use of parity-violation to study nucleon structure requires that one have a sufficiently clear understanding of the weak interaction at a fundamental level. Conversely, the search for a new SM through precision parity-violation experiments involving nuclei depends upon having a sufficiently reliable understanding of non-perturbative QCD effects. In this respect, the Q-Weak experiment, to which Jefferson Laboratory has made a substantial commitment, provides an illustrative example. This experiment will provide a probe of new physics at the TeV scale. It will be able to do so, however, only because the present program of PVES measurements will reduce the uncertainty associated with non-perturbative QCD effects in the PV asymmetry to an acceptably small level. To the extent that both the strange quark and Q-Weak endeavors are successful, Jefferson Lab will have made substantial contributions to both nuclear and particle physics by exploiting the opportunities provided by PVES.

The proposed up-grade of CEBAF will amplify these opportunities. Below, we discuss two types of PVES experiments that will build on the successes of the presently approved program: parity-violating Møller scattering and PV deep inelastic electron-deuteron scattering. At present, a PV Møller experiment is being performed at SLAC. With the 12 GeV upgrade and the luminosity provided by the accelerator, one could perform a future version of the SLAC experiment with considerably smaller uncertainties. As discussed below, precision which could be achieved would allow one to probe various aspects of supersymmetry, such as the existence of a viable supersymmetric candidate for cold dark matter.

The second prospective experiment—PV deep inelastic scattering (DIS) with a deuteron target—could be envisioned either as a probe of new physics or as a tool to study higher-twist structure functions. The motivation in either case is strong. From the perspective of new physics, a study of PV DIS would complement the recent work of the NuTeV collaboration [Ze01], which studied deep inelastic ν ($\bar{\nu}$)-nucleus scattering from iron. The results of the NuTeV experiment may be interpreted as a determination of the Q^2 -dependence of the weak mixing angle, and indicate a 3σ -deviation from the SM prediction for this quantity. It is difficult to accommodate such a sizeable discrepancy through the most widely-considered new physics models, so the NuTeV anomaly could

be particularly important in this context. However, a debate has emerged as to the size of possible non-perturbative QCD contributions that may reduce the significance of the anomaly. A study of PV DIS could provide a complementary probe of the Q^2 -dependence of $\sin^2 \theta_W$ in the deep inelastic domain. As it would involve different systematic and non-perturbative QCD effects, it would help determine whether or not a deviation from the SM exists in this regime. Alternatively, one could study the Q^2 -dependence of the PV asymmetry in this domain in order to extract information on higher-twist structure functions. In this respect, PV DIS would represent a continuation of the strange quark program, wherein parity-violation is being used to study non-perturbative nucleon structure.

The ongoing SLAC E158/Møller experiment [Ca97a] is in the process of measuring Q_{weak}^e , with their final run taking place in the summer of 2003. This is a very important measurement, and the SLAC E158/Møller collaboration is doing an excellent job. In principle though, it will be possible to achieve half of the anticipated uncertainty of the SLAC E158/Møller experiment with 12 GeV experiment at Jefferson Laboratory, as discussed below.

A new measurement with twice the precision of SLAC E158 would be a powerful tool in the search for "new physics", and at this precision, even a result in agreement with the Standard Model would have significant consequences. For example, such a result would severely constrain the viability of SUSY models that lack a candidate particle for dark matter, the non-luminous and unexplained source of 90% of the mass of the universe [Ku02]. This is illustrated in Fig. 130, which plots δQ_{weak}^e against $\delta Q_{\text{weak}}^{\text{proton}}$ for 3000 possible SUSY parameter configurations, with the expected experimental uncertainties from Jefferson Lab's Q-Weak, SLAC E158 and a 12 GeV Jefferson lab experiment superimposed. The large shaded truncated ellipse represents an area, in which if Q_{weak}^e and $Q_{\text{weak}}^{\text{proton}}$ are found to lie, there is R-parity violation and no SUSY dark matter. Clearly a second generation Møller experiment would significantly restrict the available parameter space. While this is only one example of the impact of a more precise measurement of Q_{weak}^e , others exist [Ra99a].

The parity violating asymmetry in Møller scattering measures the weak charge of the electron, Q_{weak}^e . Observables like the weak electron and proton charges, proportional to $1 - 4 \sin^2 \theta_W$, are very sensitive to the value of $\sin^2 \theta_W$ since the latter is close to 1/4. For

$$A = f(1 - 4 \sin^2 \theta_W) + D$$

where f is a kinematic factor and D is an experimental dilution factor, the uncertainty in $\sin^2 \theta_W$ is given by

$$\frac{\delta \sin^2 \theta_W}{\sin^2 \theta_W} = -\frac{\delta A}{A} \frac{1}{4} \frac{(1 - 4 \sin^2 \theta_W + D/f)}{\sin^2 \theta_W}, \quad (54)$$

with $\delta \sin^2 \theta_W / \sin^2 \theta_W \approx 0.05 \delta A / A$ for $D = 0$. The near-vanishing of the tree-level asymmetry makes such observables sensitive to $\sin^2 \theta_W$, new physics at tree-level (*e.g.*, a Z'), and new physics via loops. Radiative corrections, not all of which are suppressed by factors of $(1 - 4 \sin^2 \theta_W)$, reduce the tree-level Møller asymmetry by about 40%.

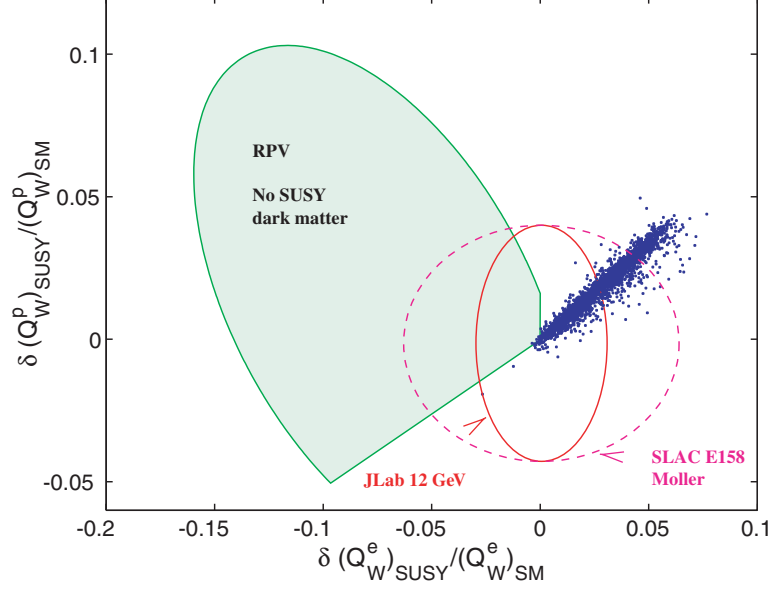


Figure 130: Relative shifts in Q_{weak}^e and $Q_{\text{weak}}^{\text{proton}}$ from SUSY effects. The blue dots indicate MSSM loop corrections for approximately 3000 SUSY-breaking parameter choices. The interior of the green truncated ellipse shows possible shifts due to R-parity violation. In this region, SUSY dark matter is excluded [Ku02]. The dashed magenta ellipse illustrates the expected uncertainty from SLAC E-158 Møller and JLab Q-Weak, while the red ellipse represents what could be achieved with a 12 GeV Møller experiment at Jefferson Laboratory.

At tree level the parity violating Møller asymmetry is [De79]

$$A_{\text{Moller}} = \frac{4m_e E G_F}{\sqrt{2}\pi\alpha} \frac{\sin^2 \theta_{\text{cm}}}{(3 + \cos^2 \theta_{\text{cm}})^2} (1 - 4 \sin^2 \theta_W) \quad (55)$$

where E is the electron beam energy. The center-of-momentum cross section is

$$\frac{d\sigma}{d\Omega} = \frac{\alpha^2}{2m_e E} \frac{(3 + \cos^2 \theta_{\text{cm}})^2}{\sin^4 \theta_{\text{cm}}} \quad (56)$$

and hence the Figure-of-Merit (FOM) defined as $A^2 d\sigma/d\Omega$ is simply proportional to the beam energy, E . All other things being equal, a measurement at 48 GeV has 4 times the FOM of a measurement at 12 GeV.

The design of the ongoing SLAC E158 is close to optimal for that facility. The 12 GeV Jefferson Lab facility can mount an improved measurement of Q_{weak}^e by employing an enormous integrated luminosity while maintaining ppb-level control of systematic uncertainties. Table 12 lists important parameters for the two experiments such as the cross section, asymmetry, and integrated luminosity. Small differences in the azimuthal acceptance and dilution have been ignored. In practical terms, the Jefferson Lab experiment would correspond to one year of running in one of the two high luminosity end-stations (32 weeks at 75% efficiency).

In Tab. 13 are compiled the proposed uncertainties for SLAC E158 and the potential Jefferson Lab 12 GeV measurement. For the Jefferson Lab measurement, systematic uncertainties are

Table 12: Parameters for the SLAC E158 experiment from the proposal compared to those for a potential Jefferson Lab experiment at 12 GeV.

Parameter	SLAC E158	12 GeV JLab
E	48 GeV	12 GeV
E'	12-24 GeV	3-6 GeV
$\langle Q^2 \rangle$	0.03 (GeV/c) ²	0.008 (GeV/c) ²
θ_{cm}	90°-120°	90°-120°
θ_{lab}	0.26°-0.46°	0.53°-0.92°
$\langle A_{\text{PV}} \rangle$	161 ppb	40 ppb
σ	16 μbarns	64 μbarns
Polarization	80%	80%
Current	9.1 μA	100 μA
LH_2 Target Length	150 cm	75 cm
Luminosity $\text{cm}^{-2}\text{s}^{-1}$	4.0×10^{38}	2.2×10^{39}
Time	1445 hours ^a	4000 hours ^b
Luminosity \times Time	$2.1 \times 10^{45} \text{ cm}^{-2}$	$3.2 \times 10^{46} \text{ cm}^{-2}$

^a20 weeks at SLAC at 43% efficiency

^b32 weeks at 75% efficiency: effectively, one year of JLab running

assumed to be limited to 1%-2% by the combination of Q^2 , beam polarization, and corrections for residual helicity-correlated differences in beam parameters. The final projected uncertainty on $\sin^2 \theta_W$ of ± 0.0004 would be competitive with the best measurements of $\sin^2 \theta_W$ at the Z^0 pole.³ More importantly, this would be the best measurement of the weak charge of the electron at low energy scales.

To put such an effort in context, all previous, ongoing, and approved Standard Model tests which employ parity violating electron scattering, along with the 12 GeV Jefferson Lab measurement under discussion are shown in Fig. 131. Since the original measurement by Prescott *et al.* [Pr78, Pr79], the difficulty of Standard Model tests employing PV electron scattering has been increasing. A 12 GeV Møller experiment would be the logical next step following successful completion of the Q-Weak (proton) experiment which is currently in preparation.

As with any precision Standard Model test, the interpretability of a 12 GeV Møller experiment is critical. The major limitation to the interpretability arises from hadronic loops in the γZ mixing diagrams [Cz96] which are also the dominant correction. If the 12 GeV Møller experiment were done today, the 3% experimental uncertainty on the measured asymmetry would be comparable to the uncertainty in the theory. Fortunately, it is likely that forthcoming results from the SLAC E158 experiment will stimulate further work in this area.

Figure 132 gives a schematic representation of the experiment. The laboratory scattering angles

³Since there are no longer any e^+e^- colliders operating near the Z pole, there will be no further high energy precision neutral current measurements until construction of some version of the Next Linear Collider.

Table 13: Projected uncertainties for ongoing SLAC E158 (from the proposal) and for a potential Jefferson Lab measurement at 12 GeV.

Uncertainties	SLAC E158	12 GeV JLab
Statistical:		
δA	10 ppb	1 ppb
$\delta A/A$	6%	3%
$\delta \sin^2 \theta_W$	0.00071	0.00036
Systematic:		
δA	4 ppb	0.4 - 0.8 ppb
$\delta A/A$	2.7%	1% - 2%
$\delta \sin^2 \theta_W$	0.00032	0.00012 - 0.00024
Combined:		
δA	11 ppb	1 ppb
$\delta A/A$	6.6%	3.2% - 3.6%
$\delta \sin^2 \theta_W$	0.00079	0.00038 - 0.00043

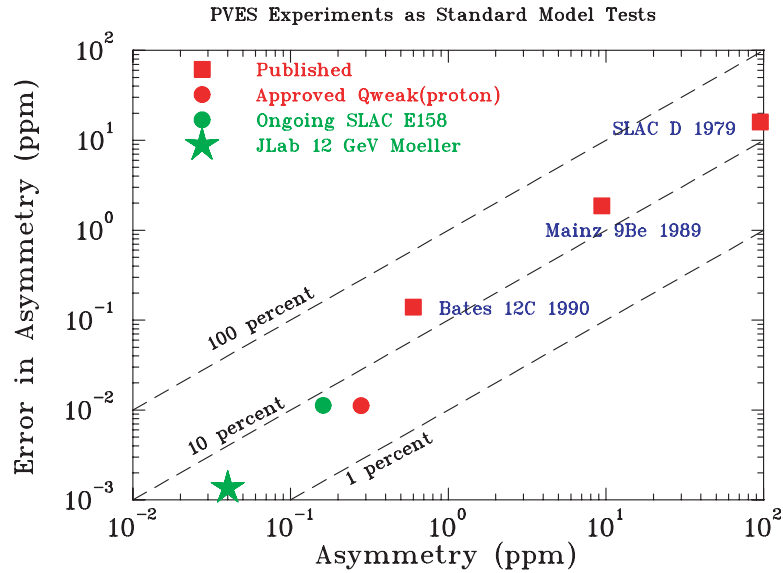


Figure 131: There has been a steady progression with time in the difficulty of Standard Models tests which employ parity violating electron scattering. (The 12 GeV Møller experiment is denoted by a star.) A new generation of experiments based on DIS might be an exception to this trend.

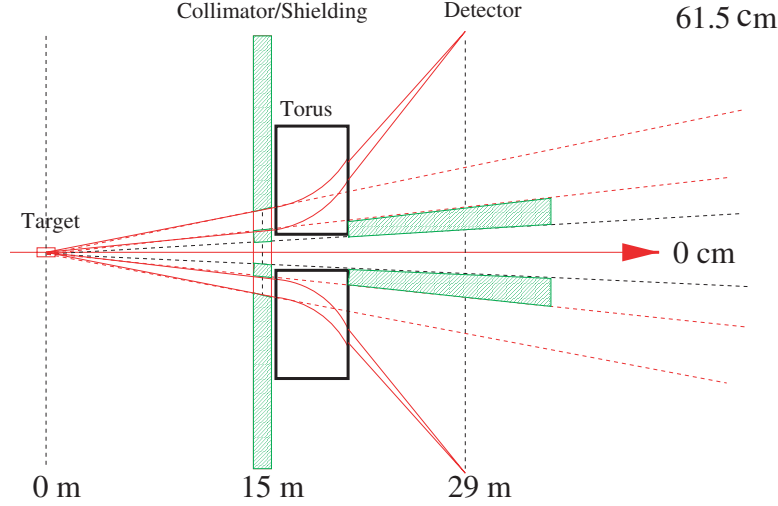


Figure 132: Schematic of a 12 GeV Møller experiment. The vertical scale is artificially magnified for visibility since the actual vertical/horizontal ratio is roughly 1:50.

are quite small, only about 0.7 degrees, and can be conveniently expressed in terms of units of the average multiple scattering angle in the thick target. To focus the Møller electrons of such small angles (momentum $4.5 \text{ GeV}/c \pm 33\%$) in an azimuthally symmetric manner, we first plan to drift the scattered electrons to a collimator. The Q^2 determination then depends only on geometry and the well-known beam energy. The electrons then enter a resistive toroidal magnet which provides a field integral tailored to the E' versus θ correlation from Møller kinematics. The $1/R$ field profile of a toroidal magnetic is well suited to this application, providing large field integrals at small radii with 75% azimuthal acceptance. Correction coils in the torus may be needed. Finally, the electrons drift to a focus on a ring of Čerenkov detectors where the Møller electron signals are integrated. Detectors at smaller and larger radii will monitor the asymmetry of backgrounds.

Despite the relatively low PV asymmetry of Møller scattering at 12 GeV, an improved measurement of Q_{weak}^e with half the proposed SLAC E158 uncertainty is achievable. This small improvement, however, is very important, when considered in terms of the allowable SUSY parameter space and SUSY dark matter.

Another PVES experiment utilizing the 11 GeV beam is a measurement of parity violation in deep inelastic scattering (DIS parity) from a deuterium target. This asymmetry is also sensitive to $\sin^2 \theta_W$. While the interpretation of DIS parity violation is not as clean as it is for Møller scattering due to higher twist contributions to the asymmetry, the experiment itself is literally several orders of magnitude easier, with an asymmetry of approximately 10^{-4} . DIS parity violation from a deuterium target was first observed by Prescott *et al.* [Pr78, Pr79] in the mid-1970's and was used to establish the Weinberg-Salam model. With the upgrade of Jefferson Lab to 12 GeV, this measurement can be repeated, with the precision necessary to once again confront the Standard Model. This measurement is made more interesting by the recent report from the NuTeV collab-

oration, using neutrino scattering on iron, of $\sin^2 \theta_W^{\text{on-shell}} = 0.2277 \pm 0.001(\text{stat}) \pm 0.0009(\text{syst})$, three standard deviations above the Standard Model predictions [Ze01]. Naturally, this difference has been interpreted in terms of physics beyond the Standard Model (new propagator or couplings, dimension six operators, extra U(1) gauge bosons, etc.) [Da01]. However, there are also more conventional explanations, including nuclear effects in the iron target [Mi02b] and QCD effects [Da01]. DIS-Parity violation using an 11 GeV beam electron beam could quite quickly achieve the statistical sensitivity needed to investigate the NuTeV result at Q^2 near that of NuTeV. Using a deuterium target, it will not suffer from the uncertainties in nuclear effects and nuclear parton distributions that were present in the NuTeV iron measurement.

The parity-violating asymmetry for scattering longitudinally polarized electrons from an unpolarized isoscalar target such as a deuteron (assuming charge symmetry) is given by [Ca78a]

$$A_d = \frac{\sigma_L - \sigma_R}{\sigma_L + \sigma_R} = - \left(\frac{3G_F Q^2}{\pi\alpha 2\sqrt{2}} \right) \frac{2C_{1u} - C_{1d} [1 + R_s(x)] + Y(2C_{2u} - C_{2d})R_v(x)}{5 + R_s(x)}. \quad (57)$$

The $C_{1u(d)}$ represents the axial Z -electron coupling times the vector Z - u quark (d quark) coupling, and the $C_{2u(d)}$ are the vector Z -electron coupling times the axial Z - u quark (d quark) coupling. Taking $\sin^2 \theta_W \approx 0.231$,

$$\begin{aligned} C_{1u} &= -\frac{1}{2} + \frac{4}{3} \sin^2 \theta_W \approx -0.192, & C_{1d} &= \frac{1}{2} - \frac{2}{3} \sin^2 \theta_W \approx 0.346, \\ C_{2u} &= -\frac{1}{2} + 2 \sin^2 \theta_W \approx -0.038, & C_{2d} &= \frac{1}{2} - 2 \sin^2 \theta_W \approx 0.038. \end{aligned}$$

Also

$$Y = \frac{1 - (1 - y)^2}{1 + (1 - y)^2 - y^2 R / (1 + R)} \text{ with } y = \nu/E.$$

Here, $\nu = E - E'$ is the energy lost by an incident electron of energy E scattering to an electron of energy E' , and the ratio $R = \sigma_L/\sigma_T \approx 0.2$ depends on x and Q^2 . The ratios $R_s(x)$ and $R_v(x)$ depend on the quark distribution functions:

$$R_s(x) = \frac{s(x) + \bar{s}(x)}{u(x) + \bar{u}(x) + d(x) + \bar{d}(x)} \quad \text{and} \quad R_v(x) = \frac{u_v(x) + d_v(x)}{u(x) + \bar{u}(x) + d(x) + \bar{d}(x)}.$$

At high x , where sea quark contributions vanish, $R_v = 1$ and $R_s = 0$, we find

$$A_d \approx 10^{-4} Q^2 (0.73 + 0.11Y).$$

The sensitivity to $\sin^2 \theta_W$ is approximately given by

$$\frac{d \sin^2 \theta_W}{\sin^2 \theta_W} \approx \frac{dA}{A} \frac{0.95 + 0.15Y}{1.0 + 1.8Y}. \quad (58)$$

The dependence of the asymmetry on Y will allow for the extraction of $2C_{1u} - C_{1d}$ and $2C_{2u} - C_{2d}$ separately. The sensitivity to the $2C_{2u} - C_{2d}$ makes the experiment quite unique. Since “new” physics may affect each of these coefficients in a different way, the ability to separate these coefficients may provide an additional tool to understand how “new” physics contributes [Ra99a].

To have the best sensitivity to $\sin^2 \theta_W$ while minimizing systematic uncertainties imposes several conditions on experimental conditions. These include requiring $x > 0.2$ to minimize uncertainties from parton distributions, and using a deuterium target where the $d(x)/u(x)$ ratio is known. At the same time, to minimize effects from higher twist, $x \lesssim 0.4$. In addition, the experiment must be run in the DIS region to ensure that the scattering is from quarks, with $Q^2 > 1 \text{ GeV}^2$ and $W^2 > 4 \text{ GeV}^2$. It is also important to keep $E'/E > 0.3$ to avoid large rates of pions and pair-symmetric backgrounds in the detectors. Given these constraints, a possible set of running conditions for an 11 GeV beam would be a scattering angle of 12.5° with spectrometer central momentum of 5.5 GeV, corresponding to $\langle x \rangle = 0.28$, $\langle Q^2 \rangle = 2.9 \text{ GeV}^2$, $\langle W^2 \rangle = 8.3 \text{ GeV}^2$ (well above the resonance region), and $\langle Y \rangle = 0.62$.

With these kinematics, a beam current of $90 \mu\text{A}$ with 80% polarization and a 60 cm liquid deuterium target, the experiment could be completed in an extremely modest amount of time. Using a set of spectrometers with a total acceptance of 12 msr and a momentum bite of $\pm 10\%$, a relative statistical uncertainty on the deuterium asymmetry of 0.6% and a corresponding uncertainty of 0.26% in $\sin^2 \theta_W$ can be achieved in only 275 “ideal” hours of beam time. In this configuration, a rate of less than 1 MHz of DIS electrons is expected, with a similar rate from pions.

The spectrometer solid angle and momentum bite assumptions are matched to the combination of the HMS and SHMS spectrometers in Hall C or the HRS/MAD combination in Hall A, allowing the experiment to be performed in either of these Halls. At these event rates, the wire chamber and time-of-flight information would not be used—events would require a coincidence between the Čerenkov counters and lead glass calorimeters in the spectrometers. Flash ADCs, similar to those planned for Hall D, will be required on the counters to run in “event mode”. The Čerenkov counters will have to be adjusted (gas mixture, pressure) to have a threshold about 6 GeV for pions. The overall target length of 60 cm is limited by the desire to keep radiative corrections down and is well matched to the optical acceptance of the spectrometers under consideration. With $90 \mu\text{A}$ of current, this then requires roughly 2 kW of cooling power, equivalent to that needed by the Q-Weak experiment [Ca01] in Hall C.

Given the relatively large asymmetry the statistical uncertainty may be made small in a short amount of beam time, and systematic effects will be the dominant source of uncertainties in this experiment. The largest of these uncertainties in A_d is expected to be from the beam polarization measurement (of order 1%). The uncertainty in A_d due to radiative corrections should be well under 1%, and the uncertainty due to the determination of the average Q^2 should be under 0.5%. The uncertainty propagated from the parton distributions [Pu02, Ma02a] is less than 0.1% in A_d . The uncertainty in $R = \sigma_L/\sigma_T$ is also well known and will contribute less than 0.4% in A_d . Because the asymmetry is several orders of magnitude larger than the Q-Weak and G0 experiments, control of helicity-correlated beam parameters should be adequate if they can be maintained at G0 levels when the beam energy is upgraded. Possible breaking of charge symmetry could lead to corrections. Fortunately, these effects are small—a large 0.5% charge symmetry violation would only contribute

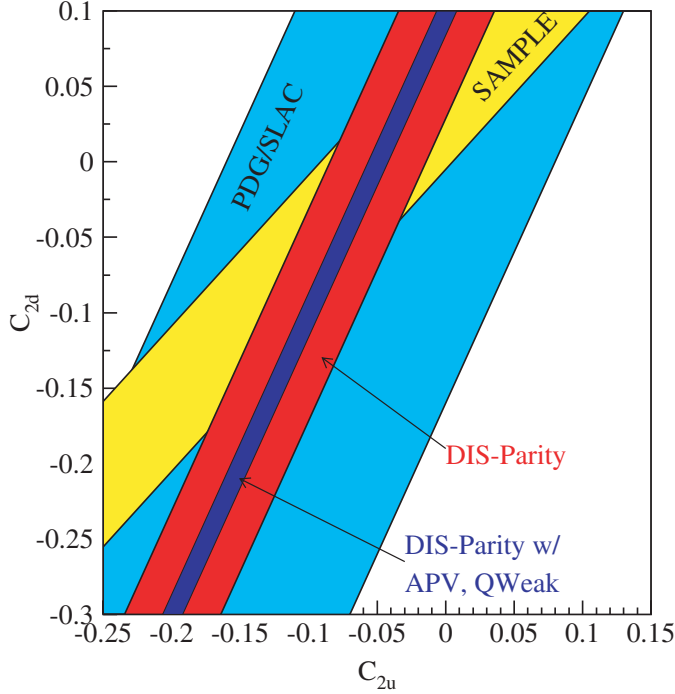


Figure 133: The limits on C_{2u} and C_{2d} listed by the particle data group [PDB], by the SAMPLE experiment [Ha01, Bepc] and by the proposed experiment (DIS-Parity) [Bo94a].

Table 14: This table lists possible sources of systematic uncertainty in the measurement of A_d . The dominate uncertainty is the knowledge of the beam polarization, and the influence of higher twist effects. Recall that $\delta \sin^2 \theta_W / \sin^2 \theta_W \approx 1/2 \delta A_d / A_d$.

Effect	δA_d (%)	Effect	δA_d (%)
Polarization	1.0%	$\delta \langle Q^2 \rangle$	0.5%
$\delta R_s, \delta R_v$	0.1%	$\delta R = \delta \sigma_L / \sigma_T$	0.4%
Charge Sym. Violation.	0.1%	Higher Twist	?

0.1% to A_d . Charge symmetry violation effects, nuclear shadowing, and the “EMC Effect” in the deuteron can also be addressed by measuring the asymmetry with a proton target, if the d/u quark ratio is sufficiently well known at the desired kinematics from other experiments. These systematic uncertainties are summarized in Tab. 14. Combining these uncertainties, the deuterium asymmetry will be measured to $\delta A_d = \pm 0.6\%$ (stat.) $\pm 1.2\%$ (syst.), or $\delta \sin^2 \theta_W \approx \pm 0.3\%$ (stat.) $\pm 0.6\%$ (syst.), excluding higher twists effects as discussed below. This uncertainty is shown in Fig 134. With the successful completion of the Jefferson Lab Q-Weak experiment, $C_{1u(d)}$ will be known to an absolute uncertainty of $\delta C_{1u(d)} = 0.005$. This will allow the proposed experiment to place an absolute uncertainty of $\delta(C_{2u} - \frac{1}{2}C_{2d}) = 0.019$. When taken together with the results from the SAMPLE experiment [Ha01] much tighter bounds are placed on C_{2u} and C_{2d} than were previously available [PDB] as illustrated in Fig. 133.

A more difficult uncertainty relates to the interpretation, because higher twist effects may not be negligible at the relatively low Q^2 of about 3 GeV^2 . This may be partially addressed by making an additional measurement at lower Q^2 , and another at higher Q^2 and x . Although the lever arm available to look for $1/Q^2$ effects is limited with a maximum beam energy of 11 GeV , these measurements would be able to determine if sizable effects are present. In addition, measurement at other laboratories, such as the proposed SLAC measurement of A_d at $Q^2 \approx 20 \text{ GeV}^2$ [Bo03] will greatly help in the understanding of higher twist effects. Higher twist effects may also be minimized by selecting a kinematic region in which $x < 0.4$, which unpolarized DIS data have already shown smaller higher twist effects. (This is consistent with the kinematics given above.) Within the context of the bag model, Castorina and Mulders [Ca85] have calculated the effect of twist-four corrections on $\sin^2 \theta_W$ as measured by DIS parity violation on deuterium and find that $\delta_{HT} \sin^2 \theta_W \approx -6.5 \times 10^{-4}/Q^2$. Fajfer and Oakes [Fa84] calculate a slightly smaller effect; although Brodsky [Br00b] comments that these calculations may yield too small of an effect at high- x . Clearly, significant theoretical support will be needed to control all of these uncertainties to the desired level. It should be pointed out that the study of parity-violating higher twist effects is quite interesting in its own right, and that a comparison with higher- Q^2 data (*e.g.* the SLAC LOI) would, by itself, be a worthwhile study.

DIS parity violation offers Jefferson Lab the opportunity to perform a measurement of $\sin^2 \theta_W$ to an 0.6% relative uncertainty by measuring a relatively *large* asymmetry of 10^{-4} . This measurement would serve as a much needed check on the recent $\sin^2 \theta_W$ results from NuTeV. At the same time by measuring the $C_{2u} - \frac{1}{2}C_{2d}$, the proposed experiment is complimentary to both the Møller and Q-Weak experiments in its sensitivity to extensions of the Standard Model.

The upgrade of CEBAF to 12 GeV will allow us to continue to build on the success of previous parity violating electron scattering experiments. Two complementary, 11 GeV PVES experiments have been outlined here, Møller scattering and DIS parity violation from deuterium. Within the Standard Model, both of these experiment will measure $\sin^2 \theta_W$, as shown in Fig. 134, but they are sensitive to different possible Standard Model extensions. The Møller experiment, while much more difficult, has a much cleaner interpretation and could have a significant impact on the understanding of dark matter with in the context of SUSY. The asymmetry in DIS parity violation from deuterium is much larger than the Møller asymmetry and is also sensitive to $\sin^2 \theta_W$. The interpretation is somewhat less clean, however, due to possible higher twist contributions to the measured asymmetry. It is important to remember that the experiments measure different couplings, and as such, are sensitive to *different* possible extensions to the Standard Model. “New” physics may present itself in some but not all of these measurements, thus requiring the complementarity presented by a broad program of measurements.

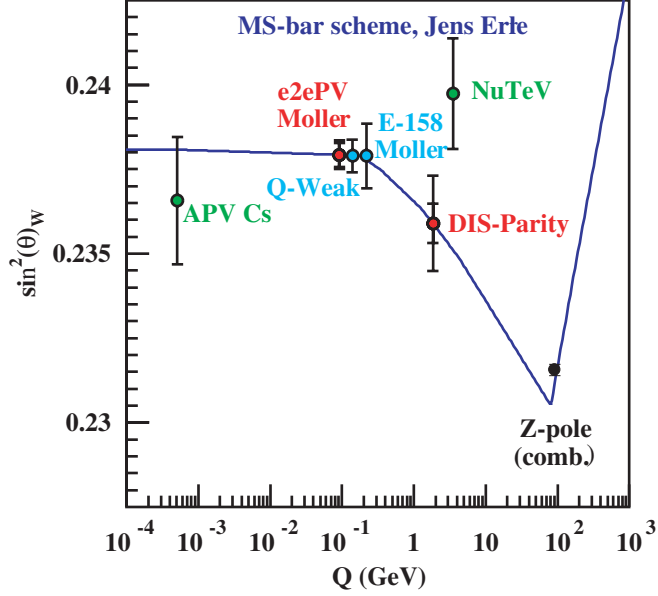


Figure 134: The running of $\sin^2\theta_W$ in the \overline{MS} scheme [Erpc], showing the two measurements discussed here (e2ePV/Møller and DIS-Parity). The inner error bars represent the statistical uncertainty and the outer represent the statistical and systematic uncertainty combined in quadrature. Also shown are the existing measurements from Cs Atomic Parity Violation [Wo97, Be99b, Mi02c], NuTeV ν DIS [Ze01], a combined Z-pole measurement [Erpc]. The proposed measurements of Q-Weak (proton) [Ca01], SLAC E-158 Møller scattering [Ca97a] are also shown with their expected uncertainties. Given the different couplings measured by the individual experiments, “new” physics may present itself by a deviation from the running curve in some but not all of these measurements.

2.D.2 Properties of Light Pseudoscalar Mesons via the Primakoff Effect

The future availability of high quality, high duty factor 12 GeV electron beams at Jefferson Lab will enable unprecedented new opportunities to perform precise measurements of meson decay widths and electromagnetic transition form factors. In particular, the high energy electro- and photoproduction of pseudoscalar mesons in the Coulomb field of a nucleus, the Primakoff effect, can be exploited to study the two photon decay widths, $\Gamma_{\gamma\gamma}$, and the transition form factors, $F_{\gamma\gamma^*P}$, where P represents the π^0 , η , and η' pseudoscalar mesons. This comprehensive program will provide fundamental tests of both QCD as well as QCD inspired models. In addition to the proposed 12 GeV upgrade to the CEBAF accelerator, a high energy photon tagging facility and an upgraded PrimEx calorimeter for detection of multiphoton states and scattered electrons will be required.

The three neutral pseudoscalar mesons, π^0 , η and η' , represent one of the most interesting systems in strong interactions. This system contains fundamental information about the effects of chiral, SU(3) and isospin breaking by the u , d , and s quark masses as well as about effects driven by chiral anomalies. Precise experimental and theoretical study of these mesons is therefore

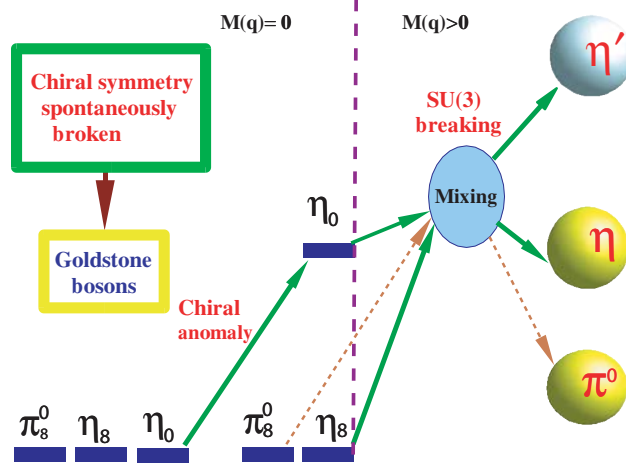


Figure 135: Symmetry breaking and quark mass effects for the light pseudoscalar mesons.

necessary for extracting and understanding that information. The QCD Lagrangian is invariant under an enlarged group of flavor symmetry transformations in the limit of massless quarks (chiral limit). This group is $SU_L(3) \times SU_R(3) \times U_A(1) \times U_{baryon}(1)$. In the full quantum theory, these symmetries are realized differently. The $U_A(1)$ symmetry turns out to be broken explicitly by the axial anomaly involving the associated Noether current $j_A^\mu = \bar{q}\gamma^\mu\gamma_5q$ and the gluon fields (see for instance [Do92]). This implies that QCD at the quantum level has a smaller symmetry, namely $SU_L(3) \times SU_R(3) \times U_{baryon}(1)$. The condensation of quark-anti-quark pairs in the QCD vacuum gives rise to a phenomenon of spontaneous breaking of this chiral symmetry down to the flavor $SU(3)$ symmetry, which is the symmetry of the vacuum. As a result, there are eight massless Goldstone Bosons (GBs) corresponding to the eight spontaneously broken symmetry generators. The eight GBs are identified with the octet of pseudoscalar mesons (π^0 , π^\pm , K^\pm , K^0 , \bar{K}^0 , and η). In reality, the quark masses are non zero (albeit small), thus breaking the chiral symmetry explicitly and giving rise to masses for the GBs. (See Fig. 135.)

The η' is prevented from being a GB of spontaneously broken $U_A(1)$ symmetry by the axial anomaly, which gives the η' a good fraction of its rather large mass. It is, however, important to note that in a certain limit in QCD, the η' does become a GB. This is the limit in which the number of colors, N_c , is large. In this limit the axial anomaly, which is proportional to $\alpha_s \sim 1/N_c$, vanishes. This limit has been recently exploited to build a highly predictive theoretical framework for studying the η' . There is a second type of anomaly that emerges when electromagnetism is turned on. This leads to a similar non-vanishing divergence of the axial currents:

$$\partial_\mu j_{Aa}^\mu \Big|_{\text{em Anomaly}} = \frac{C_a \alpha_{\text{em}}}{4\pi} \epsilon^{\mu\nu\rho\sigma} F_{\mu\nu} F_{\rho\sigma}, \quad (59)$$

where $a = 0, 3, 8$ labels the $U(3)$ generator, $C_0 = \sqrt{8/3}$, $C_3 = 1$ and $C_8 = \sqrt{1/3}$, and F is the electromagnetic field. These EM anomalies play a crucial role in the physics of the (π^0, η, η') complex, being directly responsible for the decays of the three mesons into photon pairs. In the

chiral limit, they lead to a rigorous prediction of the π^0 , η and η' decay amplitudes into two photons:

$$A(P \rightarrow \gamma\gamma) = A_{P\gamma\gamma} \epsilon^{\mu\nu\rho\sigma} \epsilon_\mu \epsilon'_\nu k_\rho k'_\sigma, \quad (60)$$

where P is one of the pseudoscalar mesons (π^0, η, η'), ϵ and k represent photon polarizations and momenta respectively, and $A_{\pi^0\gamma\gamma} = -i \frac{\alpha_{em}}{8\pi F_\pi}$, $A_{\eta_8\gamma\gamma} = -i \frac{\alpha_{em}}{8\sqrt{3}\pi F_{\eta_8}}$, and $A_{\eta_0\gamma\gamma} = -i \frac{\alpha_{em}}{\sqrt{24}\pi F_{\eta_0}}$. The F 's are the corresponding meson decay constants. While in the chiral limit SU(3) symmetry implies that $F_\pi = F_{\eta_8}$, F_{η_0} is not constrained by symmetries. However, in the limit of large number of colors (large N_c limit), one has $F_{\eta_0} = F_\pi$. Thus, in the chiral and large N_c limits the two-photon decays can be predicted. The important question is then what are the effects of the quark masses and the corrections due to the fact that $N_c = 3$.

Indeed, the relatively straightforward situation of the chiral limit becomes much more complex when the quark masses are non-vanishing. In the real world the current quark masses are estimated to be $m_u \sim m_d/2 \sim 5$ MeV and $m_s \sim 150$ MeV at the renormalization QCD scale of about 1 GeV. These masses make the π^0 and the η massive and shift the mass of the η' due to explicit breaking of chiral symmetry, while SU(3) and isospin breaking induce mixings among the three mesons. The mixings are expressed in terms of three mixing angles [Go02]. Writing the eigenstates in the chiral limit on the left, they are expressed in terms of the physical states by:

$$\begin{aligned} \pi_8^0 &= \pi^0 - \epsilon\eta - \epsilon'\eta' \\ \eta_8 &= \cos\theta (\eta + \epsilon\pi^0) + \sin\theta (\eta' + \epsilon'\pi^0) \\ \eta_0 &= -\sin\theta (\eta + \epsilon\pi^0) + \cos\theta (\eta' + \epsilon'\pi^0). \end{aligned} \quad (61)$$

A recent global analysis [Go02] has been performed that uses as input the two-photon decay widths of the η and η' and includes next to leading order chiral corrections as well as $1/N_c$ corrections. It gives: $\epsilon \sim 0.8^\circ$, $\epsilon' \sim 0.3^\circ$ and $\theta \sim -12^\circ$ for these mixing angles. The angles ϵ and ϵ' play an important role in the lifetime of the π^0 , decreasing it by approximately 4% [Go02, Mo95].

Recently, a framework that implements the chiral and $1/N_c$ corrections was developed [Go02, He97, Ka00]. This framework is a faithful representation of low energy QCD, relying only on the validity of the chiral expansion in the strange quark mass and the expansion in $1/N_c$. In particular, this implies the assumption that the η' can still be considered as an approximate GB. The framework predicts that the two-photon decays involve two mixing angles (two-mixing angle scenario [Kr98]). The decay constants of the η and η' associated with matrix elements of the two axial currents $j_{A_8}^\mu$ and $j_{A_0}^\mu$ are given by:

$$\begin{aligned} F_\eta^8 &= \cos\theta_8 F_8 & F_\eta^8 &= \sin\theta_8 F_8 \\ F_\eta^0 &= -\sin\theta_0 F_0 & F_\eta^0 &= \cos\theta_0 F_0. \end{aligned} \quad (62)$$

There is also a new low energy constant, t_1 , to be taken into account at next to leading order in the chiral expansion. It can be estimated using QCD sum rules ($t_1 = -F_\pi^2/m_\rho^4$). With this, the

decay amplitudes into two photons defined in equation 60 become:

$$\begin{aligned}
A_{\eta\gamma\gamma} &= \alpha\left(\frac{1}{24\pi F_0 F_8} \sec(\theta_0 - \theta_8)(\sqrt{3}F_0 \cos \theta_0 - 2\sqrt{6}F_8 \sin \theta_8)\right. \\
&\quad \left. - \frac{\pi}{18\sqrt{3}F_\pi} t_1((4M_K^2 - 7M_\pi^2) \cos \theta + 2\sqrt{2}(M_K^2 + 2M_\pi^2) \sin \theta)\right) \\
A_{\eta'\gamma\gamma} &= \alpha\left(\frac{1}{8\sqrt{3}\pi F_0 F_8} \sec(\theta_0 - \theta_8)(2\sqrt{2}F_8 \cos \theta_8 + F_0 \sin \theta_0)\right. \\
&\quad \left. + \frac{\pi}{18\sqrt{3}F_\pi} t_1(2\sqrt{2}(M_K^2 + 2M_\pi^2) \cos \theta + (-4M_K^2 + 7M_\pi^2) \sin \theta)\right)
\end{aligned} \tag{63}$$

Here, θ is the state mixing angle defined earlier in equation 62.

The fact that there is a well defined theoretical framework makes it very important to study the η and η' with high precision as a means to further understand fundamental aspects of QCD. In particular, more precise measurements of $\Gamma(\eta \rightarrow \gamma\gamma)$ and $\Gamma(\eta' \rightarrow \gamma\gamma)$ are crucial to the understanding of the mixing of the two mesons and their decay constants. Indeed, given the shortage of other observables that could be measured with a precision close to that of the two-photon partial widths, these are natural inputs that should be determined with good precision. It should be emphasized that more precise inputs at this level will imply a corresponding improvement in the determination of other important observables such as the decays $\eta \rightarrow \pi\pi\pi$.

Measurements of the η width have been carried out using the Primakoff effect [Br74] and $\gamma - \gamma$ fusion in $e^+ - e^-$ colliders [PDB]. These determinations are in clear disagreement. The η' width, on the other hand, has only been measured in $e^+ - e^-$ colliders [PDB]. The current results for the widths, as listed in the Particle Data Book are:

$$\Gamma(\eta \rightarrow \gamma\gamma)_{\text{Primakoff}} = 324 \pm 46 \text{ eV}$$

$$\Gamma(\eta \rightarrow \gamma\gamma)_{\text{Collider}} = 511 \pm 26 \text{ eV}$$

$$\Gamma(\eta' \rightarrow \gamma\gamma)_{\text{Collider}} = 4.27 \pm 0.19 \text{ keV}.$$

Using these inputs, a recent analysis [Go02] determines $\theta = -12^\circ$, $\theta_8 \sim -20^\circ$, $\theta_0 \sim \pm 3^\circ$, $F_8 \sim 122 \text{ MeV}$, and $F_0 \sim 116 \text{ MeV}$. These have, however, rather large errors. A new high quality Primakoff measurement of the η decay and a first Primakoff measurement of the η' can lead to a much more precise determination of these quantities.

One important question to ask is: What would be the impact of a more precise measurement of the two-photon partial widths? Right away, it would imply a corresponding improvement in the determination of the rest of the partial widths, as these are determined using the two-photon widths and the corresponding branching fractions. This would therefore have wide ranging implications. One set of decays that is particularly important is $\eta \rightarrow \pi\pi\pi$ (two different final states), which is driven by isospin breaking, and thus gives access to the quark mass ratio $(m_u - m_d)/m_s$. Over time, the theoretical analysis of this decay has progressed to the point that now rather definite predictions can be made [An96]. However, substantial discrepancy remains with the corresponding partial

widths determined in the fashion just mentioned, with the theoretical width being smaller than the experimental one. One important issue to be clarified here is whether the quoted experimental width $\Gamma(\eta \rightarrow \gamma\gamma)$ is too large, or whether the convergence of the chiral expansion is not as good as expected. A more precise measurement would thus clarify this issue. Note that the decay $\eta \rightarrow \pi\pi\pi$ plays a crucial role in determining the quark mass ratio m_u/m_d . In reference [Le96], the ratio Q given by:

$$Q^2 = \frac{m_s^2 - \hat{m}^2}{m_d^2 - m_u^2}, \quad (64)$$

where $\hat{m} = (m_u + m_d)/2$, was studied in detail. This ratio is sensitive to isospin breaking and it can be determined by the following ratio involving meson masses:

$$Q^2 = \frac{M_K^2}{M_\pi^2} \frac{M_K^2 - M_\pi^2}{(M_{K^0}^2 - M_{K^+}^2)_{QCD}} [1 + O(m_{quark}^2)] \quad (65)$$

The difficulty in extracting Q from this relation arises from the uncertainties in the electromagnetic contributions to the $K^0 - K^+$ mass difference. Another way to extract Q is by means of $\eta \rightarrow \pi\pi\pi$ decays which have negligibly small electromagnetic corrections due to chiral symmetry. The second approach thus represents a more sensitive probe of the symmetry breaking generated by $m_d - m_u$, and has the potential to deliver accurate quark mass ratios. As emphasized in [Le96], the main errors in the determination of Q using $\eta \rightarrow \pi\pi\pi$ decays is due to the experimental uncertainty in the partial width $\Gamma_{\eta \rightarrow \pi\pi\pi}$ which is determined by the two-photon width $\Gamma_{\eta \rightarrow \gamma\gamma}$ and the branching ratio. The two different methods of measuring $\Gamma_{\eta \rightarrow \gamma\gamma}$ (photon-photon collisions and Primakoff effect) yield conflicting results, as is shown in Fig. 136. This is one important example of the impact that a more accurate measurement of the η and η' two-photon widths would have for determining fundamental parameters of QCD. One of the most interesting questions has to do with the nature of the η' : is it, after all, an approximate GB or not? More precise measurements together with the theoretical framework we have in place would help answer that question via a global analysis of the different processes involving the η and η' . For instance, if such an analysis shows that the size of the $1/N_c$ corrections is natural, this would imply that it is consistent to think about the η' as an approximate GB. As such, it is clear that a more precise experimental knowledge of the two-photon partial widths will have an important impact in our understanding of fundamental issues in QCD.

The present experimental knowledge of the η meson width is presented in Fig. 137[PDB], along with the projected measurement which could be made with 12 GeV at Jefferson Lab. Most of the measurements in the figure have been performed using two photon interactions in e^+e^- collisions. One exception is the Cornell measurement of the η width [Br74] via the Primakoff effect. This gives a width which is significantly lower (at the 3σ level) than those from e^+e^- collisions. Using the same apparatus, the Cornell group measured the $\Gamma(\pi^0 \rightarrow \gamma\gamma) = 7.93 \pm 0.39$ eV, in good agreement with the world average value of 7.74 ± 0.55 eV. As such, the η width should be remeasured by the Primakoff process using state-of-the-art experimental techniques to resolve this discrepancy. The η' two photon width, in contrast, has been only measured in collider experiments which have provided an internally consistent data set. In view of the inconsistency between the two methods for the η , we also plan to measure the η' width with the Primakoff technique.

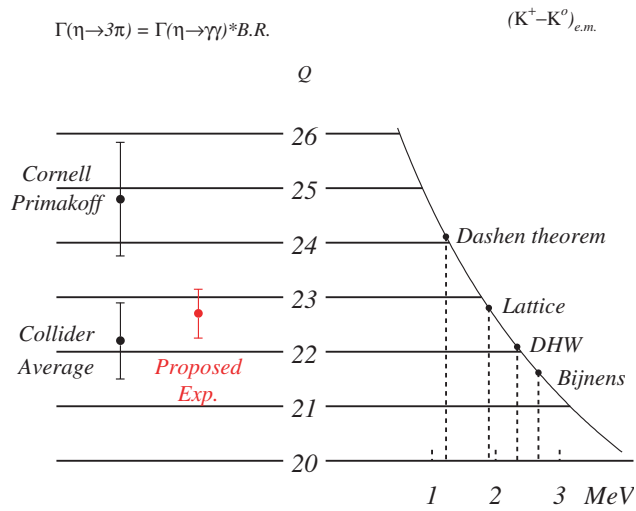


Figure 136: The importance of $\Gamma_{\eta \rightarrow \gamma\gamma}$ in the measurement of Q . The l.h.s. indicates the values of Q corresponding to the Primakoff and collider experimental results for the $\Gamma_{\eta \rightarrow \gamma\gamma}$ as well as what could be obtained with 12 GeV at Jefferson Lab. The r.h.s. shows the results for Q obtained with four different theoretical estimates for the electromagnetic self energies of the kaons. Taken from Ref. [Le96].

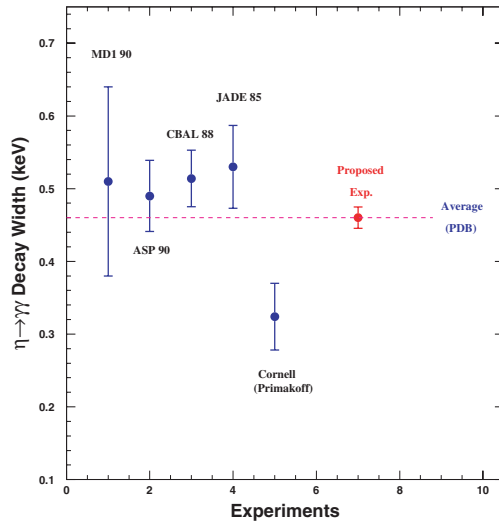


Figure 137: Two-photon decay width for the η meson. Points 1 through 4, are the results of e^+e^- collisions (for references, see[PDB]), point 5 is the result of a Primakoff experiment[Br74]. The dashed line indicates the Particle Data Book average based on these five points. Point 7 is the expected error for Jefferson Lab with 12 GeV, arbitrarily plotted to agree with the Particle Data Book average value. The plotted uncertainties combine the statistical and systematic errors in quadrature.

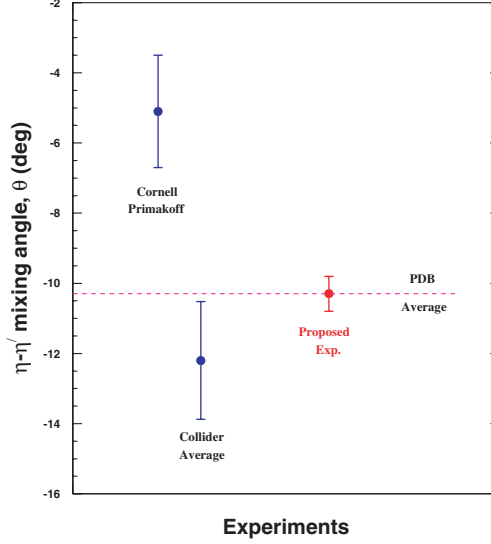


Figure 138: The $\eta - \eta'$ mixing angle as determined by a previous Primakoff measurement, $\gamma - \gamma$ collisions, and the projected result with the Jefferson Laboratory 12 GeV upgrade.

Figure 138 shows the mixing angle, θ , based on the Cornell Primakoff measurements and the collider experiments. In the figure, the mixing angles were calculated in the three mixing angle scenario of reference [Go02], (see equation 62), and the resulting angle θ is plotted. The rightmost (red) point shows the expected precision which could be obtained with 12 GeV at Jefferson Lab, projected to the Particle Data Book Average. As demonstrated in the figure, these new measurements would not only resolve the discrepancy between the previous measurements, but would greatly increase the experimental precision of this important mixing angle.

We propose to use a tagged photon beam obtained from the 11 GeV electrons to measure the widths of the $\eta, \eta' \rightarrow \gamma\gamma$ decays via the Primakoff effect in which pseudoscalar mesons are produced by the interaction of a real photon with a virtual photon from the Coulomb field of the nucleus. The formation of mesons will be identified through the invariant mass of two decay photons from the $\eta/\eta' \rightarrow \gamma\gamma$ reaction, and the meson production angles will be reconstructed by detecting the η/η' decay photons along with the additional constraint provided by a precise knowledge of the incident photon energy.. The production of mesons in the Coulomb field of a nucleus by real photons is essentially the inverse of the decay $\eta, \eta' \rightarrow \gamma\gamma$, and the cross section for this process thus provides a measure of the η, η' two-photon decay widths.

For unpolarized photons, the Primakoff cross section is given by[Be70]:

$$\frac{d\sigma_P}{d\Omega} = \Gamma_{\gamma\gamma} \frac{8\alpha Z^2 \beta^3 E^4}{m^3 Q^4} |F_{e.m.}(Q)|^2 \sin^2 \theta_m \quad (66)$$

where $\Gamma_{\gamma\gamma}$ is the decay width of the η or η' , Z is the atomic number, m , β , θ_m are the mass, velocity and production angle of the mesons, E is the energy of the incoming photon, Q is the momentum transferred to the nucleus, and $F_{e.m.}(Q)$ is the nuclear electromagnetic form factor, corrected for final state interactions of the outgoing η or η' .

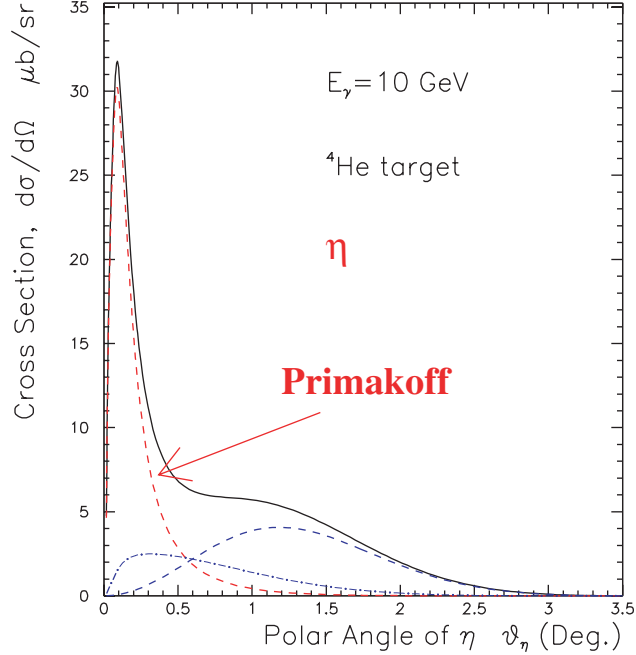


Figure 139: Differential cross sections (electromagnetic and nuclear) for the $\gamma + {}^4\text{He} \rightarrow \eta + {}^4\text{He}$ reaction at small angles at 10 GeV. The solid line is the total differential cross section from all the processes, the red dashed line is from Primakoff process, the blue dashed line is from the nuclear coherent process, and the blue dot-dash line is from the interference of the Primakoff and nuclear coherent processes.

In addition to the Primakoff effect, mesons are coherently produced in the nuclear hadronic field. There is also an interference between the strong and Primakoff production amplitudes. The cross section for the Primakoff effect to produce an η on ${}^4\text{He}$ is presented in Fig. 139 where these effects can be seen. The classical method of extracting the Primakoff amplitude from the measured differential cross sections in the forward direction relies on the different characteristic behaviors of the production mechanisms with respect to the production angle. The Primakoff cross section is zero for mesons emitted along the incident photon direction, has a sharp maximum at a very small angle, and falls at larger angles as shown in the figure. It is proportional to Z^2 , and its peak value is roughly proportional to E^4 . The nuclear coherent cross section for spin zero nuclei is also zero in the forward direction, but has a broad maximum outside the angular range of the Primakoff effect, and falls at larger angles as shown in Fig. 139, where the amplitudes are normalized to the Cornell data [Br74]. However, there are still two types of contributions under the Primakoff peak—the extended tail of the nuclear coherent mechanism, and the interference term between the two amplitudes as described above. The interference term amounts to a relatively large contribution and is also more difficult to identify since in addition to the knowledge of both amplitudes, it also requires knowing the relative phase between them. Therefore, a high precision determination of the contribution from the background amplitudes under the Primakoff peak requires good experimental information on the nuclear amplitude outside of the Primakoff region. This can be experimentally achieved by using very light spin zero nuclei as production targets. Since form factors for light

nuclei fall slowly with momentum transfer, such targets are well suited for measuring the nuclear part at large angles, thereby determining the contribution under the Primakoff peak.

Compared to the Primakoff effect to produce a π^0 , η production has a significantly smaller cross section and peaks at relatively larger production angles. This is a consequence of the much larger mass of the η which increases the momentum transfer at a given production angle. As a result, the Primakoff peak is harder to distinguish from the nuclear coherent peak. There are two ways to ameliorate this problem. One is to go to higher photon energies, which, in addition to increasing the Primakoff cross section ($\sigma_P \propto E^4$), will push the Primakoff peak to smaller angles ($\theta_{Primakoff} \sim m^2/2E^2$) as compared to those of the nuclear coherent effect ($\theta_{NC} \sim 2/EA^{1/3}$). As such, the proposed 12 GeV upgrade to the CEBAF accelerator is vital to these measurements. Another improvement is to use lighter targets such as 1H , 4He or ^{12}C , which are more bound compared to heavier nuclei, thereby enhancing coherency. In addition, due to the A dependence just mentioned, one would expect the nuclear coherent mechanism to peak at larger angles for lighter nuclei. We argue that by simultaneously going to higher photon energies and using lighter Primakoff production targets, one can make clean measurements of the widths.

We are suggesting a simultaneous measurement of the differential cross sections at forward angles on two targets: the proton and 4He . 4He has several advantages over other targets. First, it is a very compact nucleus (with a nucleon threshold of ~ 20 MeV), which will greatly enhance coherent production. Second, its form factor is very well known and falls slowly with momentum transfer. In addition, it is a spin zero nucleus, which will suppress the spin flip amplitude contribution close to zero degrees. The nuclear coherent amplitude in principle can be expressed in terms of the single-nucleon photoproduction amplitudes, properties of the nuclear ground state, and the interaction of mesons in nuclei[En64]

The use of hydrogen and helium targets will greatly help to solve the difficulties of the Cornell $\eta \rightarrow \gamma\gamma$ experiment to extract the coherent contribution under the Primakoff peak. As a production target, hydrogen is especially promising because it makes possible the selection of exclusive $\pi^0 p$ events through a missing mass cut. In principle this can be done with the many-body nuclear targets, but in practice there is the complication due to inelastic transitions and breakup channels at low excitation energy. For the nuclear targets, dynamical considerations (*i.e.* momentum transfer and the nuclear form factors) are usually invoked to ensure that coherency is satisfied to a high degree, whereas for the proton target it will be possible to guarantee coherency through kinematic cuts. The missing mass resolution that can be expected in a 12 GeV experiment, and how that resolution can be optimized, is presently under study.

The cross section calculations that are needed for a proton target are in progress. In the proton case, it is important to consider both charge and magnetic scattering from the target[Ha89], unlike the situation for a spin zero nucleus such as 4He where there is no magnetic contribution. For the coherent background amplitude, which is expected to be dominated by ρ and ω exchanges, calculations based on the Regge model developed by Vanderhaeghen, Guidal, and Laget [Va98] will

be performed. This formalism has been successfully used in extractions of the pion electromagnetic form factor from pion electroproduction data. Finally, it should be noted that a proof-of-principle exists for doing a Primakoff experiment on the proton. In the early 1970's a group at DESY measured forward π^0 photoproduction on the proton [Br70]. Their data clearly exhibit a Primakoff peak at forward angles, and the pion lifetime obtained from the data agrees, within quoted errors, with the accepted value.

In addition to these radiative width measurements, we plan a related program to study the $\gamma\gamma^*P$ vertex, where P represents the π^0 , η , or η' pseudoscalar mesons and γ^* is a virtual photon. Such measurements will enable one to study the transition regime from soft nonperturbative physics to the hard processes of perturbative QCD. We propose to measure the photon momentum dependence of the form factors $F_{\gamma\gamma^*P}(Q^2)$ and thereby map out an extension to the axial anomaly to provide a clean test of QCD predictions for exclusive processes. Measurements of the π^0 , η and η' transition form factors at very low Q^2 ($\sim 0.001\text{--}0.5\text{ GeV}^2$) are particularly important to allow a model independent extraction of the slope of the transition form factor, which measures the size of the meson's electromagnetic interaction radius. Currently, there is no first principles theoretical determination of the form factors. In ChPT there are two sources of contributions [Bi88]. One is the long distance contribution from meson loops, and the other is a counterterm or short distance contribution. ChPT pins down the first, and for the second a model is needed. The long distance contributions are small, as they only provide a small fraction of the fall off of the form factor. The simplest model is to neglect the long distance contributions and assume a vector meson dominance (monopole) type form factor,

$$F_\pi = \frac{1}{1 + Q^2/m_V^2}, \quad (67)$$

where m_V is the mass of the vector meson. Using such a model, the available data at high Q^2 fit very well with a scale $m_V \sim 0.75\text{--}0.85\text{ GeV}$. The vector meson dominance (VMD) model therefore provides an excellent fit to the current data ($Q^2 > 0.6\text{ GeV}^2$).

A determination of the slope of the π^0 form factors at low Q^2 would allow one to uniquely fix a low energy constant $\mathcal{O}(p^6)$ in the effective chiral Lagrangian[Bi88, Mo95]. By limiting the range of extrapolation to the photon point, measurements of the π^0 , η and η' transition form factors at very low Q^2 ($\sim 0.001\text{--}0.5\text{ GeV}^2$) are particularly important to measure the size of the meson's electromagnetic interaction radius in a model independent manner. With a measurement of the η and η' form factor slopes one could also have a clear test of how good the U(3) flavor symmetry implied by the large N_c limit holds. In addition, one important reason to better understand the transition from factors of π^0 , η and η' is that pseudoscalar exchange is the major contribution to the hadronic light-by-light scattering part of the muon anomalous magnetic moment[Ma02], and is thus clearly crucial for measurements of a_μ that search for “new physics” beyond the Standard model.

A number of experiments have been performed to measure these transition form factors. Exist-

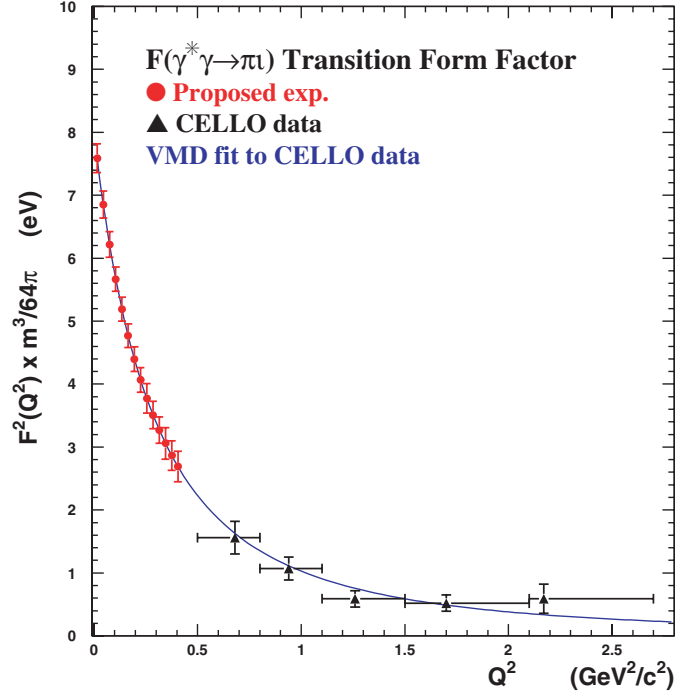


Figure 140: The π^0 transition form factor. The proposed points are projected to the VMD prediction with expected total errors. CELLO data are from reference[Be91].

ing data in the low and intermediate regions, however, are quite poor. The CELLO collaboration at PETRA has measured $F_{\gamma^*\gamma P}$ in the space-like region at large momentum transfers using the reaction $e^+e^- \rightarrow e^+e^-P$ [Be91]. In this experiment, two photons are radiated virtually by the colliding e^+e^- beams. One of the virtual photons is close to real and the other has a larger Q^2 and is tagged by the detection of an e^+ or e^- . Measurements were taken at momentum transfers ranging from 0.62 to 2.17 $(GeV/c)^2$, and the value of a was deduced by extrapolation under the assumption of vector meson dominance. The authors quote values of $a_{\pi^0} = 0.0325 \pm 0.0026$, $a_\eta = 0.428 \pm 0.063$, and $a_{\eta'} = 1.46 \pm 0.16$. Only statistical errors have been taken into account in these results, with systematic errors estimated to be of the same order as the statistical error. The results of these measurements, along with projected low Q^2 results from Jefferson Lab, are shown in Fig. 140 for the π^0 and in Fig. 141 for the η^0 , with the corresponding fits to $F_{\gamma^*\gamma P}$. From the plots, it is clear that any extraction of the slope parameter at $Q^2 = 0$ which relies on the experimental data at relatively large Q^2 is highly model dependent. Data covering the higher Q^2 region from 2 to 20 GeV^2 on these mesons have also been reported by the CLEO collaboration[As95]. Nevertheless, despite the theoretical interest in pseudoscalar meson form factors, the experimental situation remains incomplete. The low and intermediate momentum transfer region for these mesons is largely unexplored experimentally. While the L3 Collaboration has some results (with very poor Q^2 resolution) in the low Q^2 region for the η' , low and intermediate Q^2 data on the π^0 and η are totally lacking. The advent of 12 GeV electrons at Jefferson Lab, however, will make such studies possible.

In the time-like momentum transfer region, a number of experiments aimed at measuring

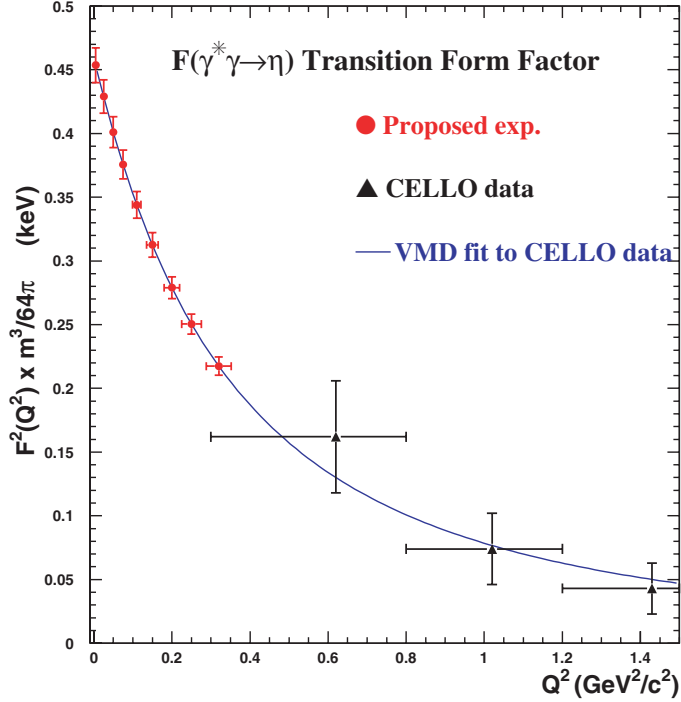


Figure 141: The η transition form factor. The proposed points are projected to the VMD prediction with expected total errors, in comparison with CELLO data[Be91].

the form factor slope a have been performed utilizing the π^0 and η Dalitz decay $\pi^0/\eta \rightarrow e^+e^-\gamma$ reaction [PDB]. The amplitude for this process involves the $F_{\gamma^*\gamma P}$ form factor which, in the usual linear expansion

$$F(x = \frac{m_{e^+e^-}^2}{m_P^2}) \approx 1 + a \frac{m_{e^+e^-}^2}{m_P^2}, \quad (68)$$

where m_P is the pseudoscalar meson mass. Such experiments suffer from small kinematically accessible ranges and significant backgrounds, and they require large final-state radiative corrections. The Particle Data Book quotes a value of $a = 0.032 \pm 0.004$ for the π^0 , in agreement with vector meson dominance. The small error is surprising since the published values for the slope range from -0.24 to $+0.12$ and it would appear that even the sign of the form factor slope has not been well determined.

In 1989, Hadjimichael and Fallieros[Ha89] suggested that the virtual Primakoff effect could access additional fundamental information about the pion, as the cross section is proportional to $|F_{\gamma^*\gamma\pi^0}(Q^2)|^2$. They examined the sensitivity of the π^0 Primakoff cross section to a for energy transfers up to 1.6 GeV. They saw only moderate sensitivity and noted that the cross section is optimized for $\theta_e \rightarrow 0$ and $\theta_\pi \rightarrow 0$ whereas pion energies above 2 GeV are favored for probing the $\gamma^*\gamma\pi^0$ vertex. We have extended these calculations to kinematical ranges available with the proposed 12 GeV electron beam at Jefferson Lab and note that good sensitivity to the $\gamma^*\gamma P$ form factor is present. The quality of data one can expect with a 12 GeV electron beam and a state-of-the-art electromagnetic calorimeter at Jefferson Lab is shown in Figs. 140 and 141.

In summary, we have described a comprehensive program to measure the two photon decay widths and transition form factors of the pseudoscalar mesons (π^0, η, η') which would be possible with the advent of 12 GeV CW electron beams at Jefferson Lab. The radiative width measurements will have a significant impact on the experimental determination of fundamental parameters of QCD, namely the light quark masses (m_u, m_d, m_s) and on the magnitude of $\eta - \eta'$ mixing. At a more general level, these measurements impact the issue of spontaneous chiral symmetry breaking in QCD, and the intriguing question of whether the η' meson can be considered as a GB in the combined chiral and large N_c limits. The proposed measurements of the π^0, η and η' transition form factors at very low Q^2 ($\sim 0.001\text{--}0.5 \text{ GeV}^2$) would provide information on the spatial distribution of the axial anomaly for each of the mesons. A determination of the slope of the π^0 and η form factors would allow one to uniquely determine a low energy constant $\mathcal{O}(p^6)$ in the effective chiral Lagrangian[Bi88] [Mo95]. With a measurement of the η' form factor slope, one could also have a clear test of how good the U(3) flavor symmetry, implied by the large N_c limit holds. In this limit, the same low energy term determines all three transition form factor slopes. One important additional reason to better understand the transition form factors of the π^0, η and η' is that pseudoscalar exchange is the major contribution to the hadronic light-by-light scattering part of the muon anomalous magnetic moment[Ma02]. It is thus important for measurements of a_μ that search for “new physics” beyond the Standard model.